8-2018

Quantification of Hydrogen-Helium Retention in Tungsten Using Laser Induced Breakdown Spectroscopy Coupled with Laser Ablation Mass Spectrometry

Guinevere Chamberlain Shaw
University of Tennessee

To the Graduate Council:

I am submitting herewith a dissertation written by Guinevere Chamberlain Shaw entitled "Quantification of Hydrogen-Helium Retention in Tungsten Using Laser Induced Breakdown Spectroscopy Coupled with Laser Ablation Mass Spectrometry." I have examined the final electronic copy of this dissertation for form and content and recommend that it be accepted in partial fulfillment of the requirements for the degree of Doctor of Philosophy, with a major in Energy Science and Engineering.

Brian D. Wirth, Major Professor

We have read this dissertation and recommend its acceptance:

Theodore M. Biewer, David C. Donovan, Madhavi Z. Martin, Steven J. Zinkle

Accepted for the Council:

Dixie L. Thompson

Vice Provost and Dean of the Graduate School

(Original signatures are on file with official student records.)

Quantification of Hydrogen-Helium Retention in Tungsten Using Laser Induced Breakdown Spectroscopy Coupled with Laser Ablation Mass Spectrometry

A Dissertation Presented for the

Doctor of Philosophy

Degree

The University of Tennessee, Knoxville

Guinevere Chamberlain Shaw

August 2018

I dedicate this work, in its entirety, to my brothers, Richard and Frank. The years that I have spent, hard at work, was to show you that we can make a better life for ourselves. You are the only other people who understand, and for that, I am forever grateful.

Acknowledgments

I will start at the beginning, before graduate school, to thank a person that gave me a chance. Dr. Veton Kepuska, I want to personally thank you for giving me a chance to work with you during my undergrad. Even thru such distance and time, we continue to keep a relationship, and without your kindness, patience, and guidance I would not be who I am today. You took a risk and gave me a chance, and I cannot thank you enough or explain how your choice has changed my life.

I arrived in Knoxville, TN newly graduated with a BS in the dead of winter. During the previous semester, I made it my mission to get an internship at Oak Ridge National Laboratory. I was driven enough to, as a millennial would say, cold email an old plasma physicist, Dr. Dave Rassmussen. I would say in a matter of months from that email, I arrived bright-eyed and boy did he sell me the 'Fusion Dream'. Dave, you deserve a sincere thank you for encouraging me to follow my interests, even though you knew exactly what I was getting myself into. Another great idea Dave had was to hand me off to my soon to be, mentor, Dr. John Caughman, what a hoot. I must say, for a crash course in experimental plasma physics, dad jokes, and comical love to all things dinosaurs, John is one of the greatest experimentalists I've ever had the pleasure to work under. John taught me, as clique as it sounds, how to think outside the box, be imaginative, and most importantly how to be a great experimentalist. John, I can never thank you enough, and I will never forget Terry Tate, the office quarterback.

During my internship at ORNL, I finally took the plunge to apply for graduate school at the University of Tennessee. I identify the Bredesen Center as the best fit for me considering I had, and still have, a significant interest in energy policy, and so I applied to the progam. This particular transition, from internship to graduate school, identified two things about myself at the time. One, I have no idea what I want to do for research and two, I still had no idea what I want to do for research. Thankfully, John introduced me to Dr. Ted Biewer, a fellow experimentalist and jack of all trades when it comes to diagnostics. Ted immediately took me under his wing and expanded knowledge on so many measurement techniques; I cannot even begin to list. However, one specific laser-based diagnostic caught my eye, and he encouraged me to begin my research. This is when low and behold; I met Dr. Brian Wirth. Which, I will admit, in the beginning, I had no idea who he was or why he was interested in taking on an experimental graduate student who had an interest in laser-based diagnostics but no nuclear engineering background. Fast-forward a month or so; there I am sitting in front of Brian Wirth, interviewing me for the Bredesen Center. To this day, I will never forget what Brian said to me, "you have so much passion, by the end of this I hope it does not burn out".

Many great beginnings start with a strong foundation. Slowly adding weight to the base and building upward. Until you reach a point where the foundation can no longer support the weight,

but no worries, stop and repair the foundation. I began by thanking Veton, Dave, John, and Ted who helped me mature and grow as a scientist. They helped me build my foundation. Now as I finish my PhD, I must thank those who have pushed me, molded me, made me grow, made me uncomfortable, but most importantly made me realize who I am as a person and as a professional.

I first would like to thank Ted. You have contributed so much to my growth as a scientist over the past five years. Even through tough times you still provided guidance and above all patience, thank you.

I'd also like to thank Dr. Madhavi Martin for being there for me personally and professionally, I very much enjoyed our days at UT. I must say I very much admire your passion and determination. I also cannot thank you enough for all of your LIBS knowledge.

Dr. David Donovan, I remember first meeting you during your interview and again at a poster session where we argued about Langmuir probe data. Now you are well on your way to becoming a professor and also managing to deal with me asking you a million questions about various analysis technique. I admire and thank you for taking the time to work with me, help me, and guide me. I greatly appreciate your ability to make me keel over laughing even on a bad day.

I'd also like to thank Dr. Steven Zinkle. I will best describe him as an old lighthouse, and I mean no offense. Many years it stands through the good and bad, always providing light to guide the way. Your ability to be so straightforward, honest and clear is hard to come by, and I greatly appreciate the time you took to help me and give me honest, trusting advice.

Dr. Brian Wirth, our relationship has changed over the past five years. As my thesis advisor, you have provided me with unwavering support, patience, and understanding. In the beginning, you gave me space to learn and develop my skills. Now and then you would put pressure on me to push me, and as much as I did not like the discomfort, it resulted in some astounding work. I will say this one last time, not to boost your ego, but your progressiveness, aggressiveness, and sheer passion for your career are admirable and somewhat contagious. I say this to you because, on some of my worst days, I would talk to you and somehow you would convince me that I should never give up and I should keep going, and just for that I will be forever grateful.

To all my friends who are still in it, like Holly, Casey, Rhea, Abdula, Pawel, Josh, Brianne, Wendy and Patrick, I will be there for you when you need it just like you were there for me. Never be afraid to reach out. I'd also like to thank Dr. Xunxiang Hu for working with me to the very end. Also Dr. Russ Doerner, Dr. Kevin Wollar, Dr. Fred Meyers, the entire Proto-MPEX crew, and everyone from the Bredesen Center. This has been quite the adventure.

Finally, most of all I'd like to thank my best friend and husband, Mark. Your endless support, patience, and understanding these past few months have been life-saving. Your endless devotion to our dreams, your career, my career, our careers, and our life together makes me believe that all of this is achievable. I love you.

The research was sponsored by the US Department of Energy Office of Fusion Energy Science under grant DE-AC05-00OR22725 with UT-Battelle LLC, and grant DOE-DE-SC0006661 with the University of Tennessee, Knoxville. This research was also sponsored by the Laboratory Directed Research and Development Program of Oak Ridge National Laboratory, managed by UT-Battelle, LLC, for the U.S. Department of Energy.

stay strong through your pain
grow flowers from it
you have helped me
grow flowers out of mine so
bloom beautifully
dangerously
loudly
bloom softly
however you need
just bloom

-milk and honey, rupi kaur

Abstract

Tungsten (W) has been selected for the ITER divertor because of its high melting temperature, low sputtering yield, and high thermal conductivity. During deuterium/tritium (D/T) plasma exposure in ITER, a large flux ($10^{24} m^{-2} s^{-1}$) of relatively low-energy (100 eV) of D/T plus helium (He) will strike the divertor. The resulting plasma surface interactions (PSI) will lead to surface damage and deformation such as bubble formation, surface blistering and/or erosion, and tritium retention. Experiments have shown that the formation of helium bubbles can have a direct effect on hydrogen retention, although the extent is not fully known. This dissertation has developed and demonstrated two new, complementary laser-based characterization techniques (LIBS and LAMS) for assessing gas concentrations in nuclear materials as a function of spatial position (depth below the surface), with an emphasis on assessing the He-H interaction synergies in tungsten that are expected to impact tritium retention in the ITER divertor and future fusion reactors. In the newly established ultrahigh vacuum setup, the LIBS capability is coupled with the ability to simultaneously pump the ablated gases into a quadrupole mass spectrometer in an existing thermal desorption system (TDS) to simultaneously (although with a small time delay) measure the ion current of the detected gas species in a QMS, this capability we define as LAMS. The gas fluxes measured in LAMS are converted to an absolute quantity of measured gas per laser ablation pulse through calibration with known leak volumes in the TDS. Results of gas concentration as a function of depth in tungsten are shown following exposure to various fluences and plasma configurations, as well as compared to other surface gas evaluation techniques. Altogether this dissertation provides significant new results that: demonstrate the ability of LIBS and LAMS to perform depth dependent gaseous species concentration measurements in nuclear materials; offer new data that comprehensively reflects the complex He-H synergistic interactions and the role of He on tritium retention expected in the ITER tungsten divertor; and provide depth dependent concentration measurements (in addition to integrated retention values) for validation of multiscale models.

Table of Contents

List of Tables

List of Figures

Chapter 1

Introduction and Motivation

Portions of this Chapter were previously published in journal Applied Surface Science. Shaw, G., Bannister, M., Biewer, T. M., Martin, M. Z., Meyer, F., and Wirth, B. D. (2018). The detection of He in tungsten following ion implantation by laser-induced breakdown spectroscopy. Applied Surface Science, 427, 695-703.

1.1 World Energy Outlook

In 2013 the U.S. Energy Information Administration (EIA) projected that world energy consumption would increase 56% by 2040 (from 524 quadrillion British thermal units (Btu) to 820 Btu)[1, 2]. Under-developed countries that do not participate in the Organization for Economic Cooperation and Development (OCED) will contribute a majority of the growth in energy consumption due to positive economic development. These non-OCED countries are expected to rely predominately on fossil fuels, which would correspondingly increase energy-related carbon dioxide emissions. Nuclear and renewable energy are the worlds fastest-growing energy sources, increasing by 2.5% per year. However, fossil fuels continue to supply almost 80% of the global electricity, and they are expected to remain the main source. Carbon dioxide emissions are projected to grow tenfold unless the global energy consumption shifts from fossil fuels to a more diverse carbon-free energy portfolio [1].

The development and use of a diverse energy portfolio for the OCED has been either encouraged or mandated to offset the use of fossil fuels in these developing countries [1]. As a part

of the global, diverse carbon-free energy portfolio, OCED countries have invested in the research and development of alternative energies like solar, biofuels, wind, nuclear, hydropower, carbon capture sequestration, natural gas, and fusion. This will have a significant contribution to reducing the consumption of fossil fuels from the projected rate [3]. The 2015 Paris Climate Change talks specifically discussed ways to decrease emissions while still providing additional energy to meet the increasing demand [4]. A sure way to produce clean energy and meet the growing demand is fusion energy generation. The larger question is, however, will fusion be ready in time?

1.2 Prospects of Fusion Power

The prospects for fusion energy as a future source of electricity will depend largely on the total cost to build and generate fusion concerning the future energy market [5]. The current energy market is dependent on the rate of economic growth, the amount of energy generated, the consumption of that energy, ancillary service requirements, and demand-side energy management. Fusion is expected to produce electricity at a rate of about 1,000 megawatts per generation unit, which is similar to what fission power plants produce. A positive attribute of fusion is that it is a low carbon energy source. The current market is dominated by fossil fuel energy sources, which have a negative effect on current and future climate change. The EPA [3] and the Paris Climate Talks [4] have encouraged a global shift from fossil fuels to a less carbon-intensive energy portfolio; however, it is difficult for many countries, including the United States, to accomplish because coal and oil are more abundant, cost-effective, and easily integrated into the electrical grid than alternative energies like nuclear, solar, wind, hydropower, and fusion. Since fusion is low-carbon emitting, in both construction and waste, it makes for a viable option. In comparison to nuclear energy, fusion will likely have less radioactive waste regulation and policies that are less stringent; however, regulatory policies for fusion have yet to be written. Altogether, fusion makes a strong case as being a viable option for a future energy source. However, the road to fusion energy remains unclear.

1.2.1 The Long Road to Fusion

The theory of fusion was developed in the early 1930s, simultaneously established with nuclear fission [6]. However, as nuclear fission expanded into the energy sector, fusion has remained

behind due to several science and engineering challenges. Fusion is how the Sun creates its energy, and during the late 1930s, the scientific community spent years trying to replicate the process in a laboratory setting. However, the conditions necessary to create sustainable fusion are anticipated to be equal to that of the inner core of the sun, making fusion intrinsically difficult. Heating the fusion fuel, which is traditionally comprised of deuterium (D) and tritium (T), to approximately 200 million degrees Celsius, creates conditions at which fusion will occur. Under these conditions, all the particles are ionized and are stripped of their electrons, which are the formal characteristics of the plasma. The conventional method to contain plasma during the fusion process is magnetic confinement [7]. The National Academy of Engineering in 2016 published a report highlighting 14 Grand Challenges for Engineering in the 21st Century [8]. The second on the list of 14 provide energy from fusion, and the NAE made a note of the technology development required to overcome the main engineering challenge of plasma confinement. This challenge encompasses both basic and applied sciences such as plasma startup, plasma instabilities, steady-state plasma, burning plasma, and physical reactor components. Many facilities like the Joint European Torus (JET), National Spherical Torus eXperiment Upgrade (NSTX-U), PISCES, Prototype Material Plasma Exposure eXperiment (Proto-MPEX), and others study these issues extensively to provide solutions to these key challenges. Despite these efforts, there is still an ongoing multidisciplinary research expedition to overcome these challenges to make fusion a future energy source [6, 8–12].

1.2.2 Plasma Facing Materials

In ITER, the reactor material components like the divertor, lower baffle, upper baffle, and first wall are expected to receive average heat loads ranging from 10-20 MW/m^2 and particle fluxes from 10^{19} - 10^{24} DT/m^{2}s, respectively [6, 8–14]. While there is not a single ideal material that can withstand this environment, the primary candidates are carbon, beryllium, and tungsten. Carbon is known for its ability to withstand high heat loads and was initially expected to be used for some parts of the divertor target. However, carbon has significant issues with hydrogen retention, redeposition, and co-deposition and has been disregarded as a material candidate. Beryllium is known for its high thermal conductivity and low atomic number and is expected to be used as a wall material. However, beryllium has disadvantages such as a low melting point and high sputtering

yield, but extensive plasma-material interaction is not expected for the first wall, except for extreme disruption events. Finally, tungsten is known for its high thermal conductivity, high melting point, and low sputtering yield and is currently planned for use as the entire divertor. However, in recent studies, tungsten has shown retention of deuterium in the presence of helium which suggests retention of tritium. Also, the tungsten surface can form hair-like tendrils in the presence of helium which leads to significant erosion of the surface and large amounts of particulates such as tungsten dust [13–16].Although each material has its caveats, ITER organization selected tungsten as the divertor material. In the design of the divertor, the selection of the plasma facing materials (PFM) must be capable of protecting the vessel structure and sub-wall components from the detrimental effects of plasma-material interactions (PMI). Therefore, the divertor and PFC materials must have a high thermal conductivity, high thermal melting point, low atomic number, low erosion yield, and low hydrogen retention, which makes tungsten the ideal material candidate.

Tungsten

Tungsten has been selected for the ITER divertor [13, 14], and is the primary material of interest of this research. This research effort specifically focuses on studies and initial results investigating the tritium inventories that are expected for this material following exposure to low-energy mixed H-He plasmas. In the divertor, the tungsten is expected to be exposed to a relatively cool, but not fully detached plasma (an electron temperature, T_e = 1-100 eV, and a density, N_e = 10^{18} - 10^{21} m^{-3}) leading to ion fluxes of 10^{24} $m^{-2}s^{-1}$ [17]. The PFCs in the divertor will also experience heat loads (>10 MW/m^2) and transient events like Edge Localized Modes (ELMs) (>1 GW/m^2). These thermal stresses can lead to extensive damage to the surface, and this damage might have an impact on the hydrogen retention in the PFCs [14].

Helium Effects in Tungsten

Helium is a noble gas with an atomic mass of 4.0026 amu and its behavior in tungsten has been extensively investigated [18–37]. When energetic helium bombards and penetrates surface, the tungsten-helium electronic and atomic interaction dissipates the incoming particle‘s energy causing it to come to rest [38]. The depth of the helium particle implantation is dependent on its initial energy. Helium is inert and insoluble; and as more helium atoms penetrate the surface,

the repulsive tungsten-helium atomic interaction provides an energetic driving force for the self-clustering of helium atoms and this clustering behavior competes with the diffusion of helium back to the surface. Once helium atoms have penetrated the surface, they tend to nucleate bubbles within a few 10s of nanometers of the surface. While the atomic interaction between helium-helium is weakly repulsive, the stronger repulsive force between tungsten and helium drives the helium atoms to cluster together. Once, the helium complex reaches a critical size the cluster becomes immobile [39].

The immobility is caused by the helium cluster absorbing sufficient helium atoms to significantly exceed the force equilibrium between it and the surrounding matrix. Once the cluster reaches a critical number of helium atoms (on the order of 6 depending on proximity to surfaces) the pressure of the helium is significant enough to induce a trap mutation. A trap mutation is when the cluster forces a tungsten atom out of its matrix space and into an interstitial, creating a vacancy in the matrix [39]. This vacancy relieves the cluster pressure and allows the cluster to absorb additional helium atoms, but it also causes the cluster to become immobile. As the helium cluster grows, either by absorbing nearby clusters or single atoms, the pressure level increases such that these clusters or embryonic bubbles far exceed the equilibrium pressure. Once the pressure reaches a critical point, the cluster then expands by dislocation loop punching. Loop-punching is when the cluster can force many surrounding tungsten atoms off their matrix sites, an action formally defined as a dislocation loop. At this point the cluster/embryonic bubble will continue to grow, leading to subsurface cracking and finally bursting which releases the helium atoms leaving a crater in the tungsten surface[38, 39]. A schematic drawing illustrates these mechanisms is shown in Figure 1.1[35]. The current research, which is to investigate the effect of helium and deuterium behavior in tungsten, is primarily based around investigations into the effect of different parameters. These include surface temperature, fluence, material type, and ion energy.

Iwakiri et al.[21] showed the temperature dependence of tungsten sub-surface microstructure following low energy helium ion irradiation. Iwakiri and co-workers showed specifically the temperature dependence of dislocation loop formation during 8 keV helium ion irradiation at temperatures from room temperature to 1073 K. The fluence during these was $1x10^{19}$ He/m^2, $5x10^{19}$ He/m^{2}and $2.6x10^{19}$ He/m^2, respectively. The results showed that with increasing irradiation temperature the dislocation loop density decreased drastically while the loop size increased.

The increase in the loop size is due to the increase in interstitial loop nucleation. As the He bombardment increases so does radiation-induced vacancies which act as a sink for He. As the He-vacancy complex begins to grow any interstitial that is pushed out by the He-vacancy complex, is absorbed by the interstitial loop. From this, it can be observed that temperature plays a role in the creation of defects in W, which is critical because helium and deuterium can be trapped in such defects.

Hino et al. [38] studied whether helium retention in tungsten, at various fluences, could be reduced by thermal annealing, also known as baking. Baking is a process that common fusion experiments use to reduce impurities in their vacuum system to improve plasma performance. This entails heating the chamber walls via a glow discharge. Hino simulated the baking process using Thermal Desorption Spectroscopy (TDS), to release helium from the samples and measuring the helium as a function of temperature and time released. Figure 1.2, shows the measured TDS results from W samples exposed to three different fluences ($1x10^{21}$, $5x10^{22}$, and $7x10^{22}$ He/m^2); during

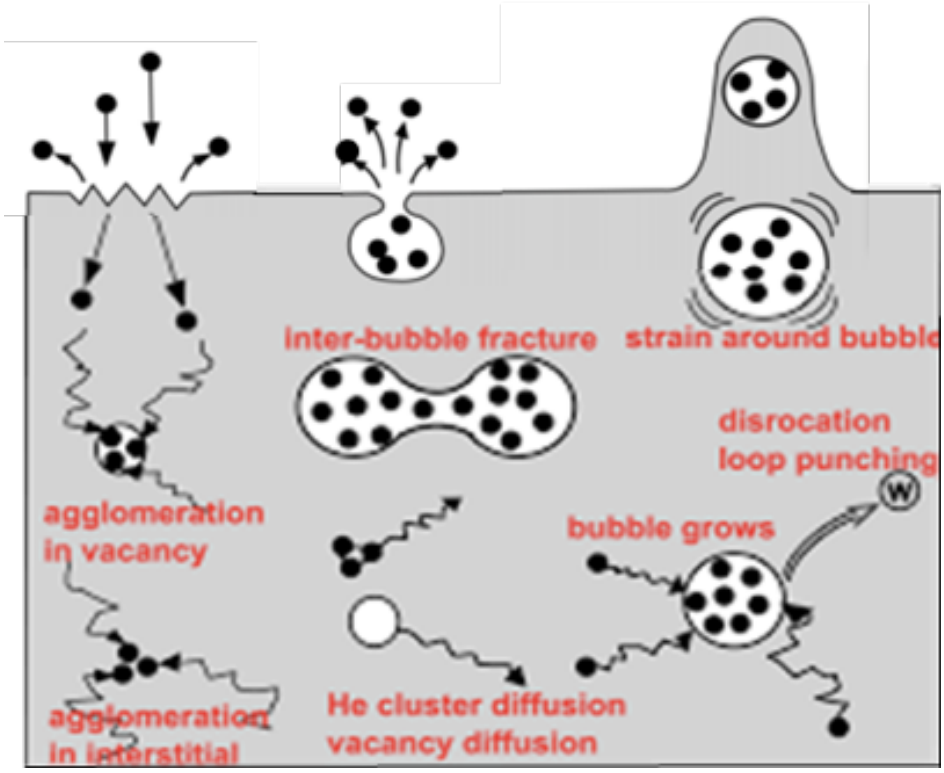

Figure 1.1: Schematic Illustration describing the process of helium implantation and how the helium evolves, as reproduced from Ref.[40].

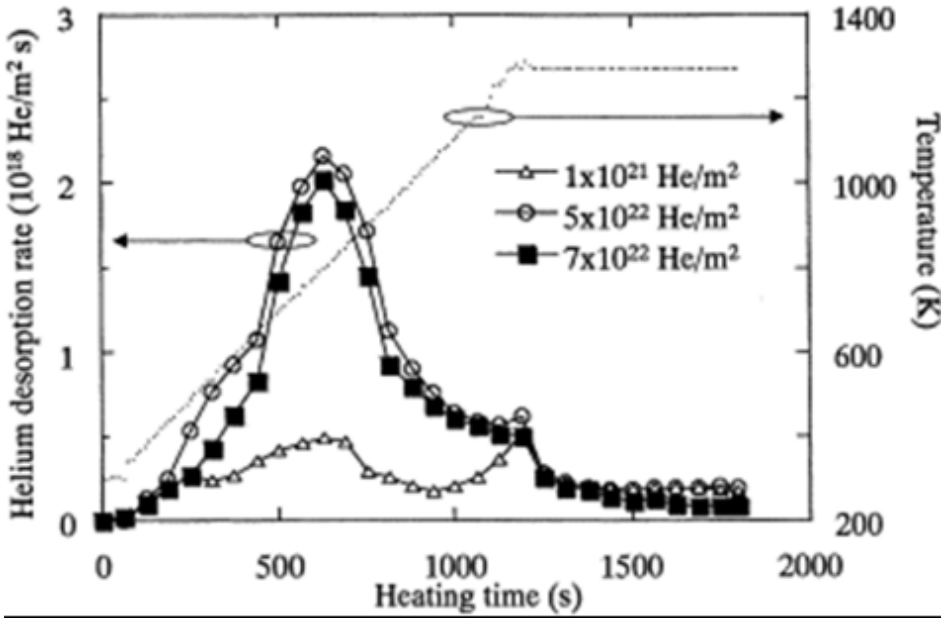

Figure 1.2: TDS measurements of He desorption rate from three exposed W samples with a variation in fluence, as reproduced from Ref. [38].

the exposure, the sample was kept at room temperature, and the ion energy was 5 keV. The thermal desorption heating ranged from room temperature to 1273 K at a heating rate of 50k/minute. Using this technique, Hino showed that helium could be desorbed at common baking temperatures of 500 to 800 K; however, it was not possible to completely desorb all of the helium retained in the W. For example, in the sample exposed to the highest fluence (7x10^{22} He/m^2), only 2x10^{22} He/m^2 was released. These findings support the investigation of another characterization technique to investigate helium retention in W.

Nishijima et al. [25] investigated helium bubble formation in single crystal and powder metallurgy W exposed to helium plasma at ion energies below 30 eV and particle flux above 1x10^{21} m^{-2}s^{-2}. The ion energies investigated were 1, 5, 10 and 30 eV. It is fundamentally known that single crystal W, which has fewer defects than the powder metallurgy W, is, therefore, less likely to retain helium or deuterium than its power metallurgy counterpart. However, the extent of this discrepancy was unknown, motivating the experiment. Nishijima exposed the samples at the parameters mentioned above and measured bubble size and hole size using TEM. Their experiment demonstrated that the investigated parameters were sufficient to produce bubbles and holes at the surface. Furthermore, for helium implantation at energies above 25 eV, there was no qualitative difference between the two types of W. This indicates that the native defects in W do not play a role

in bubble and defect formation when the W is exposed to plasma with large helium implantation fluxes. This motivates the proposed research into the role of material type at exposure parameters outside of those investigated by Nishijima; with parameters expected in ITER.

Research into the impact of ion energy is explained in an experiment performed by Nishijima et al. [41] which investigated the incident helium ion energy dependence on bubble formation in W. The ion energy varied from 1 to 64 eV at 9 discrete steps (1, 6, 7, 9, 12, 18, 26, 60, 64) in a high density plasma ($>10^{19}$ m^{-3}) performed at the linear plasma simulator NAGDIS-II. In this experiment, bubbles and holes were observed in W at incident energies above 18 eV. This indicates that there are three important characteristics in bubble formation: vacancy concentration, mobility of vacancies, and the total concentration of helium in W; however these three are only important if the experiment is over the temperature and energy thresholds of W. This threshold for ion energy was indicated to be 12 eV, thereby acting as a lower limit for the subsequent research.

Hydrogen Effects in Tungsten

Hydrogen is a light element with an atomic mass of 1.008 amu and its behavior in tungsten has been extensively studied [18, 22, 24, 25, 27–29, 37–45]. The mechanisms that govern hydrogen isotope uptake in a tungsten divertor, are very complex and are currently being investigated. When energetic hydrogen ions bombard the tungsten surface, many of the particles are reflected, returning to the divertor plasma. The remaining particles penetrate the surface and diffuse to a depth dependent on their initial energy. The depth range for hydrogen can be longer than that of helium due to differences in the solubility and diffusivity, which govern permeation.

Hydrogen diffusion, as shown in Figure 1.3, specifically the diffusion activation energy, governs the retention and migration of hydrogen in the material. This migration can occur either back to the surface or deeper into the material. Grain boundaries, impurities, bubbles, dislocations, and cavities can trap hydrogen. Hydrogen bubble formation deep below the surface can lead to surface blistering, as discussed by Causey et al. [45]. Causey et al. showed that hydrogen in tungsten diffuses to voids, creating sinks for other hydrogen atoms. The deeper diffused hydrogen atoms form vacancies, dislocations, and voids. This can be contrasted to the near-surface hydrogen clusters, which form a pressure differential similar to the helium clusters, leading to surface cracking, blistering, and even bursting, which releases the hydrogen. Hydrogen bubble formation

and blistering at the near surface is a good indication of low to moderate hydrogen retention, because of the diffusion out of the material. Similar comprehensive reviews have shown that a tungsten divertor is a good candidate based on this diffusion effect [14, 45].

Research into hydrogen effects in W has demonstrated a similar dependence of surface temperature, fluence, material type, and ion energy characteristics on the interaction between H and W. Research performed by Alimov et al. [46] investigated the temperature dependence on deuterium retention in polycrystalline ITER grade W exposed to low energy (38 eV), high flux (10^{22} D/m^{2}s) deuterium plasma. This was done by exposing W samples to a linear plasma generator (JAEA) at various temperatures (ranging from room temperature to 815 K) then using Scanning Electron Microscopy (SEM), TDS, and Nuclear Reaction Analyses (NRA) to measure retained deuterium. NRA is an ion beam analysis technique that uses highly energetic ions to generate a nuclear reaction with an impurity of interest thereby producing an alpha particle whose energy is indicative of the impurity depth. SEM was used to investigate retention on the surface of the samples visually, TDS the total retention and NRA to investigate retention as a function of depth. The description of the observations can be best described by the different analysis techniques used, SEM found that as the temperature increased very little change was observed until 600 K, where blister size decreased from the original 2-4 microns to 0.5 microns. TDS analysis demonstrated that as exposure temperature increased the TDS peak shifted towards higher temperature, which indicates higher levels of damage to the surface and increased levels of deuterium retention. NRA was used to measure the deuterium depth profile and indicated that the near surface concentration decreased by 0.2 to 0.3 atom percent as exposure temperature increased up to 490 K, whereas the concentration at depths of 1 to 7 micrometers increased once exposure temperatures were beyond the 490 K threshold. This indicates the importance of temperature on the deuterium diffusion, permeation, and retention in W.

Doerner et al.[47] investigated fuel retention in W and saturation behavior at high fluence. The researchers utilized W polycrystalline samples and exposed them at the UCSD Pisces facility, which is a linear plasma source. Figure 1.4 shows results of the deuterium desorption as a function of temperature for the tungsten samples exposed to the fluences of 1x10^{27}, 4x10^{27}, 2x10^{28} D/m^2. This work showed that deuterium retention did not saturate, but rather increases with the square root of time. Overall, this indicates that the deuterium diffusion mechanism governs fuel retention

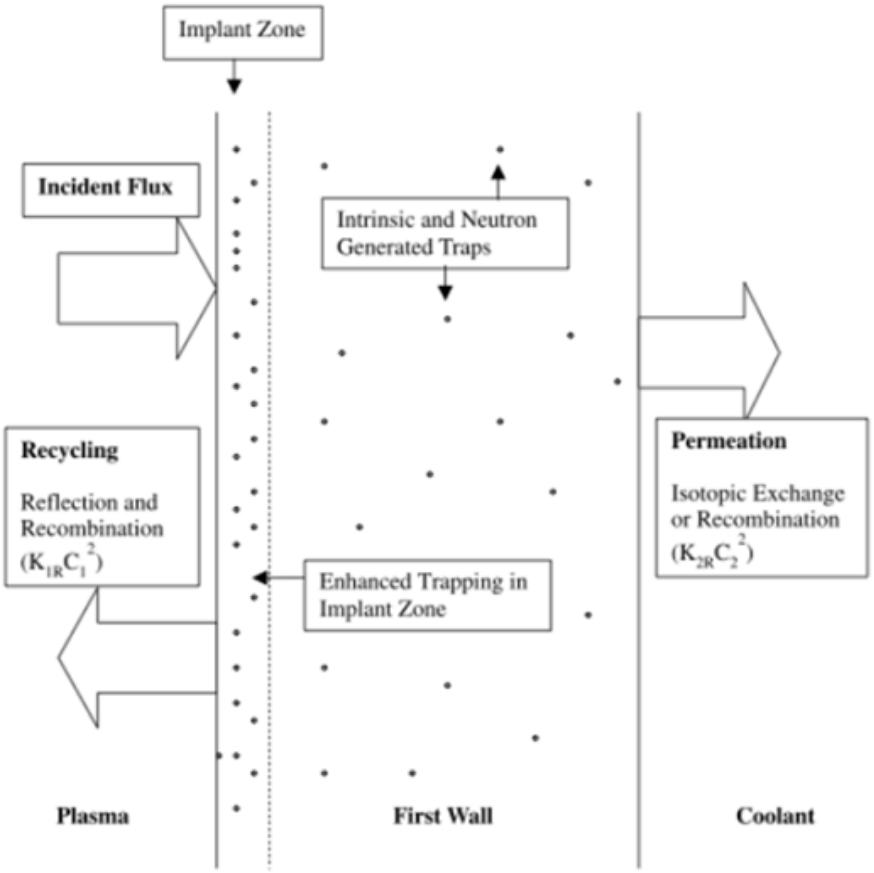

Figure 1.3: Schematic illustration identifying deuterium or hydrogen diffusion mechanisms in tungsten, as reproduced from Ref.[45].

in W and acts to inform the proposed work which will investigate if this is the case in mixed He/D (& T) plasma exposures.

Alimov et al [46] investigated deuterium retention in many different forms of tungsten, including single crystal W, powder metallurgy produced W, chemical vapor deposited W, inert plasma sprayed W, and vacuum plasma sprayed W. The samples were exposed using a deuterium ion beam at 300 K at an energy of 1.5 keV at fluences greater than or equal to $5x10^{22}$ D/m^2. For the 300 K exposures, TDS measurements indicated that the retention varied significantly from sample to sample with the single crystal W having the lowest concentration of deuterium retained, while the polycrystalline tungsten had the highest retention. NRA was also performed on the 300 K samples, measuring an average concentration of 0.1 deuterium atom percent over a 50-nanometer depth range. However, the NRA was not able to measure D concentration at deeper penetration depths. Overall, this experiment demonstrated that the retention is highly dependent on the material structure and that depth limits the use of NRA. Given this, the research in this dissertation seeks to develop a measurement technique for assessing gas concentration over an extended range of depths.

Wang et al. [48] has performed research into the effect of ion energy on deuterium retention and blister formation as a function of ion energy. These researchers used SEM to investigate samples that were exposed to an ion beam at a range of 100 eV to 1 keV, and also characterized the samples using elastic recoil detection (ERD). ERD is an ion beam analysis technique, which uses heavy energetic ions to recoil off a particle of interest, such that the measurement of the energy of the recoiled ion indicates the depth of the particle of interest. The ion implantations were performed at a normal ion incidence for 100 eV, 200 eV and 1 keV with a flux greater than $5x10^{18}$ D/m^{2}s and a fluence ranging from $1x10^{23}$ to $1x10^{25}$ D/m^2. Wang observed that ion energy had a simple effect when investigated with SEM, which was consistent with the observation by ERD. It was then hypothesized that the null result was likely due to the inability of ERD and SEM to significantly investigate as a function of depth, although it is important to highlight that these deuterium fluences are generally below the threshold for blistering of tungsten. This influences the proposed research because it points to the need to characterize the material as a function of depth below the surface.

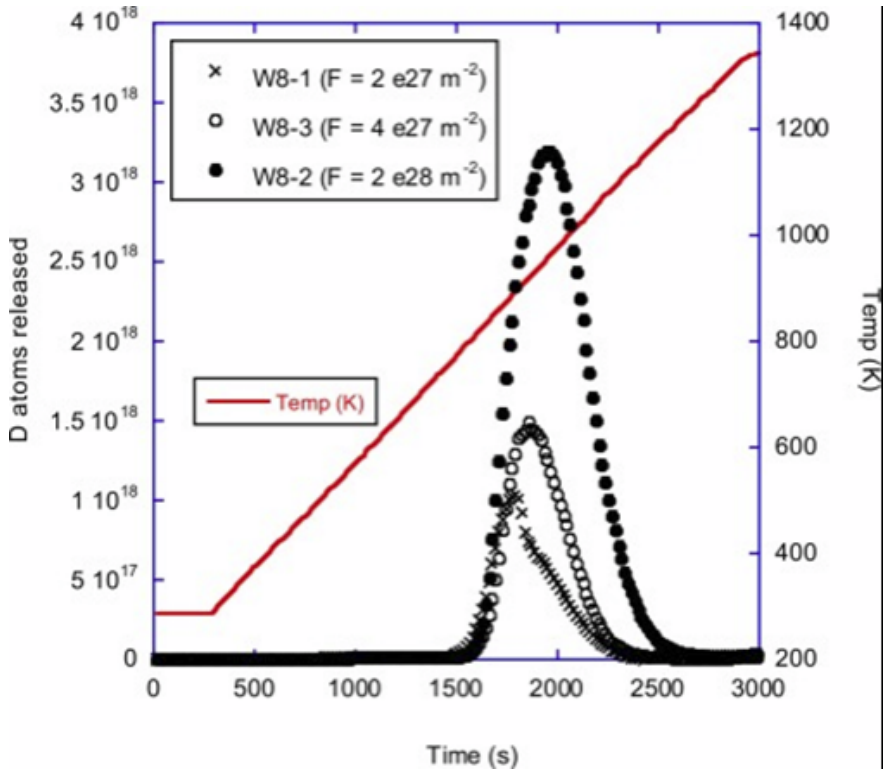

Figure 1.4: TDS measurements showing deuterium atom released on three W samples that were exposed to various fluences, as reproduced from Doerner and co-workers. [47].

Hydrogen and Helium Effects in Tungsten

The hydrogen diffusion, retention and permeation behavior is affected by the presence of helium clusters[20, 24, 30, 31, 33, 41, 45, 49–55]. Causey et. al [45] and many others [20, 24, 30, 31, 33, 41, 45, 49–55] have extensively researched and reported He-D interaction mechanisms and dependencies. If a helium bubble was near the stopping range of hydrogen, then hydrogen atoms, which would traditionally diffuse into the bulk, could be stopped by the bubbles because the bubbles act as traps, or the hydrogen would diffuse to the surface. This is beneficial because it does not allow for the hydrogen to permeate to the bulk thereby decreasing overall retention. However, if the helium bubbles are near the surface, it is possible that the bubbles will trap hydrogen and modify the H retention behavior even though H permeation may be reduced.

Research into synergistic effects of helium and deuterium in W can also be categorized as experimental efforts to evaluate the influence of surface temperature, material type, ion energy, and computational material modeling. Alimov et al. [53] investigated the temperature dependence of deuterium retention under mixed helium deuterium irradiation. This was done for varying

temperatures from 400 to 700 K (400, 460, 560, 640, and 720K) in a linear plasma source with 10% helium and 90% deuterium. The fluence was 3x10^{26} D/m^2 and the helium fluence should be approximately an order of magnitude less based on the plasma mixture. Concentration was measured as a function of depth using NRA and it was found that an increase in deuterium retention occurred at the near surface (>1 micron) and a decrease in D concentration between 1 and 7 microns for all temperatures as a result of the mixed plasma exposure compared to a profile extracted from a strictly deuterium sample as shown in Figure 1.5. This demonstrates that the presence of helium causes the deuterium diffusion and permeation behavior to be modified. This result indicates the importance of fully resolving the synergies between helium and deuterium retention as they likely interact in a non-linear fashion.

The impact of material type on retention in systems in which both helium and deuterium are present has been investigated by Baldwin et al.[24] in an experiment in which single crystal and ITER grade W were exposed to 20-60 eV mixed deuterium - helium plasma exposure in PISCES/A. In this experiment, TEM and SEM were used to image microstructure changes after plasma exposure, as a function of the plasma conditions and exposure time. This work demonstrated a minimal difference between the two different material types in both TEM and SEM. The equivalent level of damage in the single crystal sample was interpreted to be a result of the helium trapping mechanism causing increased levels of deuterium to be retained within the material. This demonstrated that the synergistic effects overcome a majority of the benefits offered by single crystalline W. This acts to motivate the following research because it demonstrates the need for further investigation to investigate conditions much more relevant to ITER.

Lee et al. [56] examined simultaneous helium-deuterium implantation in W in which the energy of the helium was varied from 70-100 eV while the deuterium energy was at a constant 55 eV. A combination of TDS and ERD was used to study deuterium retention in the sample as a function of total concentration and depth within the sample. In this, Lee and co-workers showed a 30% increase in deuterium retention due to the presence of helium. The 30% increase was found at the highest helium energy levels and overall there was a strong correlation between the increase deuterium retention and the ion energy of the helium. This was observed by an increase of the deuterium desorption peak measured by TDS in the mixed helium-deuterium exposed sample relative to the deuterium only exposure. This further demonstrates that in the presence of helium,

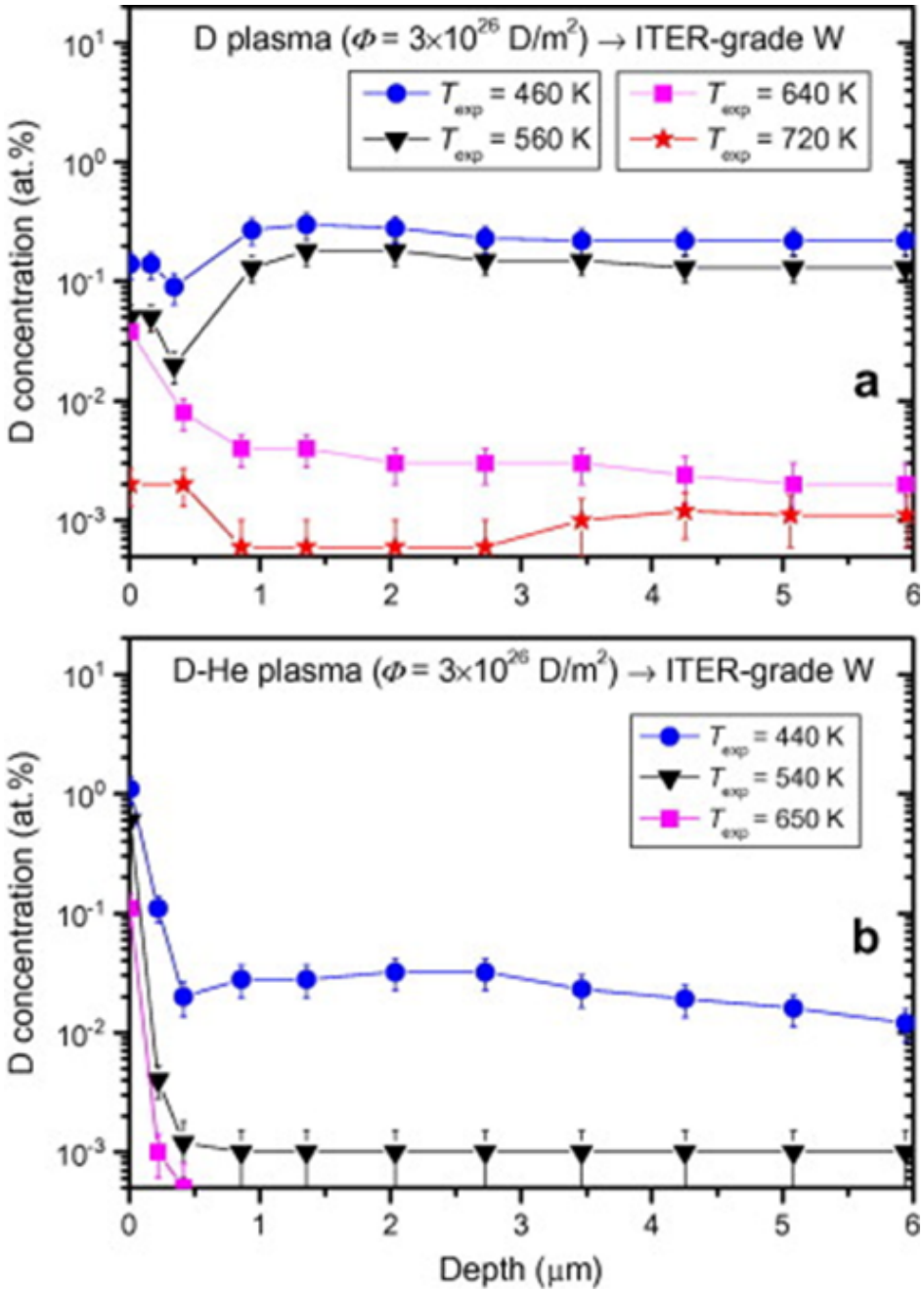

Figure 1.5: NRA measurements of deuterium concentration as a function of depth in W. The top plot shows a D only control case and is used to compare to the bottom plot which involved mixed D-He exposure. This figure has been reproduced from Ref. [53].

deuterium retention is modified. This again points to the need for additional research into the mechanisms controlling differences in deuterium diffusion, permeation and retention, as well as developing a more extensive experimental database, which is the focus of this dissertation.

Modeling and Experimental Approaches

In regards to computational materials modeling, a molecular dynamic model of a mixed helium and hydrogen bubble below a tungsten surface was performed by Bergstrom, Cusentino, and co-workers [20, 55, 57]. The simulation evaluated the hydrogen diffusion and segregation behavior for times ranging from 100 ps to as long as 8 ns with helium and hydrogen randomly inserted in bubbles below a W surface. This resulted in 80% of the randomly inserted hydrogen migrating to the surface of the bubble, as shown in Figure 1.6. This indicates that there could be a large amount of fuel retention, as the hydrogen segregates to, and is trapped around this bubble. This acts as significant motivation for the proposed research to experimentally investigate the same questions that were studied computationally to determine their accuracy and applicability.

1.3 Laser Ablation Techniques in Fusion

Conventional surface characterization techniques like Elastic Recoil Detection (ERD), Nuclear Reaction Analysis (NRA), Thermal Desorption Spectroscopy (TDS), and Secondary Ion Mass Spectroscopy (SIMS) have been traditionally used to quantify fuel retention in the near surface regions of fusion materials [22, 34, 53, 58–60]. ERD uses an energy depth relationship to determine elemental depth profiles. However, when using ERD to detect the concentration of low-Z materials as a function of depth in high-Z matrices, the resolution is directly influenced by irradiation damage, background level, and the number of counts detected [61]. NRA uses ions, such as nitrogen or He, with energies greater than about 30 MeV to probe species of interest (usually through ion, alpha reactions) and measures the number and energy distribution of alpha particles, which can provide the concentration and depth of the species of interest respectively. While NRA is ideal for determining the magnitude of the retained gas, it is not optimal for determining concentrations as a function of implantation depth [62]. TDS heats a sample with a fixed temperature rate increase in an ultra-high vacuum and measures the resulting desorbed

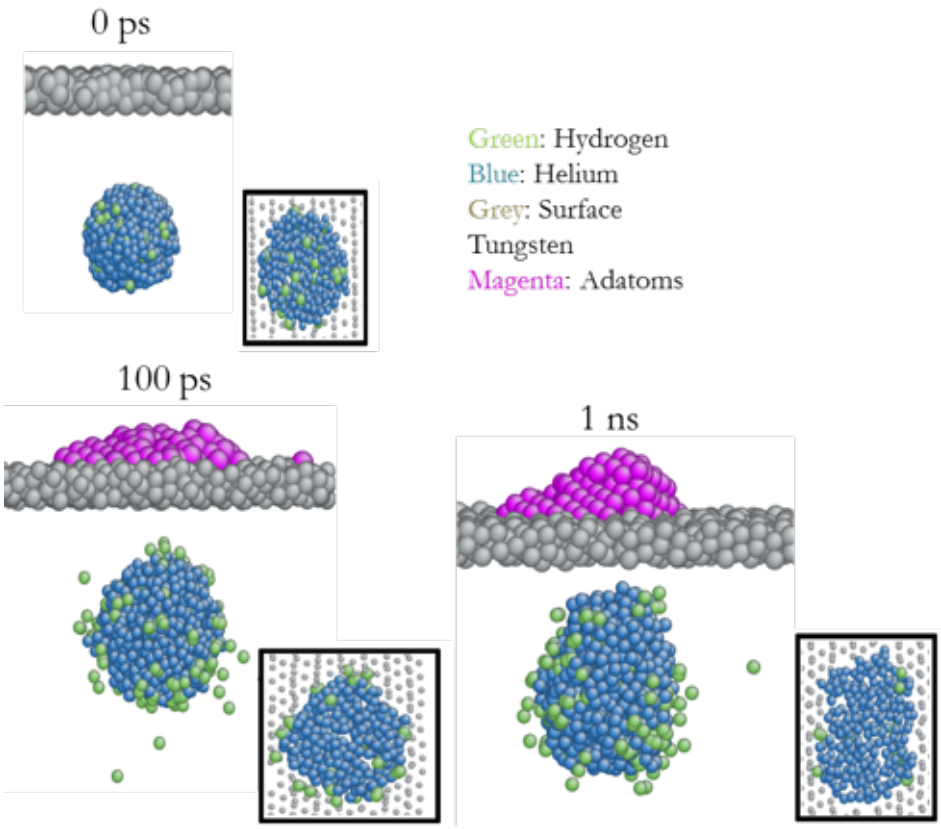

Figure 1.6: Bergstrom and Custentino show that Hydrogen and helium randomly inserted below the surface to assess hydrogen diffusion around the bubble. This figure has been reproduced from Ref.[20, 55, 57].

species in a mass spectrometer (often a high- resolution quadrupole mass spectrometer). However, in the case of detecting desorbed He, TDS is often unable to completely desorbe He once it has formed large bubbles due to the lack of thermal desorption of the insoluble He from a large bubble. SIMS is a technique suitable for examining impurity (He and D) behavior in the near surface regions at high sensitivity (several ppm) and depth resolution (several nm) [26]. However, SIMS is not quantitative [26]. Thus there is a need for a suitable characterization technique that can perform depth profiling analysis of the near surface layers without extensive surface preparation, and which is sensitive to light elements, for the investigation of fusion materials.

The development of laser-based characterization techniques can complement and expand on the capability to provide a depth profile of the gas content in fusion materials. Especially those related to questions regarding He-D interactions and gas retention. Laser Induced Breakdown Spectroscopy (LIBS) offers multi-elemental and microanalysis in the near surface with high sensitivity (ppm) and depth resolution [63–66]. LIBS is a laser ablation technique commonly used to characterize a material surface and the chemistry, specifically elemental composition. During the ablation process, the breakdown and vaporization of a small volume (~10^{-9} cm^3) occurs, forming a plasma. In the first stage (few ns) of the plasma, the light emitted appears intense from the excitation of the material. After a few hundred nanoseconds, an intense broadband continuum of light is formed because of the Bremsstrahlung process. Spectral emissions from ionized, neutral, or molecular species occur between 0.5-2 μs, 2-10 μs, and greater than 10 μs, respectively after plasma formation. The most dominant contribution to emission lines are from the de-excitation of neutral atoms, and this occurs during the 2-10 μs spectral window. The characterization of the temporal behavior and relative intensity of the plasma light is termed Optical Emission Spectroscopy (OES) and contains information about the surface elemental composition.

LIBS is a well-establish analysis technique in many fields of research including fusion[32, 47, 67–88]. Farid et al. [70] investigated the laser-induced plasma parameters, electron temperature and density of W as a function of laser wavelength and irradiance. Temporal variance in the electron temperature and density as a function of laser wavelength and irradiance were also discussed. Piip et al. [77] and Paris et al.[89] investigated the depth profile of W coated molybdenum (Mo) samples exposed to a linear plasma source, Magnum-PSI. Piip et al. exposed four W coated Mo samples to a 60% D and 40% He plasma. The maximum heat flux at the

center of the plasma was 10 MW/m^2, the maximum particle flux was $1x10^{24}$ m^{-2}s^{-1} and the particle fluence reached $1x10^{26}$ m^{-2}. The W, D, and Mo intensities were shown as a function of depth; however, limitations such as a shot to shot fluctuation, were apparent. Mercadier et al. [43] performed LIBS on carbon fiber composite (CFC) containing hydrogen (H) and D. They performed a parametric study of laser fluence, pulse duration, and gas pressure and its influence on the H and D Balmer alpha spectral lines. The results showed that LIBS parameters could be optimized to investigate light elements such as H and D. In summary, there is an apparent need for the optimization of LIBS for fusion applications; parameters such as laser fluence, gate delay, pulse duration, limits of detection (LOD) for light elements (He, H, and D), and depth resolution need extensive investigation.

Additionally, LIBS is unable to provide quantifiable results without additional calibration, benchmarking, and corroboration. Laser Ablation Mass Spectrometer (LAMS) was developed to corroborate LIBS and to produce quantifiable results. LAMS is similar to Laser Ablation Inductively Coupled Plasma Mass Spectrometry (LA-ICP-MS) as both systems perform a laser ablation and subsequently measure concentration by mass spectrometry. However, the difference between the two systems is the mass measurement technique. LA-ICP-MS uses a plasma to measure the mass while LAMS uses a Radio Frequency (RF) field along with rapidly alternating voltages across four rods making up a quadrupole. Regarding fusion relevant research, neither LA-ICP-MS or LAMS have a significant presence. However, is recent years Zlobinski et al. [90] and Gierse et al. [91] have begun to investigate the use of QMS in combination with laser-induced desorption spectroscopy (LIDS) to directly compare to TDS, in a laboratory setting (ex-situ). The research in this dissertation uses a QMS made available by a pre-existing TDS setup. In previous studies, Hu et al. [92] measure He and D confidently with the QMS. Hu et al. demonstrate that the QMS can be used when performing laser ablations, LAMS, and can be used to corroborate LIBS. The LAMS functionality, calibration, corroboration with LIBS, and results are demonstrated in this research.

1.4 Summary and Dissertation Objective

Over the process of developing the literature review, several fusion relevant and material specific dependent parameters were identified. This dissertation has focused its research efforts on tungsten, the material selected by ITER for its divertor. Second, given the plasma environment in the divertor region, it is important to study the impact on the plasma material interface (surface temperature, particle/ion energy, and fluence). Prior efforts have shown that these characteristics, as well as tungsten crystal structure, can have a significant impact on material performance. One example is the work by Alimov et al. [46],[53] who indicated the importance of surface temperature on the deuterium diffusion, permeation, and retention in W. Similarly, Iwakiri et al.[21] observed that temperature plays a role in the creation of defects in W, which is critical because helium and deuterium can be trapped in such defects. These, in combination with the numerous other examples of research efforts into the effect of material and plasma characteristics on the interaction between He and D, highlight the need for additional more comprehensive research into the mechanisms controlling differences in D diffusion, permeation, and retention, as well as developing a more extensive experimental database.

The literature review also demonstrated the need for the development of a new technique to perform both near surface and bulk depth analysis as the existing methods are unable to provide the necessary resolution. Lee et al. [51] and Wang et al. [48] performed depth-dependent analysis to quantify He and D concentration using ERDA and Alimov et al. [53] performed depth-dependent analysis to quantify He and D using NRA. However, both ERDA and NRA have limited depth resolution, ERDA bulk analysis limitation (<60 nm) and NRA is limited at the near surface (>1 micron). These findings demonstrate the need for a newly developed surface characterization technique that can resolve both the near surface and bulk in the same system. The development, benchmarking, and application of a new surface characterization technique, LIBS coupled to LAMS, was performed as part of this dissertation.

While ion energy, ion fluence, surface temperature and material type were found to play a critical role in the plasma-material interactions, the literature review also found several gaps in the fusion relevant environment parameter space. As demonstrated in Figure 1.7, these gaps are of particular interest to the fusion community given their similarities to the operational characteristics

of ITER. These performance gaps are largely a result of the difficulty in accessing a facility capable of achieving the necessary characteristics. However, computation work has been performed in these gaps to provide insight, although experimental validation is necessary. The research in this dissertation seeks to not only to demonstrate the applicability of a novel laser-ablation based surface characterization technique but also to leverage this technique to expand the current knowledge of material performance in ITER-like conditions. The secondary effort will be focused on filling part of the gaps indicated by the "green circle" demonstrated in Figure 1.7b and the lower half of the green circle in Figure 1.7a. While it was determined that completely filling the knowledge gap of plasma-material interaction was beyond the scope of this research effort, the developed laser-based surface characterization technique coupled with the shown proof of concept will provide an effective means of continuing research in the remaining gaps.

In conclusion, developing a comprehensive understanding of the synergistic effects of He and D in W is important for future fusion reactors thereby providing a purpose for experimentally investigating the gaps demonstrated in Figure 1.7. The specific experiments performed are presented in Table 1.1, as well as discussed in more detail in Chapter 5. These experiments have been designed to address the question of whether the presence of near-surface He prevents D from migrating into bulk and how to quantify these changes using d surface characterization techniques. The techniques in question are Laser Induced Breakdown Spectroscopy (LIBS) and Laser Ablation Mass Spectrometry (LAMS) which invasively measure near-surface and bulk elemental concentrations as a function of depth by simultaneously measuring the photon emission and mass of elements released by the laser ablation. The theory and application of laser ablation and LIBS/LAMS are explained in Chapter 2. Chapter 3 explains the experimental setup. In Chapter 4, the calibration methodology is thoroughly explained for both LIBS and LAMS. The research methods are explained in Chapter 5. Results and discussion are in Chapter 6. Finally, the summary and conclusion are presented in Chapter 7.

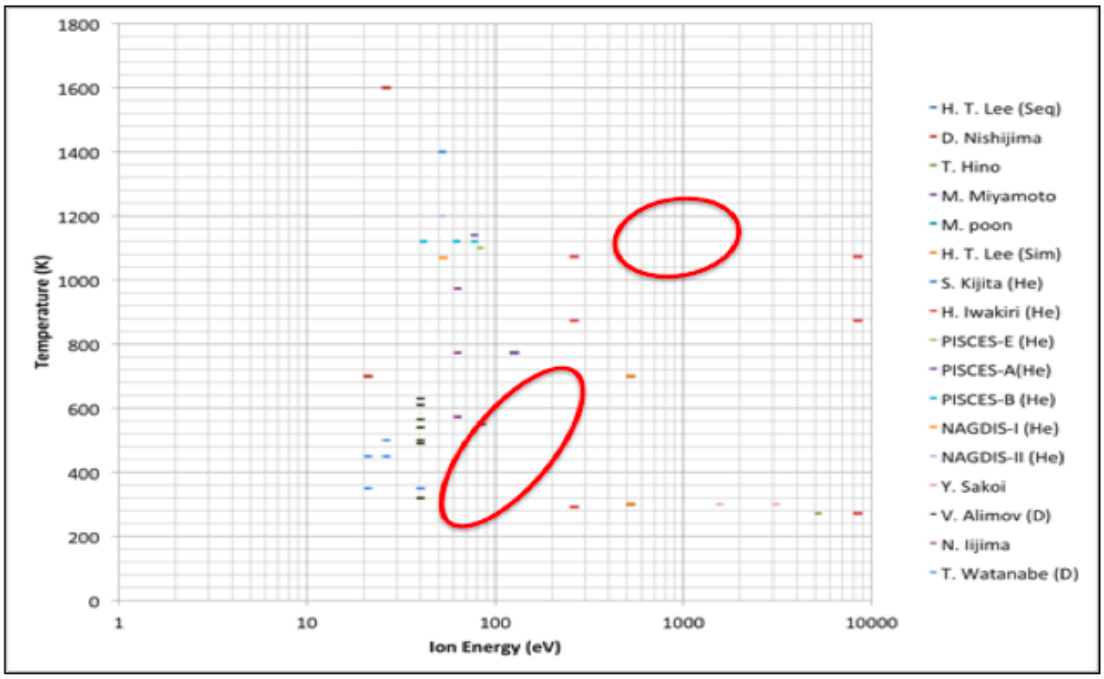

(a)

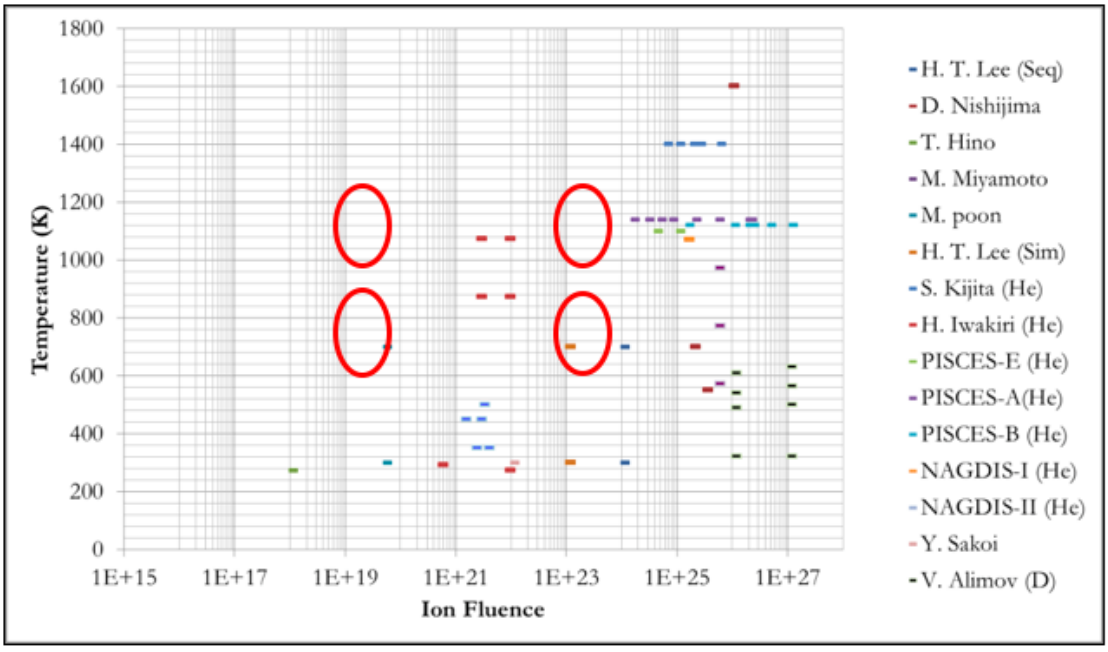

(b)

Figure 1.7: a) Experiment overview of research as a function of experimental parameters ion energy (x-axis) and surface temperature (y-axis). b) The same experiments performed in a) but shown as a function of ion fluence and surface temperature. The red circles denote gaps that exist in the literature.

Table 1.1: Experimental parameters exploring synergistic effects of a mixed He and D plasma exposure in W.

Particle	Ion Energy [eV]	Surface Temp. [^{o}C]	Flux [x10^{22}m^{-2}s^{-1}]	Material
He	75, 250	300&$>$500, $>$500	1.4, 5.4	PCW&SCW(111), PCW
90%D10%He	75, 250	300&500, 500	1.4, 1.5	PCW&SCW(111), PCW
D	75, 250	300&500, 500	0.7, 1.2	PCW&SCW(111), PCW

Chapter 2

Laser Ablations Processes and Techniques

2.1 Laser Ablation Theory

The processes governing laser ablation are laser interaction with the solid, ablation or removal of sample material, and plasma formation. The three basic processes describe the laser-induced plasma formation. The transfer of energy from the laser photons to the material lattice and the generation of free electrons induces the first process. A portion of the laser photons is reflected from the surface although the majority of the photons are absorbed [63–66]. The second process is the cascade of collisions inducing ionization, electron formation, and energy absorption, forming an ionized cloud of particles. The energy absorbed is converted into heat, resulting in the melting and vaporization of the surface. In the formation of the plasma, the laser induces heating, ionization and the plasma formation absorbs the remaining laser energy [63–66]. The laser energy, wavelength, and pulse width govern evaporation, plasma formation, and generation of spontaneous emission, crater dimensions, and the total mass removed, and heat transferred into the material. Laser pulse energies influence optical and heat penetration depth, which is the first process mentioned above.

2.2 Laser-induced Plasma

The processes of Inverse Bremsstrahlung absorb the laser photons (IB) and Photon Ionization (PI) [65, 66]. The IB process involves absorbing photons by free electrons, gaining energy from the

laser beam during collisions with neutral and ionized atoms. These collisions begin the process of vaporization and excitation through electron collisions with excited and ground-state neutrals. Electron-ion interactions dominate when the ion density is high. Electron-neutral interactions are usually two orders of magnitude smaller; however, they become important when the plasma is weakly ionized. When the plasma is weakly ionized, the IB process changes and absorption decreases significantly.

The plasma emission is important because it contains information related to the material in the form of ions and electrons. Laser-induced plasmas are unlike fusion plasmas, specifically laser-induced plasma are usually highly ionized, not in local thermodynamic equilibrium (LTE), and very dense. The common spectroscopic technique used to determine electron density is the measurement of Stark-broadened line profiles of single atoms and single charged ions [65]. The emitting species in the plasma (atoms and ions) are placed under the influence of an electric field by fast-moving electrons and relatively slow-moving ions. This perturbing electric field acts on atoms and ions and shifts their energy levels, which broadens the emission lines. This phenomenon is called Stark broadening [65]. Doppler and instrumental broadening also contribute to the broadness of the profile.

Once the density of the plasma is determined either experimentally or analytically; the electron temperature can be estimated. Similar to laboratory plasma‘s, laser induced plasma typically has electron temperatures between 1 and 10 eV. However, the plasma is constantly evolving, expanding, and cooling which is unlike a steady state fusion plasma. Temperature measurements from laser induced plasma are measured at one point in time assuming the plasma is at local thermal equilibrium (LTE) and fulfills the Griem criterion [65, 67]. If these two assumptions are made, the temperature and density measured at that single point is the average for the entire plasma then. In Figure 2.1, the laser induced plasma is shown to increase simultaneously to the incoming laser pulse and then exponentially decays after that. Traditionally, LIBS measures the plasma between 10-50 microseconds after the initial laser pulse. This is because the first 100 ns involves an electron continuum which does not show any elemental emission lines. As the plasma cools the elemental emission lines become apparent with increasing intensity.

The intensity of these emission lines are correlated to the concentration of the element that exists in the plasma, as mediated by the electron recombination cross-sections of each element.

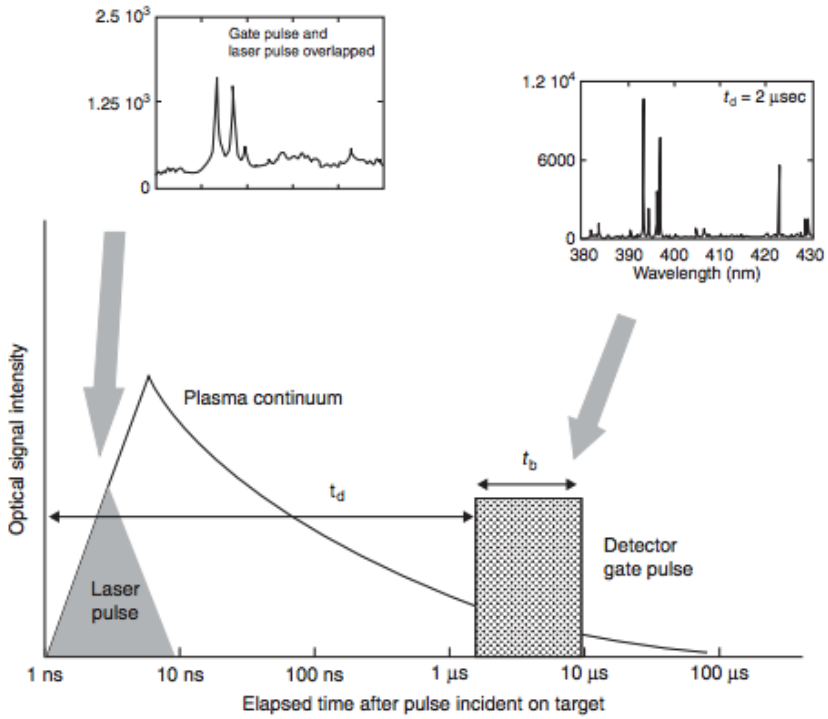

Figure 2.1: Schematic demonstrating the laser profile, creation of plasma, and the exponential plasma decay. The additional example spectral demonstrates how the spectra are dependent on the gate and time delay. Ref.[65]

However, due to the complexity of a laser induced plasma, the concentration cannot be determined directly without significant effort in developing accurate calibration techniques. Based on the material, the laser ablates multiple elements which require a specific amount of energy to ionize. In this research, the laser is a 532 nm ND: YAG laser which imparts 2.33 eV of energy per photon into the material lattice. Tungsten requires only 7 eV of energy to ionize while He requires 24 eV and deuterium requires 13.6 eV, which is significantly larger than the dominant element, W. Thus, it can be assumed that the majority of energy from the laser photons is absorbed by the W atom resulting in a laser-induced plasma that is dominated by tungsten. The concentration of W, He, and D in the plasma and thus the concentration in the surface need to be determined. This can be done by the use of calibrated reference material or knowledge of the plasma density, temperature, and atomic species and cross-sections. In this research, reference material was used as well as the evaluation of the plasma parameters and species. The approach used to quantify the concentrations is discussed in Chapter 4. In summary, determination of the elemental concentration from the

plasma emissions requires significant calibration and comparison to conventional techniques to be considered quantifiable.

The physics and mechanisms of shock wave generation by lasers has been investigated intensively [93–96]. A focused nanosecond high density ($>10^9$ W/cm^2) laser generates a plasma, whose expansion is induced by a shock wave. The shock wave is produced and driven by the laser. Once the laser strikes the surface, the shock wave propagates in two directions, both away from the target and into the target. The shock wave front grows and decays as the wave propagates into the target. The temporal shape follows a similar trend to that of the laser. As the shock wave propagates into a metallic target, plastic deformation occurs to a depth at which the peak pressure no longer exceeds the metal Hugoniot elastic limit (HEL). A metal HEL is related to the dynamic yield strength according to Johnson and Rhode [97].

$$HEL = 1 - v1 - 2v\sigma_y^{dyn} \tag{2.1}$$

Where v is the Poisson's ratio and $\sigma_y^{dyn}$is the dynamic yield strength at high strain rates. The HEL for Tungsten is <1-6.0±0.5 GPa, depending on material purity [96, 97]. The plastic deformation caused by the shock wave while propagating into the material produces compressive stresses. When the pressure of the shock wave exceeds the dynamic yield strength of the metal, plastic deformation occurs which consequently modifies the near-surface microstructure and properties [96, 97]. This critical pressure P_{sw} is related to the density of the material (ρ_o) and its elastic wave sound velocity (c), where $P_{sw} = \rho_o c^2$. For W, the density is 19.3 g/cm^3 and the elastic wave sound velocity along the longitudinal plane is 5.22x10^6 cm/s. The critical pressure for tungsten is 0.0103 GPa. In early published experiments [96, 97], the irradiated target was in a vacuum and the resulting peak shock wave pressure, for a laser power density of 0.1 GW/cm^2, is 1 GPa. For laser power density larger than 0.1 GW/cm^2 the shock wave can reach pressures on the order of 1000 GPa. The pressure of a shock wave for a 532 nm laser with a power density of 1x10^{15} W/m^2 in a W target is estimated to be 4.5 GPa for a single laser ablation, which is estimated to propagate up to 7 microns as the wave propagation is coupled to the thermal wave and decays exponentially. Thus during laser ablation, the shock wave could influence material properties and cause significant changes to the sub-surface. However, a systematic investigation into the influence

of the shock wave on defects such as bubbles has not been performed within this dissertation. A future investigation into these effects are of significant importance.

2.3 Laser Material Interactions

The laser ablation processes not only ablates a small volume but it also heats the tungsten surface surrounding the crater. The heating of a surface and the temperature increase of a surface under laser irradiation is dependent on three different processes [86, 98–100]:

- Reflection of the laser beam from the surface
- Absorption of the laser energy by the material
- Conduction of the heat through the material (heat diffusion)

The incoming light of the laser is partly reflected from the sample surface, resulting in a loss of incoming energy. If the roughness of the surface is small compared to the wavelength of the laser used, reflection is governed by the Fresnel equations [98]. Assuming a perpendicular incidence angle of the laser beam with respect to the surface gives a reflection coefficient of almost 50%. The Lambert Beer-law describes the absorption of the laser energy into the material lattice, for tungsten the light is absorbed in the first tens of nanometers [98]. After absorption, the heat diffuses through the material causing a temperature increase both in the lateral direction and in depth. Therefore diffusion of heat through the material is of great importance for LIBS and LAMS. For a general understanding, the heat transfer in a solid of finite thickness is considered and can be calculated using a semi-infinite solid configuration. This modeling assumption is valid based on the relationship between the optical and thermal penetration of the material. The change in material temperature is effected by the heat conductivity of the material, which is a material characteristic which describes the effectiveness in which energy is transported within a material. The optical penetration of the material is much less than the thermal penetration and is on the order of 10^{-6}-10^{-5} cm based on the pulse length of the material. The thermal penetration is also dependent on the pulse length, as this dictates the period over which the material is effectively heated [98, 99]. The short pulse length of the laser used in this research means that the heat will only penetrate a

short distance into the material compared to the thickness of the material [98, 99]. The formula [98] gives the radial and depth temperature changes over time due to heat diffusion through the material.

$$T(r,z,t) = T_o + \int_0^\infty d\lambda \Bigg(\frac{I}{2K\lambda} J[0,r,\lambda] J[1,\alpha\lambda] \left(e^{-z\lambda} Erfc\left[\frac{z}{\sqrt{\frac{tK\pi}{c\rho}}} - \sqrt{\frac{Kt}{c\rho}}\lambda \right] - e^{z\lambda} Erfc\left[\frac{z}{\sqrt{\frac{tK\pi}{c\rho}}} - sqrt\frac{Kt}{c\rho}\lambda \right] \right) \Bigg) \tag{2.2}$$

where K = 177 $Wm^{-1}K^{-1}$, c = 134 $Jkg^{-1}K^{-1}$ and ρ = 19300 kgm^{-3} are the thermal conductivity, specific heat and density of tungsten, respectively [101, 102]. r and z are radial position and depth into the material. t is time; however for our application with a pulsed laser, the heat source is only present for the length of the pulse width, 5 ns; then the heat source is removed, and rapid surface cooling and heat diffusion begin. The time, t, during the pulse is τ while after the laser pulse time, t is t-τ. I is the laser irradiance onto the surface of the material and is described as the laser incident flux, and J is a Bessel function. For simplification, the material constants are assumed to stay constant during the laser pulse. Based on previous research by Datz et al. [102] Tungsten reflectivity and thus absorption does not significantly change as a function of temperature under laser irradiation. The experiment was performed up to 2000K[102]. Now when z and r are equal to zero, the surface temperature is analytically approximated by:

$$T = T_o + \frac{2}{\pi} \frac{I\sqrt{t}}{\sqrt{Kc\rho}} \tag{2.3}$$

This approximation is used to determine the surface temperature induced by the laser. Temperatures that are greater than the material‘s melting point and vaporization temperature are assumed to be ablated. Both radially and as a function of depth, the temperature will decrease. However, the heat affected zones could cause helium and deuterium cluster nucleation as well as diffusion and surface desorbtion. The diffusivity of He in W at 1020 K is approximately $10^{-8} m^{-2} s^{-1}$ and the diffusion constant for deuterium in tungsten, which is temperature and pressure dependent, is $4.1x10^{-3} \exp^{\frac{-9000}{RT}}$ where R and T are the gas constant and the absolute temperature, respectively. The diffusion of He and D are dependent on the temperature of the material. The temperature radially and as a function of depth is analytically calculated to determine the heat affected zones, and the results of these calculations are presented in Chapter 4. The temperatures in these zones,

based on a single ablation during a 5-6 ns pulse, decrease drastically over small times scales and even if the temperature is high enough to cause diffusion it may not be of sufficiently long duration to induce diffusion and desorption from the surface. Also since He stays trapped even at high temperature, He diffusion may not be significantly affected, although this conjecture has not been evaluated in this dissertation However, deuterium is highly mobile in W and even if the temperature is very dynamic, it may cause deuterium to diffuse from the heat affected areas. A modeling assessment was performed using the COMSOL finite element solver on W,Si, and Cu for a single laser ablation to calculate the temperature distribution during the laser pulse and during cooling. The results of this analysis are also presented in Chapter 4. During laser ablation, the material properties may significantly change, however the investigation into the influence of differential material constants has not been evaluated in this dissertation. It is recommended that future investigation into these dependencies be performed and are of significant importance. A thorough laser material processes model can provide insight into the changes of heat diffusion into the material and more importantly the potential diffusion of He and D. Comprehensive studies have been performed by V. Alexiadas et al [103] on Cu, but not for W.

A calculation of the temperature distribution during laser heating of the material was performed using the commercially available finite element software COMSOL. Previous studies modeling laser ablation, laser heating, and laser material interaction in COMSOL have been performed by Darif et al. [104]. Specifically Ref [104] provided a detailed instruction for building a laser ablation model in COMSOL. The simulation of a single laser ablation on W was performed. Following Eq.(2.3), the T is calculated in two dimensions of r and z which assumes radial symmetry such that the origin was set to the center of the surface of the material. From times, t = 0 to t = τ, where τ = 6x10^{-6} s the sample underwent heating from the laser. The COMSOL model includes a tool that allows the user to input the melting temperature, vaporization temperature, and latent heat of vaporization. These quantities were used to determine the spatial profile of the material that was considered ablated. The model visualization represents the ablation area as white. At times greater than τ the heat source is no longer present and the sample undergoes cooling. The purpose of this calculation was to determine the heat affected zone as a function of depth and radius. He and D implanted into W may induce defects and trap within the subsurface microstructure. These defects may include bubbles, interstitials, and vacancies. Exposures performed at room temperature, it is

assumed that the implanted He and D stay trapped and do not diffuse into or out of the surface. However, when the material is heated, in this case by laser-induced heating, the heat affected areas can potentially cause He bubbles to burst and/or D to desorb from, or diffuse away from the heat affected zones. That is why it is important to model the laser heating of the material to determine the heat affected zones and how dynamic these zones are temporally.

Figure 2.2, plots the calculated temperatures for, r and z values between 0 and 50 and 3 microns, respectively. These spatial contours show the heat affected zones for times, t = 0.126 μs, 246 μs, 366 μs, 486 μs, and 1.086 μs, respectively. The region depicted in white represents the area anticipated to be removed from the surface by the ablation. At t = 0.126 μs, the heat affected zone encompasses a radius of $\sim$40 microns and a depth of 0.9 microns. The estimated temperatures in the regions are upwards of 1000K, but as time progress to 0.246 μs the peak temperature decrease to roughly 800K. If there are pre-existing defects in this area, such as He bubbles or D interstitials, then these temperatures could have an affect on the de-trapping or diffusion of these defects. It is well established that helium will remain trapped within bubbles and most defect clusters in tungsten until temperatures that begin to approach the melting temperature [45, 105]. However, if bubbles exists that are over pressurized, an increase in temperature could cause them to burst, thereby releasing He that would be measured by LIBS and LAMS.

Figure 2.3 presents results of the TDS measurements performed on polycrystalline tungsten specimens exposed to a 75 eV deuterium plasma in the PISCES/A linear plasma device at USDA [106, 107]. The deuterium release peaks are shown as a function of temperature (with a 0.5^{o}C/second heating rate) in green (m/q ratio of 3, corresponding to HD) and red (m/q ratio of 4, corresponding to D), and indicate that deuterium desorption begins at temperatures of about 400^{o}C, with a significant release peak observed at temperatures from about 550 to 800^{o}C. Based on the laser-induced heat affected zone temperature profile shown in Figure 2.3, the TDS results indicate the potential for substantial deuterium release within a heat affected zone for up to 1 microsecond following the laser ablation. A suggested way to correct for the He and D release would be to include the heat affected zones to the measured ablated volume. What is still unknown is the dynamics of any He and D present in locations subject to such heat affected zone conditions, specifically over timescales on the order of 1 microsecond. As well, it is unclear whether D will diffuse out of or into the surface for such a temperature profile containing temporal and spatial

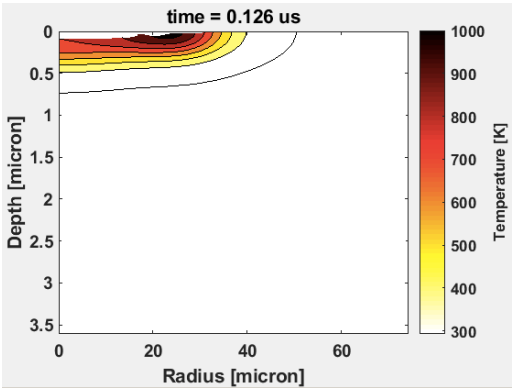

(a)

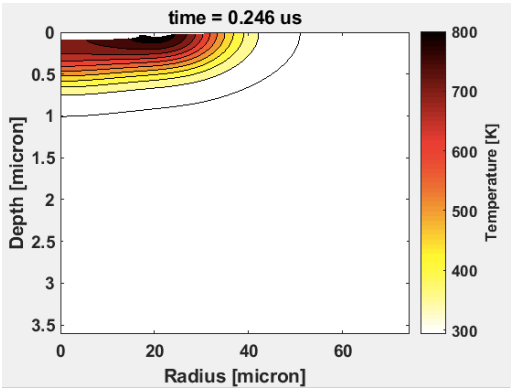

(b)

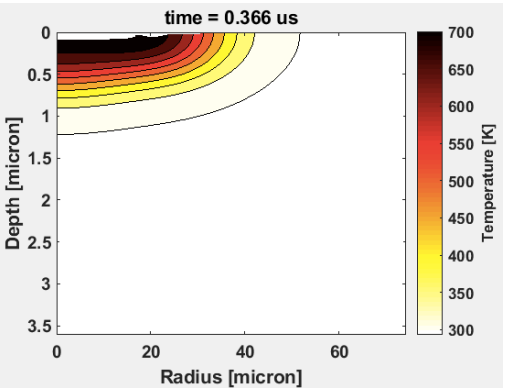

(c)

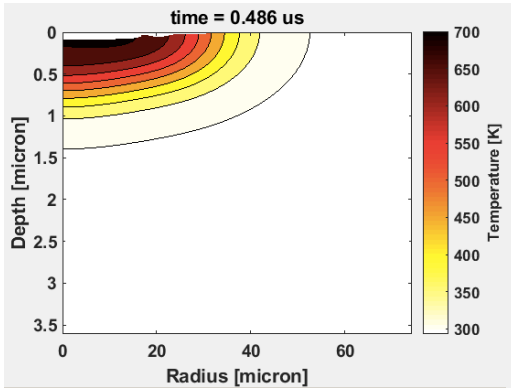

(d)

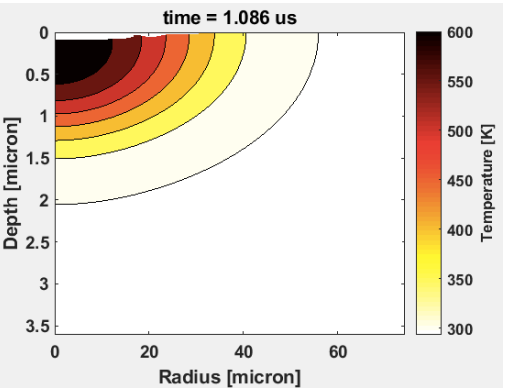

(e)

Figure 2.2: Finite element calculated temperature profiles in tungsten surrounding a laser ablation crater. The temperature scale is shown separately for each time snapshot, and the calculated time is: (a) 0.126 microsecond (b) 0.246 microsecond (c) 0.366 microsecond (d) 0.486 microsecond (e) 1.086 microsecond

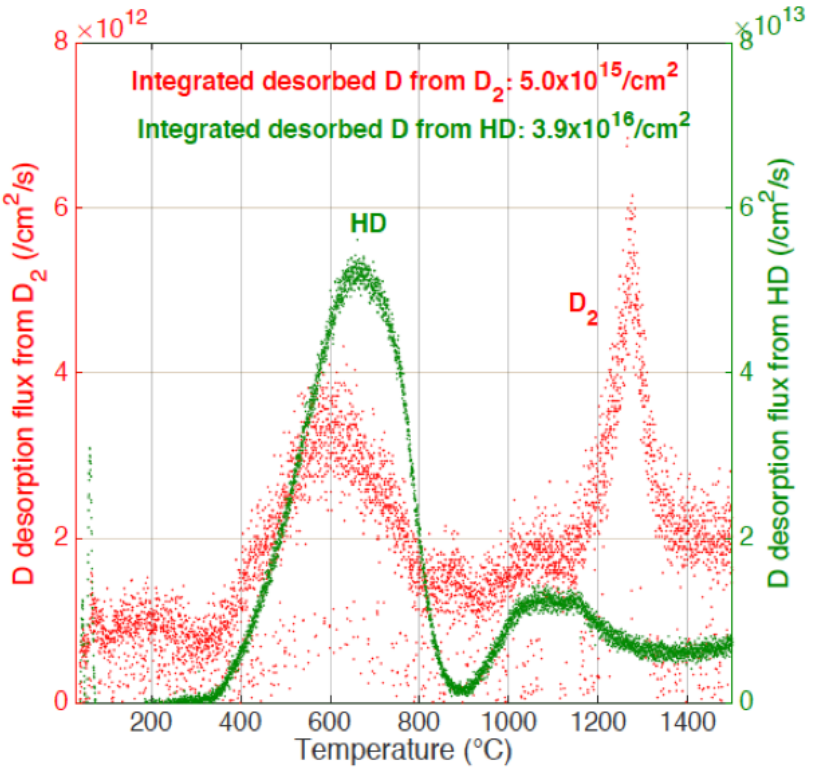

Figure 2.3: Desorption of deuterium measured by thermal desorption spectroscopy using a 0.5*C/second heating ramp. The plot shows the signal from m/q = 3 (HD) and m/q=4 (D2) from a tungsten specimen exposed to a 75 eV deuterium plasma to a fluence of 10^{25} m^{-2}. The plasma exposure was performed at PISCES/A. The desorption peak around 600^{o}C indicates the possible deuterium desorption in the laser ablation heat affected zone.

gradients. Correspondingly, within this dissertation, the LIBS and LAMS measurements and analysis have not incorporated any impact of the laser heat affected zones, but it is recommended that further investigation be performed to assess the impact of the laser heat affected zones on the resulting depth dependent concentrations. Most likely, well designed experiments with varying known gas implantation conditions will be required to specify the impact of the heat affected zones, and the corresponding uncertainty and sensitivity of the LIBS and LAMS measurements.

This issue of gas release from heat affected zones requires further study and analysis, since it could influence the resulting calculations of volumetric concentration. Future work must devise experiments specifically designed to develop an analysis method to account for such release mechanisms, or at least to provide a bounding level of uncertainty associated with the depth dependent concentration measurements resulting from heat affected zone induced desorption/release.

2.4 Laser Induced Breakdown Spectroscopy

The process of measuring emission line intensity produced by the laser-induced plasma is known as LIBS. This can be done using a spectrometer, known as spectroscopy or with photomultiplier tubes (PMTs), known as radiometry. In this research, PMTs are used instead of a spectrometer because of the UHV environment, in more detail in Section 4.1. The emission line intensity is influenced by the laser energy, plasma temperature, plasma size, atomic line transitions, sample surface, and detector response. To reduce these influences of these variables on the targeted ratio of the dominant element and the trace element, or analyte, multiple ablations should be performed. The dominant element emission line acts as an internal standard. In a LIBS spectrum, the intensity of the emission line at a specific wavelength integrated over a time interval is used to quantitatively measure the elemental composition of the material substrate. However, for analytes, the method has to be calibrated using a calibrated reference material (CRM) to determine the dependence between the measured and resultant quantities for the reference sample. Performing all of the aforementioned steps results in a quantitative methodology for measuring analyte concentrations, as discussed in Chapter 4.

2.5 Laser Ablation Mass Spectroscopy

Mass spectrometry (MS) represents the most used technique for the characterization of the charged component of a plasma plume. Quadrupole mass spectrometry (QMS) to measure laser-induced plasma, which is characterized by very high mass resolution, high efficiency, and compactness, has been studied. Kools et al. [108] studied the amount and velocity distribution of positive ions in excimer laser ablation of copper. The ion density was found to be strongly dependent on laser fluence, and this dependence was consistent with the exponential temperature dependence of an ion fraction in the Saha equation [63–66]. Experiments similar to LAMS have been performed by the fusion community [88, 109]. Zlobinski et al. [87] investigated tritium retention in W using Laser Induced Desorption (LIDS) combined with QMS. LIDS is a similar technique to LIBS; however, LIDS uses a larger beam diameter, heating an area of the surface near to its melting temperature and thereby desorbing any retained impurities. When LIDS is coupled with QMS, the concentration of

desorbed impurities can be measured. Zloblinski used LID-QMS to determine the total retention in bulk tungsten targets exposed to plasma at TEXTOR. Zlobinski showed that in the area that was exposed to the plasma, the deuterium retention was 4-10 times (2-5x$10^{20}m^{-2}$) than the area that was not directly [87].

Chapter 3

Experimental LIBS-LAMS Setup

3.1 Laser System and Beam Path

The LIBS-LAMS station was built within the low activation materials development and analysis (LAMDA) laboratory at Oak Ridge National Laboratory. The laser is a Quantel QSMART Nd: YAG 60 mJ frequency doubled laser that operates at a 532 nm wavelength coupled with an MVAT Energy Modulator operating at a 1-20 Hz frequency and a pulse width of 5 ns. The energy modulator effectively decreases the laser energy without sacrificing beam quality. The lowest laser energy coupled to the MVAT that can produce W breakdown is 1.8 mJ. The laser is externally triggered which allows for external control of the laser frequency. Within this LIBS-LAMS setup, single laser ablations were performed sequentially at the same spatial location. The internal laser frequency was disabled for the flashlamps, but the Q-Switch remained enabled. The Q-Switch is dependent on the flashlamp frequency and lases 210 microseconds after the flashlamp receives the trigger. The external trigger is setup up to only produce one laser pulse at a time.

Once the laser photons leave the laser head; they are bent 90^o by a UV Fused Silica High Power 1064/532 nm turning mirror, as illustrated in Figure 3.1. The mirror is set into a right angle kinematic mirror mount. The laser photons then pass through a tube enclosed optical cage setup. At the end of the tube is a lens mount with a 1/2-inch plano-concave beam expanding lens, with a negative focal length of 25 mm which is placed at a distance of 71.88 mm from a 25.4 mm plano-convex collimating lens, with a focal length of 97.25 mm. Figure 3.2 shows a schematic illustration of the beam expanding optics. The distance between the two lenses is related to the expanded

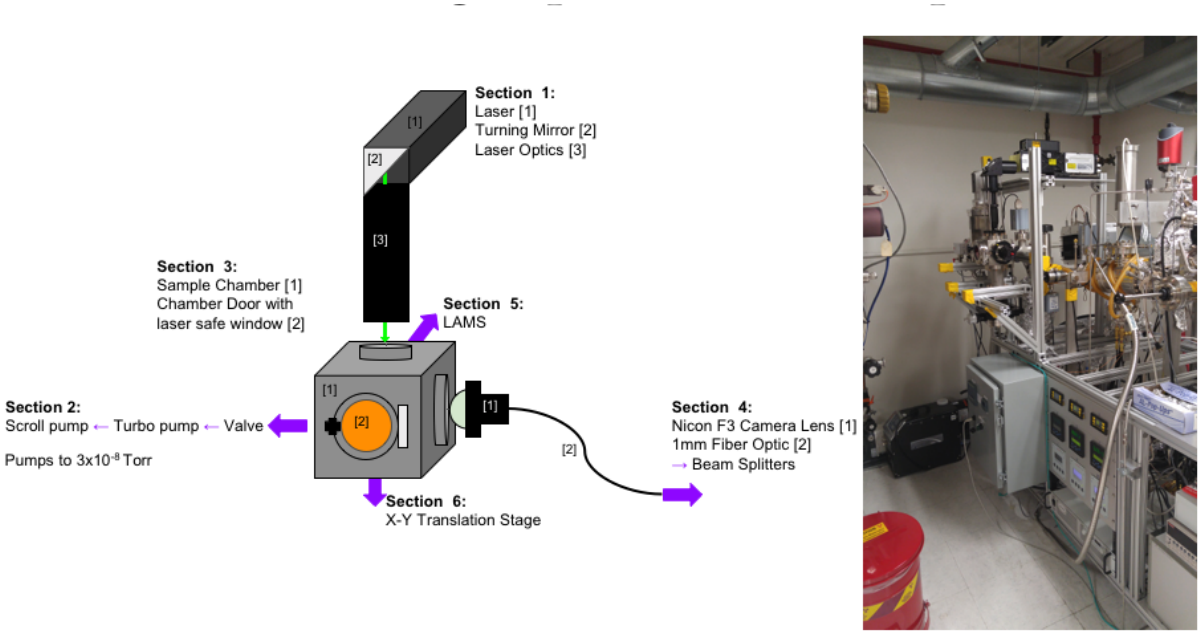

Figure 3.1: Schematic illustration showing the experimental setup of the LIBS/LAMS characterization setup (left). Actual LIBS/LAMS experimental setup (right).

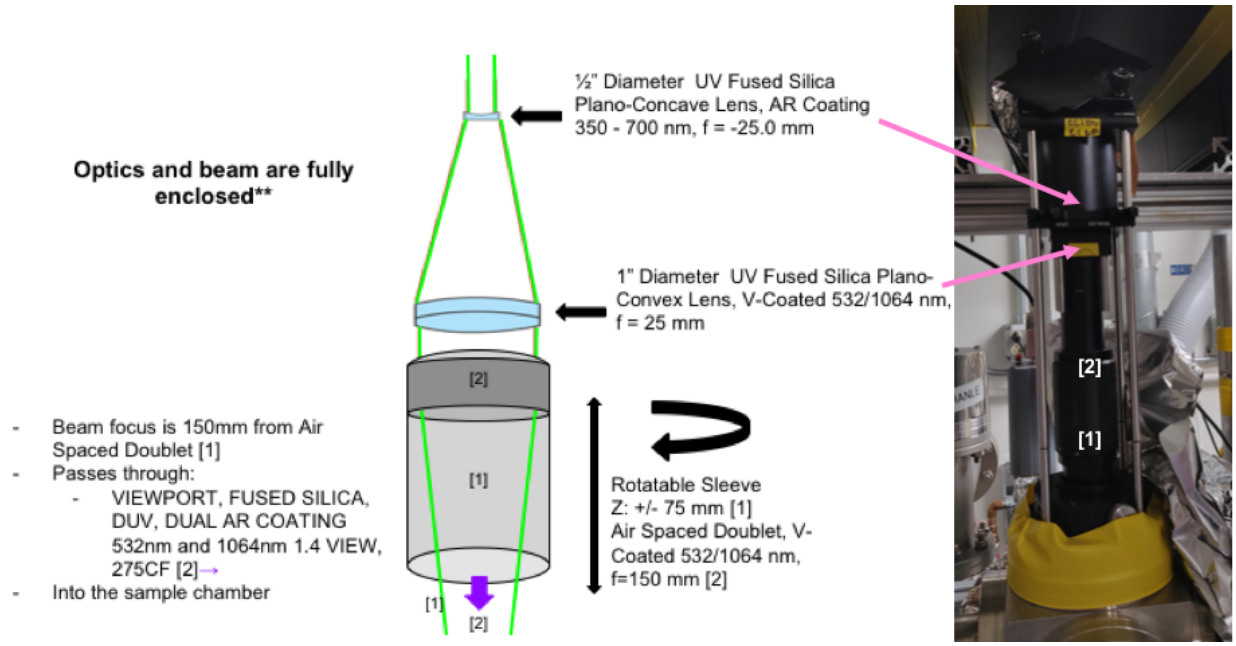

Figure 3.2: Schematic illustration showing the beam expansion and focusing optics as well as adjustable z translation (left) and a direct comparison to the acutal optical setup which is fully enclosed (right).

diameter of the photon beam at that distance. To adequately collimate the beam, the diameter of the expanded beam must be equal to the collimating lens diameter. The collimating lens is placed in its mount with the flat side facing the beam. When the beam reaches the collimating lens, the resulting beam is collimated to a beam diameter of 27.5 mm. After the collimating lens, the laser beam passes through a translating lens tube with a 1 inch, 532 nm UV fused silica air spaced doublet focusing lens, mounted inside the tube. The tube can translate the mounted lens up to 36 mm. However, additional adjustable spacers were added to increase the translation to 75 mm. Due to space limitation in the sample chamber, additional Z translation is provided by adjusting the location of the focal point. After passing through the collimating lens, the laser is focused to a working distance of 150 mm to bring the focal point to the sample stage. A Nikon F3 lens used to view the plasma was adjusted according to the placement of the focal point. Additionally, a larger (4.5 ConFlat flange) viewport was installed to allow for finer adjustment to the lens viewing window.

3.2 Specimen Chamber

The sample chamber is pumped to a UHV pressure of 5x10^{-8} Torr by a Varian TriScroll 600 oil-free dry scroll vacuum pump coupled to a Pfeiffer HiPace 80 turbo-drag-pumps (71 l/s). The pressure level of the chambers is monitored by both MKS 909AR digital and analog hot-cathode vacuum transducers. The chamber is also coupled to a pre-existing experimental station which provides the quadrupole mass spectrometer (QMS) [92] and additional vacuum pumping (>500 l/s). The central area of the sample chamber involves a 6-way stainless steel cube, purchased from Kurt Lesker, in which the laser photons enter the cube from the top and intersect the sample stage. The sample stage enters the cube from the bottom; the sample chamber vacuum pump is on the left; a 4.5 inch viewport for the LIBS optics is on the right; a vacuum compatible fast-release door, which is used to insert and retrieve samples is attached to the front of the cube; and the back of the cube is attached to the pre-existing vacuum system using a vacuum component tee. During the LIBS-LAMS experiments, the pumping to the left of the chamber is closed off using a valve; then the chamber is opened up to the pre-existing desorption measurement chamber by opening an angle valve that is connected to the tee. This is to ensure that the ablated particles are pumped

into the QMS pumping chamber. An illustration of the flow from the sample chamber into the QMS is presented in Figure 3.3. Specimens are held by a standard TEM sample holder (1 inch in diameter) that is fixed to a vacuum compatible optical post using a vacuum compatible set screw, as illustrated in Figure 3.4. The vacuum post is 15 inches in length and attaches to the CF flange using a vacuum compatible post holder which is bolted directly into the CF flange. The CF flange holds the post and sample holder and connects the sample holder, to the X-Y translation stage. The CF flange is connected to the bottom of the stage, which has a flexible bellows. The connection between the bellows and the CF flange closes the vacuum chamber from the bottom and provides the ability to translate the sample holder in both the X and Y directions.

3.3 Spectroscopy and Radiometry

The optical view of the sample stage is from the right side and uses a Nikon F3 lens coupled to a single 1 mm fiber optic. This carries the plasma light to an ORNL designed and patented diagnostic referred to as a Filterscope [110–116], which is shown in Figure 3.5. The analysis of

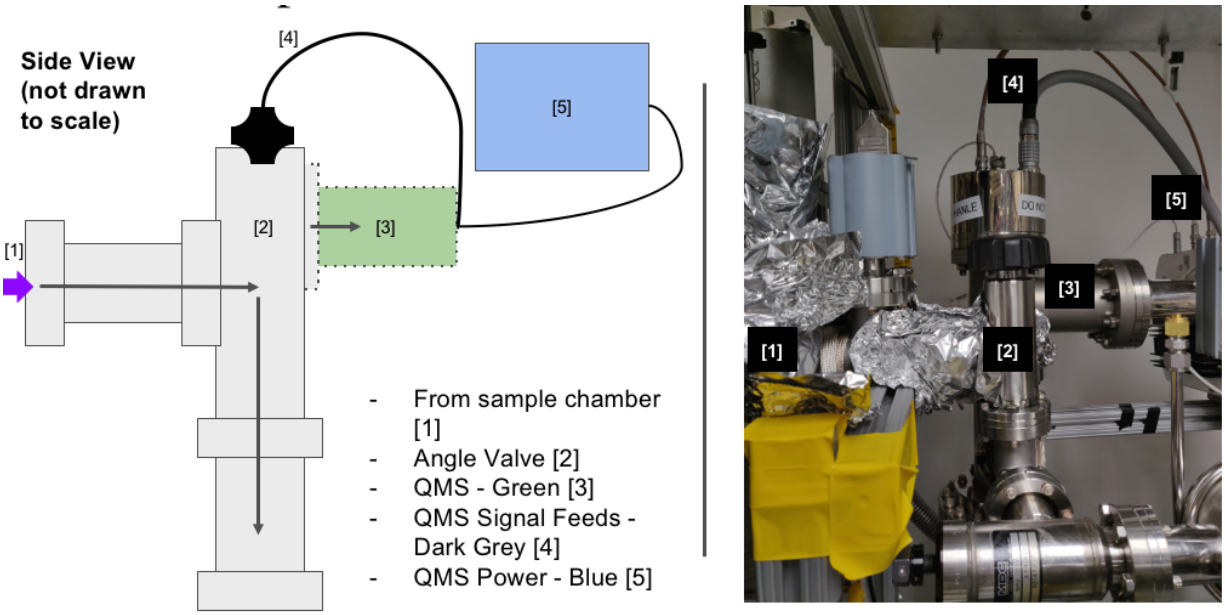

Figure 3.3: Schematic illustration showing the connection between the LIBS-LAMS sample chamber and the quadrupole mass spectrometer to measure the current of desorbed gas species (left). The actual setup of the LIBS-LAMS sample chamber vacuum connection to the QMS (right).

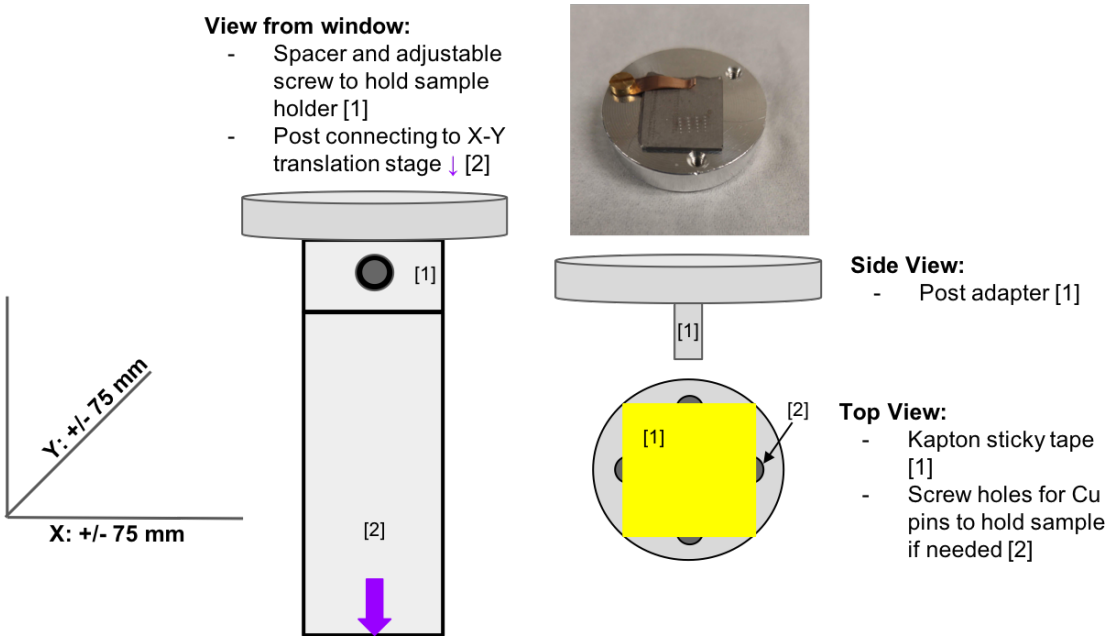

Figure 3.4: Schematic illustration of the sample stage and holder. The holder is a Ted Pella, INC. microscopy sample holder equipped with placement screws and Cu pinch pins to help secure various specimens to the holder. The use of Kapton double sided sticky tape add additional security to small specimens and is UHV compatible. The sample stage can translate the holder in the X and Y direction 75 mm. An example image of the sample holder hold a tungsten sample.

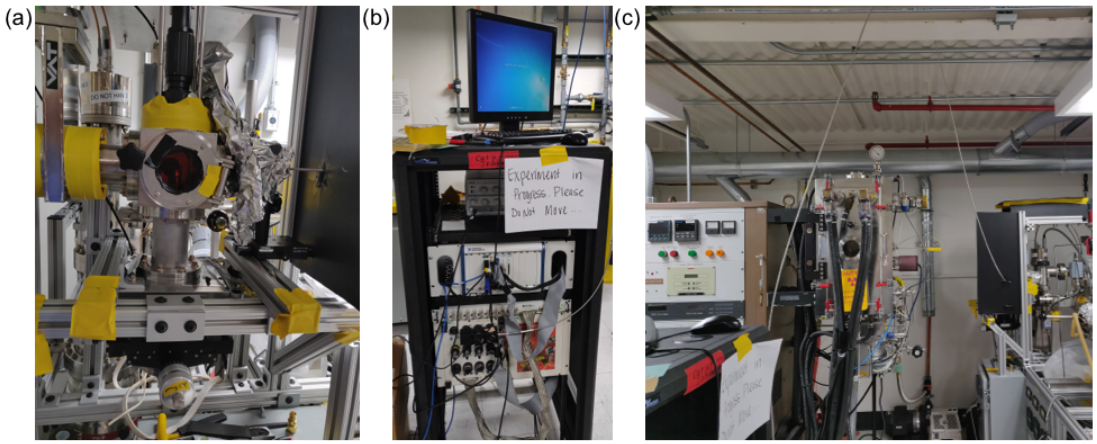

Figure 3.5: (a) demonstrates the measurement of the plasma emission using a Nikon lens (FUJI TV1.4/1 12.0) which is to the right of the cube (i.e. covered in foil with metal fiber connection from the right of image (a)). The lens focuses the captured light in a 1 mm optical fiber (metal fiber in image (a)) which transmits the light to the Filterscope. (b) demonstrates the connection of the fiber from (b) to the Filterscope PMT patch panel(b). (c) encompasses the entire fiber transmission from the sample chamber to the Filterscope.

the laser ablated plasma by a Filterscope is what we define as LIBS in the combined LIBS-LAMS UHV measurement chamber. The QMS is coupled to the measurement chamber at the back of the cube. The LIBS-LAMS measurement chamber can be closed off from external pumping and opened to the QMS, which has separate pumping capability; this allows the laser-ablated atoms, which are subsequently (partially) ionized in the laser plume particles to flow into the QMS. The analysis of the resulting gas ion fluxes in the QMS is what we define as LAMS. The LIBS-LAMS measurements following a laser ablation are performed simultaneously.

3.3.1 Filterscope

The Filterscope is a radiometric measurement technique that uses a fiber optic, a narrow bandpass filter, and a photomultiplier tube (PMT) to analyze the intensity of incoming light at specific wavelengths. The fiber optic is used to transmit the light to the PMT. A narrow band-pass filter is placed between the fiber optic and the PMT to only transmit the specific emission line of interest to the PMT. The PMT is then coupled to ORNL designed hardware and software to convert the light into a voltage signal. The ORNL designed data acquisition (DACQ) controls the PMT gain and data collection. The Filterscope, in general, is a combination of highly sensitive PMTs, ORNL designed hardware, and software to provide a high sampling rate ($>$100 KHz in some cases) measurement of incoming light. The combination of the high time resolution with the PMTs ability to detect low-intensity light, is significant because of the characteristics of nanosecond laser-induced plasmas, namely short lifetimes, small plasma volumes, and dynamic.

In our LIBS-LAMS experimental chamber, the Filterscope has the capabilities of acquiring high sampling rates (typically 100kHz, but up to 1 MHz in special setups). In this research the Filterscope was set to 100kHz sampling rate, with a multichannel optical assembly, a 0.250-second measurement window, and is externally triggered by the laser. In Figure 3.6, the multichannel optical assembly allows for three specific emission lines to be measured simultaneously from a single optical fiber. The specified narrow-width bandpass filters are centered at 400.52, 656.19 and 706.72 nm, respectively, in order to specifically detect the W I, D-alpha and He I lines. The incoming light is transmitted to the beam splitter and is then partitioned to the three separate filters such that 50% of the light is bent toward the first PMT, which is the 706.72 He I filter. The

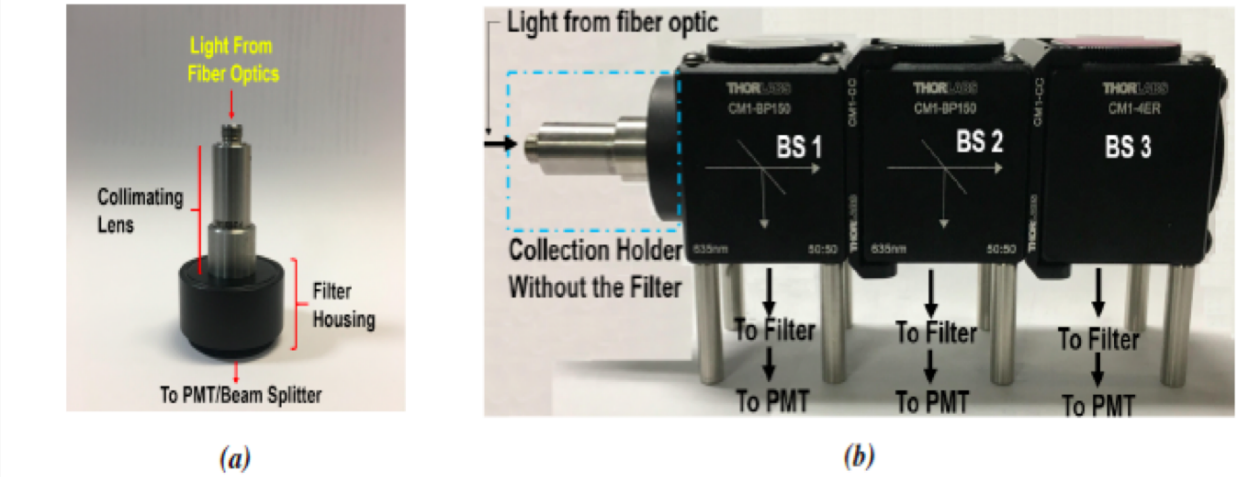

Figure 3.6: a) A photograph of the light collection system involving an optical fiber that is connected to the collimating lenses. b) The collimating lens screws into the lefthand side of the beamsplitter, which transmits the incoming light into three separate filters connected to separate PMTs.

remaining 50% of the transmitted light is then equally partitioned between the second and third filters by bending mirrors. The second PMT analyzes the 656.19 nm D-alpha light while the last filter analyzes the intensity of the 400.52 nm W I light. Once the transmitted light through the beam splitter enters the PMT, the incident photons strike a photocathode. Electrons are ejected from the photocathode surface as a consequence of the photoelectric effect. These electrons are then directed by the focusing electrode toward the electron multiplier, where electrons are multiplied by secondary electron emission. The electron multiplication process occurs many times within the tube, resulting in upwards of 109 elections that subsequently strike the anode. The electron impact on the anode generates a voltage signal recorded by the Filterscope. The conversion from volts to atoms/s is explained in more detail in Section 4.4 of Chapter 4. The Filterscope requires two separate external triggers, one to ready the DACQ and the second to take the measurement. In our LIBS-LAMS experimental setup, the first trigger is provided by a pulse generator that produces a 50 Ohm square shape pulse of 200-microsecond duration. The second trigger pulse is identical to the first and is generated by a pulse generator. However this second pulse triggers both the Filterscope and the laser. The QSMART-100 laser is set to a trigger mode that fires the external flashlamp and internal Q-Switch. Thus the laser begins lasing a signal laser pulse 210 microseconds after receiving the external trigger. The Filterscope measures a peak emission at a

time of ~0.0865s into a 0.250s measurement window using this trigger setup. The external trigger enables alignment of the data measurement in the Filterscope(s), laser ablation control, and beam quality control.

3.4 Mass Spectrometry

LAMS is initiated through the laser ablation process also used to measure LIBS, however, instead of measuring the photon emission within the laser plume, LAMS measures the mass to charge ratio of the current of ionized atoms that are ablated from the surface. After laser ablation, the pumping differential in the vacuum chamber pumps the ionized ablated atoms that remain in the gaseous state from the sample chamber and into the QMS. The measurement of released gas is performed with a Pfeiffer HiQuad quadrupole mass spectrometry system, which is attached to a pre-existing Thermal Helium Desorption Spectrometry (THDS) system that is vacuum connected to an ion implantation station [92]. This QMS has many advantages, such as a modular and flexible design, simple operation with Quadera software, extremely high measurement speed, and outstanding long-term stability [92]. In the LIBS-LAMS measurements of He and D implanted tungsten performed within this dissertation, the QMS measurements were analyzed for mass-to-charge ratios of 2, 3, 4, 12, 16, 18, 28, 32, 44, and 184 which represent H, D, He, C, N, H_2O, Si, O, CO_2, and W, respectively. During an ablation, the vacuum pressure does fluctuate, and the vacuum pressure increases slightly to values in the range of $9x10^7$ - $1x10^8$ Torr. It is important to note that this is a relatively small increase in the background pressure, and we have assumed that this pressure fluctuation does not significantly influence the mass-to-charge ratio ion currents in the QMS. Further, as a result of the increased pumping length of the gaseous species into the QMS, the measured peak appears ~0.088s after the laser ablation which is 0.005 seconds slower than the LIBS measurement. The estimated pumping speed is 680 l/s which is reasonably consistent with the small temporal difference between the LIBS and LAMS intensity peaks. The combination of laser ablation with the QMS is what is defined as LAMS and can be distinguished from Laser Ablation-Inductively Coupled Plasma- Mass Spectrometry (LA-ICP-MS) because, unlike LA-ICPMS, LAMS leverages only a single laser ablation in UHV followed by pumping the ablated species into a quadrupole mass spectrometer equipped with a Channeltron

type electron multiplier, which is similar to the PMT electron multiplier. The calibration processes for the mass spectrometer is common and is explicitly outlined in Ref.[92]. The LAMS calibration is explained in further detail in Section 4.2 of Chapter 4.

Chapter 4

Calibrating LIBS and LAMS Measurements and Results of Proof-of-Principle He Implantation Experiment

4.1 LIBS Calibration

LIBS measures light emitted from the laser-induced plasma formed during a laser ablation using a Nikon F3 lens coupled to a single 1 mm fiber optic. The single fiber optic transmits light into a three-way beam splitter, with a specific emphasis on transmitting specific wavelengths of light corresponding to analyzing He, D and W:

- He I - 706.52 nm bandpass filter with an FWHM of 1 nm, 50% of the light is transmitted through the beam splitter while 50% of the light is bent towards the next bandpass filter;
- D-alpha - 656.19 nm bandpass filter with an FWHM of 1 nm is the second filter 25% of the light is transmitted through the beam splitter while 25% of the light is bent toward the final bandpass filter; and

- W I - 400.50 nm bandpass filter with an FWHM of 5 nm is the third filter, which receives the final 25% of the transmitted light, which is bent using a bending mirror toward the bandpass filter.

Each of these bandpass filters then transmits the light to a photomultiplier tube (PMT) that is separately controlled using the input control voltage V_{cout}. The voltage signal is converted to atoms/s by calibrating the entire system. This calibration of the PMTs occurs over two steps, first calibrating the gain of the PMT, and then secondly, calibrating the normalized radiance of the light at each selected wavelength. The PMT gain calibration is the relationship between the applied voltage and measured light intensity. The normalized radiance calibration converts the voltage signal to a unit of atoms/s [Atom/s]. The two calibration steps require a calibrated light source; a known calibration curve for the light source, which is provided by the manufacturer of the calibrated light source; measured transmission Gaussian profiles for each filter; transmittance of light through the entire experimental setup (instrumental error); and the estimated S, X, and B coefficient for specific atomic transition lines. These S, X and B coefficients refer to ionization, excitation and branching coefficients, respectively (these are described more extensively in Section 4.1.3). The calibrated output of each PMT channel produces a line-normalized irradiance peak (in units of photons/s/cm^2), based on the following equation:

$$L_{A_{i-k}} = \left[\frac{V}{G}\right]_{sig} \cdot \left[\frac{G}{V}\right]_{cal} \cdot \lambda_{i-k}\Delta\lambda_{i-k} \int L_{peak} d\lambda \tag{4.1}$$

Where, A_{i-k} represents the light element A with i-k transition, λ_{i-k} is the wavelength of the i-k transition, $\Delta\lambda_{i-k}$ is the wavelength span for the normalization and is related to the responsively of the PMT. Finally, L_{Peak} is the radiance for the calibration channel, which is specific to each PMT channel setup, i.e. the specifics of the filter and calibration light source.

4.1.1 Gain calibration

The gain of the Filterscope system is G, and is given by;

$$G = G_{PMT} \cdot G_{AMP} \tag{4.2}$$

In the ORNL software G_{AMP} is defined with the value of the amplifier gain and is defined as 1. The PMT gain, G_{PMT} is the current amplification of the PMT. The current amplification defines the ratio of the anode current to the photo-electron current, i.e., the number of electrons to increase the anode current at a given voltage. The relationship between the anode current and the photo-electron current are non-linearly related to the input control voltage, as shown in Figure 4.1. The control voltage in Figure 4.1 demonstrates a power law dependence which is typical for this relationship. Due to the wavelengths selected for this analysis, each of the three PMTs has a specific G_{PMT} characteristic, and in this dissertation, the G_{PMT} for each of the three PMTs has been determined. Figure 4.1 shows the PMT gain calibration curve for the He I Filterscope. The resulting polynomial fit to the gain calibration, as shown in Figure 4.1 for the He I line, is used for the calibration.

4.1.2 Peak Spectral Irradiance

The light transmitted through the fiber optic to the beamsplitter was measured to determine the influence of the experimental system on the output signal. An Ocean Optics calibrated light source was used to calibrate the PMTs and filters, and to determine the line-normalized irradiance for each

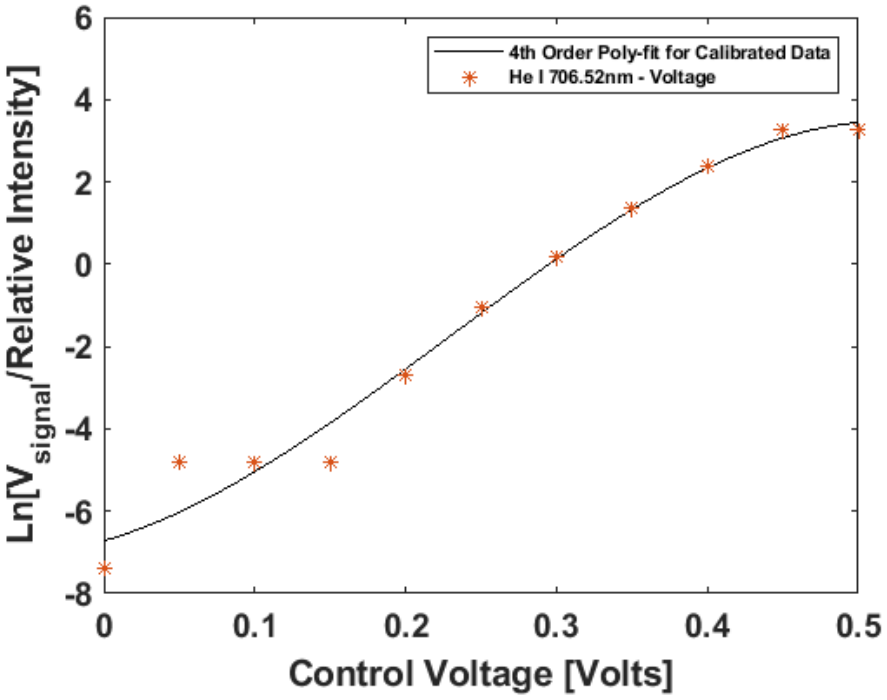

Figure 4.1: Measured influence of the adjusted PMT gain on measure light intensity

PMT. The Ocean Optics spectral radiance curve provides the expected light emission over a broad range of wavelengths. Each PMT and filter must be measured to determine the actual FWHM and transmittance. This is done using the calibrated Ocean Optics light source and the McPherson Spectrometer due to its narrow spectral window and 3 nm resolution. This spectrometer is sufficient to resolve the actual FWHM, central wavelength, and transmittance. Figure 4.2 shows the Ocean Optics calibration curve for the transmission and spectral radiance, as a function of wavelength. The three blue lines in Figure 4.2 represent the normalized transmittance of light through each Filterscope. The manufacturer specification for the bandpass filter indicates that it should be centered on the specified wavelength. However, due to drift over time, or possibly other errors, the wavelength filter may be centered to the left or the right of the specified wavelength. Thus it is important to determine the transmittance of each PMT and filter. The peak irradiance, or L_{peak}, is assessed by multiplying the entire transmission curve for each PMT by the calibration curve provided by the manufacturer (between the wavelength span of the filter). Figure 4.3, plots

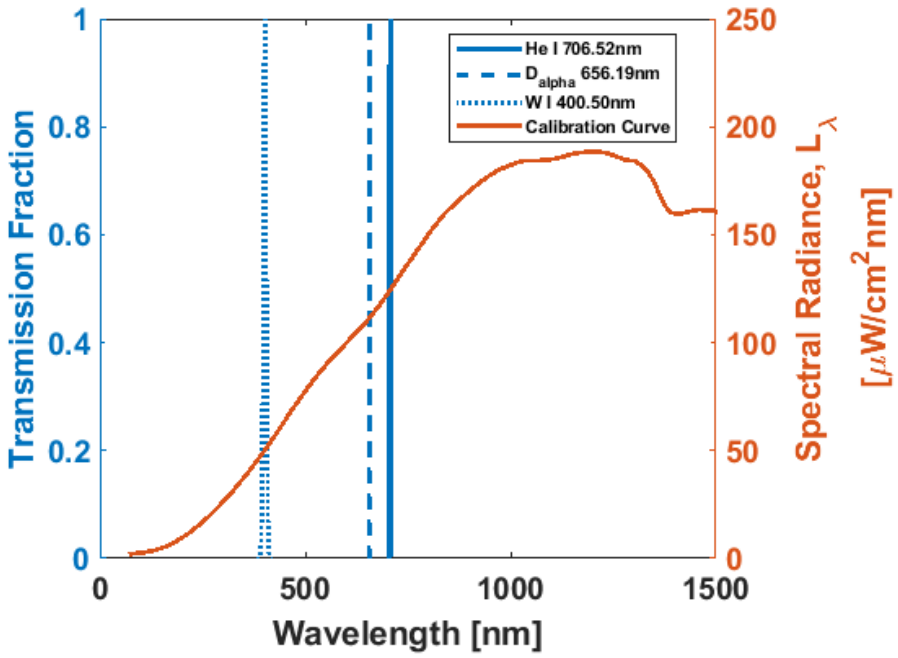

Figure 4.2: The transmission fraction for each bandpass filter He I (solid blue), D-alpha (dashed blue), and W I (dotted blue) is the normalized transmission of light for each bandpass filter (left y-axis). The Spectral irradiance of the Ocean Optics Calibrated Light Source which is a broadband white light source (solid red - right y-axis). The intersection of the bandpass filter peak and the spectral irradiance curve determines the peak spectral irradiation over the entire filter peak.

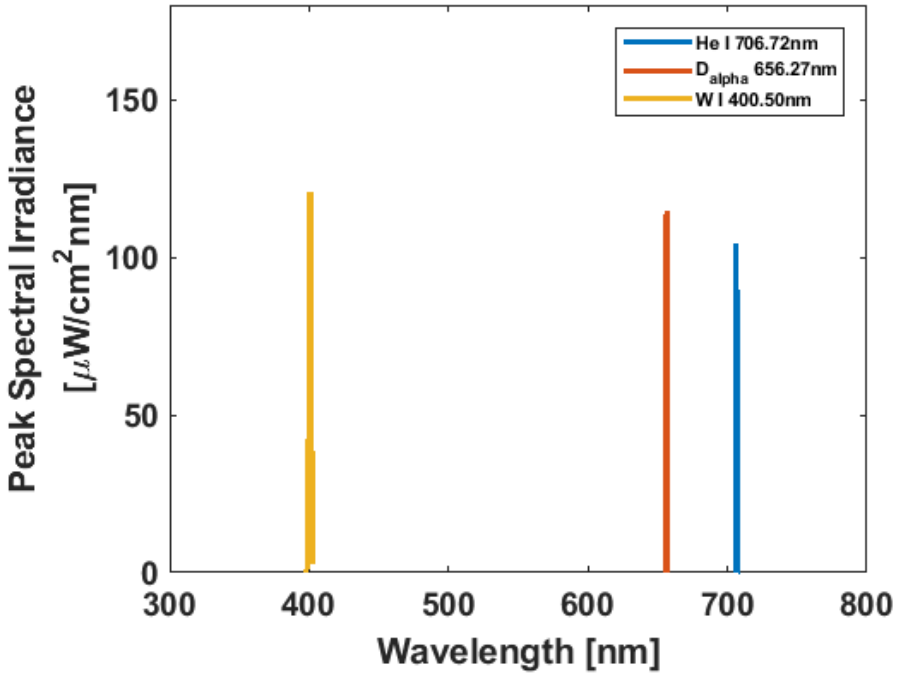

Figure 4.3: After multiplying the entire peak by the intersecting spectral irradiance from 4.2 results in the peak spectral irradiance curve for each bandpass filter.

the peak irradiance of each of the three PMTs, while Figure 4.4 shows a magnified view of the peak radiance for the He I 706.52 nm line. Line normalization uses the peak spectral curve to determine the spectral irradiance of the transition line of interest within the spectral curve. It is better to use a transition line with intensity above the half-max of the spectral curve. The measurement uncertainty is increased if instead the tail (or wings) of the Gaussian curve are used for the line normalization. The peak spectral irradiance calibrated the PMT using the centered peak rather than the line-normalized peak as the latter is specific to an atomic transition. Figure 4.5 shows the atomic transition wavelength positions that the PMTs are calibrated and centered on, these wavelengths are 706.76 nm, 656.19 nm, and 400.87 nm for the He I, D-alpha and W I lines, respectively. These positions are slightly different from the central peak of the Filterscope and the emission line. Figure 4.6 shows a view of the atomic transition line for He I, which is calibrated and centered at 706.76 nm, as compared to the emission line peak location of 706.52 nm. In Figure 4.6, the line-normalized spectral irradiance is plotted as the blue square.

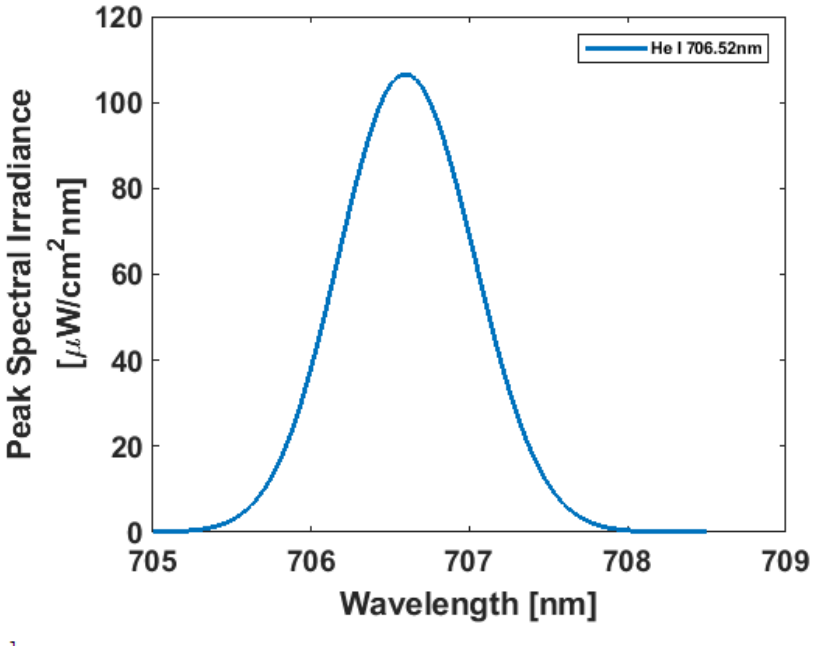

Figure 4.4: After multiplying the entire peak by the intersecting spectral irradiance from 4.2 results in the peak spectral irradiance curve for each bandpass filter. The He I peak spectral irradiance signal is only shown to demonstrate the process.

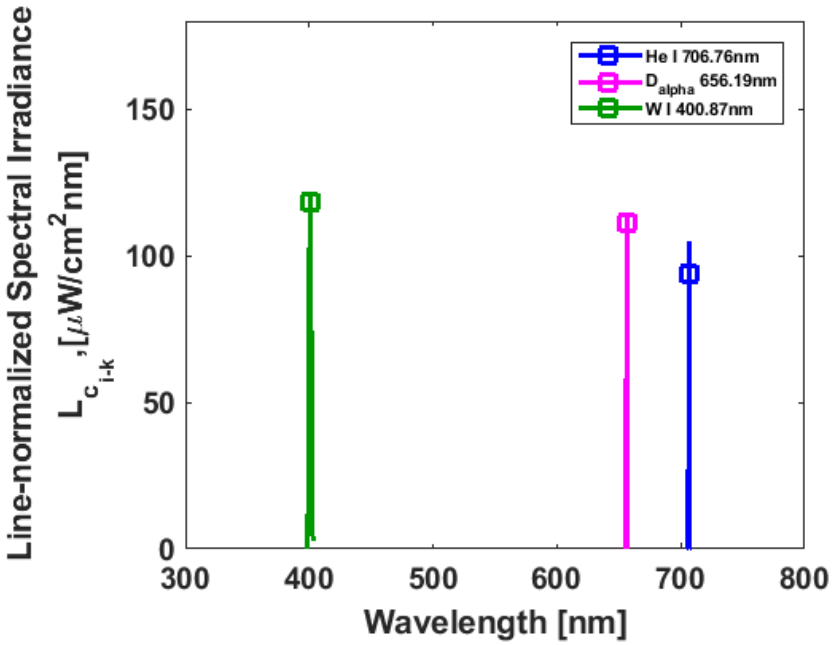

Figure 4.5: The peak spectral irradiance is shown for He I (blue solid line and same peak from 4.4), D-alpha (red solid line), and W I (orange solid line). The line normalization is performed by identifying the spectral line of interest (the respective square markers for each bandpass filter peak) based on the particular wavelength.

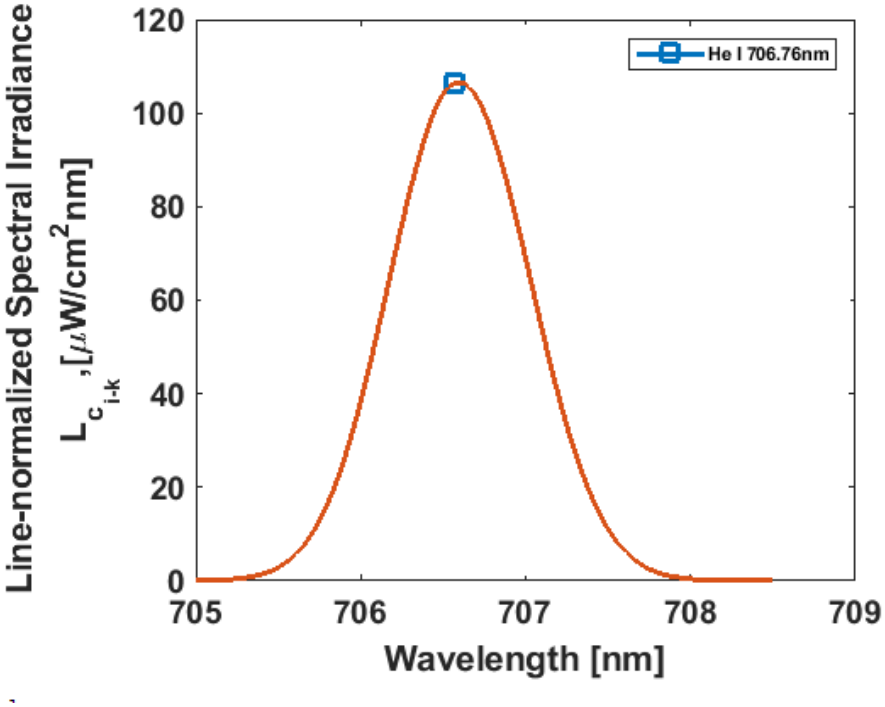

Figure 4.6: The line normalization of He (same peak from 4.5) and the corresponding line of interest, He I 706.72 nm, which has a spectral irradiance of 108 instead of using the peak spectral irradiance of 110.

The spectral irradiance at this transition also defines responsivity of the PMT. At this point, the Filterscopes have been calibrated for gain, transmission, and responsivity. However, the purpose of these calibrations is to convert the signal from volts to atoms/s. The is done first by converting the spectral radiance to Photons/s/m^2. Correspondingly, Eq.(4.3) through (4.5) describe the conversion and calibration process for the i-k transition of element A:

$$\left[\frac{W}{m^2 nm}\right] = \left[\frac{\mu W}{cm^2 nm}\right] \cdot \left[\frac{10^{-6} W}{1 \mu W}\right] \cdot \left[\frac{1 cm^2}{10^{-4} m^2}\right] \tag{4.3}$$

$$\left[\frac{Photons}{m^2 s}\right] = \left[\frac{W}{m^2 nm}\right] \cdot \left[h \cdot \frac{c}{\lambda_{i-k}}\right] \tag{4.4}$$

$$L_{A_{i-k}} = \left[\frac{V}{G}\right]_{sig} \left(\frac{1}{R_{cal}(\lambda_{i-k})}\right) \left[\frac{Photons}{cm^2 s}\right] \tag{4.5}$$

$R_{cal}(\lambda_{i-k})$ is the responsivity value at the i-k transition wavelength and is determined by the peak spectral radiance.

4.1.3 Conversion from μW/cm^{2}nm to Atoms/s

Within the fusion diagnostics community, Filterscopes can be used to determine particle flux from the wall into the SOL. Particle flux is the rate of transfer of particles per unit time and is denoted by having SI units of [atoms/sec]. It is calculated using Eq. (4.6 - 4.9) at a characteristic wavelength,λ_{i-k} were S and X are the ionization and excitation rate coefficients, respectively, and B is the branching ratio, which is the probability of a transition from an upper level to a lower level compared to the total probability of the transition.

$$\Gamma_{A_{i-k}} = L_{A_{i-k}} \lambda_{i-k} \left(\frac{S}{XB} \right)_{i-k} \left[\frac{Atoms}{s} \right] \tag{4.6}$$

$$S = < \sigma_{ion} v_e > \left[\frac{m^3}{s} \right] \tag{4.7}$$

$$X = < \sigma_{exg} v_e > \left[\frac{m^3}{s} \right] \tag{4.8}$$

$$B = \frac{A_{i-k}}{\Sigma_{k \geq i} A_{i-k}} \tag{4.9}$$

The S/(XB) coefficients can be derived from the online database FLYCHK [117]. In this work, two specific papers have been used to determine the S/XB coefficients for He, D, and W respectively. Those papers were Ref. [70, 118]. In the first paper, Farid et al. experimentally measured the dependence of time, laser irradiance, and laser wavelength on the electron density and temperature of a laser-induced plasma produced by ablating polycrystalline tungsten (PCW) [70]. This experiment is important because it demonstrates how dense the laser-induced plasma is ($> 10^{17} cm^2$) for a laser very similar to the laser used in this work, namely a 532 nm Q-Switched laser at a laser irradiance of $\sim$1x10^{15}W/m^2. From this paper, the average density and temperature can be estimated for the laser used in our research. The average density and temperature is estimated to be $\sim$1x10$^{17} cm^2$ and $\sim$2 eV, respectively. However, since this experiment was performed under ambient conditions rather than a high vacuum environment, the dependence on pressure must be determined. In the second paper by Farid [118], the pressure dependence of electron density and temperature was experimentally measured (1 ATM - 10^{-6}Torr) in a laser-induced plasma produced by ablating Cu. It is assumed that Cu and W have similar electron density

and temperature trends, so in this work, we have used the estimated density and temperature from the first paper for W. The trends for the Cu density and temperature versus pressure were then spline fit. The resulting fit coefficient and the spline function were used, in combination with the W density and temperature from the first paper, to determine the electron density and temperature for W in UHV. This leads to an estimate of the plasma density and temperature of 4x10^{18}/cm^2 and 2.2 eV.

The next step in the calibration involves using the electron density and temperature of the laser-induced plasma to determine the correct S/XB coefficients for He, D, and W. Based on the high density expected for our laser ablation conditions, the only database that can provide S/XB coefficients for He and D is FLYCHK [117, 119]. FLYCHK only contains cross-sections and ionization rates for W at this density. The S/XB coefficients used in this effort for He, D and W are ~10^{15}, ~10^{13}, and ~10^{11}, respectively. The conversion from photons/m2s to atom/s is thus completed by multiplying the result of Eq.(4.5) by the appropriate S/XB coefficients [119], such that:

$$\Gamma_{A_{i-k}} = L_{A_{i-k}} \lambda_{i-k} \left(\frac{S}{XB} \right)_{i-k} \left[\frac{Atoms}{s} \right] \tag{4.10}$$

$$S = < \sigma_{ion} v_e > \left[\frac{m^3}{s} \right] \tag{4.11}$$

$$X = < \sigma_{exg} v_e > \left[\frac{m^3}{s} \right] \tag{4.12}$$

$$B = \frac{A_{i-k}}{\Sigma_{k \geq i} A_{i-k}} \tag{4.13}$$

4.2 LAMS Calibration

LAMS, using QMS, measures an ion current of a particular mass to charge ratio. The QMS has an ability to distinguish the masses of He_3 (amu=4.0026) and D_2 (amu=4.0282), because its performance is customized to measure low mass molecules such as H (m/q = 1), H_2 (m/q = 2), HD (m/q = 3), D_2 (m/q = 4). The He, HD, and D_2 current are then converted to the instantaneous desorption rate by multiplying a proportionality coefficient, determined separately with a calibrated leak procedure described further in Ref.[120–122]. The calibration factor for the

mass spectrometer using the He standard calibrated leak was determined to be 0.0998 He mols/C. Figure 4.7 demonstrates the calibration He by leaking He into the vacuum system at a standard rate of 3.80x10^{-13} He mols/s (+-6.73%) and the average QMS signal is 3.8068x10^{-12} Amps. Figure 4.8 demonstrates the calibration of D_2 by leaking D_2 into the vacuum system at standard rate of 3.20x10^{-12} D_2 mols/s and the average QMS signal is 1.214x10^{-11} Amps. It should be noted that, during this calibration, there is a significant amount of HD present in the vacuum system when D_2 was introduced. This is due to H and HD sticking to the stainless steel walls of the vacuum chamber. The HD background can be reduced by baking the chamber, reducing exposure to atmospheric conditions, and maintaining a good UHV (10^{-9} Torr). In this research, baking was performed any time the chamber was vented (exposed to atmosphere), to reduce the presence of HD in the chamber and the vacuum pressure was consistantly kept at ~1 - 4 x10^{-8} Torr. When doing the D_2 standard calibration leak, it is assumed that the conversion coefficients for HD and D_2 are the same and the calibration factor is 0.2254 mols/C. Even with the HD background, LAMS can measure D_2.

An ablation releases both He and W, along with any other species and impurities, and creates a

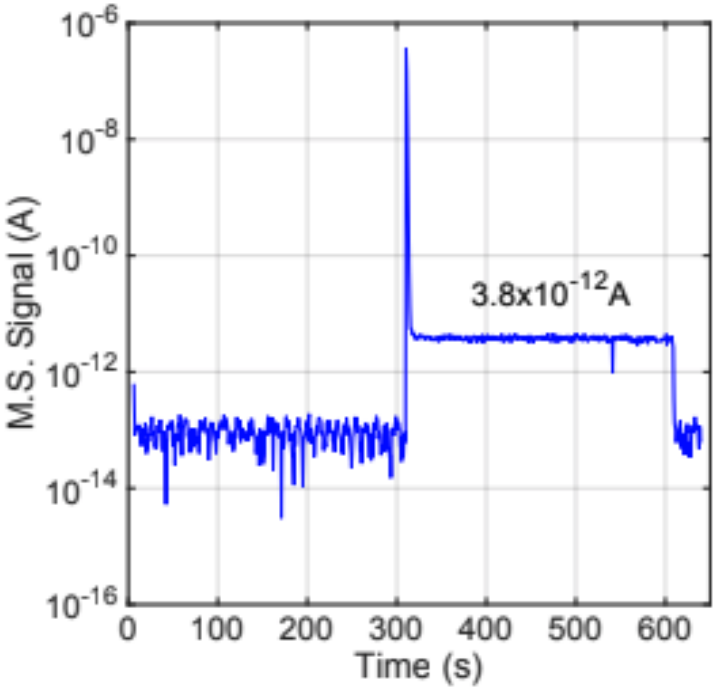

Figure 4.7: LAMS calibration using a He standard leak test.

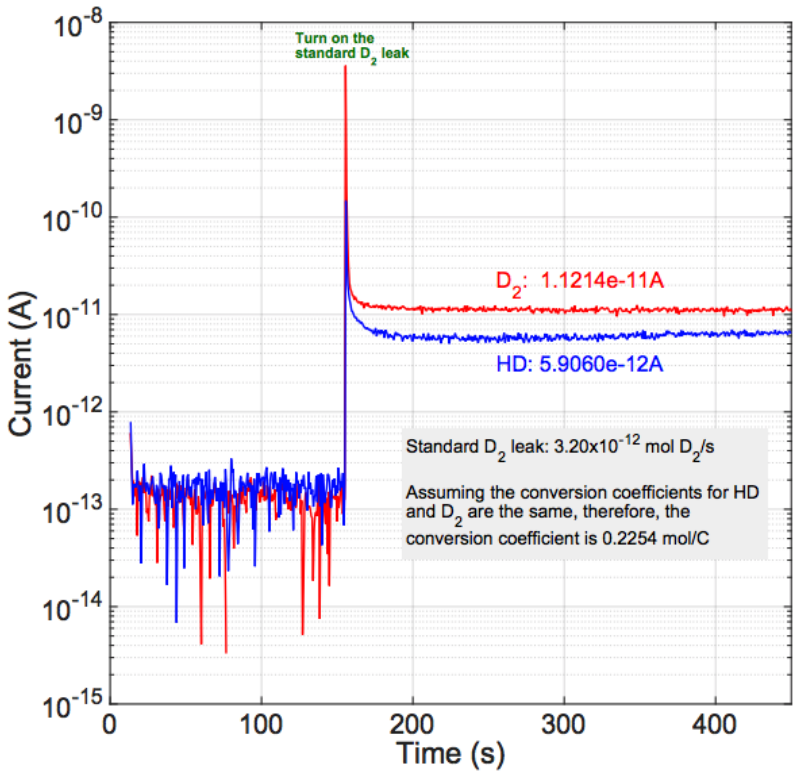

Figure 4.8: LAMS calibration using a D_2 standard leak test. The D_2 peak compared to the HD peak shows the relationship between the two peaks so that we can better distinguish D_2 from He.

crater with a specified volume, as discussed in Section 4.3. Dividing each peak by its corresponding volume results in the amount of He and D per ablated volume, as shown in Figure 4.9. A fully calibrated LAMS uses the known depth and width from accumulating craters, the correction for width expansion after accumulating ablations, and the He and D calibrated leaks to measure the volumetric concentrations as a function of depth below the surface.

4.3 Crater Analysis and Depth Profiling

It is necessary to quantify the ablated volume per laser ablation by converting the calibrated LIBS and LAMS data to a volumetric concentration from the integrated number of atoms within each laser ablation pulse. In addition to quantifying the volume of each laser ablation, it is also necessary to quantify the shape changes associated with each ablation pulse. This is essential since each successive pulse widens, as well as deepens the resulting crater, and this necessitates the development of a methodology to correctly infer the depth dependence of the volumetric

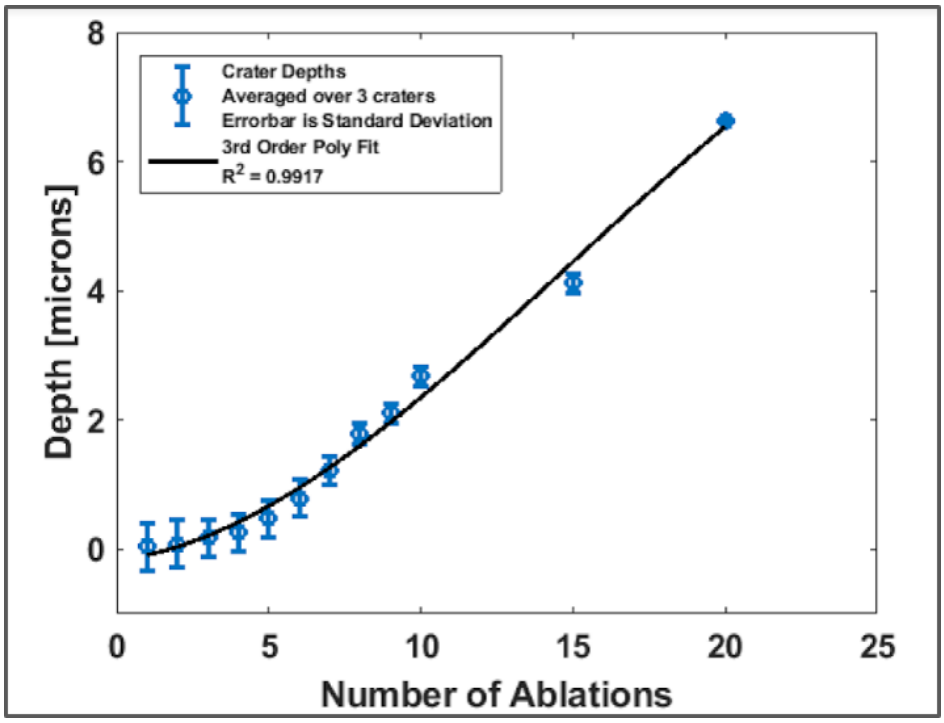

(a)

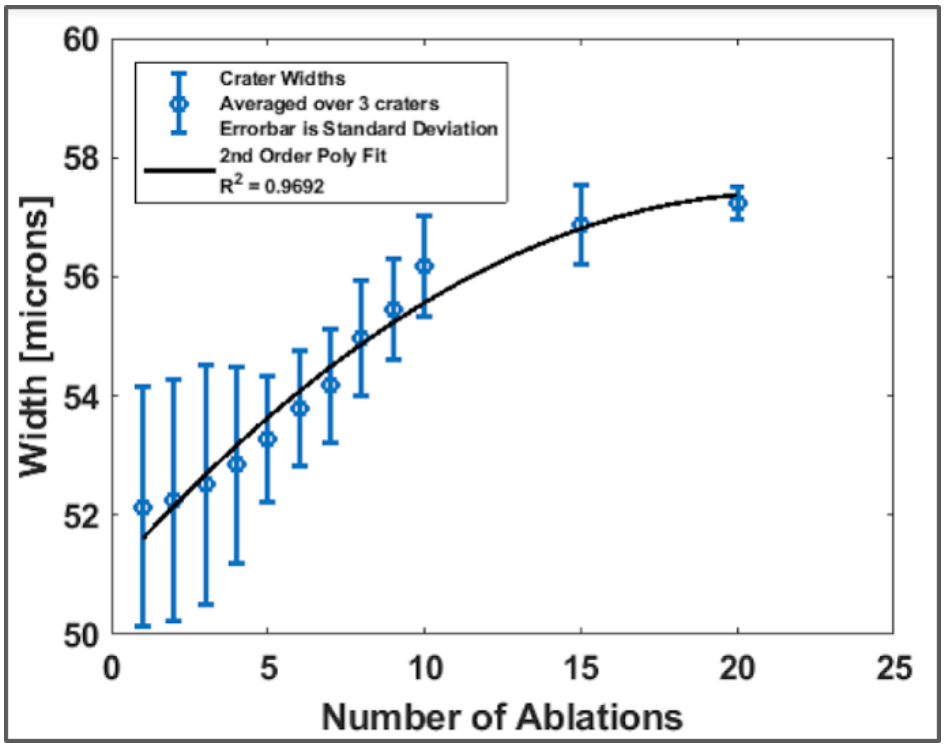

(b)

Figure 4.9: The depths and widths measured using a Keyence Digital Microscope and then fit using a polynomial regression.

concentration of the species of interest (i.e., D and He).

Ablation crater depth and width characteristics were systematically analyzed to develop a relationship governing the increase of crater width, depth and change in geometry as a function of the number of ablations. This was performed by establishing a systematic matrix of ablated craters as a function of the number of laser ablations and the experimental laser conditions. Subsequently, the depth and width of each crater were measured using a Keyence Digital Microscope. The measurement results are presented in Table 4.1 and were used to calculate the total ablated volume, as a function of laser ablation pulse. It is important to note that the ablated depths for single, and a small number of laser pulses, challenged the resolution limit of the optical microscope, as well as the limited light reflection of some measurements. The calculated volumes were compared to atomic force microscopy (AFM) measurement of a single ablation. An example AFM measurement of the tungsten surface surrounding a laser ablation crater is shown in Figure 4.10. The AFM results are compared to the calculated volumes in Figure 4.11.

A polynomial regression was fit to the measured depth and width data, and the resulting volumes have been calculated based on several different models to describe the geometry of the

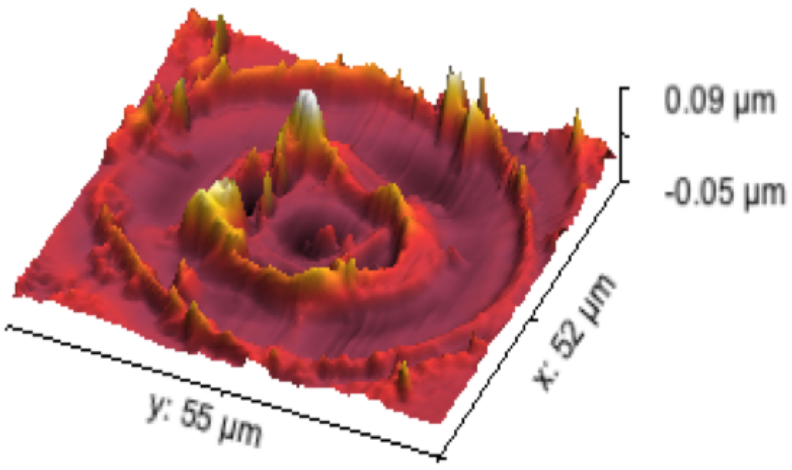

Figure 4.10: Atomic Force Microscopy image of the tungsten surface surrounding a single laser ablation crater.

Table 4.1: Depths and widths measured using the Keyence Microscope.

Accumulating Ablations	Depth* [microns]	Width* [microns]
1	0.045	52.14
2	0.081	52.25
3	0.173	52.51
4	0.253	52.84
5	0.478	53.27
6	0.792	53.78
7	1.211	54.17
8	1.789	54.98
9	2.101	55.46
10	2.681	56.17
15	4.116	56.87
20	6.624	57.23

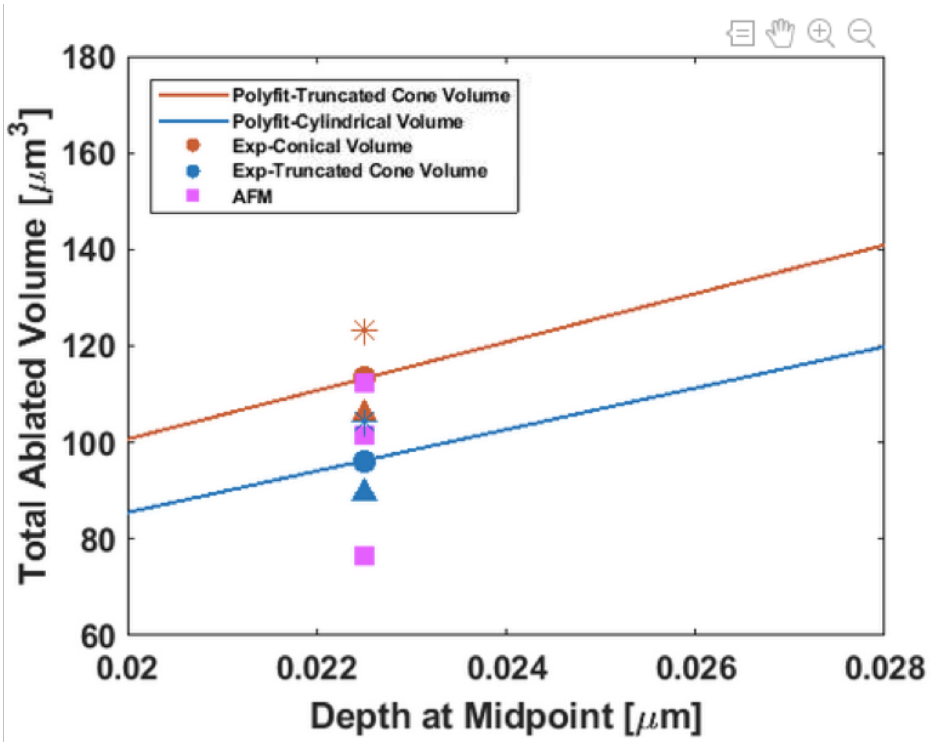

Figure 4.11: Total volume comparison of three different experimentally measured craters based on either a cylindrical or truncated cone geometry. The red and blue symbols (star, circle, and triangle) represent three experimental measured ablations used to calculate the total cylindrical and truncated conical volume, respectively. The three ablations were plotted to show the spread of the data instead of error bars. The magenta squares represent three different AFM measurements.

ablated volume. The measurements of the crater depth and width were performed using a Keyence Digital Microscope however with this optical microscope, it was not possible to accurately assess the ablation surface. Therefore a volume assumption was made to convert the measured depth and width into three geometric shapes: 1) cylindrical, 2) conical and 3) truncated conical. The calculated volumes were used in a volume sensitivity analysis and element concentration analysis. The equations used to calculate the cylindrical, conical, and truncated conical are as follows and are illustrated in Figure 4.12

Finally, a polynomial regression was fit to the measured depth and width data. calculate the cylindrical, conical, and truncated conical are as follows and corresponds to Figure 4.12. Several notable features resulted from the depth and width analysis. The ratio of the crater width to depth is initially very high (1150X) but decreases with increasing number of ablations, as the differential depth and width from one crater to the next decreases, as shown in Figure 4.13. This is due to the incremental increase in crater width being initially very high (52 microns per ablation) before

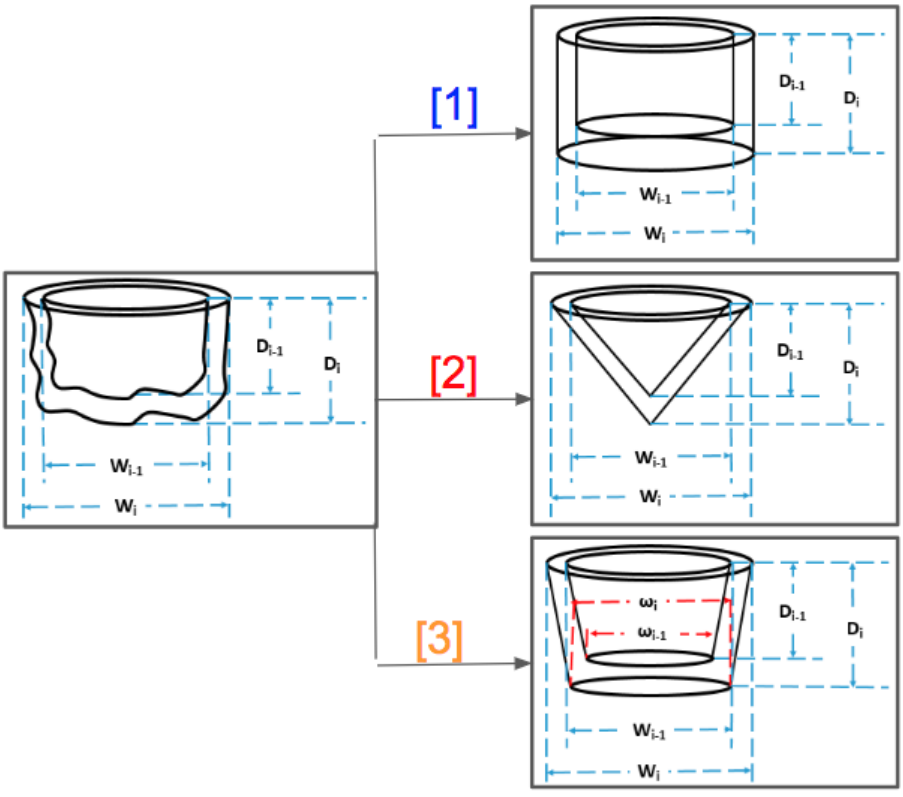

Figure 4.12: Three different regular volume geometries used to assess the ablated crater volume, namely: 1) cylindrical, 2) conical and 3) truncated cone

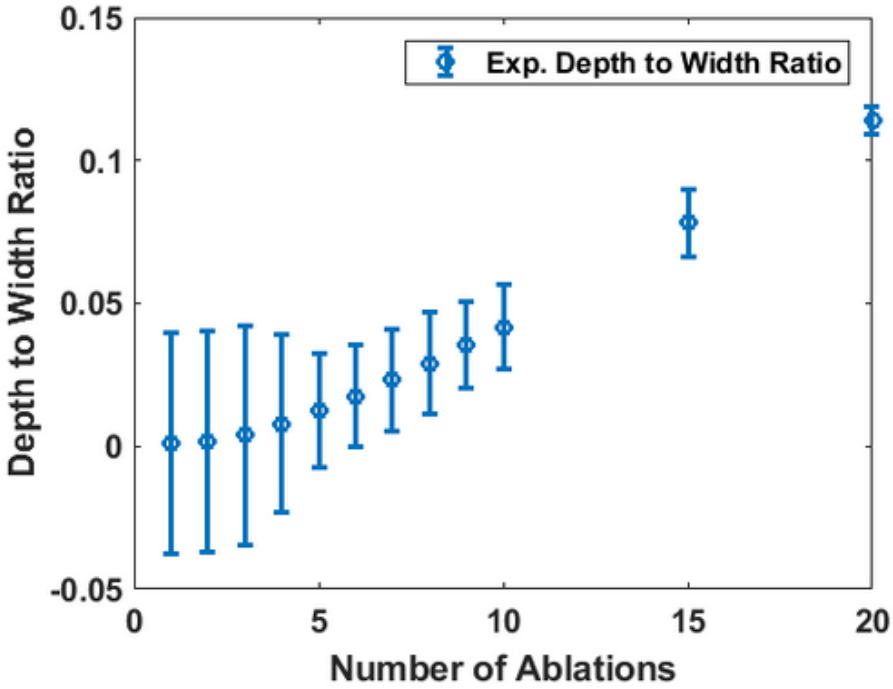

Figure 4.13: The depths and width ratio measured using a Keyence Digital Microscope.

decreasing towards a saturation width value at roughly 20 ablations (of approximately 57 microns) in combination with the rapid increase in the incremental crater depth (which increases from 0.05 microns initially to >6 after 20 ablations). The initially large crater width is a result of the focal length being located beneath the material surface. The large width to depth ablation ratio, along with the increasing crater widths as a function of number of laser ablations, highlights the need to correct for the element concentration at shallower depths (i.e., each subsequent laser pulse is ablating material at depths corresponding to previous laser shots).

Because ablation is not strictly downward, volume removal occurs both in the existing "ith" ablation layer and prior ablation layers ("i-1" to "1st"). As such, the element concentration found in layers i-1 to 1 will be present in the signal for layer i. This must be corrected to accurately represent the concentration profile. This process is numerically and graphically represented in Eq.(4.19) and Figure 4.14, respectively. The result of this volume correction are demonstrated in Section 4.4. The uncorrected concentration calculation involves dividing the ablation signal by the

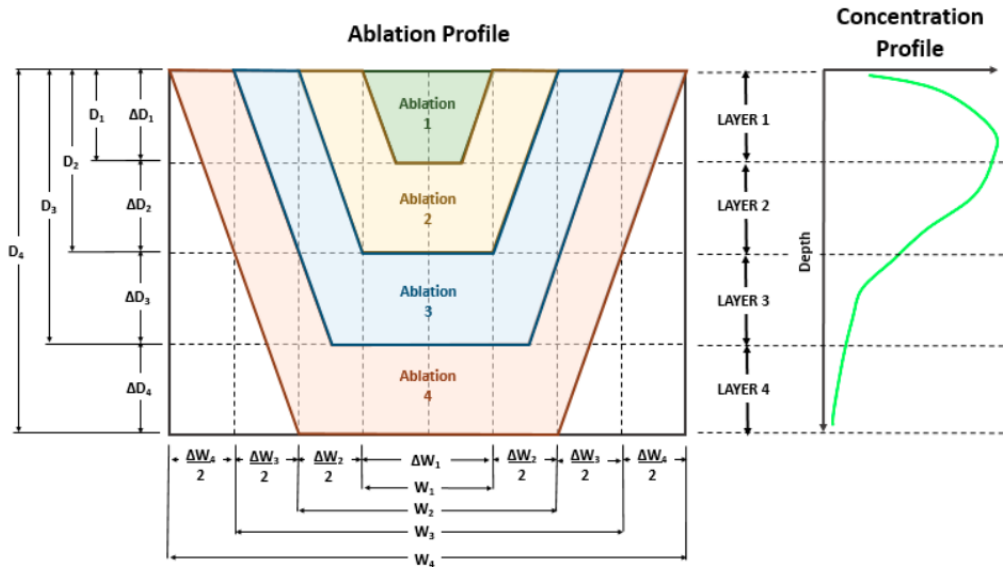

Figure 4.14: Illustration outlining the incremental width and depth per laser ablation, in addition to the reference element concentration profile. The differential depths and widths per laser ablation are also noted in this schematic. Furthermore a flat profile is assumed.

ablated volume in the "ith" ablation, as shown in Eq.(4.19)

$$V_{cyl} = pi\left[\frac{W}{2}\right]^2 D \tag{4.14}$$

$$V_{cyl_i} = \pi\left(\left[\frac{W_i}{2}\right]^2 D_i - \left[\frac{W_{i-1}}{2}\right]^2 D_{i-1}\right) \tag{4.15}$$

$$V_{con} = \pi\left[\frac{W}{2}\right]^2\left[\frac{D}{3}\right] \tag{4.16}$$

$$V_{con_i} = \pi\left(\left[\frac{W_i}{2}\right]^2\left[\frac{D_i}{3}\right] - \left[\frac{W_{i-1}}{2}\right]^2\left[\frac{D_{i-1}}{3}\right]\right) \tag{4.17}$$

$$V_{tcon} = \pi\left(\left[\frac{W}{2}\right]^2 + \frac{W\omega}{2} + \left[\frac{\omega}{2}\right]^2\right)\left[\frac{D}{3}\right]\Bigg) \tag{4.18}$$

$$\begin{aligned} V_{tcon_i} = \pi\Bigg(&\left(\left[\tfrac{W_i}{2}\right]^2 + \tfrac{W_i\omega_i}{2} + \left[\tfrac{\omega_i}{2}\right]^2\right)\left[\tfrac{D_i}{3}\right] \\ &-\left(\left[\tfrac{W_{i-1}}{2}\right]^2 + \tfrac{W_{i-1}\omega_{i-1}}{2} + \left[\tfrac{\omega_{i-1}}{2}\right]^2\right)\left[\tfrac{D_{i-1}}{3}\right]\Bigg) \end{aligned} \tag{4.19}$$

Performing a width correction for the influence of elemental concentration at layers, from layer 1 to layer i-1, involves removing the volume ablated in layers, from layer 1 to layer i-1, and

correcting the recorded signal to remove the intensity associated with shallower layers. As with the uncorrected evaluation, the first step involves assessing the volume ablated across all layers for the "ith" ablation. The volume of the layers from layer 1 to layer i-1 within the "ith" ablation is then calculated to isolate the volume of the "ith" layer ablated. This then calculates the influence of layers 1:i-1 on the signal of the "ith" ablation by multiplying the volume of each layer ablated by its previously corrected concentration. The corrected volume and signal are then used to assess the corrected element concentration within the "ith" layer ablated. It is important to note that this depth-correction procedure assumes that the concentration is homogeneous as a function of depth (e.g., increasing ablated volumes). This depth-correction process is illustrated in Figure 4.14 (albeit showing a non-uniform concentration profile as a function of depth) and specified by: Eq.(4.20)

$$C_i = \frac{Signal_i}{AblationVolume_i - \Sigma_{n=1}^{i-1} AblatedVolume_n} \tag{4.20}$$

$$C_i = \frac{Signal_i - \Sigma_{n=1}^{i-1}\left[LayerVolume_n \cdot LayerConcentration_n\right]}{AblationVolume_i - \Sigma_{n=1}^{i-1} AblatedVolume_n - \Sigma_{n=1}^{i-1}\left[LayerVolume_n\right]} \tag{4.21}$$

4.4 Proof of principle demonstration of LIBS/LAMS technique for measuring sub-surface helium concentration

A well-characterized proof-of-principle experimental measurement was performed to demonstrate the capability of LIBS/LAMS to measure the sub-surface gas concentrations in tungsten. A helium ion implanted reference material was designed to provide a nearly uniform concentration of helium in tungsten up to a given depth. This proof-of-principle experiment was motivated by previous ion implantation measurements performed by Zinkle and co-workers [123]. In that work, Zinkle et al. [123] implanted copper, nickel, and Cu- Ni alloys with He ions with energies varying between 200 - 400 keV obtaining a He concentration of 200 appm from the surface to a depth of approximately 0.7 microns. Similarly, Getto et al. [124] implanted the ferritic-martensitic alloy HT9 with helium using a National Electrostatics Corporation accelerator. The helium implantations were performed at 80,140,220,310, and 420 keV to yield an approximately flat (+-10%) concentration depth

profile over a depth range from 300 to 1000 nm, based on implantation profiles calculated using SRIM. Correspondingly, an experimental helium implantation profile was designed for six tungsten reference specimens following the implantation profile of Getto et al.[124]. All six specimens were polycrystalline tungsten (PCW) of 99.995% purity, consisting of disks that were 5 mm in diameter and 1 mm thick, purchased from GoodFellow. The specimens were polished to a 0.05 micron mirrored surface using a colloidal silica surface polish. The PC-W specimens were shipped to the University of Michigan Ion Beam Laboratory for He ion implantation. The implantation parameters are shown in Table 4.2, and involved helium implantations at energies from 410 keV - 80 keV, beginning with the highest energy of 410 keV then incrementally decreasing the helium ion energy to 80 keV, with the goal of implanting an approximately flat concentration profile of 200 appm He, over a depth range from 0.30 - 1 micron, which are similar to Ref [124]. The implantation profile for these reference specimen were calculated by SRIM [125] and is shown in Figure 4.15.

For a single sample, fifteen accumulated ablations were performed in two spatial locations

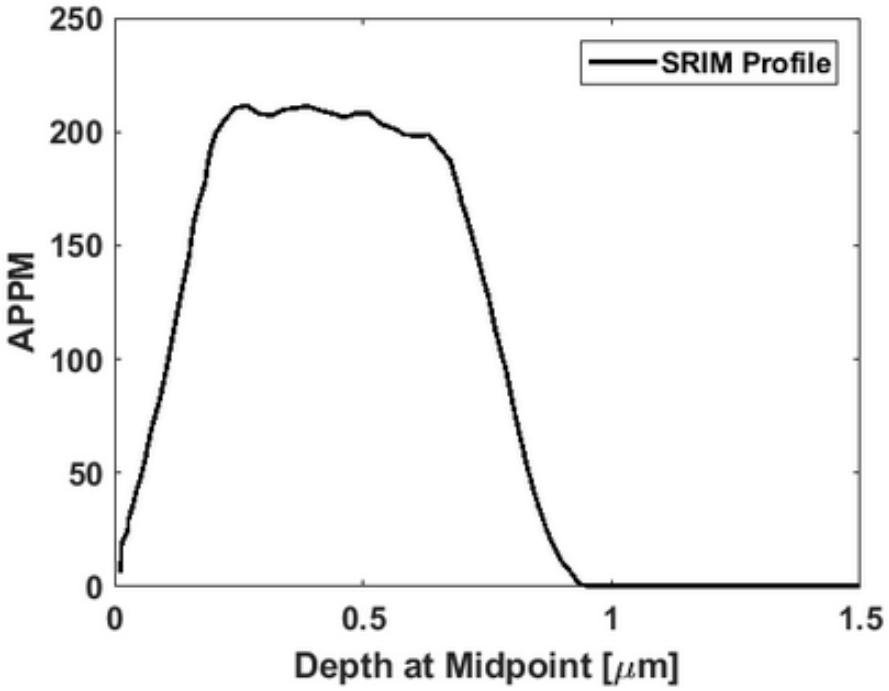

Figure 4.15: The implantation profile of 410-80 keV implanted He at a fluence range of 2.06x10^{15} to 6.02^{14} cm^{-2} in W estimated by SRIM[125].

near the center of the sample. The distance between the two laser ablation locations was 0.25 mm. The LIBS and LAMS signal was measured for each of the fifteen ablations. The method used to convert the raw LIBS signal (volts) to volumetric concentration (atoms/m^3 or He APPM) was described in Section 4.1. The conversion of the LAMS signal, which was also recorded at each of the ablations, followed the process outlined in Section 4.2. Throughout the analysis, the volume correction assumed a combination of cylindrical and truncated conical volume crater geometries (as previously defined in Figure 4.12). This is based on the optical microscopy observations of the crater, which indicated a transition from an approximately cylindrical shape to a truncated cone geometry after the 5th ablation. Based on the calculated SRIM profile, it was anticipated that the LIBS and LAMS signal of the helium concentration would increase, plateau and then decrease as a function of the total number of accumulated ablations. Additionally, one of the helium implanted PCW samples was sent for elastic recoil detection analysis. The following section discusses the results of this analysis.

4.4.1 LIBS Analysis

The unprocessed LIBS signal showing the He peaks during each of the fifteen ablations is shown in Figure 4.16. The raw LIBS signal broadly coincides with the anticipated increase, plateau, and decrease of the helium with increasing depth, although the plateau of the signal is difficult to distinguish in this view of the raw data. Following the analysis method described in Section 4.1, the voltage signal in the He Filterscope PMT is first converted to photon flux, as shown in Figure 4.17, and then subsequently translated as a function of depth below the surface (following the depth correlation per laser pulse established in Section 4.1). This is necessary to quantify the elemental concentration. Figure 4.17 shows the resulting number of photons ($m^{-2}s^{-1}$) as a function of time. Each ablation in Figure 4.17 consists of a time-dependent peak, with a marked increase and decrease of photons per area as a function of time. By integrating under each peak, the photon fluence is obtained, and Figure 4.18 shows the resulting photon fluence as a function of depth. It is important to note that it is the integrated photon fluence rather than simply the peak photon flux magnitude that correlates to the elemental concentration. This is best exemplified by comparing the first versus the eight photon flux peak in Figure 4.17, with the resulting integrated fluence

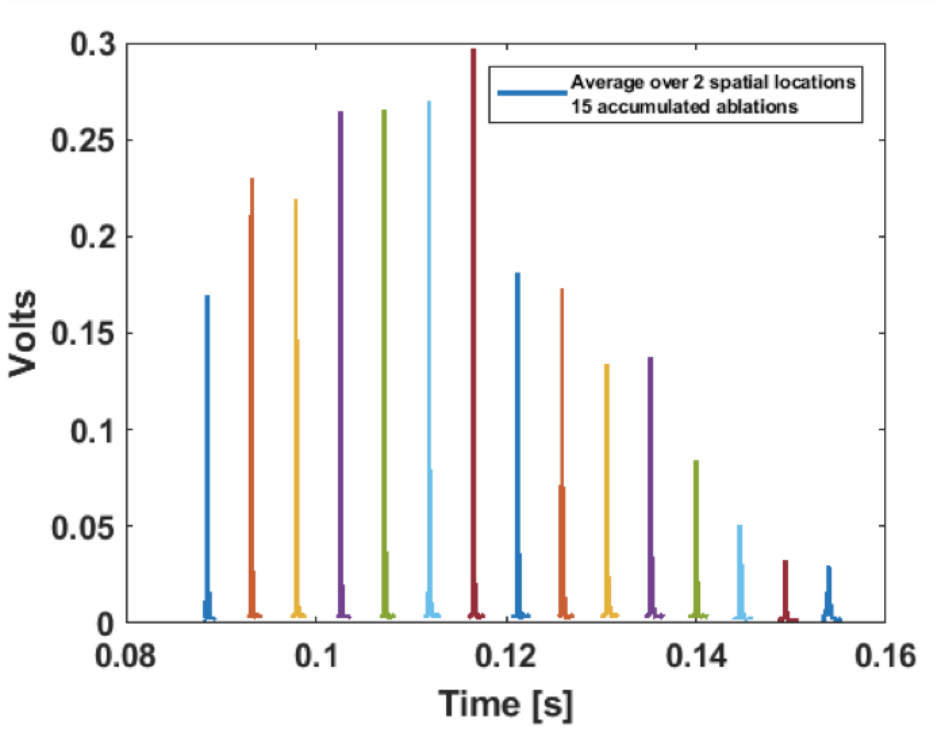

Figure 4.16: The raw LIBS signal, as measured during fifteen accumulated ablations, and averaged over two spatial locations.

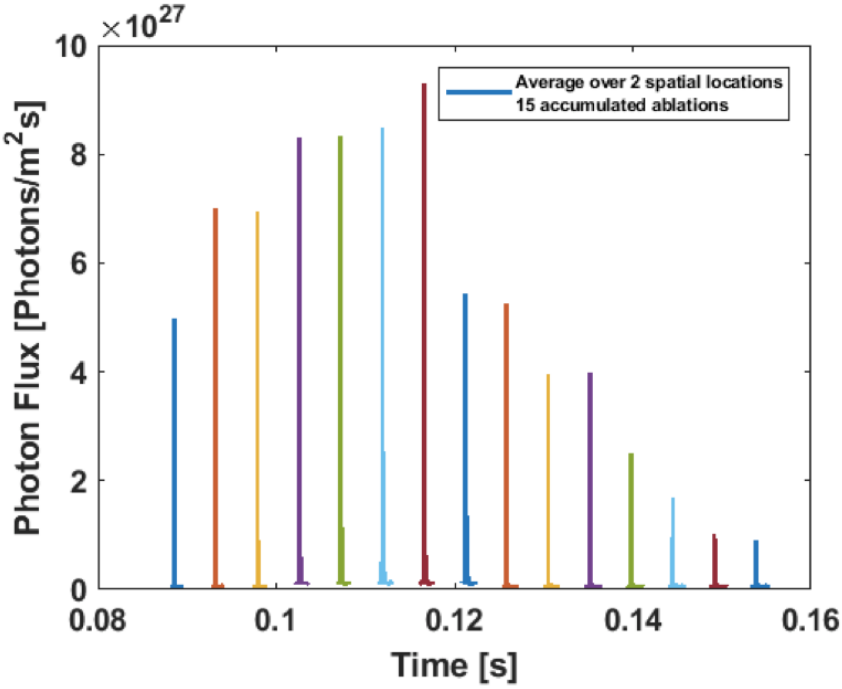

Figure 4.17: The resulting LIBS photon flux signal during fifteen accumulated ablations, averaged over two spatial locations.

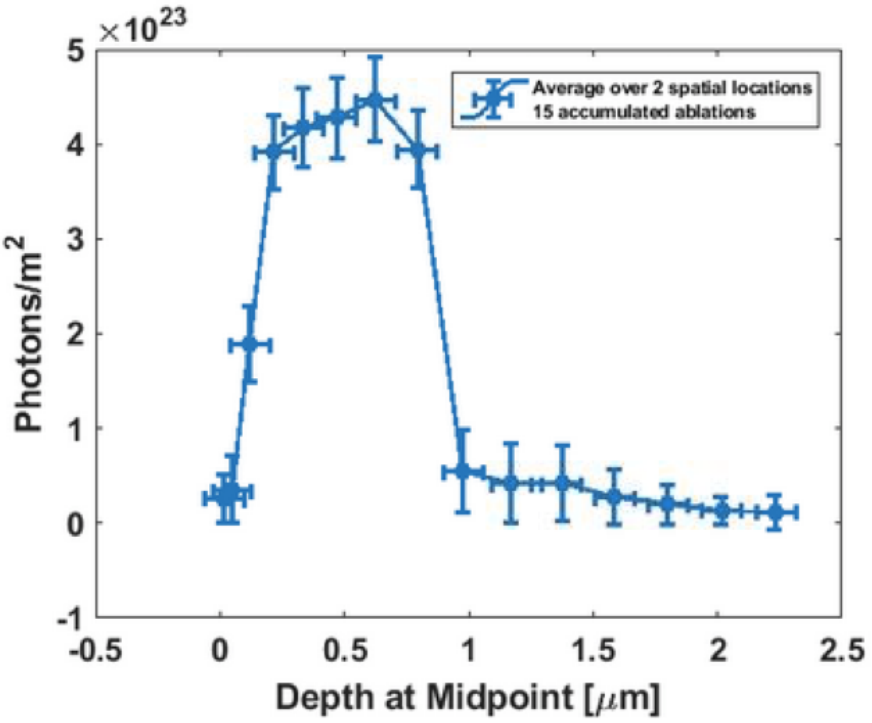

Figure 4.18: The LIBS Integrated Photon Flux signal for fifteen accumulated ablations, averaged over two spatial locations.

values presented in Figure 4.18. While the first and eighth ablation photon fluxes have similar magnitudes (Figure 4.17), following the integration over the time dependence of the photon flux, it is clear that the photon fluence is much larger in the eighth laser ablation than in the first. The temporal variation of the photon flux is shown in higher resolution in Figure 4.19, in which the larger photon fluence associated with laser ablation number eight is identifiable. The next step in the LIBS data analysis involves multiplying the integrated photon fluence by the SXB coefficient for He (as described in Section 4.1.3), and this provides the total number of atoms. The total number of atoms is then divided by the volume associated with the specified laser ablation, to obtain a volumetric concentration that is subsequently corrected based on the process described by Eq.(4.17) and illustrated in Figure 4.14. Thus, the result of the LIBS analysis is a volumetric concentration (e.g., He/m^3). Converting He atomic parts per million, the volumetric concentration is divided by the number of W atoms per volume (this is $6.32 \times 10^{28} m^{-3}$), and then multiplied by one million. Figure 4.20 plots the resulting volume corrected He concentration (in units of appm) as a function of depth (taken as the mid-point depth per accumulated laser ablation) and compared

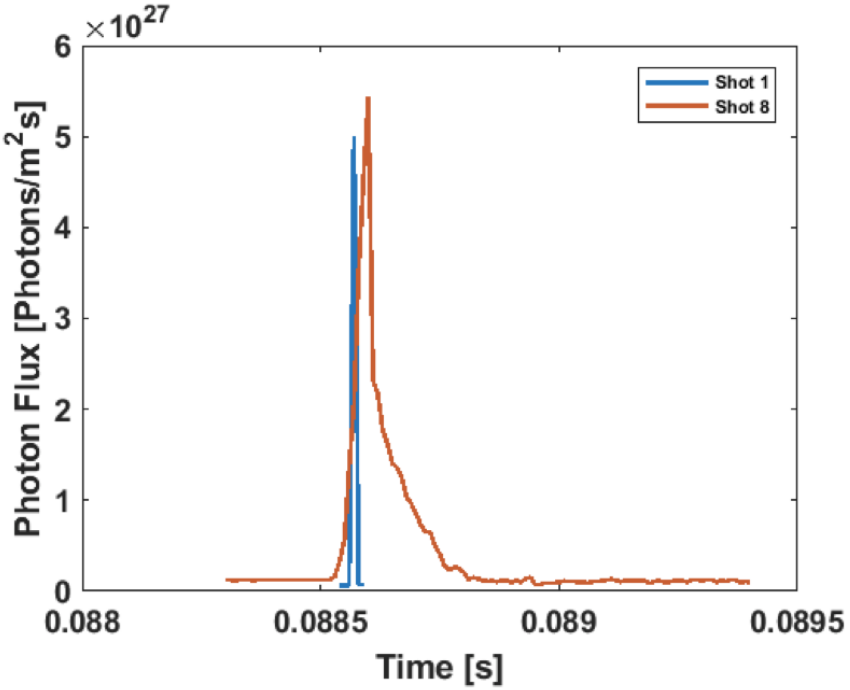

Figure 4.19: Comparison of the first ablation peak to the eighth ablation peak to demonstrate variation in peak profile.

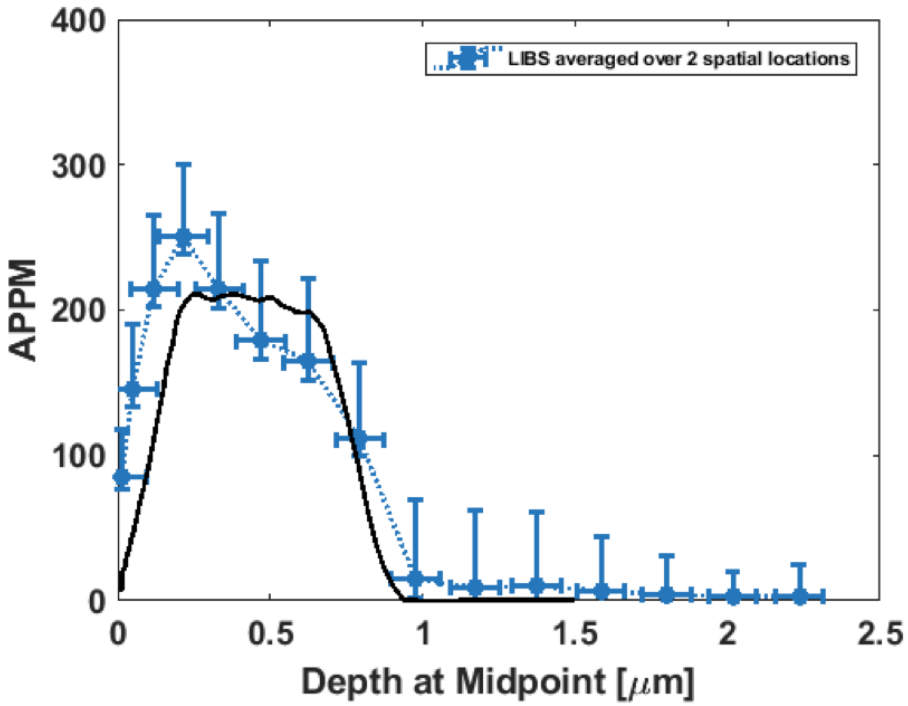

Figure 4.20: LIBS helium appm as a function of depth compared to calculated SRIM profile [125].

to the SRIM calculation. The LIBS data in Fig.4.20 has been averaged over two separate ablation locations, and the error bars represent the averaging of the signal across these two locations as well as the calculated variation in the ablated depths. Overall, the agreement between the measured LIBS helium concentrations and the calculated He implantation profile is quite good. Thus, Fig.4.20 demonstrates the ability to quantify He concentration as a function of depth with good agreement to the calculated SRIM implantation profile. This experiment demonstrates the fidelity of the developed LIBS measurement and analysis technique, enabling confidence in the subsequent application of the technique.

4.4.2 LAMS Analysis

The raw LAMS signal is obtained from the QMS, as the ablated gases are pumped into the mass spectrometer immediately following the Filterscope measurement of the light emission from the resulting ablated plasma in LIBS. Thus, the raw LAMS signal was obtained during the same fifteen accumulated ablations at two spatial locations. This raw LAMS signal is shown in Figure 4.21, which shows the measurement peaks associated with the mass-to-charge (m/q) ratio of 4

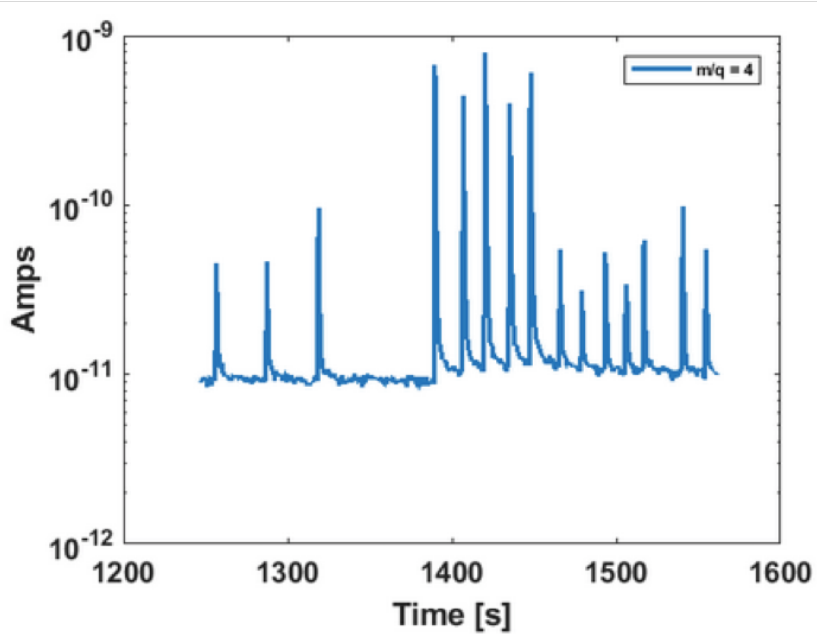

Figure 4.21: The LAMS raw signal for fifteen accumulated ablations, averaged over two spatial locations.

(He). It is important to note that the signal in m/q ratio 2 (H) and 3 (HD) was also monitored during this experiment. A small signal was observed in the m/q channel of 2, presumably due to surface adsorption of hydrogen, but the signal in this channel decreased after a few accumulated ablations. There was no significant signal in m/q = 3 channel of the QMS during the laser ablations. Figure 4.21 shows the QMS signal in the m/q ratio 4 averaged over the 2 spatial laser ablation locations for each of the 15 laser pulses. Similar to LIBS, peak integration must be performed to convert the QMS signal to atoms. The peak integration was performed with an integration period determined by the edge and decay of each peak. Again, similar to LIBS, the peak profile determines the resulting number of atoms attributed to each ablation, based on the calibration of current to a known leak volume (as described in Sect. 4.2). Figure 4.22 plots the resulting volumetric helium concentration as a function of the mid-point depth of the accumulated laser ablation. It is important to point out that the concentrations plotted in Fig.4.22 have not been depth corrected to account for the increasing ablated width with increasing number of laser pulses. Figure 4.23 plots the resulting corrected helium concentration measured by LAMS following the depth correction analysis described in Section 4.3. Figure 4.23 demonstrates a good agreement of the LAMS measurement in comparison to the SRIM calculated implantation profile, although a slightly higher concentration of helium was measured by LAMS at a depth approaching 1 micron after the implanted concentration profile begins to decrease rapidly. Overall, this measurement has demonstrated that LAMS can quantify He as a function of depth below tungsten surfaces, and have a good agreement with the calculated implantation profile, similar to the LIBS results. The level of agreement between the two provides confidence in the subsequent application of the coupled LIBS and LAMS measurement technique.

4.4.3 LIBS and LAMS Proof-of-Principle Experiment Comparison

When assessing the viability of a novel surface characterization technique, such as LIBS and LAMS, it is critical to compare the results to a conventional technique. The benchmarking of the LIBS and LABS analysis within this proof-of-principle helium implantation to produce a ‘flat-top’ helium concentration has been compared to the SRIM calculated helium implantation profiles and demonstrated good agreement with SRIM and to each other. Additionally, Figure 4.24 compares

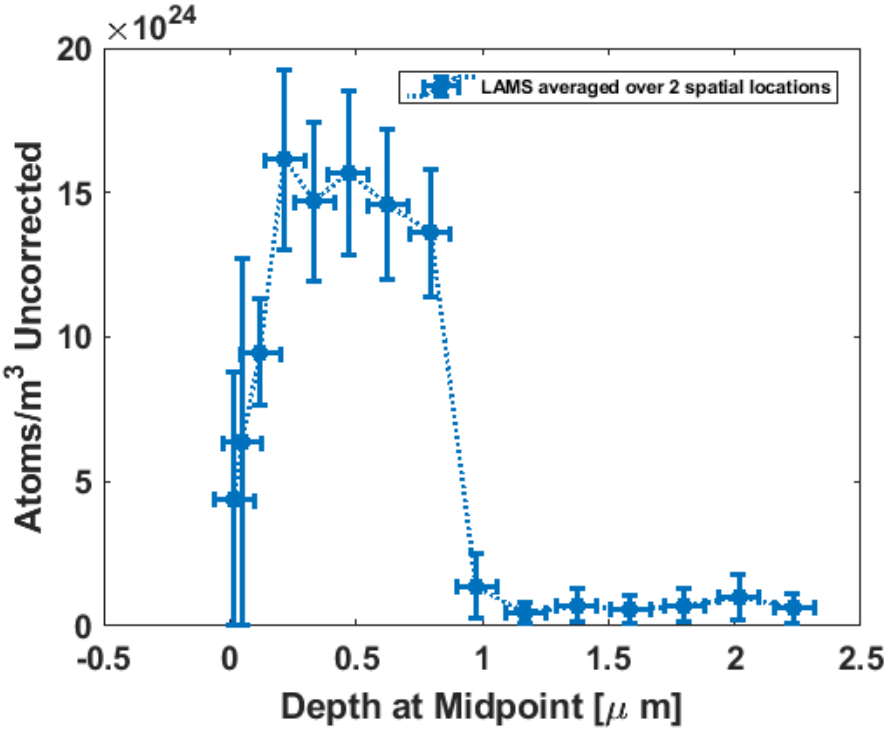

Figure 4.22: The LAMS He volumetric signal as a function of depth. The LAMS signal has yet to be corrected for volume expansion.

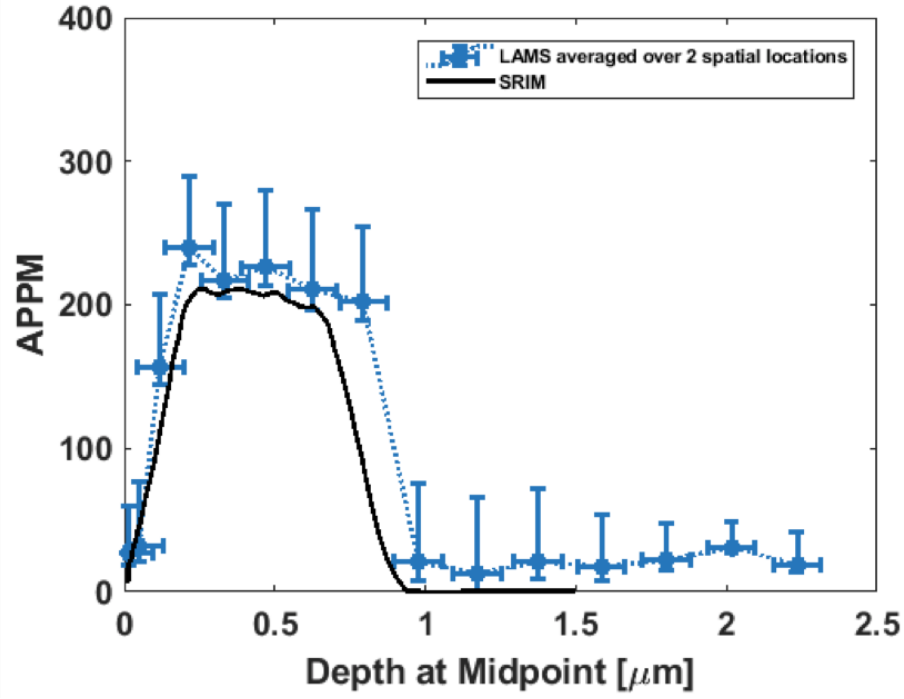

Figure 4.23: Volume corrected LAMS He concentration (appm) averaged over two spatial locations as a function of depth, and compared to the SRIM calculated implantation profile.

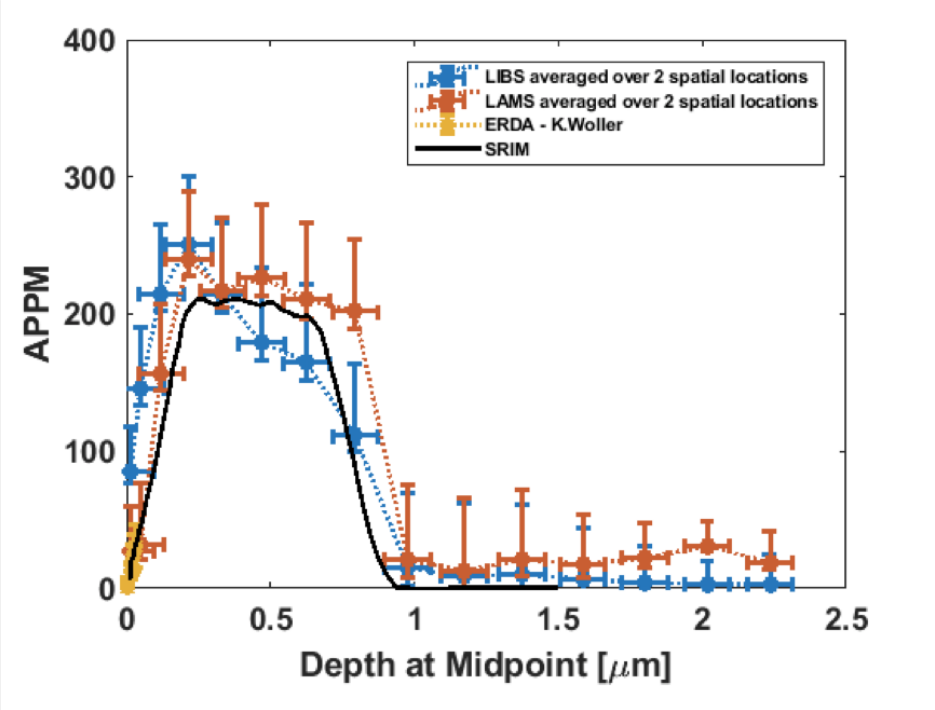

Figure 4.24: Cross comparison of Helium concentrations (appm) for LIBS (blue), LAMS (red), and ERDA (orange) to the calculated SRIM profile [125] as a function of depth.

the resulting LIBS and LAMS measurements to the ERDA measurements performed by Kevin Woller of MIT. While ERDA has a very limited depth resolution in tungsten, the ERDA results are in good agreement with the LIBS and LAMS measurements for the initial increase in helium concentration below the surface. However, as mentioned previously, ERDA is not a bulk analysis technique and was only able to measure the He appm signal to a depth of about 60 nm. Even though ERDA was not able to measure the entire He flattop profile, the results presented in Figure 4.24 in the near surface region demonstrate good agreement between the SRIM calculations, as well as the LIBS and LAMS measurements. In summary, these results demonstrated that LIBS and LAMS could be used as a surface characterization technique to quantify He and therefore other similar fusion relevant particles as a function of depth in W.

Chapter 5

Experimental Conditions of LIBS-LAMS measurements of plasma exposed W

5.1 Tungsten Specimens

GoodFellow manufactured all tungsten used in this research. The single crystal (SCW) was 5 mm in diameter and 2 mm in thickness. The polycrystalline (PCW) specimens were cut from an extruded tungsten rod of 5 mm diameter and 2 mm in thickness. Each specimen was polished using a colloidal silica polish to a surface roughness of 0.05 microns. Both sides of the sample were polished. The 5mm discs where used for the 75 eV exposures only. The 250 eV exposures used PCW cut from a 1-inch diameter tungsten rod. These discs were also 2mm in thickness. The 1-inch discs were also polished using a colloidal silica surface polish to a surface roughness of 0.05 microns.

5.2 PISCES Exposures

Single crystal, as well as polycrystalline tungsten specimen, were exposed to a voltage-biased plasma in the PISCES-A linear plasma device at the UC San Diego Center for Energy Research Facility [106, 107]. PISCES-A is a laboratory research facility at UCSD for the study of plasma material interactions for future fusion reactors [106]. From Table 5.1, The plasma exposure conditions consisted of either a 75 eV or a 250 eV bias voltage. The average surface temperature

Table 5.1: Experimental parameters exploring synergistic effects of a mixed He and D plasma exposure in W. The comma demonstrates the seperate experiments performed.

Particle	Ion Energy [eV]	Surface Temp. [^^{o}C]	Flux [x10^{22}m^{-2}s^{-1}]	Material
He	75, 250	300&>500, >500	1.4, 5.4	PCW&SCW(111), PCW
90%D10%He	75, 250	300&500, 500	1.4, 1.5	PCW&SCW(111), PCW
D	75, 250	300&500, 500	0.7, 1.2	PCW&SCW(111), PCW

was specified to be either 300^{o}C and 500^{o}C for the 75 eV exposures and only 500^{o}C for the 250 eV exposures. The particle flux for the 75 eV exposures varied from 7x10^{21} m^{-2}s^{-1} to 1.4x10^{22} m^{-2}s^{-1} for the D-only and He and D-He exposures respectively. The particle flux for the 250 eV exposures were in the range of 1.2x10^{22} m^{-2}s^{-1} to 5.4x10^{22} m^{-2}s^{-1}. Each specimen for the 75 eV case at each condition was exposed for 4000 seconds. In the 250 eV case, the He-only specimen was exposed for 100 seconds while the exposures to the D-only and mixed D-He plasma conditions were performed for 1000s and 4000s, respectively. During most exposures, two Langmuir probe measurements were performed to measure the plasma density. The plasma density measurements correlate to the flux of particles on the surface. For the D-He mixed plasma conditions, the anticipated concentration of 90%D-10%He, was confirmed using the ratio of the intensity of the D-gamma line to the He I 447.1 nm emission line. In Figure 5.1 is a view of a 1-inch PCW tungsten disc being exposed to 250 eV biased-voltage 90%D-10%He plasma.

During the exposure of the W specimens to a 250 eV He-only plasma, the sample was not completely coupled to the coolant backing, and thus the surface temperature was greater than 800^{o}C. This resulted in noticeable surface darkening that is associated with tungsten nano-tendril formation on the surface. For the other 250 eV exposures, including both the D-only and D-He plasma, the specimens were sufficiently coupled to the back surface cooling, and the surface temperature was maintained at 500^{o}C. The 75eV experiments involved two specimens, one PCW and one SC exposed simultaneously using a titanium sample holder at each temperature and each flux. During the He-only exposures, the PCW experienced an increase in surface temperature due to poor connection with the coolant backing. The temperature increase only appeared on the PCW specimen and not the single crystal. The surface of the PCW specimen did show darkening and tungsten tendril growth. Additionally, in the D-He exposure, the PCW specimen experienced a temperature increase causing the surface to darken and small tungsten tendril growth, but not as

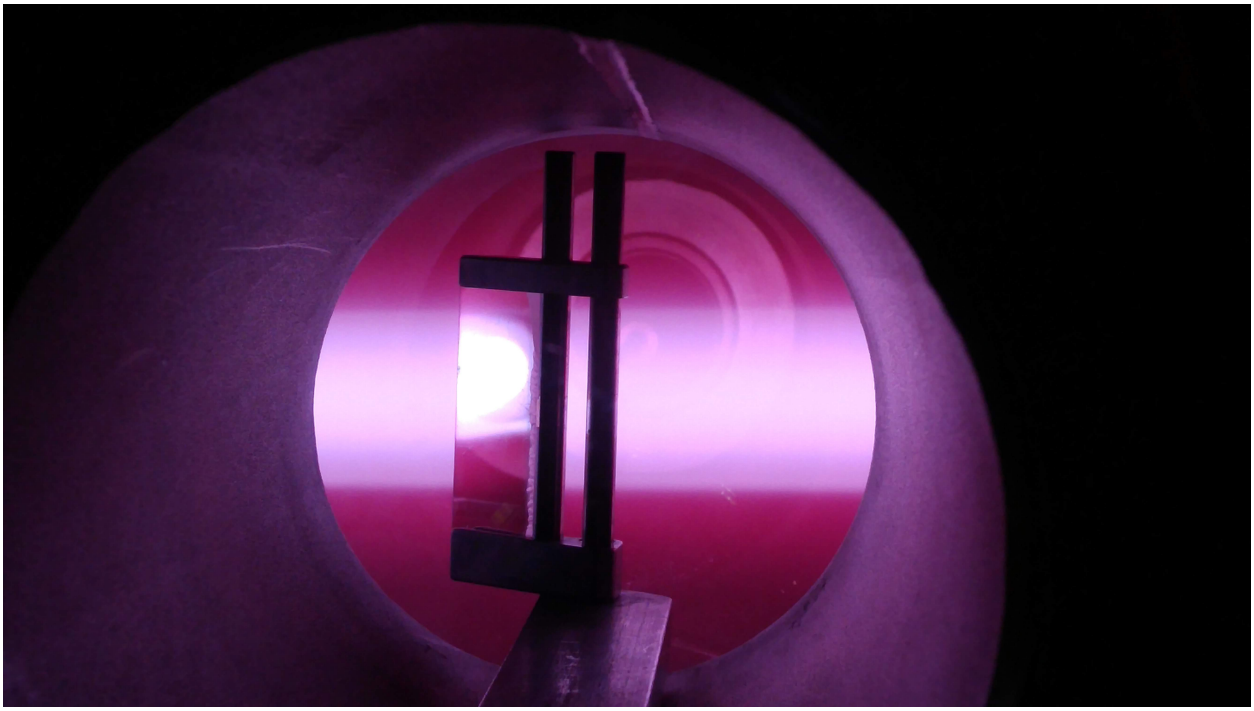

Figure 5.1: A periscope view of the sample surface during a 250 eV 90%D10%He plasma exposure at PISCES-A

significant as the PCW specimen exposed to the He-only plasma conditions. All other specimens, which were not subject to surface temperature increases retained their mirror surface finish.

5.3 LIBS and LAMS Experimental Methods

After the plasma exposures were performed at PISCES, the specimen was shipped to ORNL where the LIBS/LAMS measurements were performed. Four specimens were carefully placed on the sample holder at a time. For example, all 75 eV D-only conditions involving the PCW and SCW at 300^{o}C and 500^{o}C were mounted on the sample holder. An additional, non-plasma exposed control specimen was added to the sample holder. The 250 eV specimen where placed on the sample holder one at a time due to the larger sample size, as these samples were the same size as the sample holder. The corresponding SCW control sample was placed in the chamber with every set of specimens. Vacuum pumping was initiated once the sample holders were inserted into the measurement chamber and the LIBS/LAMS measurements where performed in an average 3x10^{-8} Torr vacuum pressure. Lower vacuum pressure decreases background signal for LAMS

measurements. Each specimen was ablated in 10 different spatial locations with five accumulating laser ablations at each location. The separation between each ablation was 0.25 mm. The purpose of multiple measurements was to determine the standard deviation in the LIBS/LAMS measurements.

A single ablation was performed, and a measurement was made simultaneously by LIBS and LAMS. The LIBS measurement is triggered off the laser pulse and lasts 0.250 seconds, capturing the entire emission of the plasma. The LAMS measurement is continuously performed following the laser pulse and in this set of measurements, the following mass-to-charge ratios of 2, 3, 4, 12, 16, 18, 28, 32, 44, and 184 were analyzed, which represent H, D, He, C, N, H2O, Si, O2, CO2, and W respectively. During an ablation the vacuum pressure does fluctuate, during which the vacuum pressure increases slightly to $9x10^{-8}$ - $4x10^{-8}$ Torr. The influence of this fluctuation is assumed not to have an effect on the measurement, since the overall background pressure in the vacuum system remains quite good.

Chapter 6

He and H interactions measured by LIBS and LAMS of plasma-exposed W

After an extensive literature review, a data gap analysis was performed as previously presented in Figure 1.7, and demonstrates that research gaps appear in gas implantation energies of 20 - 100 eV at temperatures ranging from 500-800 K. As well, there appears to be a knowledge gap between 10^{19}-10^{24} particles/m^2 at temperatures from 500 to 800 K. Each gap is important to investigate because these are the regimes similar to the environment expected in the ITER divertor.

6.1 Helium Behavior

The focus of the helium comparison section is to evaluate the ability of the LIBS and LAMS measurements of plasma exposed tungsten and to assure self-consistency between the depth-dependent helium concentrations on the plasma-exposed specimens relative to the helium ion implanted proof-of-principle experiment presented in Chapter 4. Furthermore, this section focuses on the effect of material type, temperature and plasma characteristics. Cumulatively these demonstrate the sensitivity of LIBS and LAMS measurements of He behavior in W.

6.1.1 Comparison of LIBS and LAMS measurements of He depth dependence for W exposed to He-only plasma conditions

Following the LIBS and LAMS measurements to assess He concentration as a function of depth into the material, several interesting attributes were discovered. The comparison of these experimental results are shown in Figure 6.1 which shows He concentration as a function of depth for both 75 eV and 250 eV at $\geq$500^{o}C. As noted in Chapter 5, poor thermal coupling was experienced by the tungsten samples exposed to the 250 eV He-only plasma, and the PCW specimen exposed to the 75 eV biased He plasma produced noticeable darkening of the surface associated with nano-tendril formation. It is these specimens which are shown in Figure 6.1. Since the laser has been focused specifically for mirror polished tungsten surfaces, it is difficult to provide a high level of confidence for the LIBS and LAMS measurements performed on the tungsten surfaces containing nano-tendrils. Indeed, Figure 6.1 demonstrates that the LIBS and LAMS techniques measure very high helium concentrations right below the surface, with values ranging from $\geq$500 to nearly 2000 appm He. Of course, the calibration volumes and depth correction techniques were developed for mirror polished tungsten surfaces, rather than those containing fuzz, and thus the precise concentrations may vary significantly from these reported values. Nonetheless, the LIBS and LAMS measurements agree well with each other, especially for the 250 eV He-plasma exposed samples, and demonstrate that the majority of the helium is retained within the first 100 nm (0.1 microns) below the tungsten surface.

Figure 6.2 shows a comparison of the He content as a function of depth measured by LIBS and LAMS, respectively, for SCW and PCW specimens exposed to a 75-eV biased He-only plasma at a temperature of either 300 or 500^{o}C. As Figure 6.2 shows, the LIBS and LAMS measured concentrations are in good agreement for both PCW and SCW. Also, there is no significant difference between the measured helium concentration in the SCW at 300^{o}C versus 500^{o}C exposure temperature. A comparison of the measured He concentrations in the PCW versus SCW following He-only plasma exposure at 300^{o}C indicates a higher concentration of He in the PCW sample, which is about 50% higher in the first ablation and then slightly higher at deeper depths. The He concentration profile is shown in Figure 6.2 again indicates that the majority of the helium is within about the first 100 to 120 nm below the surface, although the LAMS measurement

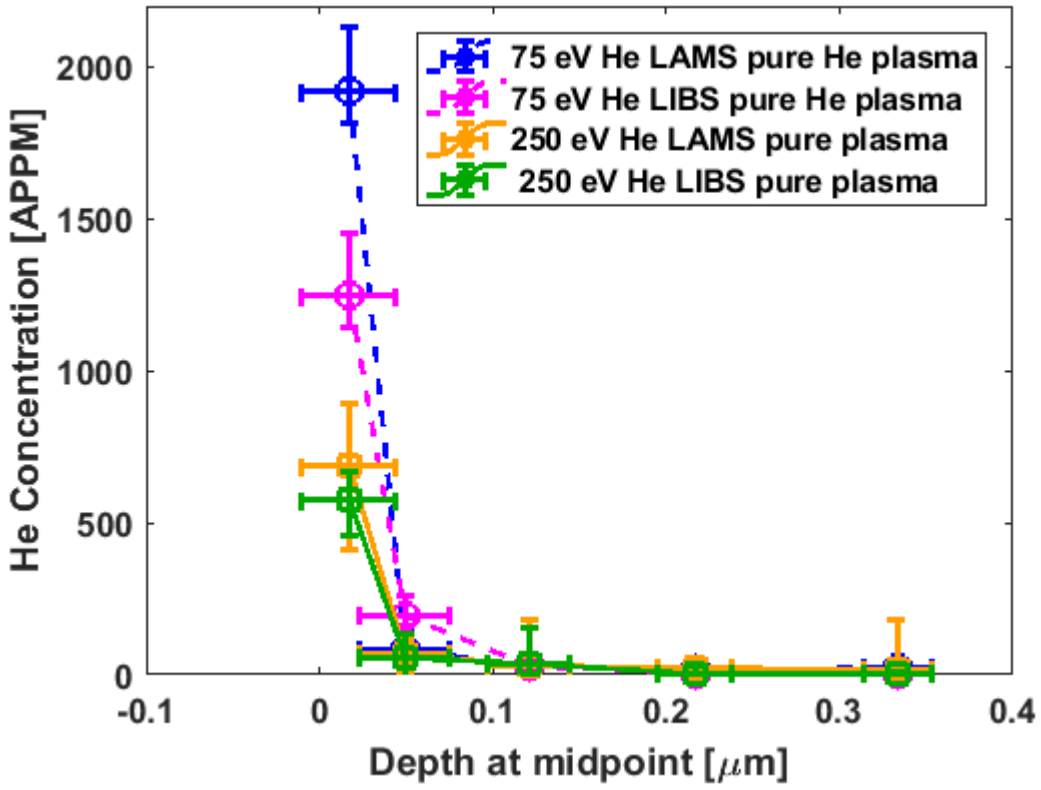

Figure 6.1: LIBS and LAMS comparison of 75 eV and 250 eV He-only plasma exposed PCW at $>500^{o}$C. The increase in He at the near surface is due to the presence of fuzz on the surface. Both PCW specimens exposed to He only plasma experience thermal contact issues which resulted in higher surface temperatures and the growth of fuzz on the surface. The substantial values of He release (concentration) are the result of the interaction between the laser and the fuzz on the surface.

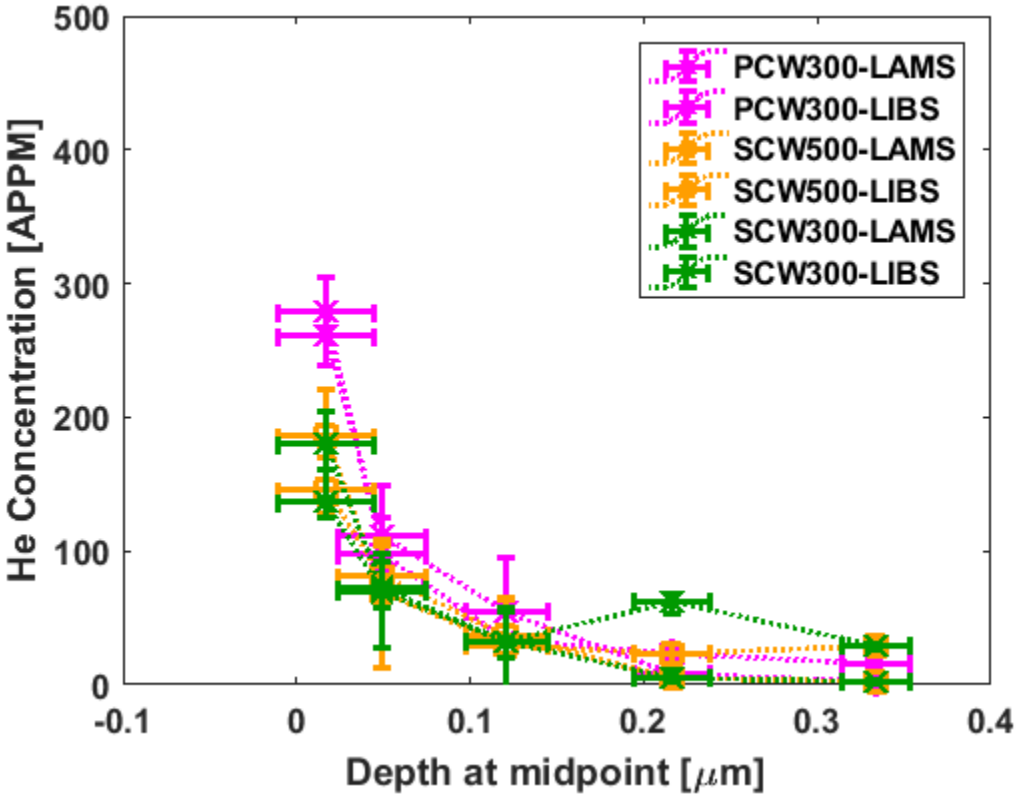

Figure 6.2: LIBS and LAMS comparison of the material type for 75 eV He only plasma exposure. The magenta, orange, and green lines are PCW at 300^{o}C, SCW at 500^{o}C, and SCW at 300^{o}C for LAMS and LIBS, respectively. The concentration of He [appm] decrease as a function of depth in all cases.

did indicate a slightly higher helium concentration at a laser ablation depth of about 210 nm below the surface (4th ablation). Notably, Figure 6.2 does not include the 500^{o}C sample due to the poor thermal contact that raised the surface temperature and resulted in the clear indication of nano-tendril, or fuzz, formation. However, the measured helium content from this specimen was shown in Figure 6.1, and indicated a much higher (~1600$\pm$300 appm) He concentration, although again it is not clear the degree of confidence to place on the ablated volume of a fuzzy surface.

Figure 6.3 shows the depth-integrated concentrations (He/m^2) measured by LIBS and LAMS for both 300 and 500^{o}C in PCW and SCW following He-only plasma exposure with a bias voltage of 75 and 250 eV (in the case of 250 eV only 500^{o}C PCW was used). From the integrated helium concentration, it is clear that there is essentially no impact of temperature for the 75 eV SCW specimens, as the integrated He concentration is nearly identical between 300 and 500^{o}C. This

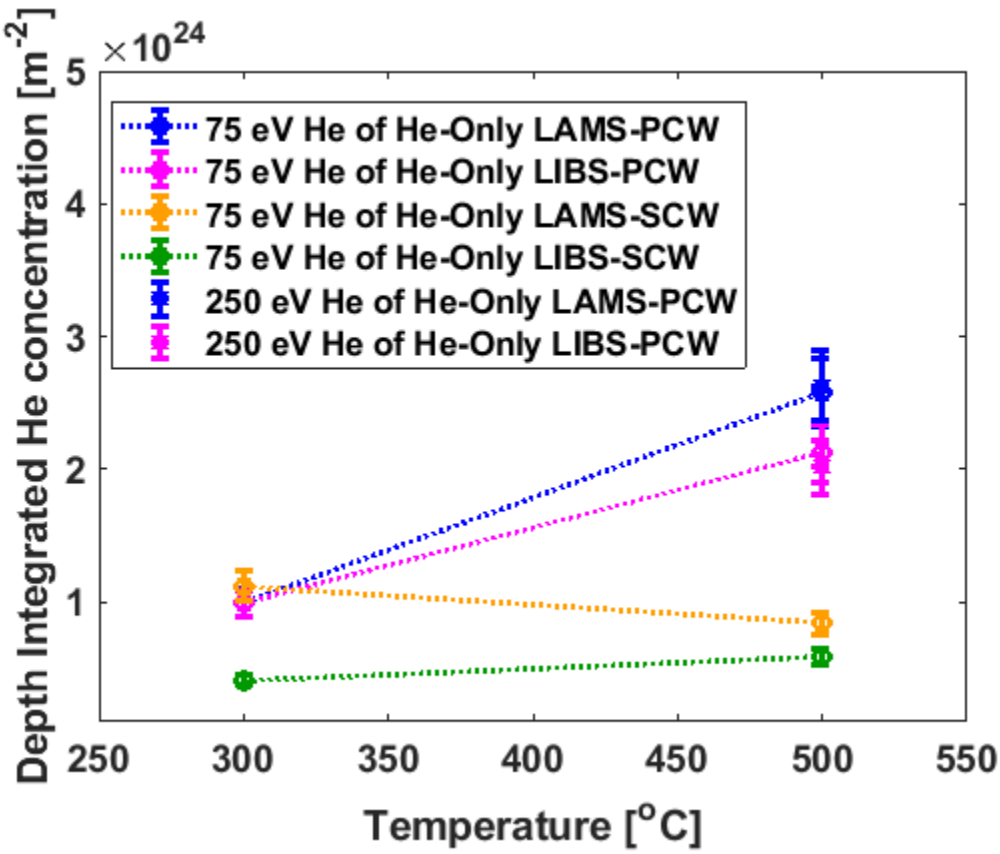

Figure 6.3: LIBS and LAMS temperature comparison of SCW and PCW exposed to He only for 75 eV and 250 eV (PCW at 500^{o}C only).

demonstrates a limited concentration dependence on temperature. For the 75 eV PCW experiment, a difference exists between the 300 and 500^{o}C exposure; however, no conclusions can be drawn due to concerns regarding the growth of fuzz on the sample. For the 250 eV PCW experiment, we believe the presence of fuzz is responsible for the higher total helium content. Although there was one LAMS measurement at the 4th ablation of the SCW at 300^{o}C that seemed to indicate a spuriously large He content. The average of the LIBS and LAMS integrated concentrations lead to the conclusion; the PCW retains more He than SCW at 300^{o}C. Also, there is essentially no significant temperature dependence (between 300 and 500^{o}C) on the He concentration retained in the SCW.

In summary, the LIBS and LAMS measured He concentration across all 75 eV He-only plasma exposed samples are in good agreement. However, for both the 75 eV and the 250 eV PCW exposure at 500^{o}C, there was an experimental issue with the sample thermal contact, increasing

temperature and the development of fuzz on the surface. As such, the only conclusion that can be drawn is that the LIBS and LAMS concentrations are within good agreement, and these measurements indicate that the vast majority of the helium is contained within about 100 nm from the surface. Additionally, there was no temperature or ion energy dependence identified for the 75 eV and 250 eV exposures.

6.1.2 Comparison of He measurements between He only and D-He mixed plasma exposure

Figure 6.4 shows a comparison between the measured He concentrations in the SCW and PCW at 300 and 500^{o}C for 75 eV He-only versus mixed 90%-10% He plasma exposure. Figure 6.4a plots the LIBS and LAMS He concentration [appm] as a function of depth [micron] for SCW (111 oriented) at 300^o C, and it is clear that there is generally good agreement between the LIBS and LAMS measurements in both conditions. Further, the measured depth dependence of the He concentration is quite similar for the samples exposed to the He-only compared to the mixed He-D plasma conditions, although the He content is larger for the He-only exposure. The decrease in the He concentration measured following the mixed D-He plasma exposure is due to the reduction of He within the mixed plasma. As noted previously, the He is about 10% of the plasma gas mixture. Measurements confirmed this dilution at PISCES/A of the ratio of D-gamma to He I 447.52 nm line. Figure 6.4b demonstrates LIBS and LAMS He concentration as a function of depth for 75 eV PCW at 300^{o}C for both plasma exposures. Similar to Figure 6.4a, LIBS, and LAMS are within good agreement. Also, there is a decrease in He concentration for the D-He experiment, which, as mentioned previously, is expected. Figure 6.4c plots the LIBS and LAMS He concentration for SCW at 500^{o}C for both He plasma exposures, with consistent results to those presented in Figure 6.4a and 6.4b. Figure 6.4d plots the LIBS and LAMS measured He concentration as a function of depth for PCW at 500^{o}C. Again, it should be noted that the He-only plasma exposure for the PCW at $\geq$500^o resulted in fuzz growth on the surface. As such, it is difficult to draw a definitive conclusion from this set of measurements, although the He content is seen to decrease with depth below the surface and once again, the LIBS and LAMS measurements are quite consistent with one another. In summary, Figure 6.4 demonstrates the clear difference in He content with plasma

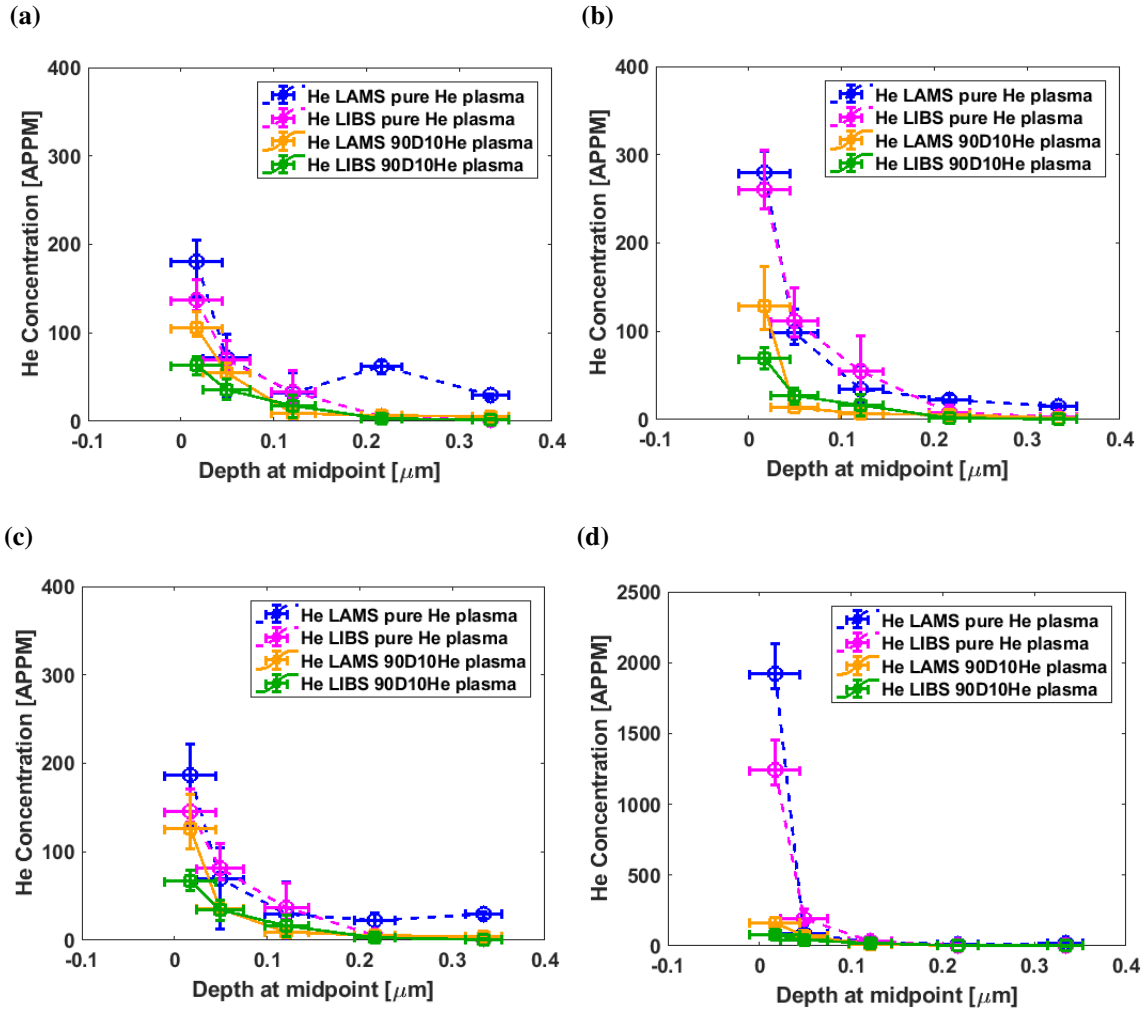

Figure 6.4: LIBS and LAMS measurements of the depth dependence of He concentrations (a) (111) SCW at 300^{o}C; (b) PCW at 300^{o}C; (c) (111) SCW at 500^{o}C; (d) PCW at 500^{o}C. In all experimental cases, He is retained at the near surface and decreases as a function of depth.

exposures conditions, and are consistent with the results previously summarized in Section. 6.1.1.

To better understand the dependencies of temperature and plasma exposure conditions, the depth-integrated helium content (H/m^2) of SCW at 300^{o}C, SCW at 500^{o}C, PCW at 300^{o}C, and PCW at 500^{o}C for both the He-only and mixed D-He exposures was performed. Figure 6.5a (reproduced from Figure 6.3) demonstrated no significant dependence on temperature for the SCW. Again, at 300^{o}C, there is an increase in the integral He content in the PCW versus SCW (based on averaging the LIBS and LAMS measurements); however, no conclusions can be made due to the presence of fuzz on the surface. Figure 6.5b shows that there is not any significant dependence

on temperature for either the SCW and PCW following mixed D-He plasma exposure with a bias voltage of 75 eV. A comparison of Figure 6.5b relative to Figure 6.5a indicates a reduced He content in tungsten following the mixed D-He plasma exposure relative to He-only exposure. This reduction is a result of the corresponding decrease in He within the plasma during the exposure.

6.1.3 Comparison of He measurements between D-only and mixed D-He plasma exposure

The initial analysis to study the sensitivity of He behavior to material and plasma conditions investigated the agreement of LIBS and LAMS, dependencies on the material, temperature, and impact of plasma exposure. Figure 6.6 demonstrates the measured He concentration by LIBS and LAMS of the resulting depth dependent He concentration retained in mixed D-He plasma exposure relative to D-only plasma exposure. As expected, the measured He retention is very low for the D-only exposed W samples, independent of temperature or whether the samples were SCW or PCW. Both results demonstrate agreement with similar experiments presented within the literature [41, 45]. Figure 6.6b was exposed to the same plasma conditions as Figure 6.6a, however PCW was used instead of SCW.

Similar to Figure 6.6a, Figure 6.6b, shows that LIBS and LAMS measurements are in good agreement and that He decreases as a function of depth. Finally, very little He is measured in the D-only exposure compared to significant He in the mixed D-He plasma exposed samples. Figures 6.6c and 6.6d demonstrate the same He concentration dependencies as observed in Figs. 6.6a and 6.6d, but with a slightly higher sample temperature of 500^{o}C relative to 300^{o}C. Overall, this analysis shows that as anticipated, the He concentration in the mixed plasma exposure was substantially higher than following D-only plasma exposure. The presence of He within the D plasma may be due to He impurities within the plasma chamber.

6.2 Deuterium behavior

The focus of the deuterium comparison section is to assess how the measured D concentration as a function of depth is impacted by the presence of He, as well as to once again assess the

(a)

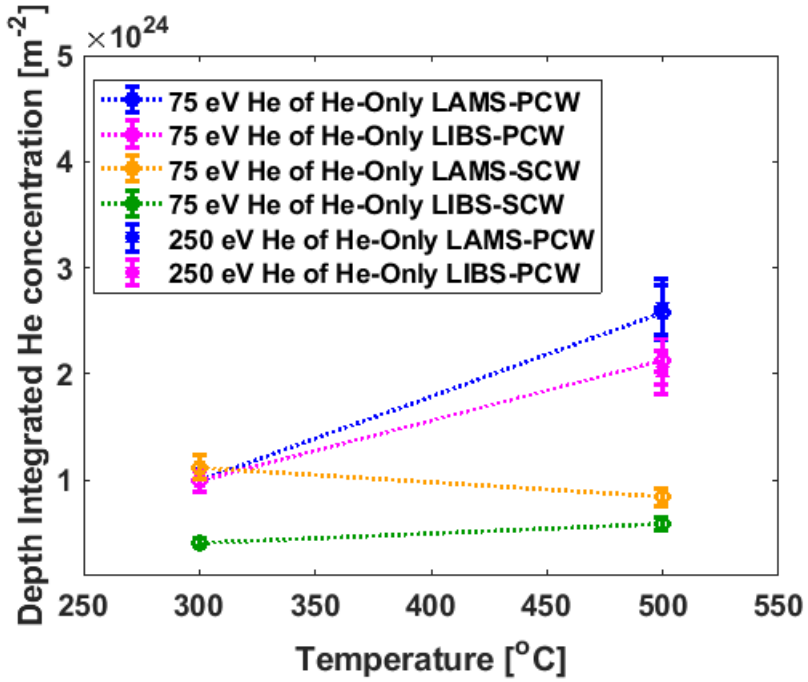

(b)

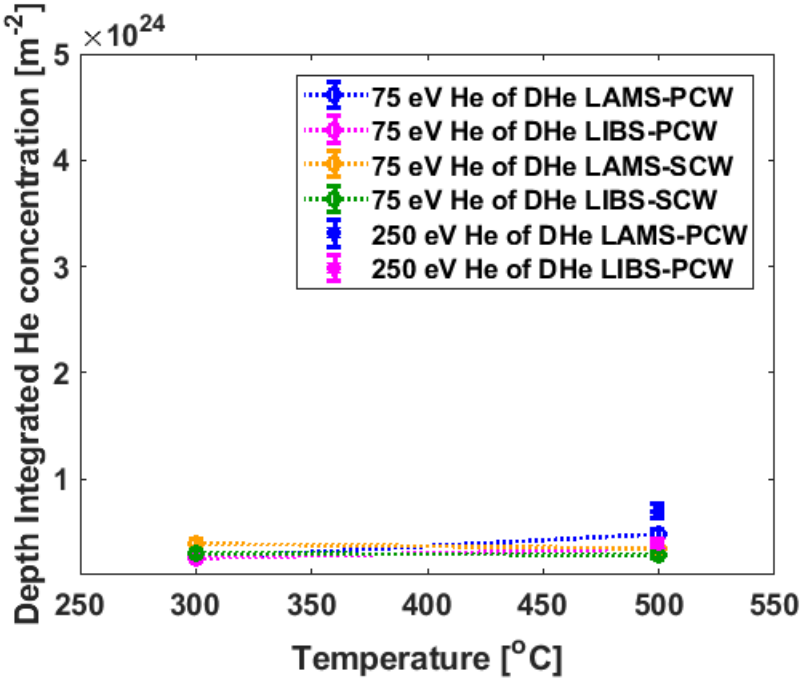

Figure 6.5: Depth integrated (over 0.05 to 0.35 microns in depth) helium concentration as a function of temperature, 300 versus 500^{o}C, He-only ((a) same plot as Fig.6.3) versus He of D-He mixed(b) for 75 eV and 250 eV

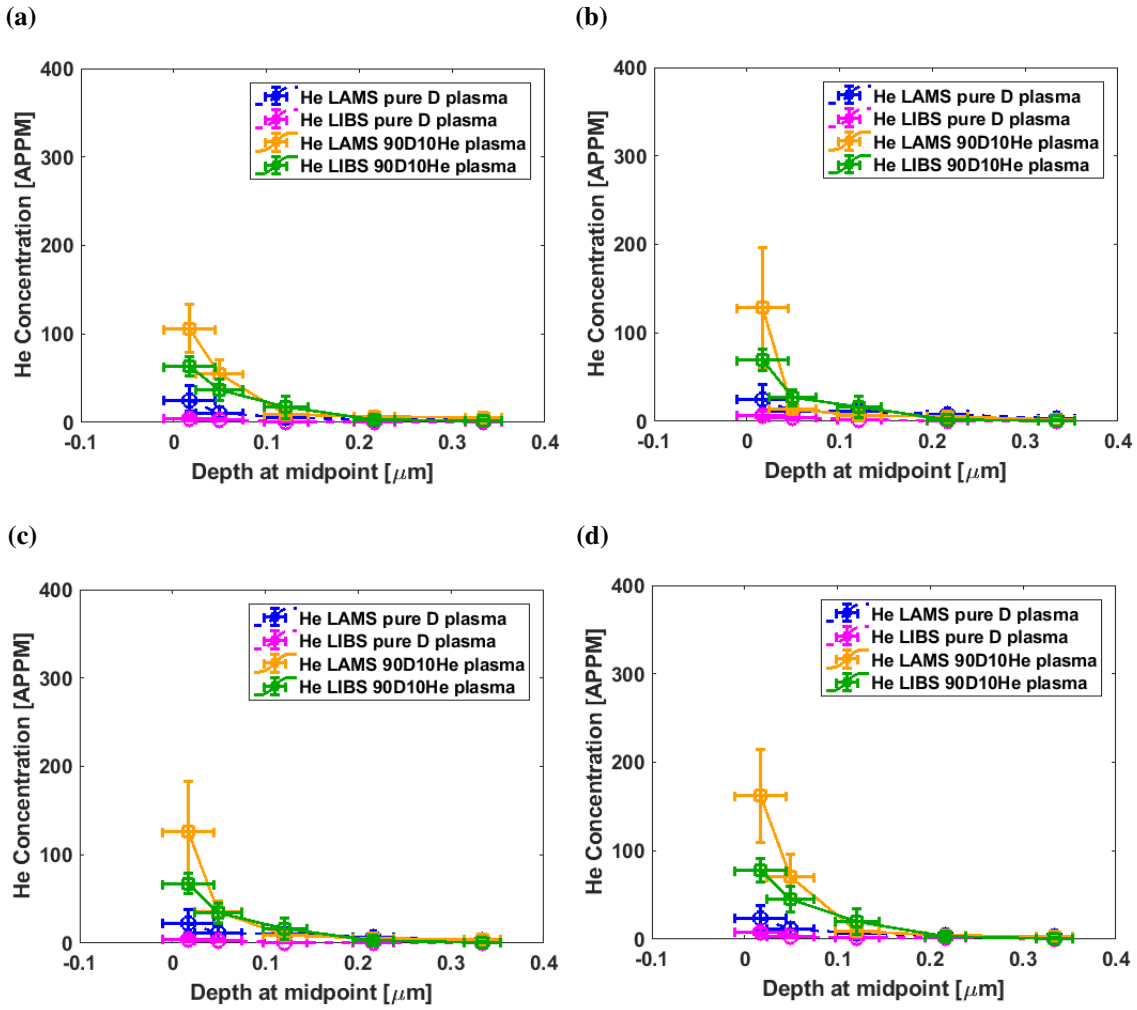

Figure 6.6: He behavior comparison in the following conditions: (a) (111) SCW at 300^{o}C; (b) PCW at 300^{o}C; (c) (111) SCW at 500^{o}C; (d) PCW at 500^{o}C. In all experimental cases, He is retained at the near surface and decreases as a function of depth. LIBS and LAMS concentrations are in good agreement. He of D-only and He of D-He are also in good agreement.

self-consistency of the LIBS and LAMS measurements. This section also addresses the effect of material type, temperature, and variation in plasma characteristics.

6.2.1 Comparison of D measurements between D-only and mixed D-He plasma exposure

Figure 6.7 presents the LIBS and LAMS measurements of deuterium concentration as a function of depth below the tungsten surfaces following exposure to either a pure D or a mixed D-He plasma with a 75 eV bias voltage, for different tungsten sample types and exposure temperature. Figure 6.7 demonstrates that the LIBS and LAMS measurements of the deuterium concentrations are in good agreement. A key conclusion from Figure 6.7 is that the deuterium concentration as a function of depth is significantly different between the two plasma exposure conditions. However, comparing the effect of SCW versus PCW, and an exposure temperature of 300 versus 500^{o}C (Figs. 6.7a - 6.7d), it is apparent that these variations have only a minor impact on the deuterium behavior. The largest observed difference results from comparing the deuterium-only plasma exposure to the mixed D-He plasma conditions. Since there is little variation with exposure temperature or material type, the discussion on the results will focus on the SCW results at 300^{o}C (Figure 6.7a).

The deuterium concentration following pure plasma exposure initially increases to a peak concentration of about 310 appm in the third ablation (~120 nm below the surface) and then slowly decreases to a value of about 195 appm. The depth dependence of the deuterium concentration is completely different in the sample exposed to the mixed 90%D-10%He plasma, with a significantly higher near surface concentration that has a D concentration greater than 400 appm, which rapidly and monotonically decreases with increasing depth below the surface.

The results presented in Figure 6.7 are very consistent with the presence of near-surface helium bubbles acting as trapping sites for deuterium, which also significantly reduce the deeper penetration (permeation) of deuterium, as suggested within the literature [53, 76, 126]. The D depth dependence measured following exposure to the pure D plasma is also expected, although we might have expected a more uniform (or slightly decreasing) deuterium concentration versus depth. It is possible that the laser heat affected zone influences the measured spatial dependence, and our depth correction procedure is not entirely appropriate for measuring the deuterium profile very near

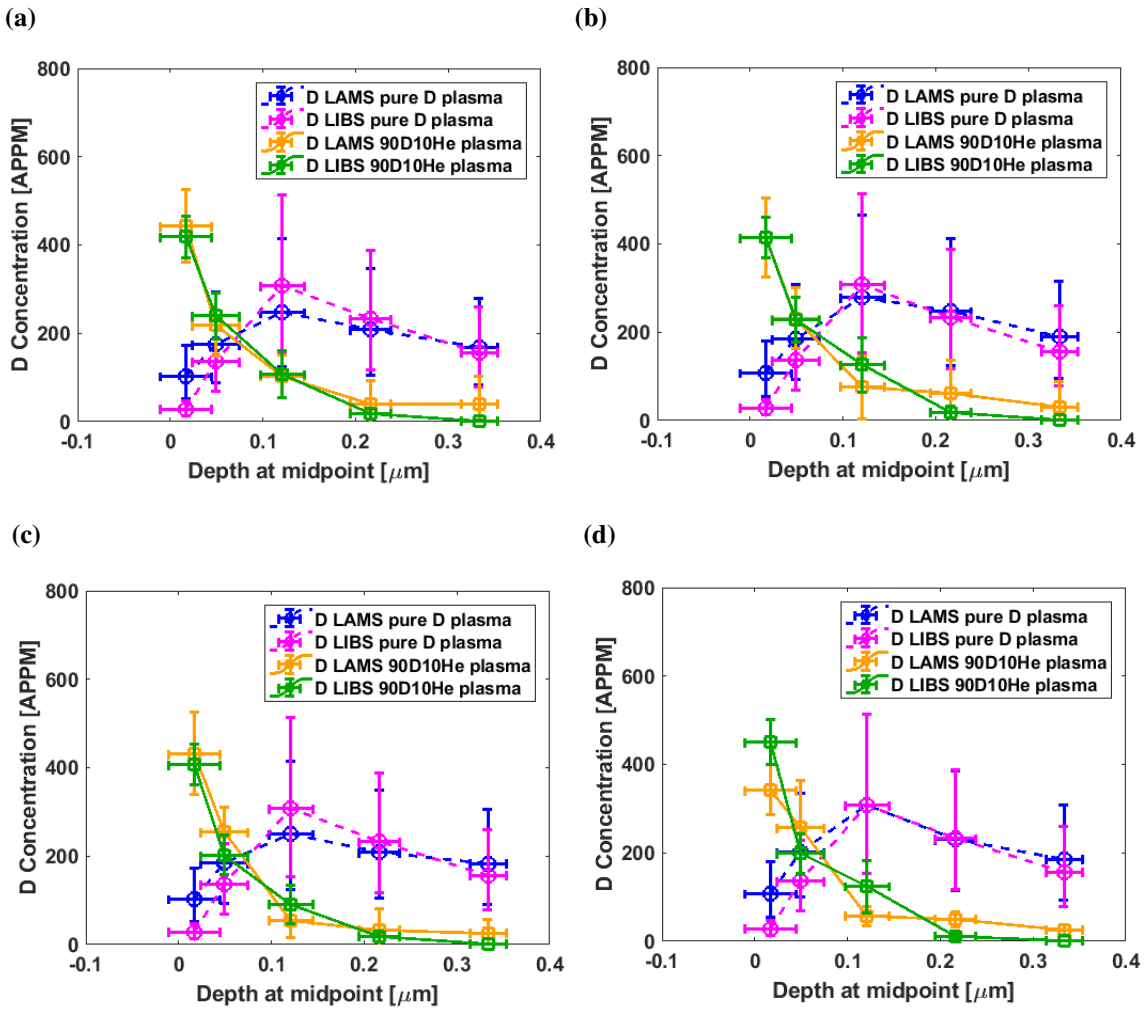

Figure 6.7: LIBS and LAMS measured D concentration as a function of depth (laser ablation) following 75 eV biased D-only or mixed 90%D-10%He exposure at: (a) (111) SCW at 300^{o}C; (b) PCW at 300^{o}C; (c) (111) SCW at 500^{o}C; (d) PCW at 500^{o}C;

the surface. However, the large difference in the near-surface deuterium concentration observed for the mixed plasma exposure relative to deuterium only exposure is certainly a robust conclusion, along with the decreased deuterium permeation. Thus, we can conclude from these measurements that in the presence of He, the D concentration increased near the tungsten surface (within the first ~100 nm), accompanied with a significant reduction in deeper deuterium permeation into the bulk (>200 nm beyond the surface). Future measurements will be performed that use more than five sequential ablations to obtain deuterium depth profiles that extend deeper below the surface.

6.2.2 Comparison of D measurements between D-only and mixed D-He plasma exposure for 250 eV

Figure 6.8 shows the LIBS and LAMS measured deuterium depth profile, comparing the behavior in a polycrystalline tungsten sample exposed to either pure deuterium or a mixed 90%D-10%He plasma biased with a 250 eV sample voltage and a sample temperature of 500^{o}C. Although the deuterium concentrations measured near the surface following the 250 eV, mixed 90%D-10%He plasma exposure are lower than shown in Figure 6.7 for 75 eV, the same basic trend is apparent, namely that the deuterium concentration is much higher near the surface with the presence of helium, but the concentrations at depths beyond 100 nm are significantly lower when compared to the deuterium-only plasma exposure. The lower near-surface concentrations following mixed plasma exposure at 250 eV relative to 75 eV biased voltage can be explained due to the surface erosion (sputtering) from the helium in the plasma at the higher bias voltages. There is also a bit more variability between the LAMS and LIBS measurements at the first two ablations for the deuterium-only plasma exposed sample shown in Figure 6.8 compared to prior measurements, but this does not in any way change the overall conclusion, which remains that the presence of helium results in an increased near surface concentration of deuterium but a substantially decreased deeper permeation and integrated D retention during the 250 eV plasma exposure of PCW at 500^{o}C.

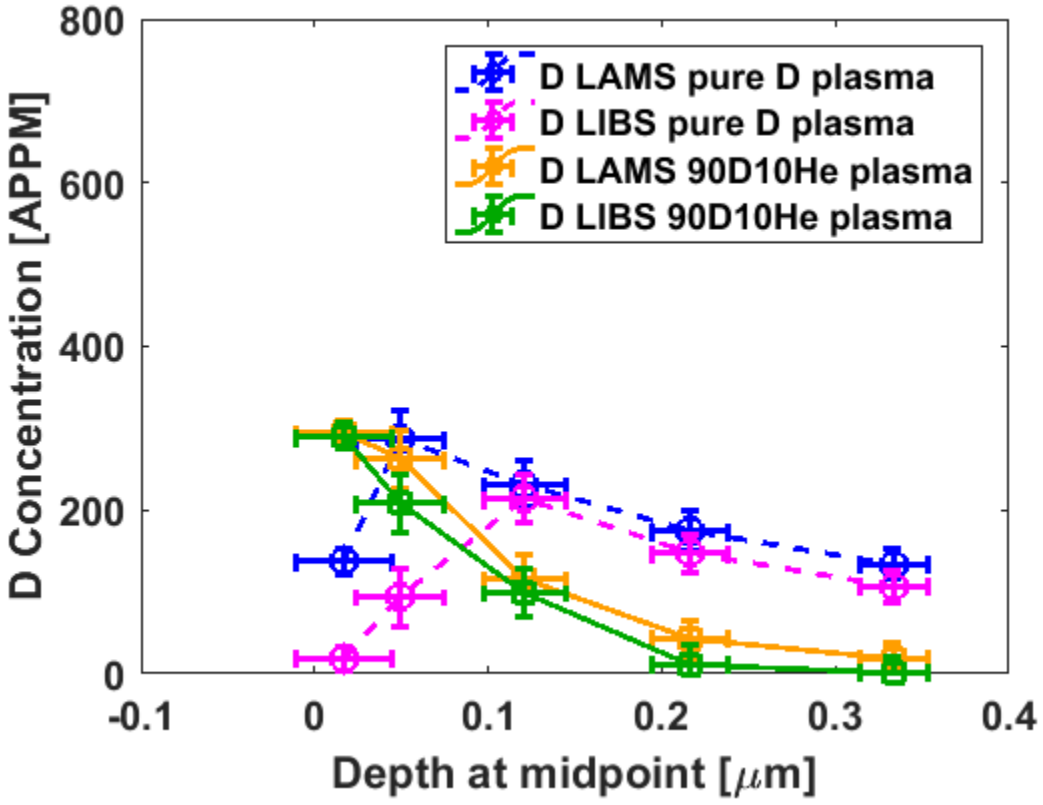

Figure 6.8: LIBS and LAMS measurements of the D concentration as a function of depth and plasma conditions in PCW at 500^{o}C for 250 eV

6.2.3 Impact of surface temperature, D-only versus D-He mixed

Figure 6.9 plots the depth-integrated D concentration (essentially the retained D) as a function of temperature for the different exposure conditions (plasma bias energy, SCW versus PCW) for a D-only plasma (Figure 6.9a) versus a mixed 90%D-10%He plasma (Figure 6.9b). Examination of Figure 6.9 does not indicate any significant impact on material type (SCW versus PCW), the bias voltage (75 versus 250 eV) or temperature on the measured D content. However, comparison of Figure 6.9b relative to 6.9a clearly illustrates that the influence of He reduced the total D content by more than 50% at all material/plasma exposure conditions, even though Figures 6.7 and 6.8 demonstrate that the near-surface concentrations of D were increased by the presence of He. This raises an outstanding question about the magnitude of the interaction, or binding/trapping energy, of D within the He-bubble layer within about 100 nm below the tungsten surface, which motivates further work. Again, however, these measurements confirm that the presence of He locally increases D(H) concentration in the near surface region while significantly decreasing deeper D (H) diffusion and permeation that leads to an overall decrease in D (H) retention.

6.3 Discussion of key results

The LIBS and LAMS measured D and He concentrations across all experiments performed are in good agreement with each other. This demonstrates that LIBS and LAMS can quantify He and D concentrations as a function of depth. This is a significant development for both LIBS and LAMS as a quantifiable characterization technique. It is also evident that LIBS and LAMS can characterize gas concentrations in solids in the near surface (~100 nm), as well as deeper (microns) below the surface. LIBS and LAMS characterization is best performed on polished surfaces, and further work will be required to quantify the laser absorption and ablation volumes for surfaces that contain nano tendrils or fuzz, although Figure 6.1 does demonstrate that helium was still measured.

The most significant scientific result obtained from these LIBS and LAMS measurements is the effect of helium on the deuterium retention and depth distributions. As clearly indicated in Figures 6.6 - 6.9, the presence of helium produces a significant near surface increase in the deuterium concentration (relative to D-only plasma exposure) and a larger reduction in the deeper deuterium concentration presumably as a result in reduced D permeation. The net effect of this is that the

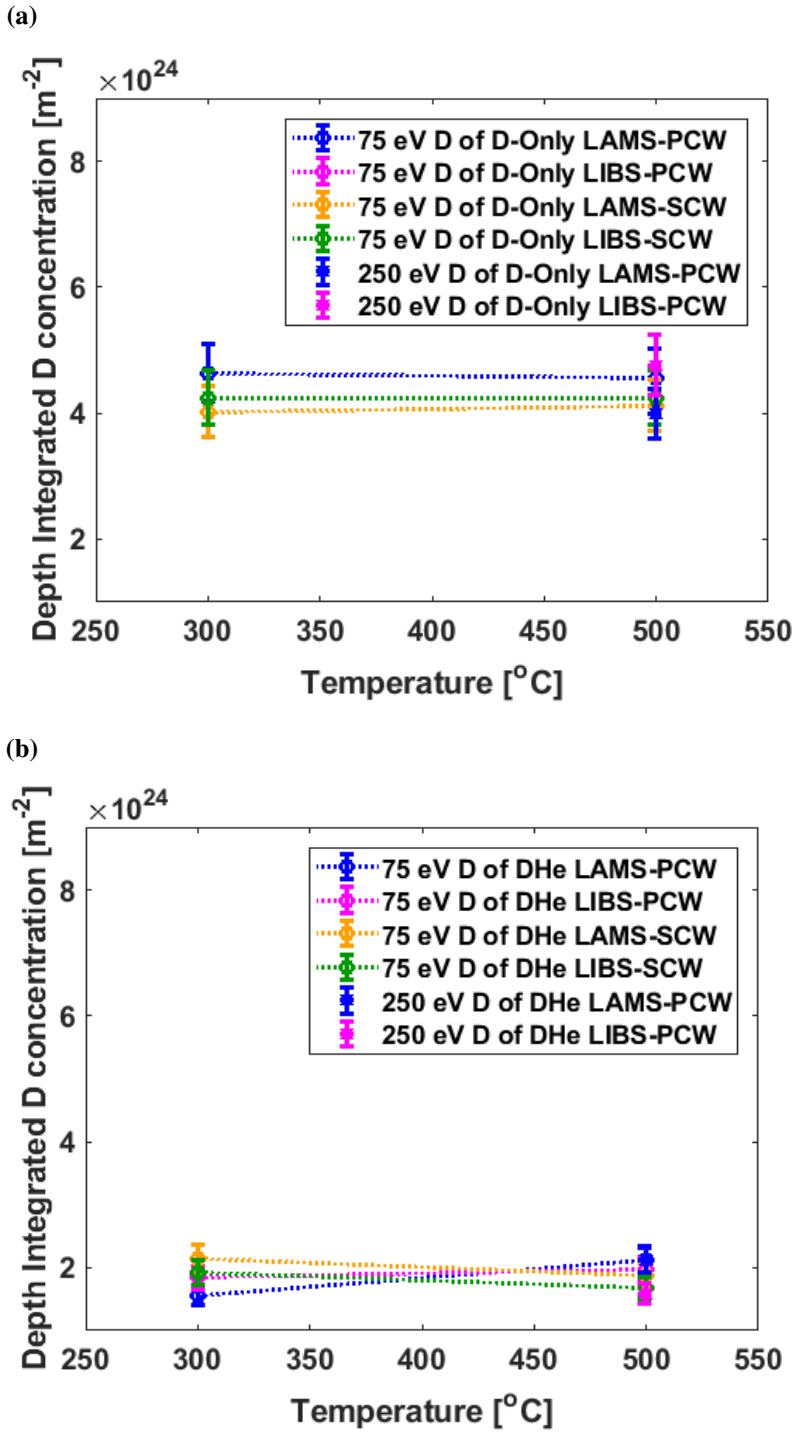

Figure 6.9: Depth integrated (over 0.05 to 0.35 microns in depth) deuterium concentrations as a function of exposure temperature for a) deuterium-only and b) mixed plasma conditions. The legend indicates variations in SCW versus PCW and bias voltage.

presence of He significantly reduces the overall deuterium retention independent of other plasma exposure variables. As discussed in the next section, this result is consistent with the emerging literature and understanding of helium-hydrogen interactions.

Finally, it is also important to note that the measured deuterium depth dependence in the samples exposed to deuterium-only plasma was somewhat different than the flat or nearly depth-independent profile we anticipated. It is possible that the lower near surface D concentration is measured by LIBS and LAMS, the result of incorrectly accounting for heat affected zone effects in performing the depth/volumetric correction, and this is recommended for further systematic study and analysis.

6.4 Comparison of D behavior measured as a function of plasma conditions to literature

In this section, we discuss how the LIBS and LAMS measurements of deuterium concentration as a function of depth below the tungsten surface are influenced by the presence of He (presented in the prior sections of Chapter 6), and compare our measurements to the available literature. This comparison is focused on the results obtained by Alimov and co-workers [53].

Alimov exposed two tungsten samples to a pure D and a mixed D plasma at low-energy (38 eV/D), to investigate the influence of helium on deuterium retention. Alimov used Nuclear Reaction Analysis (NRA), to show that the presence of helium in a mixed plasma leads to a sharp decrease in D concentration in bulk, with an increase in the near surface D concentration. When Alimov compared exposure conditions, he concluded that deuterium concentration was much larger deeper below the surface following D-only exposure. Figure 6.10 plots a ratio of the D concentration measured following the D-only plasma exposure divided by the concentration measured following the mixed D-He plasma exposure. This figure replots the data presented by Alimov et al. [53], and indicates that the effect of helium is to increase the near surface deuterium concentration (ratio < 1) and significantly decrease the deeper permeation and diffusion of deuterium (ratios $>>1$). Figure 6.11 similarly plots the LIBS and LAMS measured data for both PCW and SCW following 75 eV plasma exposure at 300 and 500^{o}C, in comparison from the

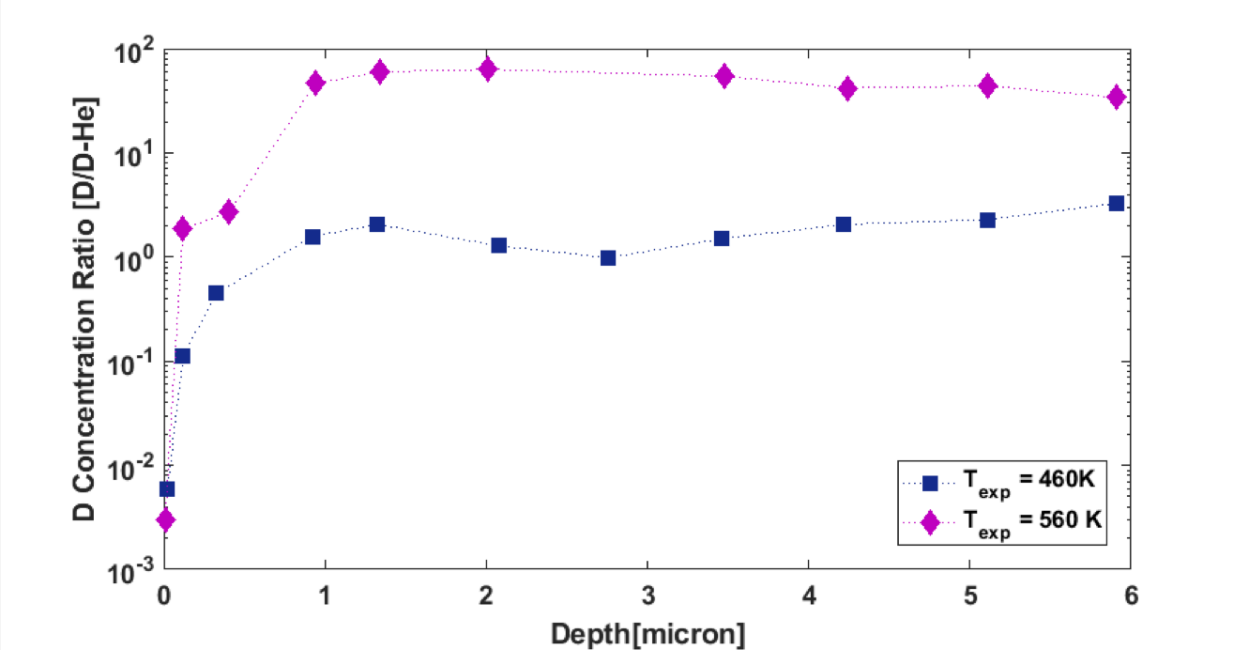

Figure 6.10: Ratio of the D concentration following D-only exposure divided by the mixed D-He exposure as a function of depth for exposure temperatures of 460 and 560 K. Alimov et al. performed D and DHe exposure at 76 eV and a fluence of 3.6×10^{26} m^{-2}. This plot has been obtained by performing a ratio of the D concentrations measured by Alimov and co-workers for the D-only versus the D-He mixed plasma exposure[53].

Alimov data [53]. The LIBS and LAMS measurements in this work are in excellent qualitative and quantitative agreement with Alimov et al. [53] on the influence of helium on hydrogen behavior.

Figure 6.12 shows a similar D ratio plot, now for LIBS and LAMS measurements of the D depth dependent concentration for 250 eV plasma exposure at 500^{o}C. Also included in Figure 6.12 are the results from the Alimov et al. [53] measurements with a 75 eV plasma exposure at 460 and 560 K. Once again, the influence of helium on the deuterium behavior is clear and consistent. The presence of helium results in a higher deuterium concentration within the first 50-100 nm below the surface, and for deeper depths ($>$100 nm) below the surface, the presence of helium significantly reduces the deuterium concentrations (ratio $>>$ 1). The overall effect of this He-D interaction is to reduce the overall concentration of D retained in tungsten during mixed D-He plasma exposure.

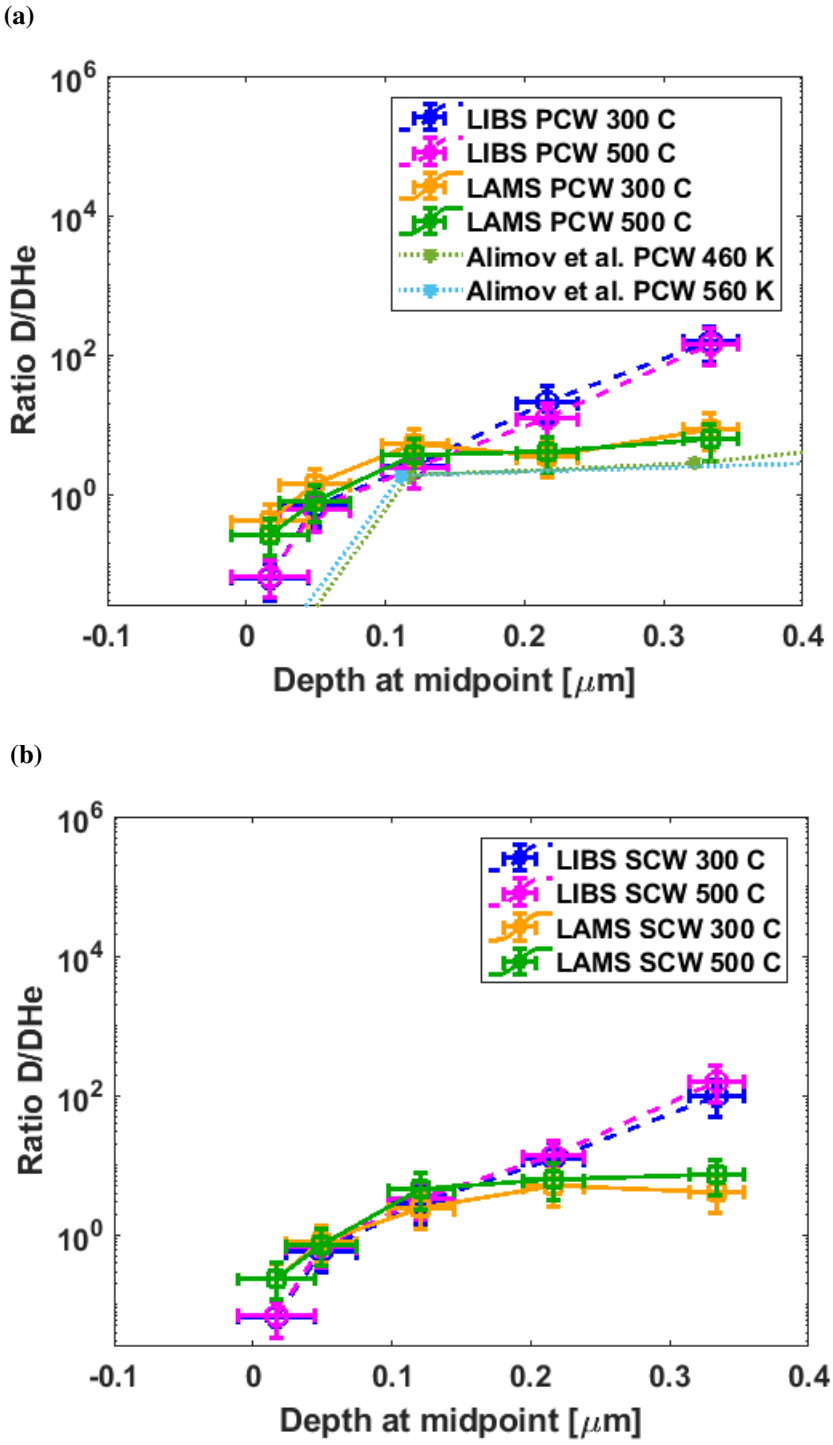

Figure 6.11: Ratio of measured D concentration (D-only divided by D-He plasma exposure as a function of depth, measured by LIBS and LAMS) following 75 eV plasma exposure for a) PCW at a temperature of 300 and 500^{o}C, compared to the Alimov results at 460 and 560 K, and b) SCW at 300 and 500^{o}C.

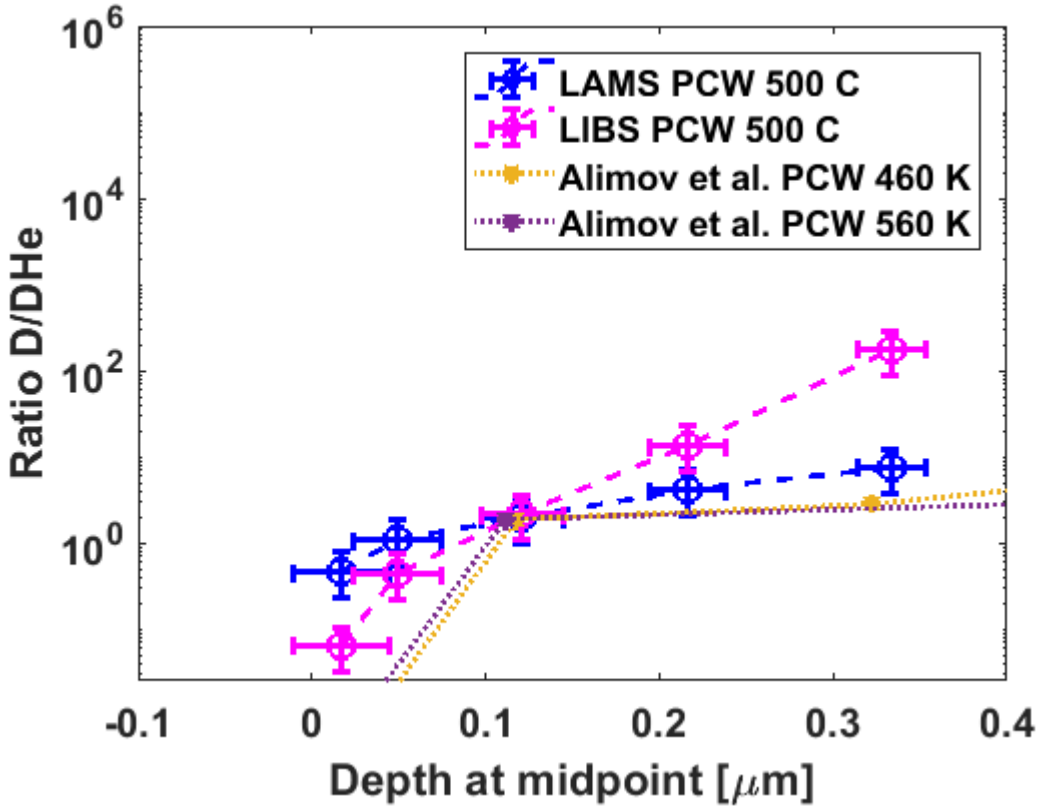

Figure 6.12: Ratio of measured D concentration (D-only divided by D-He plasma exposure) following 250 eV plasma exposure for a) PCW at a temperature of 500^{o}C, compared to the Alimov results at 460 and 560 K

6.5 Summary and next steps

The work performed demonstrates that LIBS and LAMS provide a reliable means of assessing near-surface and the bulk concentration of fusion relevant gasses in tungsten. The LIBS and LAMS measurements are consistent with conventional techniques and provide additional benefits beyond the conventional techniques in that they effectively measure gas concentration over a range of depths into the surface. This study provides additional novelty through establishing an effective methodology for quantifying gas retention in a laboratory setting. Prior efforts using laser-based characterization were constrained to qualitative analysis [77, 87, 127].

LIBS and LAMS measurements have observed that He retention within the material was limited to the near surface. This was anticipated due to the low ion energy and is furthermore supported by simulation and modeling studies found in literature [20, 55, 57]. When He-only experiments were compared to the results of D-He experiments, there was no material dependence. Finally, when considering He-only plasma experiments, there was not a significant impact of ion energy or temperature on the profile of material concentration.

When D-only plasma experiments were performed, the LIBS and LAMS measurements indicated significant D concentration only in the near surface but also within the bulk, indicating D diffusion into the bulk of the material sample. When the D-only case was compared to mixed 90%D-10%He plasma exposure, it is clear that, in the presence of He, D retention was significantly impacted. The presence of helium resulted in higher concentrations of D in the surface of the sample material, indicating trapping. However, at deeper depths, the impact of helium was to significantly reduce the deuterium concentration (relative to D-only exposures), consistent with the hypothesis that helium bubbles decrease deuterium permeation.

Future research efforts will continue to compare LIBS and LAMS to conventional analysis techniques such as TDS, ERDA, and GDOES, in addition to providing further measurements that involve more laser ablations to probe the He and D concentration dependence at deeper depths below the tungsten surface. Further work will also include research focused on better understanding the effect of fuzz on the applicability of the LIBS and LAMS technique. Developing this understanding is important, as fuzz is commonly produced in instances of pure He plasma.

This work will be complemented by additional modeling and experiments to evaluate the heat transfer and laser material interactions.

Chapter 7

Conclusion and Future Outlook

7.1 Research Summary

This dissertation developed and demonstrated two new, complementary laser based characterization techniques for assessing gas concentrations in nuclear materials as a function of spatial position (depth below the surface), with an emphasis on assessing the He-H interaction synergies in tungsten that are expected to impact tritium retention in the divertor of ITER and future fusion reactors. While LIBS is a standard characterization technique for identifying elements in materials, in this work, we established a LIBS capability in a vacuum with the use of Filterscopes to specifically identify the light emission from the ablated plasma of tungsten, helium, and hydrogen; and developed the techniques to quantify the absolute quantity of D and He. In the newly established ultrahigh vacuum setup, this LIBS capability is coupled with the ability to simultaneously pump the ablated gases into the quadrupole mass spectrometer in a previously established thermal desorption system to simultaneously (although with a small time delay) measure the ion current of the detected gas species in the QMS, this capability we refer to as LAMS. The gas fluxes measured in LAMS have also been converted to an absolute quantity of measured gas per laser ablation pulse through calibration with known leak volumes in the thermal desorption system setup.

Chapter 4 then discusses the results from a proof-of-principle experiment specifically designed to demonstrate the ability of LIBS and LAMS to quantify the volumetric concentration of helium as a function of depth below a tungsten surface. In this experiment, polycrystalline tungsten was ion

implanted with helium ions of varying energy between 400 and 80 keV to create a nearly uniform implantation profile of He at a concentration of about 200 appm from a depth of about 300 to 800 nm. These specimens were then transferred to our ultrahigh vacuum LIBS and LAMS system, and 15 sequential laser ablations were performed at two different spatial locations near the center of the implanted region. Another of the implanted samples was sent for Elastic Recoil Detection Analysis (ERDA) of the helium depth dependent concentrations. The resulting LIBS and LAMS measured He concentration profiles agree very well with each other, and the predicted implantation profile from the SRIM code. Furthermore, while the ERDA measurements were limited to a depth of about 60 nm below the surface, these measurements agreed with the initial LIBS, and LAMS measured He concentrations. Thus, the proof-of-principle measurement successfully demonstrated the ability of LIBS and LAMS to accurately quantify the He concentration from depths of about 30 nm to well greater than 1 micron below a tungsten surface.

Subsequently, we used LIBS and LAMS to measure the D and He concentrations below tungsten specimens exposed to 75 or 250 eV biased plasmas in the PISCES/A linear plasma device at UCSD, in which the plasma conditions involved either D-only, He-only, or mixed D-He gas (ion) species. These experiments were designed to evaluate the He-H interaction synergies that impact predictions of tritium permeation and retention in the tungsten divertor of ITER. The LIBS and LAMS measurements have observed that He retention in the plasma exposed samples is limited to the near-surface region within depths of about 100 nm. When He-only experiments were compared to the results of D-He experiments, there was no material dependence (e.g., SCW versus PCW), although it is important to note that SCW following 75 eV He-only plasma exposure at 300^{o}C retained slightly less He than PCW. However, more detailed conclusions on the impact of material type on He retention is limited by the experimental setup that resulted in nano-tendril, or fuzz, formation for higher exposure temperatures. In considering the He-only plasma experiments, there was not a significant impact of ion energy or temperature on the depth profile of the sub-surface He concentration.

When D-only plasma experiments were performed, the LIBS and LAMS measurements indicated significant D concentration not only in the near surface but also within the bulk, indicating D diffusion into the bulk of the material sample. When the D-only case was compared to mixed 90%D-10%He plasma exposure, it became clear that, in the presence of He, the

total D retention was significantly reduced. However, the presence of He did result in higher concentrations of D in the near surface region where the He was located, indicating a trapping interaction between He and H. However, at deeper depths the impact of helium was to significantly reduce the deuterium concentration (relative to D-only exposures), consistent with the hypothesis that helium bubbles decrease deuterium permeation.

A comparison of our LIBS and LAMS measurements with similar investigations performed in the literature, confirms the effect of He on H retention, depth dependent concentration and permeation noted above. The conclusion from this research is derived by comparing the results of this work to similar investigations performed in the literature. When the ratio of D concentration to D-He found in this work was compared to that obtained by Alimov et al. [53] good agreement was found. This good agreement between the results obtained by NRA by Alimov et al.[53] and our LIBS and LAMS characterization provides further validation of this new, laser-based characterization technique.

Thus, this work has demonstrated the development of new laser-based characterization techniques (LIBS and LAMS) to quantify gas concentrations in nuclear materials. The evaluation of He and D behavior following low-energy plasma exposure to tungsten has confirmed, based on the ability to assess the depth-dependent concentration with a resolution of less than 100 nm. LIBS and LAMS also demonstrate that while the presence of He decreases the total retention of D in tungsten, it does locally increase the near surface concentration of D and simultaneously decreases the deeper diffusion and permeation of D. Future research will be required to assess the trapping strength of this D-He interaction required to assess the impact of He on tritium retention in the tungsten divertor of ITER.

7.2 Future Aspects

In addition to the physics question regarding the trapping strength of H to He just noted above, several laser ablation related questions are uncovered by the development of a new surface characterization technique that should be investigated further to understand better the influence that the LIBS/LAMS characterization process has on the surface and subsurface micro-structure. This includes a further investigation into the laser-induced heat affected zones. The finite element

modeling of the temperature distributions indicated that the temperature in these zones are high enough to diffuse both He and D, possibly desorb D or burst pre-existing bubbles of He and D. This effect would certainly influence the volumetric gas concentration that is quantified following the laser ablation. However, this dependence was not investigated in this research and warrants future investigation. The LIBS/LAMS results were performed on a subset of plasma exposure parameters as part of an introduction to a larger set of parameters yet to be investigated. As shown in Figures 1.7a and 1.7b, there exists a large parameter space that is of vital importance to the fusion community. This is because the specified conditions are directly related to what is anticipated in ITER. It is therefore suggested that further LIBS/LAMS inter-technique comparison should be performed that also increases the range of assessed materials and exposure conditions.

While this work has demonstrated a robust LIBS/ LAMS, there are opportunities for additional well-designed benchmark studies, particularly to performing similar 'flat-top' implantation with deuterium to complement the proof-of-principle experiment with He that was presented in Chapter 4. Such well designed D-implantation experiments would also provide the ability to assess the impact of the laser heat affected zone on deuterium release. In regards to the LIBS analysis, further testing of the laser parameters and further measurements of the temperature and density of the ablated plasma are desired to improve confidence in the SXB coefficients used to quantify the He and H concentrations. Future work involving LIBS and LAMS characterization of He and H interactions below tungsten surfaces should also be performed that combine the laser-based characterization with other conventional analysis techniques including nuclear reaction analysis, elastic recoil detection analysis, and thermal desorption spectroscopy. Such measurements and cross-technique comparisons will be helpful in quantifying the He-H interactions and providing a wealth of spatially resolved experimental data for the validation of computational models.

Bibliography

[1] U. EIA, "Annual energy outlook 2013," *US Energy Information Administration, Washington, DC*, pp. 60–62, 2013. 1

[2] R. Inglesi-Lotz, "The impact of renewable energy consumption to economic growth: A panel data application," *Energy Economics*, vol. 53, pp. 58–63, 2016. 1

[3] M. Fowlie, L. Goulder, M. Kotchen, S. Borenstein, J. Bushnell, L. Davis, M. Greenstone, C. Kolstad, C. Knittel, R. Stavins *et al.*, "An economic perspective on the epa's clean power plan," *Science*, vol. 346, no. 6211, pp. 815–816, 2014. 2

[4] E. Tambo, W. Duo-Quan, and X.-N. Zhou, "Tackling air pollution and extreme climate changes in china: Implementing the paris climate change agreement," *Environment international*, vol. 95, pp. 152–156, 2016. 2

[5] C. B. Chou, J. Jhaveri, J. W. Baldwin, P. M. Hannam, K. Keller, W. Peng, S. Rabin, A. P. Ravikumar, A. M. Trierweiler, X. T. Wang *et al.*, "Fusion energy." 2

[6] F. Chen, *An indispensable truth: how fusion power can save the planet*. Springer Science & Business Media, 2011. 2, 3

[7] F. F. Chen, *Introduction to plasma physics*. Springer Science & Business Media, 2012. 3

[8] N. A. of Engineering, "Grand challenges for engineering: Imperatives, prospects, and priorities," 2016. 3

[9] S. J. Zinkle, "Challenges in Developing Materials for Fusion Technology-Past, Present and Future," *Fusion Science and Technology*, vol. 64, no. 2, pp. 65–75, 2013.

[10] S. J. Zinkle, A. Möslang, T. Muroga, and H. Tanigawa, "Multimodal options for materials research to advance the basis for fusion energy in the ITER era," *Nuclear Fusion*, vol. 53, no. 10, p. 104024, 2013.

[11] W. Wampler, C. Skinner, H. Kugel, and A. Roquemore, "Measurement of lithium and deuterium on nstx carbon tiles," *Journal of Nuclear Materials*, vol. 390, pp. 1009–1012, 2009.

[12] S. Woodruff, "Summary of US Fusion Program Planning Documents relating to Innovative Confinement Concepts (1992âĂŞ2005)," *Journal of fusion energy*, vol. 26, no. 1-2, pp. 247–250, 2007. 3

[13] J. W. Davis, V. R. Barabash, A. Makhankov, L. Plöchl, and K. T. Slattery, "Assessment of tungsten for use in the ITER plasma facing components," *Journal of nuclear materials*, vol. 258, pp. 308–312, 1998. 4

[14] R. A. Pitts, S. Carpentier, F. Escourbiac, T. Hirai, V. Komarov, S. Lisgo, A. S. Kukushkin, A. Loarte, M. Merola, and A. S. Naik, "A full tungsten divertor for ITER: physics issues and design status," *Journal of Nuclear Materials*, vol. 438, pp. S48–S56, 2013. 3, 4, 9

[15] Y. Ueda, J. W. Coenen, G. De Temmerman, R. P. Doerner, J. Linke, V. Philipps, and E. Tsitrone, "Research status and issues of tungsten plasma facing materials for ITER and beyond," *Fusion engineering and design*, vol. 89, no. 7, pp. 901–906, 2014.

[16] "Report on Science Challenges and Research Opportunities in Plasma Materials Interactions," Department of Energy, Report, 2015.

[17] R. Pitts, S. Carpentier, F. Escourbiac, T. Hirai, V. Komarov, S. Lisgo, A. Kukushkin, A. Loarte, M. Merola, A. S. Naik *et al.*, "A full tungsten divertor for iter: Physics issues and design status," *Journal of Nuclear Materials*, vol. 438, pp. S48–S56, 2013. 4

[18] E. Bernard, R. Sakamoto, M. Tokitani, S. Masuzaki, H. Hayashi, H. Yamada, and N. Yoshida, "Temperature impact on the micro structure of tungsten exposed to He irradiation in LHD," *Journal of Nuclear Materials*, vol. 484, pp. 24–29, 2017. 4, 8

[19] K. D. Hammond, S. Blondel, L. Hu, D. Maroudas, and B. D. Wirth, "Large-scale atomistic simulations of low-energy helium implantation into tungsten single crystals," *Acta Materialia*, 2018.

[20] M. A. Cusentino, K. D. Hammond, F. Sefta, N. Juslin, and B. D. Wirth, "A comparison of interatomic potentials for modeling tungsten-hydrogen-helium plasma-surface interactions," *Journal of Nuclear Materials*, 2015. 12, 15, 16, 95

[21] H. Iwakiri, K. Yasunaga, K. Morishita, and N. Yoshida, "Microstructure evolution in tungsten during low-energy helium ion irradiation," *Journal of nuclear materials*, vol. 283, pp. 1134–1138, 2000. 5, 19

[22] K. B. Woller, D. G. Whyte, G. M. Wright, R. P. Doerner, and G. De Temmerman, "Helium concentration in tungsten nano-tendril surface morphology using Elastic Recoil Detection," *Journal of Nuclear Materials*, vol. 438, pp. S913–S916, 2013. 8, 15

[23] R. Sakamoto, E. Bernard, A. Kreter, C. Martin, B. Pégourié, G. Pieters, B. Rousseau, C. Grisolia, and N. Yoshida, "Surface Morphology in Tungsten and RAFM Steel Exposed to Helium Plasma in PSI-2," *Phys. Scr*, 2017. [Online]. Available: http://iopscience.iop.org/article/10.1088/1402-4896/aa93a2/pdf

[24] M. J. Baldwin, R. P. Doerner, D. Nishijima, K. Tokunaga, and Y. Ueda, "The effects of high fluence mixed-species (deuterium, helium, beryllium) plasma interactions with tungsten," *Journal of Nuclear Materials*, vol. 390, pp. 886–890, 2009. 8, 12, 13

[25] D. Nishijima, M. Y. Ye, N. Ohno, and S. Takamura, "Incident ion energy dependence of bubble formation on tungsten surface with low energy and high flux helium plasma irradiation," *Journal of nuclear materials*, vol. 313, pp. 97–101, 2003. 7, 8

[26] K. O. E. Henriksson, K. Nordlund, A. Krasheninnikov, and J. Keinonen, "The depths of hydrogen and helium bubbles in tungsten: a comparison," *Fusion science and technology*, vol. 50, no. 1, pp. 43–57, 2006. 17

[27] M. J. Baldwin and R. P. Doerner, "Helium induced nanoscopic morphology on tungsten under fusion relevant plasma conditions," *Nuclear Fusion*, vol. 48, no. 3, p. 35001, 2008. 8

[28] D. Xu, T. Bus, S. C. Glade, and B. D. Wirth, "Thermal helium desorption spectrometry of helium-implanted iron," *Journal of Nuclear Materials*, vol. 367âĂŞ370, P, pp. 483–488, 2007. [Online]. Available: http://www.sciencedirect.com/science/article/pii/S0022311507004205

[29] N. Yoshida, H. Iwakiri, K. Tokunaga, and T. Baba, "Impact of low energy helium irradiation on plasma facing metals," *Journal of nuclear materials*, vol. 337, pp. 946–950, 2005. 8

[30] M. Miyamoto, D. Nishijima, M. J. Baldwin, R. P. Doerner, Y. Ueda, K. Yasunaga, N. Yoshida, and K. Ono, "Microscopic damage of tungsten exposed to deuteriumâĂŞhelium mixture plasma in PISCES and its impacts on retention property," *Journal of Nuclear Materials*, vol. 415, no. 1, pp. S657–S660, 2011. 12

[31] M. Miyamoto, D. Nishijima, Y. Ueda, R. P. Doerner, H. Kurishita, M. J. Baldwin, S. Morito, K. Ono, and J. Hanna, "Observations of suppressed retention and blistering for tungsten exposed to deuteriumâĂŞhelium mixture plasmas," *Nuclear Fusion*, vol. 49, no. 6, p. 65035, 2009. 12

[32] "Helium-Ion-Implantation in Tungsten: Progress towards a Coherent Understanding of the Damage Formed and its Effects on Properties," in *Procedia IUTAM*, 2017. 17

[33] Y. Ueda, M. Fukumoto, J. Yoshida, Y. Ohtsuka, R. Akiyoshi, H. Iwakiri, and N. Yoshida, "Simultaneous irradiation effects of hydrogen and helium ions on tungsten," *Journal of Nuclear Materials*, vol. 386, pp. 725–728, 2009. 12

[34] Y. Ueda, H. Y. Peng, H. T. Lee, N. Ohno, S. Kajita, N. Yoshida, R. Doerner, G. De Temmerman, V. Alimov, and G. Wright, "Helium effects on tungsten surface morphology and deuterium retention," *Journal of Nuclear Materials*, vol. 442, no. 1âĂŞ3, Supplement 1, pp. S267–S272, 2013. [Online]. Available: http://www.sciencedirect.com/science/article/pii/S0022311512005582 15

[35] S. Sharafat, A. Takahashi, Q. Hu, and N. M. Ghoniem, "A description of bubble growth and gas release of helium implanted tungsten," *Journal of Nuclear Materials*, 2009. 5

[36] E. Jobiliong, H. Suyanto, A. M. Marpaung, S. N. Abdulmadjid, N. Idris, R. Hedwig, M. Ramli, M. Pardede, M. M. Suliyanti, and K. Kagawa, "Spectral and Dynamic Characteristics of Helium Plasma Emission and its Effect on a Laser-Ablated Target Emission in a Double-Pulse Laser-Induced Breakdown Spectroscopy (LIBS) Experiment," *Applied spectroscopy*, vol. 69, no. 1, pp. 115–123, 2015.

[37] M. J. Baldwin and R. P. Doerner, "Formation of helium induced nanostructure âĂŸfuzz'on various tungsten grades," *Journal of Nuclear Materials*, vol. 404, no. 3, pp. 165–173, 2010. 4, 8

[38] T. Hino, Y. Yamauchi, and Y. Hirohata, "Helium retention of plasma facing materials," *Journal of nuclear materials*, vol. 266, pp. 538–541, 1999. 4, 5, 6, 7

[39] J. Roth and K. Schmid, "Hydrogen in tungsten as plasma-facing material," *Physica Scripta*, vol. 2011, no. T145, p. 14031, 2011. 5

[40] A. M. Ito, A. Takayama, Y. Oda, T. Tamura, R. Kobayashi, T. Hattori, S. Ogata, N. Ohno, S. Kajita, and M. Yajima, "Molecular dynamics research on formation mechanism of tungsten nanostructure induced by helium plasma irradiation," in *the 21st International Conference on Plasma Surface Interactions in Controlled Fusion Devices (PSI 21), Kanazawa, Japan*, Conference Proceedings. 6

[41] D. Nishijima, H. Iwakiri, K. Amano, M. Y. Ye, N. Ohno, K. Tokunaga, N. Yoshida, and S. Takamura, "Suppression of blister formation and deuterium retention on tungsten surface due to mechanical polishing and helium pre-exposure," *Nuclear fusion*, vol. 45, no. 7, p. 669, 2005. 8, 12, 82

[42] J. Winter, "Wall conditioning in fusion devices and its influence on plasma performance," *Plasma Physics and Controlled Fusion*, vol. 38, no. 9, pp. 1503–1542, 1996. [Online]. Available: {%}3CGotohttp://iopscience.iop.org/0741-3335/38/9/001/pdf/0741-3335{_}38{_}9{_}001.pdf

[43] L. Mercadier, J. Hermann, C. Grisolia, and A. Semerok, "Plume segregation observed in hydrogen and deuterium containing plasmas produced by laser ablation of carbon fiber tiles

from a fusion reactor," *Spectrochimica Acta Part B: Atomic Spectroscopy*, vol. 65, no. 8, pp. 715–720, 2010. 18

[44] M. Fukumoto, H. Kashiwagi, Y. Ohtsuka, Y. Ueda, M. Taniguchi, T. Inoue, K. Sakamoto, J. Yagyu, T. Arai, and I. Takagi, "Deuterium trapping in tungsten damaged by high-energy hydrogen ion irradiation," *Journal of Nuclear Materials*, vol. 390, pp. 572–575, 2009.

[45] R. A. Causey, "Hydrogen isotope retention and recycling in fusion reactor plasma-facing components," *Journal of nuclear materials*, vol. 300, no. 2, pp. 91–117, 2002. 8, 9, 10, 12, 30, 82

[46] V. K. Alimov and B. M. U. Scherzer, "Deuterium retention and re-emission from tungsten materials," *Journal of nuclear materials*, vol. 240, no. 1, pp. 75–80, 1996. 9, 11, 19

[47] R. P. Doerner, M. J. Baldwin, T. C. Lynch, and J. H. Yu, "Retention in tungsten resulting from extremely high fluence plasma exposure," *Nuclear Materials and Energy*, 2016. 9, 12, 17

[48] W. Wang, J. Roth, S. Lindig, and C. H. Wu, "Blister formation of tungsten due to ion bombardment," *Journal of Nuclear Materials*, vol. 299, no. 2, pp. 124–131, 2001. 11, 19

[49] Y. Ueda, H. Kashiwagi, M. Fukumoto, Y. Ohtsuka, and N. Yoshida, "Effects of helium ions on hydrogen Isotope behavior in tungsten," *Fusion Science and Technology*, vol. 56, no. 1, pp. 85–90, 2009. 12

[50] F. Sefta, K. D. Hammond, N. Juslin, and B. D. Wirth, "Tungsten surface evolution by helium bubble nucleation, growth and rupture," *Nuclear Fusion*, vol. 53, no. 7, p. 73015, 2013.

[51] H. T. Lee, E. Markina, Y. Otsuka, and Y. Ueda, "Deuterium ion-driven permeation in tungsten with different microstructures," in *Physica Scripta T*, vol. T145, 2011. 19

[52] H. T. Lee, A. A. Haasz, J. W. Davis, and R. G. Macaulay-Newcombe, "Hydrogen and helium trapping in tungsten under single and sequential irradiations," *Journal of nuclear materials*, vol. 360, no. 2, pp. 196–207, 2007.

[53] V. K. Alimov, B. Tyburska-Püschel, S. Lindig, Y. Hatano, M. Balden, J. Roth, K. Isobe, M. Matsuyama, and T. Yamanishi, "Temperature dependence of surface morphology and deuterium retention in polycrystalline ITER-grade tungsten exposed to low-energy, high-flux D plasma," *Journal of Nuclear Materials*, vol. 420, no. 1, pp. 519–524, 2012. 12, 14, 15, 19, 85, 91, 92, 99

[54] V. K. Alimov, B. Tyburska-Püschel, Y. Hatano, J. Roth, K. Isobe, M. Matsuyama, and T. Yamanishi, "The effect of displacement damage on deuterium retention in ITER-grade tungsten exposed to low-energy, high-flux pure and helium-seeded deuterium plasmas," *Journal of Nuclear Materials*, vol. 420, no. 1, pp. 370–373, 2012.

[55] Z. Bergstrom, M. A. Cusentino, B. Wirth, and P. P. S. I. Collaboration, "A Molecular Dynamics Study of Sub-Surface Mixed Hydrogen-Helium Bubbles in Tungsten," in *APS Meeting Abstracts*, Conference Proceedings. 12, 15, 16, 95

[56] H. T. Lee, M. Ishida, Y. Ohtsuka, and Y. Ueda, "The influence of nitrogen on deuterium permeation through tungsten," in *Physica Scripta*, vol. T159, 2014. 13

[57] B. D. Wirth, K. Nordlund, D. G. Whyte, and D. Xu, "Fusion materials modeling: Challenges and opportunities," *MRS bulletin*, vol. 36, no. 03, pp. 216–222, 2011. 15, 16, 95

[58] D. Donovan, D. Buchenauer, J. Whaley, and R. Friddle, "Characterization of a compact ECR plasma source and its applications to studies of helium ion damage to tungsten," *Physica Scripta*, vol. 2016, no. T167, p. 14040, 2016. 15

[59] D. C. Donovan, D. A. Buchenauer, J. A. Whaley, R. W. Friddle, and G. Wright, "Characterization of helium bubble growth in tungsten exposed to low-flux plasmas," Sandia National Laboratories (SNL-CA), Livermore, CA (United States), Report, 2014.

[60] M. Kelemen, A. Založnik, P. Vavpetič, M. Pečovnik, P. Pelicon, A. Hakola, A. Lahtinen, J. Karhunen, K. Piip, P. Paris, M. Laan, K. Krieger, M. Oberkofler, H. van der Meiden, and S. Markelj, "Micro-NRA and micro-3HIXE with3He microbeam on samples exposed in ASDEX Upgrade and Pilot-PSI machines," *Nuclear Instruments and Methods in Physics*

Research, Section B: Beam Interactions with Materials and Atoms, vol. 404, pp. 179–184, 2017. 15

[61] W. A. Lanford, "Analysis for hydrogen by nuclear reaction and energy recoil detection," *Nuclear Instruments and Methods in Physics Research Section B: Beam Interactions with Materials and Atoms*, vol. 66, no. 1-2, pp. 65–82, 1992. 15

[62] J. Pisonero, L. Lobo, N. Bordel, A. Tempez, A. Bensaoula, N. Badi, and A. Sanz-Medel, "Quantitative depth profile analysis of boron implanted silicon by pulsed radiofrequency glow discharge time-of-flight mass spectrometry," *Solar Energy Materials and Solar Cells*, vol. 94, no. 8, pp. 1352–1357, 2010. 15

[63] D. A. Cremers and A. K. Knight, *LaserâĂŘInduced Breakdown Spectroscopy*. Wiley Online Library, 2006. 17, 23, 33

[64] J. P. Singh and S. N. Thakur, *Laser-induced breakdown spectroscopy*. Elsevier, 2007.

[65] G. F. Knoll, *Radiation detection and measurement*. John Wiley & Sons, 2010. 23, 24, 25

[66] R. Noll, *Laser-induced breakdown spectroscopy*. Springer, 2012, pp. 7–15. 17, 23, 33

[67] N. Farid, S. S. Harilal, H. Ding, and A. Hassanein, "Dynamics of ultrafast laser plasma expansion in the presence of an ambient," *Applied Physics Letters*, vol. 103, no. 19, 2013. 17, 24

[68] N. Farid, S. Bashir, and K. Mahmood, "Effect of ambient gas conditions on laser-induced copper plasma and surface morphology," *Physica Scripta*, vol. 85, no. 1, 2012.

[69] N. Farid, S. Harilal, O. El-Atwani, H. Ding, and A. Hassanein, "Experimental simulation of materials degradation of plasma-facing components using lasers," *Nuclear Fusion*, vol. 54, no. 1, p. 012002, jan 2014. [Online]. Available: http://stacks.iop.org/0029-5515/54/i=1/a=012002?key=crossref.70f1aa5d8c1f3eb9d5ab0deb47919a5a

[70] N. Farid, C. Li, H. Wang, and H. Ding, "Laser-induced breakdown spectroscopic characterization of tungsten plasma using the first, second, and third harmonics of an Nd: YAG laser," *Journal of Nuclear Materials*, vol. 433, no. 1, pp. 80–85, 2013. 17, 51

[71] N. Farid, H. Wang, C. Li, X. Wu, H. Y. Oderji, H. Ding, and G. N. Luo, "Effect of background gases at reduced pressures on the laser treated surface morphology, spectral emission and characteristics parameters of laser produced Mo plasmas," *Journal of Nuclear Materials*, vol. 438, no. 1-3, pp. 183–189, 2013.

[72] N. Farid, P. Dasgupta, and G. M. O'Connor, "Onset and evolution of laser induced periodic surface structures on indium tin oxide thin films for clean ablation using a repetitively pulsed picosecond laser at low fluence," *Journal of Physics D: Applied Physics*, vol. 51, no. 15, 2018.

[73] D. Nishijima, Y. Ueda, R. P. Doerner, M. J. Baldwin, and K. Ibano, "Laser-induced breakdown spectroscopy measurement of a small fraction of rhenium in bulk tungsten," *Spectrochimica Acta - Part B Atomic Spectroscopy*, vol. 141, pp. 94–98, 2018.

[74] D. Nishijima and R. P. Doerner, "Stark width measurements and Boltzmann plots of W i in nanosecond laser-induced plasmas," *Journal of Physics D: Applied Physics*, vol. 48, no. 32, 2015.

[75] D. Nishijima, R. P. Doerner, E. M. Hollmann, and M. Miyamoto, "Laser-induced breakdown spectroscopy thickness measurements of films thinner than ablation rate," *Spectrochimica Acta - Part B Atomic Spectroscopy*, vol. 136, pp. 34–38, 2017.

[76] S. Kajita, S. Takamura, N. Ohno, D. Nishijima, H. Iwakiri, and N. Yoshida, "Sub-ms laser pulse irradiation on tungsten target damaged by exposure to helium plasma," *Nuclear Fusion*, vol. 47, no. 9, p. 1358, 2007. 85

[77] K. Piip, G. De Temmerman, H. J. van der Meiden, A. Lissovski, J. Karhunen, M. Aints, A. Hakola, P. Paris, M. Laan, and J. Likonen, "LIBS analysis of tungsten coatings exposed to Magnum PSI ELM-like plasma," *Journal of Nuclear Materials*, vol. 463, pp. 919–922, 2015. 17, 95

[78] L. Peter and R. Noll, "Material ablation and plasma state for single and collinear double pulses interacting with iron samples at ambient gas pressures below 1 bar," *Applied Physics B: Lasers and Optics*, vol. 86, no. 1, pp. 159–167, 2007.

[79] V. Philipps, T. Loarer, H. G. Esser, S. Vartanian, U. Kruezi, S. Brezinsek, and G. Matthews, "Dynamic fuel retention and release under ITER like wall conditions in JET," *Journal of Nuclear Materials*, vol. 438, pp. S1067–S1071, 2013.

[80] N. Gierse, S. Brezinsek, J. W. Coenen, T. F. Giesen, A. Huber, M. Laengner, S. Möller, M. Nonhoff, V. Philipps, and A. Pospieszczyk, "In situ deuterium inventory measurements of aC: D layers on tungsten in TEXTOR by laser induced ablation spectroscopy," *Physica Scripta*, vol. 2014, no. T159, p. 14054, 2014.

[81] A. Malaquias, V. Philipps, A. Huber, A. Hakola, J. Likonen, J. Kolehmainen, S. Tervakangas, M. Aints, P. Paris, and M. Laan, "Development of ITER relevant laser techniques for deposited layer characterisation and tritium inventory," *Journal of Nuclear Materials*, vol. 438, pp. S936–S939, 2013.

[82] A. Huber, B. Schweer, V. Philipps, N. Gierse, M. Zlobinski, S. Brezinsek, W. Biel, V. Kotov, R. Leyte-Gonzales, and P. Mertens, "Development of laser-based diagnostics for surface characterisation of wall components in fusion devices," *Fusion engineering and design*, vol. 86, no. 6, pp. 1336–1340, 2011.

[83] Q. Xiao, A. Huber, G. Sergienko, B. Schweer, P. Mertens, A. Kubina, V. Philipps, and H. Ding, "Application of laser-induced breakdown spectroscopy for characterization of material deposits and tritium retention in fusion devices," *Fusion Engineering and Design*, vol. 88, no. 9, pp. 1813–1817, 2013.

[84] G. C. Shaw, T. M. Biewer, J. B. O. Caughman, R. Goulding, K. Leonard, J. Lore, M. Martin, R. Martin, J. Rapp, and B. Wirth, "Laser-based diagnostics for characterizing materials exposed to a plasma environment," *Bulletin of the American Physical Society*, vol. 58, 2013.

[85] G. Shaw, M. Bannister, T. M. Biewer, M. Z. Martin, F. Meyer, and B. D. Wirth, "The Detection of He in Tungsten following Ion Implantation by Laser-Induced Breakdown Spectroscopy," *Applied Surface Science*, 2017.

[86] J. H. Yu, M. Simmonds, M. J. Baldwin, and R. P. Doerner, "Deuterium desorption from tungsten using laser heating," *Nuclear Materials and Energy*, vol. 12, pp. 749–754, 2017. 27

[87] M. Zlobinski, V. Philipps, B. Schweer, A. Huber, M. Reinhart, S. Möller, G. Sergienko, U. Samm, A. Manhard, and K. Schmid, "Hydrogen retention in tungsten materials studied by Laser Induced Desorption," *Journal of Nuclear Materials*, vol. 438, pp. S1155–S1159, 2013. 33, 34, 95

[88] A. Založnik, S. Markelj, T. Schwarz-Selinger, and K. Schmid, "Deuterium atom loading of self-damaged tungsten at different sample temperatures," *Journal of Nuclear Materials*, vol. 496, pp. 1–8, 2017. 17, 33

[89] P. Paris, A. Hakola, K. Bystrov, G. De Temmerman, M. Aints, I. Jõgi, M. Kiisk, J. Kozlova, M. Laan, and J. Likonen, "Erosion of marker coatings exposed to Pilot-PSI plasma," *Journal of Nuclear Materials*, vol. 438, pp. S754–S757, 2013. 17

[90] M. Zlobinski, V. Philipps, B. Schweer, A. Huber, S. Brezinsek, C. Schulz, S. Möller, U. Samm, and T. Team, "Laser induced desorption as tritium retention diagnostic method in ITER," *Fusion engineering and design*, vol. 86, no. 6, pp. 1332–1335, 2011. 18

[91] N. Gierse, S. Brezinsek, A. Huber, A. Kirschner, M. Laenger, V. Philipps, A. Pospieszczyk, B. Schweer, M. Z. Tokar, and M. Zlobinski, "Laser-induced ablation spectroscopy (LIAS) for the in-situ characterization of the wall in fusion experiments," *Verhandlungen der Deutschen Physikalischen Gesellschaft*, 2013. 18

[92] X. Hu, K. G. Field, S. Taller, Y. Katoh, and B. D. Wirth, "Impact of neutron irradiation on thermal helium desorption from iron," *Journal of Nuclear Materials*, vol. 489, pp. 109–117, 2017. 18, 37, 42, 43

[93] A. Vertes, P. Juhasz, M. De Wolf, and R. Gijbels, "Hydrodynamic modelling of laser plasma ionization processes," *International Journal of Mass Spectrometry and Ion Processes*, vol. 94, no. 1-2, pp. 63–85, 1989. 26

[94] S. N. Luo, D. C. Swift, T. E. Tierney IV, D. L. Paisley, G. A. Kyrala, R. P. Johnson, A. A. Hauer, O. Tschauner, and P. D. Asimow, "Laser-induced shock waves in condensed matter: Some techniques and applications," in *High Pressure Research*, vol. 24, no. 4, 2004, pp. 409–422.

[95] R. Fabbro, P. Peyre, L. Berthe, and X. Scherpereel, "Physics and applications of laser-shock processing," *Journal of Laser Applications*, vol. 10, no. 6, pp. 265–279, 1998. [Online]. Available: http://lia.scitation.org/doi/10.2351/1.521861

[96] C. S. Montross, T. Wei, L. Ye, G. Clark, and Y.-W. Mai, "Laser shock processing and its effects on microstructure and properties of metal alloys: a review," *International journal of fatigue*, vol. 24, no. 10, pp. 1021–1036, 2002. 26

[97] J. Johnson and R. Rohde, "Dynamic deformation twinning in shock-loaded iron," *Journal of Applied Physics*, vol. 42, no. 11, pp. 4171–4182, 1971. 26

[98] M. Sparks, "Theory of laser heating of solids: Metals," *Journal of Applied Physics*, vol. 47, no. 3, pp. 837–849, 1976. 27, 28

[99] B. J. Bartholomeusz, "Laser-induced surface heating," *Journal of Applied Physics*, vol. 73, no. 3, pp. 1066–1072, 1993. 27, 28

[100] Z. H. Shen, S. Y. Zhang, J. Lu, and X. W. Ni, "Mathematical modeling of laser induced heating and melting in solids," *Optics and Laser Technology*, vol. 33, no. 8, pp. 533–537, 2001. 27

[101] B. Movchan and A. Demchishin, "Structure and properties of thick condensates of nickel, titanium, tungsten, aluminum oxides, and zirconium dioxide in vacuum." *Fiz. Metal. Metalloved. 28: 653-60 (Oct 1969).*, 1969. 28

[102] S. Datz and E. H. Taylor, "Ionization on platinum and tungsten surfaces. i. the alkali metals," *The Journal of Chemical Physics*, vol. 25, no. 3, pp. 389–394, 1956. 28

[103] V. Alexiades and D. Autrique, "Enthalpy model for heating, melting, and vaporization in laser ablation," *analysis*, vol. 30, no. 32, p. 11, 2010. 29

[104] M. Darif, N. Semmar, and F. Orléans Cedex, "Numerical simulation of si nanosecond laser annealing by comsol multiphysics," in *Proceedings of the COMSOL Conference 2008 Hannover*, 2008. 29

[105] S. Kajita, S. Takamura, N. Ohno, D. Nishijima, H. Iwakiri, and N. Yoshida, "Sub-ms laser pulse irradiation on tungsten target damaged by exposure to helium plasma," *Nuclear Fusion*, vol. 47, no. 9, p. 1358, 2007. 30

[106] D. Goebel, G. Campbell, and R. Conn, "Plasma surface interaction experimental facility (pisces) for materials and edge physics studies," *Journal of Nuclear Materials*, vol. 121, pp. 277–282, 1984. 30, 71

[107] Y. Hirooka, R. Conn, T. Sketchley, W. Leung, G. Chevalier, R. Doerner, J. Elverum, D. Goebel, G. Gunner, M. Khandagle *et al.*, "A new plasma-surface interactions research facility: Pisces-b and first materials erosion experiments on bulk-boronized graphite," *Journal of Vacuum Science & Technology A: Vacuum, Surfaces, and Films*, vol. 8, no. 3, pp. 1790–1797, 1990. 30, 71

[108] J. Kools and J. Dieleman, "Angle-resolved time-of-flight studies on ground-state neutrals formed by near-threshold excimer laser ablation of copper," *Journal of applied physics*, vol. 74, no. 6, pp. 4163–4167, 1993. 33

[109] N. Gierse, *Assessment of Laser Induced Ablation Spectroscopy (LIAS) as a method for quantitative in situ surface diagnostic in plasma environments*. Forschungszentrum Jülich, 2014. 33

[110] R. J. Colchin, D. L. Hillis, R. Maingi, C. C. Klepper, and N. H. Brooks, "The filterscope," *Review of scientific instruments*, vol. 74, no. 3, pp. 2068–2070, 2003. 38

[111] H. Ray, T. M. Biewer, E. A. Unterberg, D. T. Fehling, and R. C. Isler, "Examining Helium Line Intensities and Ratios in a Linear Helium Plasma to Identify Te and ne," in *APS Meeting Abstracts*, Jabref, Conference Proceedings.

[112] H.-K. Na, M. Kwon, D.-C. Seo, K. Young, G. Gettelfinger, T. Brown, H. Park, D. Johnson, L. Morrisand, and R. Ellis, "Engineering Design Description of Diagnostic Cassettes for Bay J for KSTAR," in *IEEE International Conference on Plasma Science*, 2003.

[113] J. H. Lee, H. K. Na, S. G. Lee, J. G. Bak, D. C. Seo, S. H. Seo, S. T. Oh, W. H. Ko, J. Chung, Y. U. Nam, K. D. Lee, E. M. Ka, Y. K. Oh, M. Kwon, and S. H. Jeong, "Diagnostics for first plasma and development plan on KSTAR," *Review of Scientific Instruments*, vol. 81, no. 6, 2010.

[114] N. H. Brooks, R. J. Colchin, D. T. Fehling, D. L. Hillis, Y. Mu, and E. Unterberg, "Filterscopes: Spectral line monitors for long-pulse plasma devices," in *Review of Scientific Instruments*, vol. 79, no. 10, 2008.

[115] Z. Xu, Z. W. Wu, W. Gao, Y. J. Chen, C. R. Wu, L. Zhang, J. Huang, J. F. Chang, X. J. Yao, W. Gao, P. F. Zhang, Z. Jin, Y. M. Hou, and H. Y. Guo, "Filterscope diagnostic system on the Experimental Advanced Superconducting Tokamak (EAST)," *Review of Scientific Instruments*, vol. 87, no. 11, 2016.

[116] E. M. Hollmann and A. Y. Pigarov, "Multi-fluid code simulation of DIII-D filterscope data including reflection of light from plasma-facing surfaces," in *Contributions to Plasma Physics*, vol. 44, no. 1-3, 2004, pp. 301–306. 38

[117] H.-K. Chung, M. Chen, W. Morgan, Y. Ralchenko, and R. Lee, "Flychk: Generalized population kinetics and spectral model for rapid spectroscopic analysis for all elements," *High energy density physics*, vol. 1, no. 1, pp. 3–12, 2005. 51, 52

[118] N. Farid, S. S. Harilal, H. Ding, and A. Hassanein, "Emission features and expansion dynamics of nanosecond laser ablation plumes at different ambient pressures," *Journal of Applied Physics*, vol. 115, no. 3, 2014. 51

[119] R. K. Janev, W. D. Langer, E. Douglass Jr *et al.*, *Elementary processes in hydrogen-helium plasmas: cross sections and reaction rate coefficients*. Springer Science & Business Media, 2012, vol. 4. 52

[120] D. Xu, T. Bus, S. C. Glade, and B. D. Wirth, "Thermal helium desorption spectrometry of helium-implanted iron," *Journal of Nuclear Materials*, vol. 367, pp. 483–488, 2007. 52

[121] D. Xu and B. D. Wirth, "Post-implantation thermal desorption of helium from poly-and single-crystalline iron," *Journal of Nuclear Materials*, vol. 386, pp. 395–399, 2009.

[122] X. Hu, D. Xu, and B. D. Wirth, "Quantifying he-point defect interactions in fe through coordinated experimental and modeling studies of he-ion implanted single-crystal fe," *Journal of Nuclear Materials*, vol. 442, no. 1-3, pp. S649–S654, 2013. 52

[123] S. Zinkle, R. Dodd, G. Kulcinski, and K. Farrell, "Helium bubble formation in cu, ni and cu-ni alloys," *Journal of Nuclear Materials*, vol. 117, pp. 213–217, 1983. 61

[124] E. Getto, Z. Jiao, A. Monterrosa, K. Sun, and G. Was, "Effect of irradiation mode on the microstructure of self-ion irradiated ferritic-martensitic alloys," *Journal of Nuclear Materials*, vol. 465, pp. 116–126, 2015. 61, 62

[125] J. F. Ziegler, M. D. Ziegler, and J. P. Biersack, "SRIMâĂŞThe stopping and range of ions in matter (2010)," *Nuclear Instruments and Methods in Physics Research Section B: Beam Interactions with Materials and Atoms*, vol. 268, no. 11, pp. 1818–1823, 2010. 62, 66, 70

[126] R. P. Doerner, M. J. Baldwin, and P. C. Stangeby, "An equilibrium model for tungsten fuzz in an eroding plasma environment," *Nuclear Fusion*, vol. 51, no. 4, p. 43001, 2011. 85

[127] P. Paris, M. Aints, A. Hakola, M. Kiisk, J. Kolehmainen, M. Laan, J. Likonen, C. Ruset, K. Sugiyama, and S. Tervakangas, "Determination of elemental depth profiles by multi-spot averaging technique of LIBS spectra," *Fusion engineering and design*, vol. 86, no. 6, pp. 1125–1128, 2011. 95

Appendix

Appendix A

75 eV and 250 eV LIBS Analysis Matlab script

This appendix contains the Matlab script that outlines the data input from MDSplus (Filterscope data acquisition), data organization and structure depending on number of ablations, the full calibration of LIBS signal from volts to atoms/s (see Chapter 4), the volume correction due to width expansion based on the number of ablations, and finally the conversion from He[D]/m^3 to He concentration in appm. The MATLAB script is the same routine used for the flattop analysis.

```
clear;
clc;
load('75NEW.mat');
load('avgBG.mat');
load('vol_analysis.mat');
load('derror.mat');
lamp_calib = xlsread('lamp_calib2.xlsx');% Wavelength|uW/cm^2/nm
rel_calib = xlsread('rel_calib.xlsx');% Bias Voltage|Lamp Watts|T2|T7|T8
```

```
tubes = 1:1:3;
number_of_tubes = 3;
filts = 5;
len.DHe = length(volts.DHe_y);
len.D = length(volts.D_y);
len.He = length(volts.He_y);
rows.DHe = (1:1:len.DHe)';
rows.D = (1:1:len.D)';
rows.He = (1:1:len.He)';
len.DHey = zeros(len.DHe,number_of_tubes);
len.Dy = zeros(len.D,number_of_tubes);
len.Hey = zeros(len.He,number_of_tubes);
```

```
for ii = 1:len.DHe
    for jj = 1:number_of_tubes
        if ischar(volts.DHe_y{ii,jj}) == 1
            volts.DHe_y{ii,jj} = 0;
        end
        if ischar(volts.DHe_x{ii,jj}) == 1
            volts.DHe_x{ii,jj} = 0;
        end
        len.DHey(ii,jj) = length(volts.DHe_y{ii,jj});
        volts.DHe_x{ii,jj} = volts.DHe_x{ii,jj}(1:len.DHey(ii,jj),:);
    end
end

for ii = 1:len.D
    for jj = 1:number_of_tubes
        if ischar(volts.D_y{ii,jj}) == 1
            volts.D_y{ii,jj} = 0;
        end
        if ischar(volts.D_x{ii,jj}) == 1
            volts.D_x{ii,jj} = 0;
        end
        len.Dy(ii,jj) = length(volts.D_y{ii,jj});
        volts.D_x{ii,jj} = volts.D_x{ii,jj}(1:len.Dy(ii,jj),:);
    end
end

for ii = 1:len.He
```

```
    for jj = 1:number_of_tubes
        if ischar(volts.He_y{ii,jj}) == 1
            volts.He_y{ii,jj} = 0;
        end
        if ischar(volts.He_x{ii,jj}) == 1
            volts.He_x{ii,jj} = 0;
        end
        len.Hey(ii,jj) = length(volts.He_y{ii,jj});
        volts.He_x{ii,jj} = volts.He_x{ii,jj}(1:len.Hey(ii,jj),:);
    end
end
```

```
% Background LIBS only
% remove zeros
for jj = 1:number_of_tubes
    for ii = 1:length(volts.DHe_y)
        volts.DHe_y{ii,jj}(volts.DHe_y{ii,jj}==0) = [];
        volts.DHe_x{ii,jj}(volts.DHe_x{ii,jj}==0) = [];
    end
end

for jj = 1:number_of_tubes
    for ii = 1:length(volts.D_y)
        volts.D_y{ii,jj}(volts.D_y{ii,jj}==0) = [];
        volts.D_x{ii,jj}(volts.D_x{ii,jj}==0) = [];
    end
end

for jj = 1:number_of_tubes
    for ii = 1:length(volts.He_y)
        volts.He_y{ii,jj}(volts.He_y{ii,jj}==0) = [];
        volts.He_x{ii,jj}(volts.He_x{ii,jj}==0) = [];
    end
end
```

```
% figure;
% plot(volts.D_y{1,1}(:,1));
% hold on;
% for ii = 1:40
%     if ((length(volts.D_y{ii}) > 0) && (length(volts.D_y{ii}) > 9000))
%         plot(volts.D_y{ii,1}(:,1));
%     end
% end
% hold off;
% set(gca, 'FontWeight', 'Bold');
% ax = gca;
% ax.FontSize =14;
% xlabel('Time [s]')
% ylabel('Volts [V]')
```

```
% l = legend('All the raw D signal for all the He only 250 eV exposed W')
```

```
%Cell to Matrix background DHE 75 eV
for ii = 1:length(volts.DHe_y)
    if ((length(volts.DHe_y{ii}) > 0) && (length(volts.DHe_y{ii}) > 9000))
        DHe.libs_He(:,ii) = volts.DHe_y{ii,1}(8850:9000,1);
        DHe.libs_H(:,ii) = volts.DHe_y{ii,2}(8850:9000,1);
        DHe.libs_He_x(:,ii) = volts.DHe_x{ii,1}(8850:9000,1);
        DHe.libs_H_x(:,ii) = volts.DHe_x{ii,2}(8850:9000,1);
    end
end
for ii = 1:length(volts.DHe_y)
    if ((length(volts.DHe_y{ii}) > 0) && (length(volts.DHe_y{ii}) > 9000))
        [DHe.pksHe(ii,:),DHe.locsHe(ii,:)] = max(DHe.libs_He(:,ii));
        [DHe.pksH(ii,:),DHe.locsH(ii,:)] = max(DHe.libs_H(:,ii));
    end
end

for ii = 1:length(volts.DHe_y)
    if (DHe.locsHe > 0)
        DHe.libs_He(DHe.locsHe(ii,:)-16:DHe.locsHe(ii,:)+94,ii)=...
            DHe.libs_He(DHe.locsHe(ii,:)-...
            16:DHe.locsHe(ii,:)+94,ii) - avg_BG_libs_He;
        DHe.libs_H(DHe.locsH(ii,:)-16:DHe.locsH(ii,:)+94,ii)=...
            DHe.libs_H(DHe.locsH(ii,:)-...
            16:DHe.locsH(ii,:)+94,ii) - avg_BG_libs_H;
    end
end
for ii=1:length(volts.DHe_y)
DHe.libs_He(DHe.libs_He<=0) = DHe.libs_He(1,ii);
DHe.libs_H(DHe.libs_H<=0) = DHe.libs_H(1,ii);
end
%Flux_libs(6:75,:);Flux_libs(81:225,:)
DHe.libs_He_bgsub = [DHe.libs_He(:,6:75),DHe.libs_He(:,81:225)];
DHe.libs_H_bgsub = [DHe.libs_H(:,6:75),DHe.libs_H(:,81:225)];

DHe.libs_He_xbg = [DHe.libs_He_x(:,6:75),DHe.libs_He_x(:,81:225)];
DHe.libs_H_xbg = [DHe.libs_H_x(:,6:75),DHe.libs_H_x(:,81:225)];
```

```
% He only 75 eV
for ii = 1:length(volts.He_y)
    if ((length(volts.He_y{ii}) > 0) && (length(volts.He_y{ii}) > 8940))
        He.libs_He(:,ii) = volts.He_y{ii,1}(8600:8940,1);
        He.libs_H(:,ii) = volts.He_y{ii,2}(8600:8940,1);
        He.libs_He_x(:,ii) = volts.He_x{ii,1}(8600:8940,1);
        He.libs_H_x(:,ii) = volts.He_x{ii,2}(8600:8940,1);
    end
end
for ii = 1:length(volts.He_y)
    if ((length(volts.He_y{ii}) > 0) && (length(volts.He_y{ii}) > 8940))
```

```
        [He.pksHe(ii,:),He.locsHe(ii,:)] = max(He.libs_He(:,ii));
        [He.pksH(ii,:),He.locsH(ii,:)] = max(He.libs_H(:,ii));
    end
end

for ii = 1:length(volts.He_y)
    if (He.locsHe > 0)
        He.libs_He(He.locsHe(ii,:)-16:He.locsHe(ii,:)+94,ii)=...
            He.libs_He(He.locsHe(ii,:)-...
            16:He.locsHe(ii,:)+94,ii) - avg_BG_libs_He;
        He.libs_H(He.locsH(ii,:)-16:He.locsH(ii,:)+94,ii)=...
            He.libs_H(He.locsH(ii,:)-...
            16:He.locsH(ii,:)+94,ii) - avg_BG_libs_H;
    end
end
for ii=1:length(volts.He_y)
He.libs_He(He.libs_He<=0) = He.libs_He(1,ii);
He.libs_H(He.libs_H<=0) = He.libs_H(1,ii);
end
He.libs_He_bgsub = [He.libs_He(:,4:end),He.libs_He(:,end)];
He.libs_H_bgsub = [He.libs_H(:,4:end),He.libs_H(:,end)];

He.libs_He_xbg = [He.libs_He_x(:,4:end),He.libs_He_x(:,end)];
He.libs_H_xbg = [He.libs_H_x(:,4:end),He.libs_H_x(:,end)];
```

```
% D only for 75 eV
for ii = 1:length(volts.D_y)
    if ((length(volts.D_y{ii}) > 0) && (length(volts.D_y{ii}) > 9000))
        D.libs_He(:,ii) = volts.D_y{ii,1}(8850:9000,1);
        D.libs_H(:,ii) = volts.D_y{ii,2}(8850:9000,1);
        D.libs_He_x(:,ii) = volts.D_x{ii,1}(8850:9000,1);
        D.libs_H_x(:,ii) = volts.D_x{ii,2}(8850:9000,1);
    end
end
for ii = 1:length(volts.D_y)
    if ((length(volts.D_y{ii}) > 0) && (length(volts.D_y{ii}) > 9000))
        [ D.pksHe(ii,:), D.locsHe(ii,:)] = max( D.libs_He(:,ii));
        [ D.pksH(ii,:), D.locsH(ii,:)] = max( D.libs_H(:,ii));
    end
end

for ii = 1:length(volts.D_y)
    if ( D.locsHe > 0)
         D.libs_He(D.locsHe(ii,:)-16:D.locsHe(ii,:)+94,ii)=...
             D.libs_He(D.locsHe(ii,:)-...
             16:D.locsHe(ii,:)+94,ii) - avg_BG_libs_He;
         D.libs_H(D.locsH(ii,:)-16:D.locsH(ii,:)+94,ii)=...
             D.libs_H(D.locsH(ii,:)-...
             16:D.locsH(ii,:)+94,ii) - avg_BG_libs_H;
    end
end
for ii=1:length(volts.D_y)
```

```
D.libs_He(D.libs_He<=0) = D.libs_He(1,ii);
D.libs_H(D.libs_H<=0) = D.libs_H(1,ii);
end
%Flux_libs(6:75,:);Flux_libs(81:225,:)
D.libs_He_bgsub = D.libs_He(:,115:304);
D.libs_H_bgsub = D.libs_H(:,115:304);

D.libs_He_xbg = D.libs_He_x(:,115:304);
D.libs_H_xbg = D.libs_H_x(:,115:304);
```

```
%MAKE EVERY FIVE
numb  = 5;
libs.He_dhebgsub5 = zeros((length(DHe.libs_He_bgsub(:,1))),...
    numb,(length(DHe.libs_He_bgsub(1,:)))/numb);
libs.He_dbgsub5 = zeros((length(D.libs_He_bgsub(:,1))),...
    numb,(length(D.libs_He_bgsub(1,:)))/numb);
libs.He_hebgsub5 = zeros((length(He.libs_He_bgsub(:,1))),...
    numb,(length(He.libs_He_bgsub(1,:)))/numb);

libs.He_dhebgsub5x = zeros((length(DHe.libs_He_bgsub(:,1))),...
    numb,(length(DHe.libs_He_xbg(1,:)))/numb);
libs.He_dbgsub5x = zeros((length(D.libs_He_bgsub(:,1))),...
    numb,(length(D.libs_He_xbg(1,:)))/numb);
libs.He_hebgsub5x = zeros((length(He.libs_He_bgsub(:,1))),...
    numb,(length(He.libs_He_xbg(1,:)))/numb);

libs.H_dhebgsub5 = zeros((length(DHe.libs_H_bgsub(:,1))),...
    numb,(length(DHe.libs_H_bgsub(1,:)))/numb);
libs.H_dbgsub5 = zeros((length(D.libs_H_bgsub(:,1))),...
    numb,(length(D.libs_H_bgsub(1,:)))/numb);
libs.H_hebgsub5 = zeros((length(He.libs_H_bgsub(:,1))),...
    numb,(length(He.libs_H_bgsub(1,:)))/numb);

libs.H_dhebgsub5x = zeros((length(DHe.libs_He_bgsub(:,1))),...
    numb,(length(DHe.libs_H_xbg(1,:)))/numb);
libs.H_dbgsub5x = zeros((length(D.libs_He_bgsub(:,1))),...
    numb,(length(D.libs_H_xbg(1,:)))/numb);
libs.H_hebgsub5x = zeros((length(He.libs_He_bgsub(:,1))),...
    numb,(length(He.libs_H_xbg(1,:)))/numb);
```

```
X.shiftdhe = DHe.libs_He_x(:,1).*ones(length(DHe.libs_He_x(:,1)),5).*...
    [1,1.1,1.2,1.3,1.4];
X.shiftd = D.libs_He_x(:,1).*ones(length(D.libs_He_x(:,1)),5).*...
    [1,1.1,1.2,1.3,1.4];
X.shifthe = He.libs_He_x(:,1).*ones(length(He.libs_He_x(:,1)),5).*...
    [1,1.1,1.2,1.3,1.4]
```

```


clear cool;
```

```
clear count;
clear count2;
count = 0;
count2 = 0;
for ii= 1:length(DHe.libs_He_bgsub(1,:))
    count = count+1;
    cool(:,count) = DHe.libs_He_bgsub(:,ii);
    if count/numb==1
        count2 = count2+1;
        libs.He_dhebgsub5(:,:,count2) = cool;
        count =0;
    end
end
clear cool;
clear count;
clear count2;
count = 0;
count2 = 0;
for ii= 1:length(DHe.libs_H_bgsub(1,:))
    count = count+1;
    cool(:,count) = DHe.libs_H_bgsub(:,ii);
    if count/numb==1
        count2 = count2+1;
        libs.H_dhebgsub5(:,:,count2) = cool;
        count =0;
    end
end
```

```
clear cool;
clear count;
clear count2;
count = 0;
count2 = 0;
for ii= 1:length(D.libs_He_bgsub(1,:))
    count = count+1;
    cool(:,count) = D.libs_He_bgsub(:,ii);
    if count/numb==1
        count2 = count2+1;
        libs.He_dbgsub5(:,:,count2) = cool;
        count =0;
    end
end
clear cool;
clear count;
clear count2;
count = 0;
count2 = 0;
for ii= 1:length(D.libs_H_bgsub(1,:))
    count = count+1;
    cool(:,count) = D.libs_H_bgsub(:,ii);
    if count/numb==1
        count2 = count2+1;
```

```
        libs.H_dbgsub5(:,:,count2) = cool;
        count =0;
    end
end
```

```
clear cool;
clear count;
clear count2;
count = 0;
count2 = 0;
for ii= 1:length(He.libs_He_bgsub(1,:))
    count = count+1;
    cool(:,count) = He.libs_He_bgsub(:,ii);
    if count/numb==1
        count2 = count2+1;
        libs.He_hebgsub5(:,:,count2) = cool;
        count =0;
    end
end
clear cool;
clear count;
clear count2;
count = 0;
count2 = 0;
for ii= 1:length(He.libs_H_bgsub(1,:))
    count = count+1;
    cool(:,count) = He.libs_H_bgsub(:,ii);
    if count/numb==1
        count2 = count2+1;
        libs.H_hebgsub5(:,:,count2) = cool;
        count =0;
    end
end
```

```
for ii = 1:length(libs.He_dbgsub5(:,1))
    for jj = 1:numb
abl.avgHe_dhe(ii,jj,1) = mean(libs.He_dhebgsub5(ii,jj,1:10));%PCW 500 C
abl.avgHe_dhe(ii,jj,2) = mean(libs.He_dhebgsub5(ii,jj,11:20));%BG W
abl.avgHe_dhe(ii,jj,3) = mean(libs.He_dhebgsub5(ii,jj,21:30));%SCW 500 C
abl.avgHe_dhe(ii,jj,4) = mean(libs.He_dhebgsub5(ii,jj,31:40));%PCW 300 C
abl.avgHe_dhe(ii,jj,5) = mean(libs.He_dhebgsub5(ii,jj,41:43));%SCW 300 C

abl.avgH_dhe(ii,jj,1) = mean(libs.H_dhebgsub5(ii,jj,1:10));%PCW 500 C
abl.avgH_dhe(ii,jj,2) = mean(libs.H_dhebgsub5(ii,jj,11:20));%BG W
abl.avgH_dhe(ii,jj,3) = mean(libs.H_dhebgsub5(ii,jj,21:30));%SCW 500 C
abl.avgH_dhe(ii,jj,4) = mean(libs.H_dhebgsub5(ii,jj,31:40));%PCW 300 C
abl.avgH_dhe(ii,jj,5) = mean(libs.H_dhebgsub5(ii,jj,41:43));%SCW 300 C

abl.avgHe_dhe_err(ii,jj,1) = std(libs.He_dhebgsub5(ii,jj,1:10));%PCW 500 C
abl.avgHe_dhe_err(ii,jj,2) = std(libs.He_dhebgsub5(ii,jj,11:20));%BG W
```

```
abl.avgHe_dhe_err(ii,jj,3) = std(libs.He_dhebgsub5(ii,jj,21:30));%SCW 500 C
abl.avgHe_dhe_err(ii,jj,4) = std(libs.He_dhebgsub5(ii,jj,31:40));%PCW 300 C
abl.avgHe_dhe_err(ii,jj,5) = std(libs.He_dhebgsub5(ii,jj,41:43));%SCW 300 C

abl.avgH_dhe_err(ii,jj,1) = std(libs.H_dhebgsub5(ii,jj,1:10));%PCW 500 C
abl.avgH_dhe_err(ii,jj,2) = std(libs.H_dhebgsub5(ii,jj,11:20));%BG W
abl.avgH_dhe_err(ii,jj,3) = std(libs.H_dhebgsub5(ii,jj,21:30));%SCW 500 C
abl.avgH_dhe_err(ii,jj,4) = std(libs.H_dhebgsub5(ii,jj,31:40));%PCW 300 C
abl.avgH_dhe_err(ii,jj,5) = std(libs.H_dhebgsub5(ii,jj,41:43));%SCW 300 C
    end
end
```

```
for ii = 1:length(libs.He_dbgsub5(:,1))
    for jj = 1:numb
abl.avgHe_d(ii,jj,1) = mean(libs.He_dbgsub5(ii,jj,1:10));%PCW 500 C
abl.avgHe_d(ii,jj,2) = mean(libs.He_dbgsub5(ii,jj,11:20));%BG W
abl.avgHe_d(ii,jj,3) = mean(libs.He_dbgsub5(ii,jj,21:30));%SCW 500 C
abl.avgHe_d(ii,jj,4) = mean(libs.He_dbgsub5(ii,jj,31:38));%PCW 300 C

abl.avgH_d(ii,jj,1) = mean(libs.H_dbgsub5(ii,jj,1:10));%PCW 500 C
abl.avgH_d(ii,jj,2) = mean(libs.H_dbgsub5(ii,jj,11:20));%BG W
abl.avgH_d(ii,jj,3) = mean(libs.H_dbgsub5(ii,jj,21:30));%SCW 500 C
abl.avgH_d(ii,jj,4) = mean(libs.H_dbgsub5(ii,jj,31:38));%PCW 300 C

abl.avgHe_d_err(ii,jj,1) = std(libs.He_dbgsub5(ii,jj,1:10));%PCW 500 C
abl.avgHe_d_err(ii,jj,2) = std(libs.He_dbgsub5(ii,jj,11:20));%BG W
abl.avgHe_d_err(ii,jj,3) = std(libs.He_dbgsub5(ii,jj,21:30));%SCW 500 C
abl.avgHe_d_err(ii,jj,4) = std(libs.He_dbgsub5(ii,jj,31:38));%PCW 300 C

abl.avgH_d_err(ii,jj,1) = std(libs.H_dbgsub5(ii,jj,1:10));%PCW 500 C
abl.avgH_d_err(ii,jj,2) = std(libs.H_dbgsub5(ii,jj,11:20));%BG W
abl.avgH_d_err(ii,jj,3) = std(libs.H_dbgsub5(ii,jj,21:30));%SCW 500 C
abl.avgH_d_err(ii,jj,4) = std(libs.H_dbgsub5(ii,jj,31:38));%PCW 300 C
    end
end
```

```
for ii = 1:length(libs.He_hebgsub5(:,1))
    for jj = 1:numb
abl.avgHe_he(ii,jj,1) = mean(libs.He_hebgsub5(ii,jj,1:10));%PCW 500 C
abl.avgHe_he(ii,jj,2) = mean(libs.He_hebgsub5(ii,jj,11:20));%BG W
abl.avgHe_he(ii,jj,3) = mean(libs.He_hebgsub5(ii,jj,21:30));%SCW 500 C
abl.avgHe_he(ii,jj,4) = mean(libs.He_hebgsub5(ii,jj,31:40));%PCW 300 C
abl.avgHe_he(ii,jj,5) = mean(libs.He_hebgsub5(ii,jj,41:50));%SCW 300 C

abl.avgH_he(ii,jj,1) = mean(libs.H_hebgsub5(ii,jj,1:10));%PCW 500 C
abl.avgH_he(ii,jj,2) = mean(libs.H_hebgsub5(ii,jj,11:20));%BG W
abl.avgH_he(ii,jj,3) = mean(libs.H_hebgsub5(ii,jj,21:30));%SCW 500 C
abl.avgH_he(ii,jj,4) = mean(libs.H_hebgsub5(ii,jj,31:40));%PCW 300 C
abl.avgH_he(ii,jj,5) = mean(libs.H_hebgsub5(ii,jj,41:50));%SCW 300 C
```

```
abl.avgHe_he_err(ii,jj,1) = std(libs.He_hebgsub5(ii,jj,1:10));%PCW 500 C
abl.avgHe_he_err(ii,jj,2) = std(libs.He_hebgsub5(ii,jj,11:20));%BG W
abl.avgHe_he_err(ii,jj,3) = std(libs.He_hebgsub5(ii,jj,21:30));%SCW 500 C
abl.avgHe_he_err(ii,jj,4) = std(libs.He_hebgsub5(ii,jj,31:40));%PCW 300 C
abl.avgHe_he_err(ii,jj,5) = std(libs.He_hebgsub5(ii,jj,41:50));%SCW 300 C

abl.avgH_he_err(ii,jj,1) = std(libs.H_hebgsub5(ii,jj,1:10));%PCW 500 C
abl.avgH_he_err(ii,jj,2) = std(libs.H_hebgsub5(ii,jj,11:20));%BG W
abl.avgH_he_err(ii,jj,3) = std(libs.H_hebgsub5(ii,jj,21:30));%SCW 500 C
abl.avgH_he_err(ii,jj,4) = std(libs.H_hebgsub5(ii,jj,31:40));%PCW 300 C
abl.avgH_he_err(ii,jj,5) = std(libs.H_hebgsub5(ii,jj,41:50));%SCW 300 C
    end
end
```

```
%LIBS
%%%%%%%%%%%%%%%%%%%%%%%%%%%%%%%%%%%%%%%%%%%%%%%%%%%%%%%%%%%%%%%%%%%%%%%%%%%%
%Part 1 calibration%%%%%%%%%%%%%%%%%%%%%%%%%%%%%%%%%%%%%%%%%%%%%%%%%%%%%%%%
%%%%%%%%%%%%%%%%%%%%%%%%%%%%%%%%%%%%%%%%%%%%%%%%%%%%%%%%%%%%%%%%%%%%%%%%%%%%
Norm_signal = [(rel_calib(:,3)./rel_calib(:,2)),(rel_calib(:,4)./rel_calib(:,2)),...
    (rel_calib(:,5)./rel_calib(:,2))];
%Tube2, 7, 8 (He is in 8, H in tube 7, W in tube 2)

subzero = [(Norm_signal(:,1) - rel_calib(1,3)),(Norm_signal(:,2) -...
    rel_calib(1,3)),(Norm_signal(:,3) - rel_calib(1,3))];

Natlog = log(subzero);

poly_natlog = [(polyfit(rel_calib(:,1),Natlog(:,1),3))',...
    (polyfit(rel_calib(:,1),Natlog(:,2),3))',...
    (polyfit(rel_calib(:,1),Natlog(:,3),3))'];

new_recalib = linspace(0,0.50,100)';

polyval_natlog = [(polyval(poly_natlog(:,1)',new_recalib(:,1))),...
    (polyval(poly_natlog(:,2)',new_recalib(:,1))),...
    (polyval(poly_natlog(:,3)',new_recalib(:,1)))];

tube_coeff = [poly_natlog(:,3),poly_natlog(:,2),poly_natlog(:,1)]';
%coefficients associated with the polynomial now in T8,7,2 = He,H,W
CALcntrl = rel_calib(9,1);
CALvolt = [rel_calib(9,5),rel_calib(9,4),rel_calib(9,3)]; %T8,T7,T2
```

```
PMT.volt_He5dhe = abl.avgHe_dhe; %%%Place your first shot y-axis here
PMT.volt_H5dhe = abl.avgH_dhe; %%%Place your first shot y-axis here

PMT.volt_He5errdhe = abl.avgHe_dhe_err;
PMT.volt_H5errdhe = abl.avgH_dhe_err;
```

```
PMT.volt_He5d = abl.avgHe_d; %%%Place your first shot y-axis here
PMT.volt_H5d = abl.avgH_d; %%%Place your first shot y-axis here

PMT.volt_He5errd = abl.avgHe_d_err;
PMT.volt_H5errd = abl.avgH_d_err;

PMT.volt_He5he = abl.avgHe_he; %%%Place your first shot y-axis here
PMT.volt_H5he = abl.avgH_he; %%%Place your first shot y-axis here

PMT.volt_He5errhe = abl.avgHe_he_err;
PMT.volt_H5errhe = abl.avgH_he_err;

PMT.cntr = ones(111,3).*0.55; %T8,T7,T2
```

```
for ii = 1:2
ksig(:,ii) = polyval(tube_coeff(ii,:),PMT.cntr(:,ii));
%Tube coeffs 8,7,2 to PMTcnt 8,7,2 (He,H,W)
end

kcal = [polyval(tube_coeff(:,1),CALcntrl),...
    polyval(tube_coeff(:,2),CALcntrl),...
    polyval(tube_coeff(:,3),CALcntrl)]; %T8,T7,T2
```

```
for ii = 1:numb
VG.sig_He5dhe(:,:,ii) = PMT.volt_He5dhe(:,:,ii)./(log(ksig(1,1)*1));

VG.sig_He5errdhe(:,:,ii) = sqrt((PMT.volt_He5errdhe(:,:,ii).^2)./...
    (log(ksig(1,1)*1).^2));

VG.sig_H5dhe(:,:,ii) = PMT.volt_H5dhe(:,:,ii)./(log(ksig(1,2)*1));

VG.sig_H5errdhe(:,:,ii) = sqrt((PMT.volt_H5errdhe(:,:,ii).^2)./...
    (log(ksig(1,2)*1).^2));
end
```

```
for ii = 1:4
VG.sig_He5d(:,:,ii) = PMT.volt_He5d(:,:,ii)./(log(ksig(1,1)*1));

VG.sig_He5errd(:,:,ii) = sqrt((PMT.volt_He5errd(:,:,ii).^2)./...
    (log(ksig(1,1)*1).^2));

VG.sig_H5d(:,:,ii) = PMT.volt_H5d(:,:,ii)./(log(ksig(1,2)*1));

VG.sig_H5errd(:,:,ii) = sqrt((PMT.volt_H5errd(:,:,ii).^2)./...
    (log(ksig(1,2)*1).^2));
end
```

```
for ii = 1:numb
VG.sig_He5he(:,:,ii) = PMT.volt_He5he(:,:,ii)./(log(ksig(1,1)*1));

VG.sig_He5errhe(:,:,ii) = sqrt((PMT.volt_He5errhe(:,:,ii).^2)./...
    (log(ksig(1,1)*1).^2));

VG.sig_H5he(:,:,ii) = PMT.volt_H5he(:,:,ii)./(log(ksig(1,2)*1));

VG.sig_H5errhe(:,:,ii) = sqrt((PMT.volt_H5errhe(:,:,ii).^2)./...
    (log(ksig(1,2)*1).^2));
end
```

```
%LIBS
%%%%%%%%%%%%%%%%%%%%%%%%%%%%%%%%%%%%%%%%%%%%%%%%%%%%%%%%%%%%%%%%%%%%%%%%%%%%%%%
%Part 2 Calibration%%%%%%%%%%%%%%%%%%%%%%%%%%%%%%%%%%%%%%%%%%%%%%%%%%%%%%%%%%%
%%%%%%%%%%%%%%%%%%%%%%%%%%%%%%%%%%%%%%%%%%%%%%%%%%%%%%%%%%%%%%%%%%%%%%%%%%%%%%%
lamda_o = [706.50,656.20,400.50,501.35,598.1]'; %filters in nm
FWHM = [.5,.5,2,1,5]'; %nm
wav_filt(:,1) = linspace(705.0,708.5,512);%nm
wav_filt(:,2) = linspace(654.8,657.8,512);%nm
wav_filt(:,3) = linspace(398,403,512);%nm
wav_filt(:,4) = linspace(500,503,512);%nm
wav_filt(:,5) = linspace(595.5,600.5,512);%nm

wav_lamp = linspace(300,1050,512)';

wavelength_A = lamp_calib(:,1); %nm to angrstoms
filts = 5;

for i = 1:filts
    pp = spline(wavelength_A,lamp_calib(:,2));
    yy(:,i) = ppval(pp,wav_lamp);
end

for ii = 1:filts
    gauss(:,ii) = exp(-((4*log(2).*((lamda_o(ii,1)-wav_filt(:,ii)).^2))./...
        (FWHM(ii,1).^2)));
end

prod = gauss.*yy;
```

```
Rcali_k = zeros(1,1);
lami_k = [706.51,656.19,400.87,501.71,597.90];
tolerance=0.004;
for jj = 1:filts
    for ii = 1:length(wav_filt)
        if min(abs(wav_filt(ii,jj)-lami_k(1,jj)))<tolerance
            Rcali_k(jj,1) = prod(ii,jj);
        end
```

```
    end
end
```

```
Rcali_k_Wm2 = Rcali_k.*(1E-6).*(1/1E-4); % [W/m^2]
```

```
for ii = 1:numb
L.aikHe5dhe(:,:,ii) = (1/Rcali_k_Wm2(1,1)).*...
    (VG.sig_He5dhe(:,:,ii)); % [W/m^2]
L.aikHe5errdhe(:,:,ii) = sqrt(((1/Rcali_k_Wm2(1,1)).^2).*...
    (VG.sig_He5errdhe(:,:,ii)).^2); % [W/m^2]

L.aikH5dhe(:,:,ii) = (1/Rcali_k_Wm2(2,1)).*...
    (VG.sig_H5dhe(:,:,ii)); % [W/m^2]
L.aikH5errdhe(:,:,ii) = sqrt(((1/Rcali_k_Wm2(2,1)).^2).*...
    (VG.sig_H5errdhe(:,:,ii)).^2); % [W/m^2]
end
```

```
for ii = 1:4
L.aikHe5d(:,:,ii) = (1/Rcali_k_Wm2(1,1)).*...
    (VG.sig_He5d(:,:,ii)); % [W/m^2]
L.aikHe5errd(:,:,ii) = sqrt(((1/Rcali_k_Wm2(1,1)).^2).*...
    (VG.sig_He5errd(:,:,ii)).^2); % [W/m^2]

L.aikH5d(:,:,ii) = (1/Rcali_k_Wm2(2,1)).*...
    (VG.sig_H5d(:,:,ii)); % [W/m^2]
L.aikH5errd(:,:,ii) = sqrt(((1/Rcali_k_Wm2(2,1)).^2).*...
    (VG.sig_H5errd(:,:,ii)).^2); % [W/m^2]
end
```

```
for ii = 1:numb
L.aikHe5he(:,:,ii) = (1/Rcali_k_Wm2(1,1)).*...
    (VG.sig_He5he(:,:,ii)); % [W/m^2]
L.aikHe5errhe(:,:,ii) = sqrt(((1/Rcali_k_Wm2(1,1)).^2).*...
    (VG.sig_He5errhe(:,:,ii)).^2); % [W/m^2]

L.aikH5he(:,:,ii) = (1/Rcali_k_Wm2(2,1)).*...
    (VG.sig_H5he(:,:,ii)); % [W/m^2]
L.aikH5errhe(:,:,ii) = sqrt(((1/Rcali_k_Wm2(2,1)).^2).*...
    (VG.sig_H5errhe(:,:,ii)).^2); % [W/m^2]
end
```

```
%Conversion of [W/m^2] to [Photons/m^2s]
for ii = 1:numb
Photon.flux5Hedhe(:,:,ii) = L.aikHe5dhe(:,:,ii)./...
    ((6.63E-34*(3E8/(lami_k(1,1)))));
Photon.flux5Heerrdhe(:,:,ii) = sqrt((L.aikHe5dhe(:,:,ii).^2)./...
```

```
    (((6.63E-34*(3E8/(lami_k(1,1))))).^2));

Photon.flux5Hdhe(:,:,ii) = L.aikH5dhe(:,:,ii)./...
    ((6.63E-34*(3E8/(lami_k(1,2)))));
Photon.flux5Herrdhe(:,:,ii) = sqrt((L.aikH5dhe(:,:,ii).^2)./...
    (((6.63E-34*(3E8/(lami_k(1,2))))).^2));
end
```

```
%Conversion of [W/m^2] to [Photons/m^2s]
for ii = 1:4
Photon.flux5Hed(:,:,ii) = L.aikHe5d(:,:,ii)./...
    ((6.63E-34*(3E8/(lami_k(1,1)))));
Photon.flux5Heerrd(:,:,ii) = sqrt((L.aikHe5d(:,:,ii).^2)./...
    (((6.63E-34*(3E8/(lami_k(1,1))))).^2));

Photon.flux5Hd(:,:,ii) = L.aikH5d(:,:,ii)./...
    ((6.63E-34*(3E8/(lami_k(1,2)))));
Photon.flux5Herrd(:,:,ii) = sqrt((L.aikH5d(:,:,ii).^2)./...
    (((6.63E-34*(3E8/(lami_k(1,2))))).^2));
end
```

```
%Conversion of [W/m^2] to [Photons/m^2s]
for ii = 1:numb
Photon.flux5Hehe(:,:,ii) = L.aikHe5he(:,:,ii)./...
    ((6.63E-34*(3E8/(lami_k(1,1)))));
Photon.flux5Heerrhe(:,:,ii) = sqrt((L.aikHe5he(:,:,ii).^2)./...
    (((6.63E-34*(3E8/(lami_k(1,1))))).^2));

Photon.flux5Hhe(:,:,ii) = L.aikH5he(:,:,ii)./...
    ((6.63E-34*(3E8/(lami_k(1,2)))));
Photon.flux5Herrhe(:,:,ii) = sqrt((L.aikH5he(:,:,ii).^2)./...
    (((6.63E-34*(3E8/(lami_k(1,2))))).^2));
end
```

```
%SXB
%lami_k = [7067.6,6561.9,4008,5017.1,5979.0]
load('SXB.mat');

p = spline(SXB.Te_iHe,single(SXB.irc_He),SXB.Tenew);
pp = spline(SXB.Te_exHe,single(SXB.excr_He),SXB.Tenew);

f = spline(SXB.Te_iD,single(SXB.irc_D),SXB.Tenew);
ff = spline(SXB.Te_exD,single(SXB.excr_D),SXB.Tenew);

fff = abs((f./ff)*.3)';
ppp = abs((p./pp)*1.5)' ;

ww = (SXB.Coeffw./SXB.Coeffw399)*.3*1e-9;
```

```
sxb.coe5Hedhe = ones(length(Photon.flux5Hedhe(:,1)),5).*...
    [1000,1000,1000,5000,10000];
sxb.coe5Hdhe = ones(length(Photon.flux5Hdhe(:,1)),5).*...
    [100,100,100,500,5000];
SXB.coeHe5dhe = (SXB.coe(3,1)*(1e-9))./sxb.coe5Hedhe;
SXB.coeH5dhe = (SXB.coe(3,2)*(1e-9))./sxb.coe5Hdhe;

sxb.coe5Hed = ones(length(Photon.flux5Hed(:,1)),5).*...
    [10000,10000,10000,10000,10000];
sxb.coe5Hd = ones(length(Photon.flux5Hd(:,1)),5).*...
    [5000,500,100,100,100];
SXB.coeHe5d = (SXB.coe(3,1)*(1e-9))./sxb.coe5Hed;
SXB.coeH5d = (SXB.coe(3,2)*(1e-9))./sxb.coe5Hd;

sxb.coe5Hehe = ones(length(Photon.flux5Hehe(:,1)),5).*...
    [1000,1000,1000,5000,10000];
sxb.coe5Hhe = ones(length(Photon.flux5Hhe(:,1)),5).*...
    [10000,10000,10000,10000,10000];
SXB.coeHe5he = (SXB.coe(3,1)*(1e-9))./sxb.coe5Hehe;
SXB.coeH5he = (SXB.coe(3,2)*(1e-9))./sxb.coe5Hhe;
```

```
for ii = 1:5
    Atom.spsHedhe(:,ii,:) = Photon.flux5Hedhe(:,ii,:).*...
        SXB.coeHe5dhe(:,ii); %[Atoms/s]
    Atom.spsHdhe(:,ii,:) = Photon.flux5Hdhe(:,ii,:).*...
        SXB.coeH5dhe(:,ii); %[Atoms/s]
    Atom.spsHeerrdhe(:,ii,:) = Photon.flux5Heerrdhe(:,ii,:).*...
        SXB.coeHe5dhe(:,ii); %[Atoms/s]
    Atom.spsHerrdhe(:,ii,:) = Photon.flux5Herrdhe(:,ii,:).*...
        SXB.coeH5dhe(:,ii); %[Atoms/s]
end

for ii = 1:5
    Atom.spsHed(:,ii,:) = Photon.flux5Hed(:,ii,:).*...
        SXB.coeHe5d(:,ii); %[Atoms/s]
    Atom.spsHd(:,ii,:) = Photon.flux5Hd(:,ii,:).*...
        SXB.coeH5d(:,ii); %[Atoms/s]
    Atom.spsHeerrd(:,ii,:) = Photon.flux5Heerrd(:,ii,:).*...
        SXB.coeHe5d(:,ii); %[Atoms/s]
    Atom.spsHerrd(:,ii,:) = Photon.flux5Herrd(:,ii,:).*...
        SXB.coeH5d(:,ii); %[Atoms/s]
end

for ii = 1:5
    Atom.spsHehe(:,ii,:) = Photon.flux5Hehe(:,ii,:).*...
        SXB.coeHe5he(:,ii); %[Atoms/s]
    Atom.spsHhe(:,ii,:) = Photon.flux5Hhe(:,ii,:).*...
        SXB.coeH5he(:,ii); %[Atoms/s]
    Atom.spsHeerrhe(:,ii,:) = Photon.flux5Heerrhe(:,ii,:).*...
        SXB.coeHe5he(:,ii); %[Atoms/s]
    Atom.spsHerrhe(:,ii,:) = Photon.flux5Herrhe(:,ii,:).*...
```

```
        SXB.coeH5he(:,ii); %[Atoms/s]
end
```

```
for jj = 1:5
    for ii = 1:5
    Atom.sHedhe(ii,jj) = trapz(X.shiftdhe(:,1),Atom.spsHedhe(:,ii,jj));
    Atom.sHdhe(ii,jj) = trapz(X.shiftdhe(:,1),Atom.spsHdhe(:,ii,jj));
    Atom.sHeerrdhe(ii,jj) = trapz(X.shiftdhe(:,1),Atom.spsHeerrdhe(:,ii,jj));
    Atom.sHerrdhe(ii,jj) = trapz(X.shiftdhe(:,1),Atom.spsHerrdhe(:,ii,jj));
    end
end

for jj = 1:4
    for ii = 1:5
    Atom.sHed(ii,jj) = trapz(X.shiftd(:,1),Atom.spsHed(:,ii,jj));
    Atom.sHd(ii,jj) = trapz(X.shiftd(:,1),Atom.spsHd(:,ii,jj));
    Atom.sHeerrd(ii,jj) = trapz(X.shiftd(:,1),Atom.spsHeerrd(:,ii,jj));
    Atom.sHerrd(ii,jj) = trapz(X.shiftd(:,1),Atom.spsHerrd(:,ii,jj));
    end
end

for jj = 1:5
    for ii =1:5
    Atom.sHehe(ii,jj) = trapz(X.shifthe(:,1),Atom.spsHehe(:,ii,jj));
    Atom.sHhe(ii,jj) = trapz(X.shifthe(:,1),Atom.spsHhe(:,ii,jj));
    Atom.sHeerrhe(ii,jj) = trapz(X.shifthe(:,1),Atom.spsHeerrhe(:,ii,jj));
    Atom.sHerrhe(ii,jj) = trapz(X.shifthe(:,1),Atom.spsHerrhe(:,ii,jj));
end
end
```

```
for jj = 1:5
    for jj = 1:5
    Atom.sHedhe_nsxb(ii,jj) = trapz(X.shiftdhe(:,1),...
        Photon.flux5Hedhe(:,ii,jj));
    Atom.sHdhe_nsxb(ii,jj) = trapz(X.shiftdhe(:,1),...
        Photon.flux5Hdhe(:,ii,jj));
    Atom.sHeerrdhe_nsxb(ii,jj) = trapz(X.shiftdhe(:,1),...
        Photon.flux5Heerrdhe(:,ii,jj));
    Atom.sHerrdhe_nsxb(ii,jj) = trapz(X.shiftdhe(:,1),...
        Photon.flux5Herrdhe(:,ii,jj));
    end
end

for jj = 1:4
    for ii= 1:5
    Atom.sHed_nsxb(ii,jj) = trapz(X.shiftd(:,1),...
        Photon.flux5Hed(:,ii,jj));
    Atom.sHd_nsxb(ii,jj) = trapz(X.shiftd(:,1),...
        Photon.flux5Hd(:,ii,jj));
    Atom.sHeerrd_nsxb(ii,jj) = trapz(X.shiftd(:,1),...
```

```
        Photon.flux5Heerrd(:,ii,jj));
    Atom.sHerrd_nsxb(ii,jj) = trapz(X.shiftd(:,1),...
        Photon.flux5Herrd(:,ii,jj));
    end
end

for jj = 1:5
    for ii = 1:5
    Atom.sHehe_nsxb(ii,jj) = trapz(X.shifthe(:,1),...
        Photon.flux5Hehe(:,ii,jj));
    Atom.sHhe_nsxb(ii,jj) = trapz(X.shifthe(:,1),...
        Photon.flux5Hhe(:,ii,jj));
    Atom.sHeerrhe_nsxb(ii,jj) = trapz(X.shifthe(:,1),...
        Photon.flux5Heerrhe(:,ii,jj));
    Atom.sHerrhe_nsxb(ii,jj) = trapz(X.shifthe(:,1),...
        Photon.flux5Herrhe(:,ii,jj));
    end
end
```

```
Atom.sHeerrdhe = Atom.sHeerrdhe./1E1;
Atom.sHerrdhe = Atom.sHerrdhe./1E1;
Atom.sHeerrd = Atom.sHeerrd./1E1;
Atom.sHerrd = Atom.sHerrd./1E1;
Atom.sHeerrhe = Atom.sHeerrhe./1E1;
Atom.sHerrhe = Atom.sHerrhe./1E1;
```

```
abl_vol.m3 = abl_vol.cylp.*1e-18;
vol.m3 = vol.cylp.*1e-18;
vol.m3err = vol.cylp_err.*1e-18;
```

```
Atom.Heucdhe = Atom.sHedhe./abl_vol.m3(1:5);
Atom.Heucerrdhe = Atom.sHeerrdhe./vol.m3err(1:5);
Atom.Hucdhe = Atom.sHdhe./abl_vol.m3(1:5);
Atom.Hucerrdhe = Atom.sHerrdhe./vol.m3err(1:5);
appm.Heucdhe = (Atom.Heucdhe./6.32E28).*1E6;
appm.Heucerrdhe = (Atom.Heucerrdhe./6.32E28).*1E6;
appm.Hucdhe = (Atom.Hucdhe./6.32E28).*1E6;
appm.Hucerrdhe = (Atom.Hucerrdhe./6.32E28).*1E6;
```

```
Atom.Heucd = Atom.sHed./abl_vol.m3(1:5);
Atom.Heucerrd = Atom.sHeerrd./vol.m3err(1:5);
Atom.Hucd = Atom.sHd./abl_vol.m3(1:5);
Atom.Hucerrd = Atom.sHerrd./vol.m3err(1:5);
appm.Heucd = (Atom.Heucd./6.32E28).*1E6;
appm.Heucerrd = (Atom.Heucerrd./6.32E28).*1E6;
appm.Hucd = (Atom.Hucd./6.32E28).*1E6;
```

```
appm.Hucerrd = (Atom.Hucerrd./6.32E28).*1E6;
```

```
Atom.Heuche = Atom.sHehe./abl_vol.m3(1:5);
Atom.Heucerrhe = Atom.sHeerrhe./vol.m3err(1:5);
Atom.Huche = Atom.sHhe./abl_vol.m3(1:5);
Atom.Hucerrhe = Atom.sHerrhe./vol.m3err(1:5);
appm.Heuche = (Atom.Heuche./6.32E28).*1E6;
appm.Heucerrhe = (Atom.Heucerrhe./6.32E28).*1E6;
appm.Huche = (Atom.Huche./6.32E28).*1E6;
appm.Hucerrhe = (Atom.Hucerrhe./6.32E28).*1E6;
```

```
new_ablations = linspace(1,5,5);
vnm = ones(length(new_ablations),length(new_ablations)).*...
    (1:length(new_ablations));
vnm = triu(vnm,1);
vnm(1,1) = 1;
vnm(:,1) = vnm(1,:);
for ii = 1:5
    for jj = 1:5
        for kk = 1:5
        if vnm(ii,jj) > 0
            sig.Hedhe(ii,jj,kk) = Atom.sHedhe(vnm(ii,jj),kk);
            sig.Heerrdhe(ii,jj,kk) = Atom.sHeerrdhe(vnm(ii,jj),kk);
            sig.Hdhe(ii,jj,kk) = Atom.sHdhe(vnm(ii,jj),kk);
            sig.Herrdhe(ii,jj,kk) = Atom.sHerrdhe(vnm(ii,jj),kk);
        elseif vnm(ii,jj) == 0
            sig.Hedhe(ii,jj,kk) = 0;
            sig.Heerrdhe(ii,jj,kk) = 0;
            sig.Hdhe(ii,jj,kk) = 0;
            sig.Herrdhe(ii,jj,kk) = 0;
            end
        end
    end
end
```

```
for ii = 1:5
    for jj = 1:5
        for kk = 1:4
        if vnm(ii,jj) > 0
            sig.Hed(ii,jj,kk) = Atom.sHed(vnm(ii,jj),kk);
            sig.Heerrd(ii,jj,kk) = Atom.sHeerrd(vnm(ii,jj),kk);
            sig.Hd(ii,jj,kk) = Atom.sHd(vnm(ii,jj),1);
            sig.Herrd(ii,jj,kk) = Atom.sHerrd(vnm(ii,jj),kk);
        elseif vnm(ii,jj) == 0
            sig.Hed(ii,jj,kk) = 0;
            sig.Heerrd(ii,jj,kk) = 0;
            sig.Hd(ii,jj,kk) = 0;
            sig.Hderrd(ii,jj,kk) = 0;
            end
```

```
        end
    end
end
```

```
for ii = 1:5
    for jj = 1:5
        for kk = 1:5
        if vnm(ii,jj) > 0
            sig.Hehe(ii,jj,kk) = Atom.sHehe(vnm(ii,jj),kk);
            sig.Heerrhe(ii,jj,kk) = Atom.sHeerrhe(vnm(ii,jj),kk);
            sig.Hhe(ii,jj,kk) = Atom.sHhe(vnm(ii,jj),kk);
            sig.Herrhe(ii,jj,kk) = Atom.sHerrhe(vnm(ii,jj),kk);
        elseif vnm(ii,jj) == 0
            sig.Hehe(ii,jj,kk) = 0;
            sig.Heerrhe(ii,jj,kk) = 0;
            sig.Hhe(ii,jj,kk) = 0;
            sig.Herrhe(ii,jj,kk) = 0;
            end
        end
    end
end
```

```
for ii = 1:5
    for jj = 1:5
        for kk = 1:5
        if vnm(ii,jj) > 0
            flux.Hematdhe(ii,jj,kk) = sig.Hedhe(ii,jj,kk)*...
                frac_vol.cylp(ii,jj);
            flux.Heerrmatdhe(ii,jj,kk) = sqrt((sig.Heerrdhe(ii,jj,kk).^2)*...
                (frac_vol.cylp(ii,jj).^2));
            flux.Hmatdhe(ii,jj,kk) = sig.Hdhe(ii,jj,kk)*...
                frac_vol.cylp(ii,jj);
            flux.Herrmatdhe(ii,jj,kk) = sqrt((sig.Herrdhe(ii,jj,kk).^2)*...
                (frac_vol.cylp(ii,jj).^2));
        elseif vnm(ii,jj) == 0
            flux.Hematdhe(ii,jj,kk) = 0;
            flux.Heerrmatdhe(ii,jj,kk) = 0;
            flux.Hmatdhe(ii,jj,kk) = 0;
            flux.Herrmatdhe(ii,jj,kk) = 0;
            end
        end
    end
end
```

```
for ii = 1:5
    for jj = 1:5
        for kk = 1:4
        if vnm(ii,jj) > 0
            flux.Hematd(ii,jj,kk) = sig.Hed(ii,jj,kk)*...
```

```
                frac_vol.cylp(ii,jj);
            flux.Heerrmatd(ii,jj,kk) = sqrt((sig.Heerrd(ii,jj,kk).^2)*...
                (frac_vol.cylp(ii,jj).^2));
            flux.Hmatd(ii,jj,kk) = sig.Hd(ii,jj,kk)*...
                frac_vol.cylp(ii,jj);
            flux.Herrmatd(ii,jj,kk) = sqrt((sig.Herrd(ii,jj,kk).^2)*...
                (frac_vol.cylp(ii,jj).^2));
        elseif vnm(ii,jj) == 0
            flux.Hematd(ii,jj,kk) = 0;
            flux.Heerrmatd(ii,jj,kk) = 0;
            flux.Hmatd(ii,jj,kk) = 0;
            flux.Herrmatd(ii,jj,kk) = 0;
            end
        end
    end
end
```

```
for ii = 1:5
    for jj = 1:5
        for kk = 1:5
        if vnm(ii,jj) > 0
            flux.Hemathe(ii,jj,kk) = sig.Hehe(ii,jj,kk)*...
                frac_vol.cylp(ii,jj);
            flux.Heerrmathe(ii,jj,kk) = sqrt((sig.Heerrhe(ii,jj,kk).^2)*...
                (frac_vol.cylp(ii,jj).^2));
            flux.Hmathe(ii,jj,kk) = sig.Hhe(ii,jj,kk)*...
                frac_vol.cylp(ii,jj);
            flux.Herrmathe(ii,jj,kk) = sqrt((sig.Herrhe(ii,jj,kk).^2)*...
                (frac_vol.cylp(ii,jj).^2));
        elseif vnm(ii,jj) == 0
            flux.Hemathe(ii,jj,kk) = 0;
            flux.Heerrmathe(ii,jj,kk) = 0;
            flux.Hmathe(ii,jj,kk) = 0;
            flux.Herrmathe(ii,jj,kk) = 0;
            end
        end
    end
end
```

```
for jj =1:5
for ii = 1:5
    flux.Hecdhe(ii,jj) = sum(flux.Hematdhe(ii,:,jj));
    flux.Hecerrdhe(ii,jj) = sum(flux.Heerrmatdhe(ii,:,jj));
    flux.Hcdhe(ii,jj) = sum(flux.Hmatdhe(ii,:,jj));
    flux.Hcerrdhe(ii,jj) = sum(flux.Herrmatdhe(ii,:,jj));
end
end

flux.Hecm3dhe = flux.Hecdhe./abl_vol.m3(1:5); %[Atoms/m^3]
```

```
flux.Hecerrm3dhe = flux.Hecerrdhe./vol.m3err(1:5); %[Atoms/m^3]
appm.Hecdhe = (flux.Hecm3dhe./6E28).*1E6;
appm.Hecerrdhe = (flux.Hecerrm3dhe./6E28).*1E6;

flux.Hcm3dhe = flux.Hcdhe./abl_vol.m3(1:5);
flux.Hcerrm3dhe = flux.Hcerrdhe./vol.m3err(1:5);
appm.Hcdhe = (flux.Hcm3dhe./6E28).*1E6;
appm.Hcerrdhe = (flux.Hcerrm3dhe./6E28).*1E6;
```

```
for jj =1:4
    for ii = 1:5
    flux.Hecd(ii,jj) = sum(flux.Hematd(ii,:,jj));
    flux.Hecerrd(ii,jj) = sum(flux.Heerrmatd(ii,:,jj));
    flux.Hcd(ii,jj) = sum(flux.Hmatd(ii,:,jj));
    flux.Hcerrd(ii,jj) = sum(flux.Herrmatd(ii,:,jj));
    end
end

flux.Hecm3d = flux.Hecd./abl_vol.m3(1:5); %[Atoms/m^3]
flux.Hecerrm3d = flux.Hecerrd./vol.m3err(1:5); %[Atoms/m^3]
appm.Hecd = (flux.Hecm3d./6E28).*1E6;
appm.Hecerrd = (flux.Hecerrm3d./6E28).*1E6;

flux.Hcm3d = flux.Hcd./abl_vol.m3(1:5);
flux.Hcerrm3d = flux.Hcerrd./vol.m3err(1:5);
appm.Hcd = (flux.Hcm3d./6E28).*1E6;
appm.Hcerrd = (flux.Hcerrm3d./6E28).*1E6;
```

```
for jj =1:5
for ii = 1:5
    flux.Heche(ii,jj) = sum(flux.Hemathe(ii,:,jj));
    flux.Hecerrhe(ii,jj) = sum(flux.Heerrmathe(ii,:,jj));
    flux.Hche(ii,jj) = sum(flux.Hmathe(ii,:,jj));
    flux.Hcerrhe(ii,jj) = sum(flux.Herrmathe(ii,:,jj));
end
end

flux.Hecm3he = flux.Heche./abl_vol.m3(1:5); %[Atoms/m^3]
flux.Hecerrm3he = flux.Hecerrhe./vol.m3err(1:5); %[Atoms/m^3]
appm.Heche = (flux.Hecm3he./6E28).*1E6;
appm.Hecerrhe = (flux.Hecerrm3he./6E28).*1E6;

flux.Hcm3he = flux.Hche./abl_vol.m3(1:5);
flux.Hcerrm3he = flux.Hcerrhe./vol.m3err(1:5);
appm.Hche = (flux.Hcm3he./6E28).*1E6;
appm.Hcerrhe = (flux.Hcerrm3he./6E28).*1E6;
```

```
save('75eV_final_libs.mat','appm');
```

Appendix B

75 eV and 250 eV LAMS Analysis Matlab script

This appendix contains the Matlab script that outlines data input from Quadera (Quadrupole data acquisition), data organization and structure depending on number of ablations, the full calibration of LAMS signal from amps to atoms/s (see Chapter 4), the volume correction due to width expansion based on the number of ablations, and finally the conversion from He[D]/m^3 to He concentration in appm. The Matlab script is the same routine used for the flattop analysis.

```
%%%%%%%%%%%%%%%%%%%%%%%%%%%%%%%%%%%%%%%%%%%%%%%%%%%%%%%%%%%%%%%%%%%%%%%%%%%%
% %MUST BE FOMARTED ACCORDING TO YOUR LAB BOOK- THIS IS USER DEPENDENT
%%%%%%%%%%%%%%%%USER IMPUT!!%%%%%%%%%%%%%%%%%%%%%%%%%%%%%%%%%%%%%%%%%%%%%%%%
%%%%%%%%%%%%%%%%%%%%%%%%%%%%%%%%%%%%%%%%%%%%%%%%%%%%%%%%%%%%%%%%%%%%%%%%%%%%
% %Si-He data from lab book!!!!!!!!!!!!!!!!!!!!!!!!
%%%%%%%%%%%%%%%%%%%%%%%%%%%%%%%%%%%%%%%%%%%%%%%%%%%%%%%%%%%%%%%%%%%%%%%%%%%%
%%%%%%%%%%%%%%%%%%%%%%%%%%%%%%%%%%%%%%%%%%%%%%%%%%%%%%%%%%%%%%%%%%%%%%%%%%%%
%QMS DATA FROM XUNXIANG WILL BE NAMED LAMS FROM HERE ON OUT!!!
%%%%%%%%%%%%%%%%%%%%%%%%%%%%%%%%%%%%%%%%%%%%%%%%%%%%%%%%%%%%%%%%%%%%%%%%%%%%
%LAMS
clear;
clc;
dhetb = readtable('75hed.txt'); %%reading the data in
dtb = readtable('75Donly.txt'); %%reading the data in
hetb = readtable('75_d2.txt'); %%reading the data in

load('vol_analysis.mat');
```

```
%LAMS
%Elements from the data file
% x-axis is time
dhe.H = table2array(dhetb(:,3));
dhe.He3 = table2array(dhetb(:,6));
dhe.He = table2array(dhetb(:,9));

dhe.time = table2array(dhetb(:,2)); %% The time is the same for all elements!!

dhe.W = table2array(dhetb(:,12));
dhe.C = table2array(dhetb(:,15));
dhe.N = table2array(dhetb(:,18));
dhe.H2O= table2array(dhetb(:,21));
dhe.Si = table2array(dhetb(:,24));
dhe.O = table2array(dhetb(:,27));
dhe.CO2 = table2array(dhetb(:,30));
```

```
%LAMS for D Only 250 eV
%Elements from the data file
% x-axis is time
%LAMS
%Elements from the data file
% x-axis is time
d.H = table2array(dtb(:,3));
d.He3 = table2array(dtb(:,6));
d.He = table2array(dtb(:,9));

d.time = table2array(dtb(:,2)); %% The time is the same for all elements!!

d.W = table2array(dtb(:,12));
d.C = table2array(dtb(:,15));
```

```
d.N = table2array(dtb(:,18));
d.H2O= table2array(dtb(:,21));
d.Si = table2array(dtb(:,24));
d.O = table2array(dtb(:,27));
d.CO2 = table2array(dtb(:,30));
```

```
he.H = table2array(hetb(:,3));
he.He3 = table2array(hetb(:,6));
he.He = table2array(hetb(:,9));

he.time = table2array(hetb(:,2)); %% The time is the same for all elements!!

he.W = table2array(hetb(:,12));
he.C = table2array(hetb(:,15));
he.N = table2array(hetb(:,18));
he.H2O= table2array(hetb(:,21));
he.Si = table2array(hetb(:,24));
he.O = table2array(hetb(:,27));
he.CO2 = table2array(hetb(:,30));
```

```
dhe.lams(:,1) = [dhe.He(1200:2760);dhe.He(3000:3450);dhe.He(3600:5070);...
    dhe.He(5200:5630);dhe.He(5730:6148)];
dhe.lams(:,2) = [dhe.H(1200:2760);dhe.H(3000:3450);dhe.H(3600:5070);...
    dhe.H(5200:5630);dhe.H(5730:6148)];
dhe.lams(:,3) = [dhe.He3(1200:2760);dhe.He3(3000:3450);dhe.He3(3600:5070);...
    dhe.He3(5200:5630);dhe.He3(5730:6148)];
dhe.lams(:,4) = [dhe.W(1200:2760);dhe.W(3000:3450);dhe.W(3600:5070);...
    dhe.W(5200:5630);dhe.W(5730:6148)];
dhe.lams(:,5) = [dhe.C(1200:2760);dhe.C(3000:3450);dhe.C(3600:5070);...
    dhe.C(5200:5630);dhe.C(5730:6148)];

dhe.x_lams(:,1) = [dhe.time(1200:2760,1);dhe.time(3000:3450,1);...
    dhe.time(3600:5070,1);dhe.time(5200:5630,1);dhe.time(5730:6148,1)];

[dhe.lams_pks,dhe.lams_locs] = findpeaks(dhe.lams(:,5),'MinPeakHeight',2.2e-11);
dhe.lblams = dhe.lams_locs-10;
dhe.rblams = dhe.lams_locs+10;

dhe.bgsig = mean(dhe.lams(1000:1200,:));
dhe.lams_bgsub = dhe.lams-dhe.bgsig;

for ii = 1:5
dhe.lams_bgsub(dhe.lams_bgsub<=0) = dhe.bgsig(1,ii);
end
```

```
d.lams(:,1) =  [d.He(2000:3800);d.He(4250:4650);d.He(4800:6450);...
    d.He(6800:7400);d.He(7750:8600);d.He(9000:9700);d.He(9850:10325);...
    d.He(10700:11115)];
```

```
d.lams(:,2) =  [d.H(2000:3800);d.H(4250:4650);d.H(4800:6450);d.H(6800:7400);...
    d.H(7750:8600);d.H(9000:9700);d.H(9850:10325);d.H(10700:11115)];
d.lams(:,3) =  [d.He3(2000:3800);d.He3(4250:4650);d.He3(4800:6450);...
    d.He3(6800:7400);d.He3(7750:8600);d.He3(9000:9700);d.He3(9850:10325);...
    d.He3(10700:11115)];
d.lams(:,4) =  [d.W(2000:3800);d.W(4250:4650);d.W(4800:6450);d.W(6800:7400);...
    d.W(7750:8600);d.W(9000:9700);d.W(9850:10325);d.W(10700:11115)];
d.lams(:,5) =  [d.C(2000:3800);d.C(4250:4650);d.C(4800:6450);d.C(6800:7400);...
    d.C(7750:8600);d.C(9000:9700);d.C(9850:10325);d.C(10700:11115)];

d.x_lams(:,1) =  [d.time(2000:3800);d.time(4250:4650);...
    d.time(4800:6450);d.time(6800:7400);d.time(7750:8600);...
    d.time(9000:9700);d.time(9850:10325);d.time(10700:11115)];

[d.lams_pks,d.lams_locs] = findpeaks(d.lams(:,5),'MinPeakHeight',6E-12);
d.lblams = d.lams_locs-10;
d.rblams = d.lams_locs+10;

d.bgsig = mean(d.lams(3700:4100,:));
d.lams_bgsub = d.lams-d.bgsig;

for ii = 1:5
d.lams_bgsub(d.lams_bgsub<=0) = d.bgsig(1,ii);
end
```

```
he.lams(:,1) = [he.He(300:3600);he.He(3720:end)];
he.lams(:,2) = [he.H(300:3600);he.H(3720:end)];
he.lams(:,3) = [he.He3(300:3600);he.He3(3720:end)];
he.lams(:,4) = [he.W(300:3600);he.W(3720:end)];
he.lams(:,5) = [he.C(300:3600);he.C(3720:end)];

he.x_lams(:,1) = [he.time(300:3600);he.time(3720:end)];

[he.lams_pks,he.lams_locs] = findpeaks(he.lams(:,5),'MinPeakHeight',3.16*10^-11);
he.lblams = he.lams_locs-10;
he.rblams = he.lams_locs+10;

he.bgsig = mean(he.lams(2500:3000,:));
he.lams_bgsub = he.lams-he.bgsig;

for ii = 1:5
he.lams_bgsub(he.lams_bgsub<=0) = he.bgsig(1,ii);
end
```

```
for ii = 1:length(dhe.lams(1,:))
    for jj = 1:length(dhe.lblams)
        dhe.int_lams(jj,ii) = ...
            trapz(dhe.x_lams(dhe.lblams(jj,1):dhe.rblams(jj,1),1),...
            dhe.lams_bgsub(dhe.lblams(jj,1):dhe.rblams(jj,1),ii));
    end
```

```
end

dhe.flux_lams_He(:,1) = dhe.int_lams(:,1).*(0.0998*6.022E23);
dhe.flux_lams_H(:,1) = dhe.int_lams(:,2).*(0.2254*6.022E23);
```

```
for ii = 1:length(d.lams(1,:))
    for jj = 1:length(d.lblams)
        d.int_lams(jj,ii) = trapz(d.x_lams(d.lblams(jj,1):d.rblams(jj,1),1),...
            d.lams_bgsub(d.lblams(jj,1):d.rblams(jj,1),ii));
    end
end

d.flux_lams_He(:,1) = d.int_lams(115:304,1).*(0.0998*6.022E23);
d.flux_lams_H(:,1) = d.int_lams(115:304,2).*(0.2254*6.022E23);
```

```
for ii = 1:length(he.lams(1,:))
    for jj = 1:260
        he.int_lams(jj,ii) = trapz(he.x_lams(he.lblams(jj,1):he.rblams(jj,1),1),...
            he.lams_bgsub(he.lblams(jj,1):he.rblams(jj,1),ii));
    end
end

he.flux_lams_He(:,1) = he.int_lams(:,1).*(0.0998*6.022E23);
he.flux_lams_H(:,1) = he.int_lams(:,2).*(0.2254*6.022E23);
```

```
clear coolhe;
clear coolh;
count = 0;
count2 = 0;
numb  = 5;

dhe.flux_lamsHe5 = zeros(numb,(length(dhe.flux_lams_He(:,1)))/numb);
dhe.flux_lamsH5 = zeros(numb,(length(dhe.flux_lams_H(:,1)))/numb);
for ii= 1:length(dhe.flux_lams_He(:,1))
    count = count+1;
    coolhe(count,:) = dhe.flux_lams_He(ii,:);
    coolh(count,:) = dhe.flux_lams_H(ii,:);
    if count/numb==1
        count2 = count2+1;
        dhe.flux_lamsHe5(:,count2) = coolhe;
        dhe.flux_lamsH5(:,count2) = coolh;
        count =0;
    end
end
```

```
clear coolhe;
clear coolh;
```

```
count = 0;
count2 = 0;
numb  = 5;

d.flux_lamsHe5 = zeros(numb,(length(d.flux_lams_He(:,1)))/numb);
d.flux_lamsH5 = zeros(numb,(length(d.flux_lams_H(:,1)))/numb);
for ii= 1:length(d.flux_lams_He(:,1))
    count = count+1;
    coolhe(count,:) = d.flux_lams_He(ii,:);
    coolh(count,:) = d.flux_lams_H(ii,:);
    if count/numb==1
        count2 = count2+1;
        d.flux_lamsHe5(:,count2) = coolhe;
        d.flux_lamsH5(:,count2) = coolh;
        count =0;
    end
end
```

```
clear coolhe;
clear coolh;
count = 0;
count2 = 0;
numb  = 5;

he.flux_lamsHe5 = zeros(numb,(length(he.flux_lams_He(:,1)))/numb);
he.flux_lamsH5 = zeros(numb,(length(he.flux_lams_H(:,1)))/numb);
for ii= 1:length(he.flux_lams_He(:,1))
    count = count+1;
    coolhe(count,:) = he.flux_lams_He(ii,:);
    coolh(count,:) = he.flux_lams_H(ii,:);
    if count/numb==1
        count2 = count2+1;
        he.flux_lamsHe5(:,count2) = coolhe;
        he.flux_lamsH5(:,count2) = coolh;
        count =0;
    end
end
```

```
for jj = 1:5
    dhe.avgfluxlamsHe(jj,1) = mean(dhe.flux_lamsHe5(jj,1:10))./1e3;
    dhe.avgfluxlamsHe(jj,2) = mean(dhe.flux_lamsHe5(jj,11:20))./1e3;
    dhe.avgfluxlamsHe(jj,3) = mean(dhe.flux_lamsHe5(jj,21:30))./1e3;
    dhe.avgfluxlamsHe(jj,4) = mean(dhe.flux_lamsHe5(jj,31:40))./1e3;
    dhe.avgfluxlamsHe(jj,5) = mean(dhe.flux_lamsHe5(jj,41:45))./1e3;

    dhe.avgfluxlamsHe_err(jj,1) = std(dhe.flux_lamsHe5(jj,1:10))./1e4;
    dhe.avgfluxlamsHe_err(jj,2) = std(dhe.flux_lamsHe5(jj,11:20))./1e4;
    dhe.avgfluxlamsHe_err(jj,3) = std(dhe.flux_lamsHe5(jj,21:30))./1e4;
    dhe.avgfluxlamsHe_err(jj,4) = std(dhe.flux_lamsHe5(jj,31:40))./1e4;
    dhe.avgfluxlamsHe_err(jj,5) = std(dhe.flux_lamsHe5(jj,41:45))./1e4;
```

```
end


for jj = 1:5
   dhe.avgfluxlamsH(jj,1) = mean(dhe.flux_lamsH5(jj,1:10))./1e5;
    dhe.avgfluxlamsH(jj,2) = mean(dhe.flux_lamsH5(jj,11:20))./1e5;
    dhe.avgfluxlamsH(jj,3) = mean(dhe.flux_lamsH5(jj,21:30))./1e5;
    dhe.avgfluxlamsH(jj,4) = mean(dhe.flux_lamsH5(jj,31:40))./1e5;
    dhe.avgfluxlamsH(jj,5) = mean(dhe.flux_lamsH5(jj,41:45))./1e5;

    dhe.avgfluxlamsH_err(jj,1) = std(dhe.flux_lamsH5(jj,1:10))./1e6;
    dhe.avgfluxlamsH_err(jj,2) = std(dhe.flux_lamsH5(jj,11:20))./1e6;
    dhe.avgfluxlamsH_err(jj,3) = std(dhe.flux_lamsH5(jj,21:30))./1e6;
    dhe.avgfluxlamsH_err(jj,4) = std(dhe.flux_lamsH5(jj,31:40))./1e6;
    dhe.avgfluxlamsH_err(jj,5) = std(dhe.flux_lamsH5(jj,41:45))./1e6;
end


% for jj = 1:numb
%     dhe.avgfluxlamsHe(jj,:) = mean(he.flux_lamsHe5(jj,:))./1e3;
%     dhe.avgfluxlamsH(jj,:) = mean(dhe.flux_lamsH5(jj,:))./1e5;
%     dhe.avgfluxlamsHe_err(jj,:) = std(he.flux_lamsHe5(jj,:))./1e4;
%     dhe.avgfluxlamsH_err(jj,:) = std(dhe.flux_lamsH5(jj,:))./1e6;
% end
% dhe.avgfluxlamsH(1,1) = 1.255*1e9;
% dhe.avgfluxlamsH(4:end,1) = dhe.avgfluxlamsH(4:end,1)./2.1;
```

```
for jj = 1:5
    d.avgfluxlamsHe(jj,1) = mean(d.flux_lamsHe5(jj,1:10))./1e3;
    d.avgfluxlamsHe(jj,2) = mean(d.flux_lamsHe5(jj,11:20))./1e3;
    d.avgfluxlamsHe(jj,3) = mean(d.flux_lamsHe5(jj,21:30))./1e3;
    d.avgfluxlamsHe(jj,4) = mean(d.flux_lamsHe5(jj,31:38))./1e3;


    d.avgfluxlamsHe_err(jj,1) = std(d.flux_lamsHe5(jj,1:10))./1e4;
    d.avgfluxlamsHe_err(jj,2) = std(d.flux_lamsHe5(jj,11:20))./1e4;
    d.avgfluxlamsHe_err(jj,3) = std(d.flux_lamsHe5(jj,21:30))./1e4;
    d.avgfluxlamsHe_err(jj,4) = std(d.flux_lamsHe5(jj,31:38))./1e4;

end


for jj = 1:5
   d.avgfluxlamsH(jj,1) = mean(d.flux_lamsH5(jj,1:10))./1e5;
    d.avgfluxlamsH(jj,2) = mean(d.flux_lamsH5(jj,11:20))./1e5;
    d.avgfluxlamsH(jj,3) = mean(d.flux_lamsH5(jj,21:30))./1e5;
    d.avgfluxlamsH(jj,4) = mean(d.flux_lamsH5(jj,31:38))./1e5;


    d.avgfluxlamsH_err(jj,1) = std(d.flux_lamsH5(jj,1:10))/1e6;
    d.avgfluxlamsH_err(jj,2) = std(d.flux_lamsH5(jj,11:20))/1e6;
    d.avgfluxlamsH_err(jj,3) = std(d.flux_lamsH5(jj,21:30))/1e6;
```

```
    d.avgfluxlamsH_err(jj,4) = std(d.flux_lamsH5(jj,31:38))/1e6;

end

% for jj = 1:numb
%     d.avgfluxlamsHe(jj,:) = mean(d.flux_lamsHe5(jj,:))./1e3;
%     d.avgfluxlamsH(jj,:) = mean(dhe.flux_lamsH5(jj,:))./5e4;
%     d.avgfluxlamsHe_err(jj,:) = std(d.flux_lamsHe5(jj,:))./1e4;
%     d.avgfluxlamsH_err(jj,:) = std(dhe.flux_lamsH5(jj,:))./5e5;
% end
% d.avgfluxlamsH(1,1) = 5.8746*1E8;
% d.avgfluxlamsH(2,1) = 2.4137*1E9;
% d.avgfluxlamsH(5,1) = 4.6641*1E9;
```

```
for jj = 1:5
    he.avgfluxlamsHe(jj,1) = mean(he.flux_lamsHe5(jj,11))./1e3;
    he.avgfluxlamsHe(jj,2) = mean(he.flux_lamsHe5(jj,14:23))./1e3;
    he.avgfluxlamsHe(jj,3) = mean(he.flux_lamsHe5(jj,24:33))./1e3;
    he.avgfluxlamsHe(jj,4) = mean(he.flux_lamsHe5(jj,34:43))./1e3;
    he.avgfluxlamsHe(jj,5) = mean(he.flux_lamsHe5(jj,44:52))./1e3;

    he.avgfluxlamsHe_err(jj,1) = std(he.flux_lamsHe5(jj,11))./1e4;
    he.avgfluxlamsHe_err(jj,2) = std(he.flux_lamsHe5(jj,14:23))./1e4;
    he.avgfluxlamsHe_err(jj,3) = std(he.flux_lamsHe5(jj,24:33))./1e4;
    he.avgfluxlamsHe_err(jj,4) = std(he.flux_lamsHe5(jj,34:43))./1e4;
    he.avgfluxlamsHe_err(jj,5) = std(he.flux_lamsHe5(jj,44:52))./1e4;
end


for jj = 1:5
    he.avgfluxlamsH(jj,1) = mean(he.flux_lamsH5(jj,11))./1e5;
    he.avgfluxlamsH(jj,2) = mean(he.flux_lamsH5(jj,14:23))./1e5;
    he.avgfluxlamsH(jj,3) = mean(he.flux_lamsH5(jj,24:33))./1e5;
    he.avgfluxlamsH(jj,4) = mean(he.flux_lamsH5(jj,34:43))./1e5;
    he.avgfluxlamsH(jj,5) = mean(he.flux_lamsH5(jj,44:52))./1e5;

    he.avgfluxlamsH_err(jj,1) = std(he.flux_lamsH5(jj,11))./1e6;
    he.avgfluxlamsH_err(jj,2) = std(he.flux_lamsH5(jj,14:23))./1e6;
    he.avgfluxlamsH_err(jj,3) = std(he.flux_lamsH5(jj,24:33))./1e6;
    he.avgfluxlamsH_err(jj,4) = std(he.flux_lamsH5(jj,34:43))./1e6;
    he.avgfluxlamsH_err(jj,5) = std(he.flux_lamsH5(jj,44:52))./1e6;
end
```

```
abl_vol.m3 = abl_vol.cylp.*1e-18;
vol.m3 = vol.cylp.*1e-18;
vol.m3err = vol.cylp_err.*1e-18;
```

```
for ii = 1:5
```

```
Atom.Heucdhe(ii,:) = dhe.avgfluxlamsHe(ii,:)./abl_vol.m3(ii,:);
Atom.Heucerrdhe(ii,:) = dhe.avgfluxlamsHe_err(ii,:)./vol.m3err(ii,:);
Atom.Hucdhe(ii,:) = dhe.avgfluxlamsH(ii,:)./abl_vol.m3(ii,:);
Atom.Hucerrdhe(ii,:) = dhe.avgfluxlamsH_err(ii,:)./vol.m3err(ii,:);
appm.Heucdhe(ii,:) = (Atom.Heucdhe(ii,:)./6.32E28).*1E6;
appm.Heucerrdhe(ii,:) = (Atom.Heucerrdhe(ii,:)./6.32E28).*1E6;
appm.Hucdhe(ii,:) = (Atom.Hucdhe(ii,:)./6.32E28).*1E6;
appm.Hucerrdhe(ii,:) = (Atom.Hucerrdhe(ii,:)./6.32E28).*1E6;
end
```

```
for ii = 1:5
Atom.Heucd(ii,:) =d.avgfluxlamsHe(ii,:)./abl_vol.m3(ii,:);
Atom.Heucerrd(ii,:) =d.avgfluxlamsHe_err(ii,:)./vol.m3err(ii,:);
Atom.Hucd(ii,:) =d.avgfluxlamsH(ii,:)./abl_vol.m3(ii,:);
Atom.Hucerrd(ii,:) =d.avgfluxlamsH_err(ii,:)./vol.m3err(ii,:);
appm.Heucd(ii,:) =(Atom.Heucd(ii,:)./6.32E28).*1E6;
appm.Heucerrd(ii,:) =(Atom.Heucerrd(ii,:)./6.32E28).*1E6;
appm.Hucd(ii,:) =(Atom.Hucd(ii,:)./6.32E28).*1E6;
appm.Hucerrd(ii,:) =(Atom.Hucerrd(ii,:)./6.32E28).*1E6;
end
```

```
for ii = 1:5
Atom.Heuche(ii,:) = he.avgfluxlamsHe(ii,:)./abl_vol.m3(ii,:);
Atom.Heucerrhe(ii,:) = he.avgfluxlamsHe_err(ii,:)./vol.m3err(ii,:);
Atom.Huche(ii,:) = he.avgfluxlamsH(ii,:)./abl_vol.m3(ii,:);
Atom.Hucerrhe(ii,:) = he.avgfluxlamsH_err(ii,:)./vol.m3err(ii,:);
appm.Heuche(ii,:) = (Atom.Heuche(ii,:)./6.32E28).*1E6;
appm.Heucerrhe(ii,:) = (Atom.Heucerrhe(ii,:)./6.32E28).*1E6;
appm.Huche(ii,:) = (Atom.Huche(ii,:)./6.32E28).*1E6;
appm.Hucerrhe(ii,:) = (Atom.Hucerrhe(ii,:)./6.32E28).*1E6;
end
```

```
new_ablations = linspace(1,5,5);
vnm = ones(length(new_ablations),length(new_ablations)).*(1:length(new_ablations));
vnm = triu(vnm,1);
vnm(1,1) = 1;
vnm(:,1) = vnm(1,:);
for ii = 1:5
    for jj = 1:5
        for kk = 1:5
        if vnm(ii,jj) > 0
            sig.Hedhe(ii,jj,kk) =  dhe.avgfluxlamsHe(vnm(ii,jj),kk);
            sig.Heerrdhe(ii,jj,kk) =  dhe.avgfluxlamsHe_err(vnm(ii,jj),kk);
            sig.Hdhe(ii,jj,kk) =  dhe.avgfluxlamsH(vnm(ii,jj),kk);
            sig.Herrdhe(ii,jj,kk) =  dhe.avgfluxlamsH_err(vnm(ii,jj),kk);
        elseif vnm(ii,jj) == 0
            sig.Hedhe(ii,jj,kk) =  0;
            sig.Heerrdhe(ii,jj,kk) =  0;
            sig.Hdhe(ii,jj,kk) =  0;
```

```
            sig.Herrdhe(ii,jj,kk) =  0;
        end
        end
    end
end
```

```
for ii = 1:5
    for jj = 1:5
        for kk = 1:4
        if vnm(ii,jj) > 0
            sig.Hed(ii,jj,kk) = d.avgfluxlamsHe(vnm(ii,jj),kk);
            sig.Heerrd(ii,jj,kk) = d.avgfluxlamsHe_err(vnm(ii,jj),kk);
            sig.Hd(ii,jj,kk) = d.avgfluxlamsH(vnm(ii,jj),kk);
            sig.Herrd(ii,jj,kk) = d.avgfluxlamsH_err(vnm(ii,jj),kk);
        elseif vnm(ii,jj) == 0
            sig.Hed(ii,jj,kk) = 0;
            sig.Heerrd(ii,jj,kk) = 0;
            sig.Hd(ii,jj,kk) = 0;
            sig.Herrd(ii,jj,kk) = 0;
        end
        end
    end
end
```

```
for ii = 1:5
    for jj = 1:5
        for kk = 1:5
        if vnm(ii,jj) > 0
            sig.Hehe(ii,jj,kk) =  he.avgfluxlamsHe(vnm(ii,jj),kk);
            sig.Heerrhe(ii,jj,kk) =  he.avgfluxlamsHe_err(vnm(ii,jj),kk);
            sig.Hhe(ii,jj,kk) =  he.avgfluxlamsH(vnm(ii,jj),kk);
            sig.Herrhe(ii,jj,kk) =  he.avgfluxlamsH_err(vnm(ii,jj),kk);
        elseif vnm(ii,jj) == 0
            sig.Hehe(ii,jj,kk) =  0;
            sig.Heerrhe(ii,jj,kk) =  0;
            sig.Hhe(ii,jj,kk) =  0;
            sig.Herrhe(ii,jj,kk) =  0;
        end
        end
    end
end
```

```
for ii = 1:5
    for jj = 1:5
        for kk = 1:5
        if vnm(ii,jj) > 0
            flux.Hematdhe(ii,jj,kk) = sig.Hedhe(ii,jj,kk)*frac_vol.cylp(ii,jj);
            flux.Heerrmatdhe(ii,jj,kk) = sqrt((sig.Heerrdhe(ii,jj,kk).^2)*...
                (frac_vol.cylp(ii,jj).^2));
```

```
            flux.Hmatdhe(ii,jj,kk) = sig.Hdhe(ii,jj,kk)*frac_vol.cylp(ii,jj);
            flux.Herrmatdhe(ii,jj,kk) = sqrt((sig.Herrdhe(ii,jj,kk).^2)*...
                (frac_vol.cylp(ii,jj).^2));
        elseif vnm(ii,jj) == 0
            flux.Hematdhe(ii,jj,kk) = 0;
            flux.Heerrmatdhe(ii,jj,kk) = 0;
            flux.Hmatdhe(ii,jj,kk) = 0;
            flux.Herrmatdhe(ii,jj,kk) = 0;
        end
        end
    end
end
```

```
for ii = 1:5
    for jj = 1:5
        for kk = 1:4
        if vnm(ii,jj) > 0
            flux.Hematd(ii,jj,kk) = sig.Hed(ii,jj,kk)*frac_vol.cylp(ii,jj);
            flux.Heerrmatd(ii,jj,kk) = sqrt((sig.Heerrd(ii,jj,kk).^2)*...
                (frac_vol.cylp(ii,jj).^2));
            flux.Hmatd(ii,jj,kk) = sig.Hd(ii,jj,kk)*frac_vol.cylp(ii,jj);
            flux.Herrmatd(ii,jj,kk) = sqrt((sig.Herrd(ii,jj,kk).^2)*...
                (frac_vol.cylp(ii,jj).^2));
        elseif vnm(ii,jj) == 0
            flux.Hematd(ii,jj,kk) = 0;
            flux.Heerrmatd(ii,jj,kk) = 0;
            flux.Hmatd(ii,jj,kk) = 0;
            flux.Herrmatd(ii,jj,kk) = 0;
        end
        end
    end
end
```

```
for ii = 1:5
    for jj = 1:5
        for kk = 1:5
        if vnm(ii,jj) > 0
            flux.Hemathe(ii,jj,kk) = sig.Hehe(ii,jj,kk)*frac_vol.cylp(ii,jj);
            flux.Heerrmathe(ii,jj,kk) = sqrt((sig.Heerrhe(ii,jj,kk).^2)*...
                (frac_vol.cylp(ii,jj).^2));
            flux.Hmathe(ii,jj,kk) = sig.Hhe(ii,jj,kk)*frac_vol.cylp(ii,jj);
            flux.Herrmathe(ii,jj,kk) = sqrt((sig.Herrhe(ii,jj,kk).^2)*...
                (frac_vol.cylp(ii,jj).^2));
        elseif vnm(ii,jj) == 0
            flux.Hemathe(ii,jj,kk) = 0;
            flux.Heerrmathe(ii,jj,kk) = 0;
            flux.Hmathe(ii,jj,kk) = 0;
            flux.Herrmathe(ii,jj,kk) = 0;
        end
        end
```

```
    end
end
```

```
for ii =1:5
    for jj = 1:5
    flux.Hecdhe(ii,jj) = sum(flux.Hematdhe(ii,:,jj));
    flux.Hecerrdhe(ii,jj) = sum(flux.Heerrmatdhe(ii,:,jj));
    flux.Hcdhe(ii,jj) = sum(flux.Hmatdhe(ii,:,jj));
    flux.Hcerrdhe(ii,jj) = sum(flux.Herrmatdhe(ii,:,jj));
    end
end

for ii = 1:5
flux.Hecm3dhe(ii,:) = flux.Hecdhe(ii,:)./abl_vol.m3(ii,:); %[Atoms/m^3]
flux.Hecerrm3dhe(ii,:) = flux.Hecerrdhe(ii,:)./vol.m3err(ii,:); %[Atoms/m^3]
appm.Hecdhe(ii,:) = (flux.Hecm3dhe(ii,:)./6E28).*1E6;
appm.Hecerrdhe(ii,:) = (flux.Hecerrm3dhe(ii,:)./6E28).*1E6;

flux.Hcm3dhe(ii,:) = flux.Hcdhe(ii,:)./abl_vol.m3(ii,:);
flux.Hcerrm3dhe(ii,:) = flux.Hcerrdhe(ii,:)./vol.m3err(ii,:);
appm.Hcdhe(ii,:) = (flux.Hcm3dhe(ii,:)./6E28).*1E6;
appm.Hcerrdhe(ii,:) = (flux.Hcerrm3dhe(ii,:)./6E28).*1E6;
end
```

```
for ii =1:5
    for jj = 1:4
    flux.Hecd(ii,jj) = sum(flux.Hematd(ii,:,jj));
    flux.Hecerrd(ii,jj) = sum(flux.Heerrmatd(ii,:,jj));
    flux.Hcd(ii,jj) = sum(flux.Hmatd(ii,:,jj));
    flux.Hcerrd(ii,jj) = sum(flux.Herrmatd(ii,:,jj));
    end
end

for ii = 1:5
flux.Hecm3d(ii,:) = flux.Hecd(ii,:)./abl_vol.m3(ii,:); %[Atoms/m^3]
flux.Hecerrm3d(ii,:) = flux.Hecerrd(ii,:)./vol.m3err(ii,:); %[Atoms/m^3]
appm.Hecd(ii,:) = (flux.Hecm3d(ii,:)./6E28).*1E6;
appm.Hecerrd(ii,:) = (flux.Hecerrm3d(ii,:)./6E28).*1E6;

flux.Hcm3d(ii,:) = flux.Hcd(ii,:)./abl_vol.m3(ii,:);
flux.Hcerrm3d(ii,:) = flux.Hcerrd(ii,:)./vol.m3err(ii,:);
appm.Hcd(ii,:) = (flux.Hcm3d(ii,:)./6E28).*1E6;
appm.Hcerrd(ii,:) = (flux.Hcerrm3d(ii,:)./6E28).*1E6;
end
```

```
for ii =1:5
    for jj = 1:5
    flux.Heche(ii,jj) = sum(flux.Hemathe(ii,:,jj));
    flux.Hecerrhe(ii,jj) = sum(flux.Heerrmathe(ii,:,jj));
```

```
    flux.Hche(ii,jj) = sum(flux.Hmathe(ii,:,jj));
    flux.Hcerrhe(ii,jj) = sum(flux.Herrmathe(ii,:,jj));
    end
end

for ii = 1:5
flux.Hecm3he(ii,:) = flux.Heche(ii,:)./abl_vol.m3(ii,:); %[Atoms/m^3]
flux.Hecerrm3he(ii,:) = flux.Hecerrhe(ii,:)./vol.m3err(ii,:); %[Atoms/m^3]
appm.Heche(ii,:) = (flux.Hecm3he(ii,:)./6E28).*1E6;
appm.Hecerrhe(ii,:) = (flux.Hecerrm3he(ii,:)./6E28).*1E6;

flux.Hcm3he(ii,:) = flux.Hche(ii,:)./abl_vol.m3(ii,:);
flux.Hcerrm3he(ii,:) = flux.Hcerrhe(ii,:)./vol.m3err(ii,:);
appm.Hche(ii,:) = (flux.Hcm3he(ii,:)./6E28).*1E6;
appm.Hcerrhe(ii,:) = (flux.Hcerrm3he(ii,:)./6E28).*1E6;
end
```

```
appm_LAMS = appm;
save('HED75_final_lams.mat','appm_LAMS')
```

Appendix C

Initial Results and Analysis Demonstrating Ability of LIBS to measure He depth dependence below W surfaces in ambient conditions

This Appendix contains the results from an initial proof-of-principle experiment performed using laser induced breakdown spectroscopy to measure the depth dependent helium content below tungsten surfaces. Although this work was performed under ambient conditions, it served as the proof-of-principle for developing the (ultra?) high vacuum LIBS system, the calibration procedure and coupling to LAMS, for quantifying the gas concentration below tungsten surfaces. The text and figures within this appendix were previously published in the journal Applied Surface Science. Shaw, G., Bannister, M., Biewer, T. M., Martin, M. Z., Meyer, F., and Wirth, B. D. (2018). The detection of He in tungsten following ion implantation by laser-induced breakdown spectroscopy. Applied Surface Science, 427, 695-703.

The research described in the article motivate all the work presented in the dissertation. Even though the LIBS demonstration was performed using a different experimental setup and not in UHV, it still qualitatively measured He as a function of depth in W. The continued research mentioned in this article was performed in this dissertation.

Abstract

Laser-induced breakdown spectroscopy (LIBS) results are presented that provide depth-resolved identification of He implanted in polycrystalline tungsten (PC-W) targets by a 200 keV He+ ion beam, with a surface temperature of approximately 900^{o}C and a peak fluence of 10^{23} m^{-2}. He retention, and the influence of He on deuterium and tritium recycling, permeation, and retention in PC-W plasma facing components are important questions for the divertor and plasma facing components in a fusion reactor, yet are difficult to quantify. The purpose of this work is to demonstrate the ability of LIBS to identify helium in tungsten; to investigate the sensitivity of laser parameters including, laser energy and gate delay, that directly influence the sensitivity and depth resolution of LIBS; and to perform a proof-of-principle experiment using LIBS to measure relative He intensities as a function of depth. The results presented demonstrate the potential not only to identify helium but also to develop a methodology to quantify gaseous impurity concentration in PC-W as a function of depth.

Keywords: Laser Induced Breakdown Spectroscopy; Plasma Material Interactions; Plasma Facing Components; Helium Retention in Tungsten

Introduction

ITER, the international tokamak experimental reactor, has selected tungsten (W) as the divertor due to its high melting point, low sputtering yield, and high thermal conductivity [1, 2]. The plasma conditions in the divertor, include helium (He), deuterium (D), and tritium (T) at energies ranging from 10 to 1000 eV, will induce surface and bulk modification in the plasma facing components. The PFC surface response to the plasma can include erosion, blistering and dust formation, as well as impact the recycling, retention, and permeation of the tritium fuel. The motivation for conducting these experiments is to investigate fuel retention, and more precisely, the development of new technique(s) to quantify gas retention as a function of depth, which is important because it demonstrates the total fuel retention, and provides experimental data necessary for the validation of computational models [3].

Multiple studies in the literature demonstrate the effects of He exposure on hydrogen isotope, or specifically deuterium (D), retention in PC-W [4-6]. Miyamoto et al. [7] found that the D retention with He exposure is 10% less than for samples exposed only to D plasma. They performed their experiment with simultaneous DâĂŞHe plasma exposures with 1âĂŞ20% He+ at ∼573 K and 55 eV/ion. They observed that bubbles, presumably containing He, were formed deeper than the expected He ion range, which suggests that D retention decreases when the depth of the implanted D is less than the depth of the He bubbles. Baldwin et al. [8] showed that bubble formation decreased D permeation and hypothesized that the bubbles provide interconnected pathways from the bulk to the surface, which, in turn, reduces D retention. Their experiment involved PC-W targets at a fixed temperature ranging from ∼420-1100 K that were exposed either to a D only plasma, or mixed D plasmas containing either He or argon or a D plasma following pre-exposure with a He plasma. After He-D exposure, with implanted He fluences that were greater than that of D, the D retention decreased by 2% when compared to a D-only case. Baldwin and Doerner

used Nuclear Reaction Analysis (NRA) to show that D was trapped in the same area that the He bubbles were located, which suggested that the decrease in D retention is related the bubbles locally trapping D and limiting permeation [3-8]. Ueda et al. [9] found that the He and D ion stopping ranges influenced the extent to which He can block D diffusion into the bulk. In their study, experiments were performed at ∼473 K with 1âĂŞ1.5 keV of D only and 0.6-1.5 keV mixed He+ and D. When the implantation depth of the He was similar to that of D, the D retention decreased when compared to D-only irradiation and blistering was suppressed. However, when the He ion range was significantly less than the H ion range, there was no decrease in D retention or blistering.

Conventional surface characterization techniques like Elastic Recoil Detection (ERD), Nuclear Reaction Analysis (NRA), Thermal Desorption Spectroscopy (TDS), and Secondary Ion Mass Spectroscopy (SIMS) are used to quantify fuel retention in the near surface regions of fusion materials [9-13]. ERD uses an energy depth relationship to determine elemental depth profiles. However, when using ERD to detect the concentration of low-Z materials as a function of depth in high-Z matrices, the resolution is directly influenced by irradiation damage, background level, and the number of counts detected [14]. NRA uses ions, such as nitrogen or 3He, with energies greater than about 30 MeV to probe species of interest (usually through ion, alpha reactions) and measures the number and energy distribution of alpha particles, which can provide the concentration and depth of the species of interest respectively. While NRA is ideal for determining the magnitude of the retained gas, it is not optimal for determining concentrations as a function of implantation depth [14]. TDS heats a sample with a fixed temperature rate increase in an ultra-high vacuum and measures the resulting desorbed species in a mass spectrometer (often a high-resolution quadrupole mass spectrometer). However, in the case of detecting desorbed He, TDS is often unable to completely desorb He once it has formed large bubbles due to the lack of thermal desorption of the insoluble He from a large bubble. SIMS is a technique suitable for examining impurity (He and D) behavior in the near surface regions at high sensitivity (several ppm) and depth resolution (several nm) [15]. However, SIMS is not quantitative [16]. These surface characterization techniques are commonly used to investigate fusion material. However, the need for a suitable diagnostic technique that can perform depth profiling analysis of the near surface layers without extensive surface preparation, which is sensitive to light elements, inexpensive, and remote, is imperative for the investigation of fusion materials.

The development of laser-based characterization techniques can complement and expand on the capability to provide a depth profile of the gas content in fusion materials. Especially those related to questions regarding He-D interactions and gas retention. Laser Induced Breakdown Spectroscopy (LIBS) offers multi-elemental and microanalysis in the near surface with high sensitivity (ppm) and depth resolution [17-20]. LIBS is a laser ablation technique commonly used to characterize a material surface and the chemistry, specifically elemental composition. During the ablation process, the breakdown and vaporization of a small volume (∼10-9 cm^3) occur, forming a plasma. In the first stage (few ns) of the plasma, the light emitted appears intense from the excitation of the material. After a few hundred nanoseconds, an intense broadband continuum of light is formed because of the bremsstrahlung process. Spectral emissions from ionized, neutral, or molecular species occur between 0.5-2 μs, 2-10 μs, and >10 Îijs, respectively after plasma formation. The most dominate contribution to emission lines are from the de-excitation of neutral atoms, and this occurs during the 2-10 μs spectral window. The characterization of the temporal behavior and relative intensity of the plasma light is termed Optical Emission Spectroscopy (OES) and contains information about the surface elemental composition.

LIBS is a well-establish analysis technique in many fields of research including fusion[21-29]. Farid et al. [25] investigated the laser-induced plasma parameters, electron temperature and density of W as a function of laser wavelength and irradiance. Temporal variance in the electron temperature and density as a function of laser wavelength and irradiance were also discussed. Piip et al. [26] and Paris et al.[27] investigated the depth profile of W coated molybdenum (Mo) samples exposed to a linear plasma source, Magnum-PSI. Piip et al. exposed four W coated Mo samples to a 60% D and 40% He plasma. The maximum heat flux at the center of the plasma was $\sim$10 MW/m2, the maximum particle flux was $\sim$1x10^{24} m^{-2}s^{-1} and the particle fluence reached $\sim$1x10^{26} m^{-2}. The W, D, and Mo intensities were shown as a function of depth; however, limitations such as a shot to shot fluctuation, were apparent. Mercadier et al. [28] performed LIBS on carbon fiber composite (CFC) containing hydrogen (H) and D. They performed a parametric study of laser fluence, pulse duration, and gas pressure and its influence on the H and D Balmer alpha spectral lines. The results showed that LIBS parameters could be optimized to investigate light elements such as H and D. In summary, there is an apparent need for the optimization of LIBS for fusion applications; parameters such as laser fluence, gate delay, pulse duration, limits of detection (LOD) for light elements (He, H, and D), and depth resolution need extensive investigation.

The purpose of this work is to demonstrate the ability of LIBS to identify helium in tungsten; to investigate the sensitivity of laser parameters including, laser energy and gate delay, that directly influence the sensitivity and depth resolution of LIBS; and to perform a proof-of-principle experiment using LIBS to measure relative He intensity as a function of depth. The initial section of the methodology discusses our approach to assessing the impact of LIBS experimental parameters, such as laser energy and gate delay, on the measured LIBS signal intensity. Section 3 presents initial results that demonstrate the ability to identify He, and its depth dependence by LIBS on a polycrystalline PC-W specimen following 200 keV He ion implantation at a temperature of $\sim$900^{o}Cto a peak fluence of 10^{23} m^{-2}. Based on these results, we discuss a procedure to perform a relative depth analysis and the dependence of the signal on laser parameters. Following an initial comparison of the measured He depth profile with the expected implantation profile, we discuss plans for additional research to compare the LIBS results to other conventional techniques.

Experiments

Specimens

The LIBS measurements were performed on sheet stock polycrystalline tungsten (PC-W), previously investigated by Meyer, Hijazi, and Parish et al. [30, 31] using multiple surface and bulk characterizations techniques, including Scanning Electron Microscopy (SEM) and X-ray Photoelectron Spectroscopy (XPS). Five PC-W specimens were cut from the sheet stock into 13 x 13 mm squares with a 0.45 mm thickness. One sample was sent to Luvak INC. to determine bulk impurity concentration by Direct Current Plasma Emission Spectroscopy (DCPES). The impurity content in the bulk W, by weight, is as follows: 0.022% Cu, 0.0002% H, <0.0005% Sulfur, 0.002% C, <0.001% N, and 0.001% O. Correspondingly, the PC-W specimen is $\sim$99.97% pure. The remaining four specimens were cleaned and polished to a dull metal finish before the He implantation.

Table C.1: A list of He exposure conditions on the four W specimens evaluated in this work. Sample 1 serves as a control sample to provide background W signal, area, and volume profiling. Samples 2-4 were exposed to identical He ion implantation and were used to determine the change in He I signal intensity as a function of laser power, gate delay, and depth into the sample. Due to signal interference and laser reflections, the samples were not polished.

He Implantation Parameters				
Specimen	**E (keV)**	**Fluence (m^2)**	**T (^oC)**	**t (mins)**
1	-	-	-	-
2	200	$1x10^{23}$	905	75
3	200	$1x10^{23}$	901	75
4	200	$1x10^{23}$	904	75

He Implantation

As shown in Table C.1, three of the four PC-W samples were exposed to a 200 keV He+ ion beam. The first specimen in Table C.1 is the control sample; it was used to determine the shot-to-shot variation and background spectra from un-exposed PC-W. Specimens two thru four were exposed to approximately identical conditions; this was done to maintain consistency across experiments. The exposures were performed at the Oak Ridge National Laboratory (ORNL) Multicharge Ion Research Facility (MIRF) [32], using a high current beam decelerator module and CAPRICE electron cyclotron resonance (ECR) ion source. The MIRF ion beam is Gaussian in shape and is produced on a single stationary beam line. The average beam size is 3-5 mm in diameter, and it was centered on the specimen. The temperature was measured using a thermocouple attached to the top left edge of the specimen. The implantations were performed using a heated stage to ensure that the samples were heated to $\sim 900^oC$ and implanted to a peak fluence of 10^{23} m^{-2} at a peak flux of $\sim 2.2x10^{19}$ He $m^{-2}s^{-1}$ and an exposure time was approximately 75 min. The software, The Stopping, and Range of Ions in Matter (SRIM) [33] were used to determine the relative implantation depth of a 200 keV He^+ ion, which was about 500 nm on average.

The implantation is performed under vacuum, following which the samples are removed and placed into a small sample case at ambient conditions. Then the specimens were transferred to the LIBS station. LIBS analysis was performed on each specimen, about 2 to 3 weeks after being implanted with He. The lapse in time between implantation and analysis was due to scheduling delays in accessing the LIBS station user facility. Oxides are expected to form on the PC-W specimen surface due to exposure to the atmosphere. However, in LIBS analysis, lines such as N, O, Na, and H were monitored, and these lines were observed to decrease after ablating away the first surface layer. Further, the position of these lines did not interfere with the He or W lines of interest.

Our choice of the helium ion energy, flux, and exposure time was based on ensuring a deep,

sufficiently concentrated layer of helium for the proof of principle experiments. It is to demonstrate LIBS detection of He in W. While the ion energy and fluence are larger than what is expected in a divertor plasma, it is important to determine if LIBS could resolve steps by ablation, into and out of the He implanted area. The higher ion energy increases the area beneath the surface, which allows an increase in the number of ablation laser pulses (measurements). The increase in the number of measurements also provided a basis to determine the limits of detection of He as a function of laser energy, crater size, and gate delay.

Laser Induced Breakdown Spectroscopy

The laser ablation experiments were performed at the Center for Renewable Carbon LIBS station user facility [18]. The LIBS station uses a Quantel Big Sky CFR Ultra Q-Switched ND: YAG laser with a frequency doubled, wavelength output of 532 nm. According to specification from the manufacturer, the maximum laser energy is 50 mJ per pulse. The pulse duration is four ns, and the repetition rate is variable from 1 to 20 Hz. The beam diameter at the exit is 5 mm, and the fluence is 0.51 J/cm^2. When the laser is operated at 2 Hz, all the processes such as plasma formation, optical emission, gated detection, data collection, and analysis are completed within 500 ms before the next pulse arrives at the sample. The LIBS station setup included the laser, spectrometer, camera, digital focal point alignment, and XY-Z manipulation stage. The entire station is computer operated through a single software package developed by the facility technician. The sample stage uses both a Keyence INC. Autofocusing alignment laser (632 nm) and digital X-Y-Z manipulation stage to maintain an optimal laser focal point and sample position. At the exit of the laser head, the beam travels a horizontal distance of 12 inches where the incident beam is then reflected vertically down at an angle of incidence of 45 degrees. The mirror use in this setup is a right-angle prism Nd: YAG Mirror, for 532 nm and 1064 nm. The beam is then focused using a 1-inch diameter UV-Fused Silica Plano-Convex Lens with a focal length of 200.0 mm and a V-Coat for 532/1064 nm. The beam is focused normal to the sampleâĂŹs surface. The ablation-induced plasma formation is viewed using a single low O-H optical fiber. The single fiber optic is at a fixed position separated from the sample stage and views the sample at a 45-degree angle from the laser line. The fiber delivered light to a broadband Echelle spectrometer from Catalina Scientific model SE 200A. The model SE 200A uses the High Order dispersion model that is high resolution, has a spectral range of 190 nm to 1100 nm, and a spectral resolution of the broadband spectrum of 0.04 nm. The spectrometer separates light using multiple orders of diffraction into wavelengths, and the resulting spectra are linked, linearized, and reconstituted using the KestrelSpec^{TM} software. This software interfaces with the spectrometer and the ICCD detector to the computer where the in-house software is used to control the laser and stage. The spectrometer connects directly to an Andor Technologies 1024x1024 pixel intensified 2D-charged coupled (ICCD) camera. The spectral data is collected at a gate delay of 0.5 μs and a gate width of 750 μs. All laser ablation experiments were performed in the atmosphere.

LIBS Parameter Analysis

Peaks of Interest

The elements of interest in this work are only W and He. Figure **??** shows the LIBS OES spectra of PC-W specimen 1 (control). In this figure, the full broadband spectra, between 200 nm and 800nm, is shown. Over these wavelengths, the spectra are rich and dense with multiple peaks. Due to the dense nature of the small lines in this spectra, light impurities, like He, are difficult to identify. For simplicity, only three lines will be referenced for the remainder of this work, which we define as peaks of interest (POIs). The first peak is the brightest peak, as shown in the dense

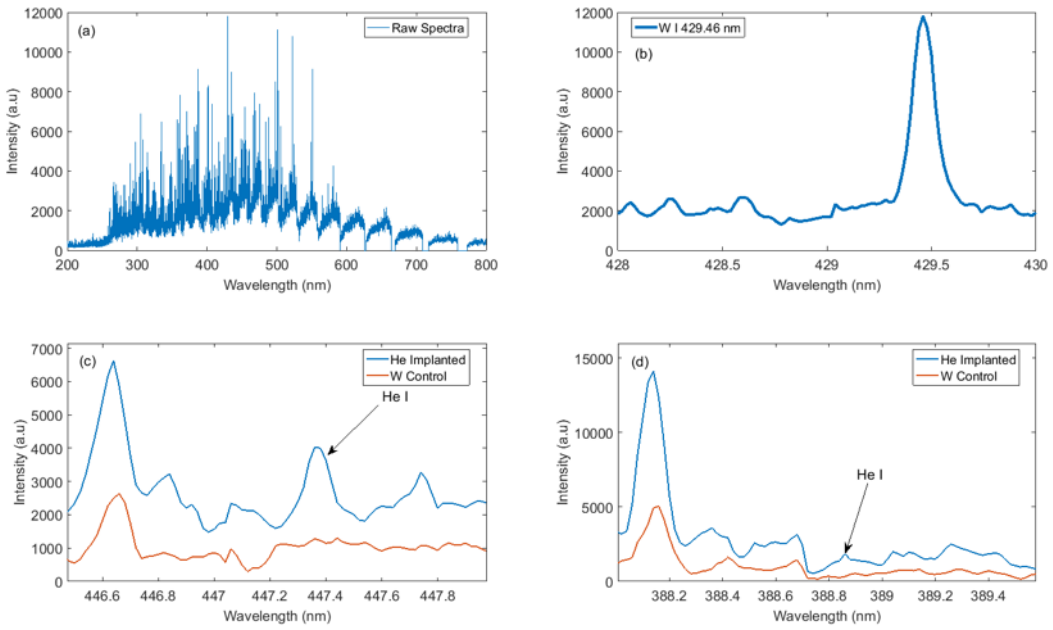

Figure C.1: The reconstituted spectra (a) from the W control (Sample 1) without He implantation. The most intense peak is the W I line at 429.46 nm. A magnified view of the reconstituted spectra (b) from the W control (Sample) without He implantation. The major peak within this region of wavelengths is the W I line at 429.46 nm. The reconstituted spectrum (c) focusing on wavelengths around the W I line at 429.46 nm and He I line at 447.4 nm, which compares the W control, orange, (Sample 1) without He implantation and a He implanted specimen, blue (Sample 4). The reconstituted spectrum (d) focusing on wavelengths around the W I line at 403.57 nm and He I line at 388.86 nm, which compares the W control, orange, (Sample 1) without He implantation and a He implanted specimen, blue (Sample 4).

spectra of Figure C.1(a) and more closely in Figure C.1(b), and is the W I peak at 429.46 nm. This neutral W I line was used instead of the others due to its prominence. The second and third POI lines are associated with helium, namely He I at 388.86 nm and 447.14 nm, respectively. Figure C.1(c) and Figure C.1(d) shows the LIBS OES spectra of PC-W specimen 4, which was implanted with He. These two neutral He I lines, shown in Figure C.1(c) and Figure C.1(d), were used in our analysis because the NIST atomic standard database, Applied Photonics^{TM} LIBS

spectral database and best practices [34], and the University of Delaware OSCAR LIBS database [35], provided sufficient evidence that those lines can be clearly identified as helium using LIBS. Additional work performed by Eseller et al. [36] demonstrated that 447.14 nm, 587.56 nm, and 388.86 nm are detectable and that the 587.56 nm line was dominant. However, in our investigation of specimens 2-4, the 587.56 nm line was not present. However, the POIs at 447.14 nm and 388.86 nm were present.

Signal Analysis

Select signal analysis was performed to determine the shot-to-shot variation [34]. This analysis was specifically focused on the W I 429.46 nm line to ascertain the significance of the laser fluctuations. A single laser ablation was performed, and then specimen 1 (the control) was translated for another laser ablation at a different surface location to evaluate the repeatability of the signal. This was performed over 40 times at a laser energy of 50 mJ and gate delay of 0.5 μs, with a gate width of 750 μs. The peak intensity of the W I 429.46 nm line for all 40 ablations was measured, and the standard deviation was calculated. Over the 40 ablations for the W I line (429.46 nm) the average peak intensity and the standard deviation are $1.18\text{x}10^4$ a.u. and 127 a.u., respectively. A spectral window of 3-5 nm to the left and the right of the POI was averaged, and then this average was subtracted from the full spectral window, including the peak to remove the background. This was done to isolate each POI from shot-to-shot variation and laser fluctuation. It is evident from Figure C.1, that the signal is dominated by the continuum background and background noise. The background noise was observed in each spectrum, for each specimen, with and without He implantation. This can be largely contributed to performing the experimental measurements in an ambient atmosphere. In specimens 2-4 (which were implanted with He), the signal-to-noise ratio of each of the POIs at 429.46 nm, 388.86 nm, and 447.14 nm were $\sim$10.64, $\sim$2.34, and $\sim$2.35, respectively.

Per Pulse Energy Analysis

Figure C.2 shows the experimentally measured spectral intensities of the three POIs in the PC-W Specimen 2 following 200 keV He implantation to a fluence of $1\text{x}10^{23}$ ions m^{-2}, as a function of laser energy. The laser energy was varied incrementally from 4 mJ (lowest laser setting) to 50 mJ (highest laser setting) with an increment of 0.5 mJ, and the laser energy measured using a Coherent FieldMax II-Top Laser Power and Energy Meter. The measured peak intensity values shown in Figure C.2 are the result of averaging five pulses at each laser energy setting. The He I lines show a slight signal intensity increase with increasing laser energy and essentially reach a maximum value at 50 mJ. The W I line intensity increased more dramatically with increasing laser power. 50 mJ was selected as the laser power for the subsequent results presented in this article, with the belief that this pulse energy would result in a robust and consistent signal.

Gate Delay

Figure C.3 shows the spectral intensities of the three POIs in PC-W Specimen 3 following 200 keV He implantation to a fluence of $1\text{x}10^{23}$ ions $\text{m}-2$, as a function of the gate delay used for the OES. The gate delay was initially set to 0.5 μs after laser impact and incremented by 0.1 μs for

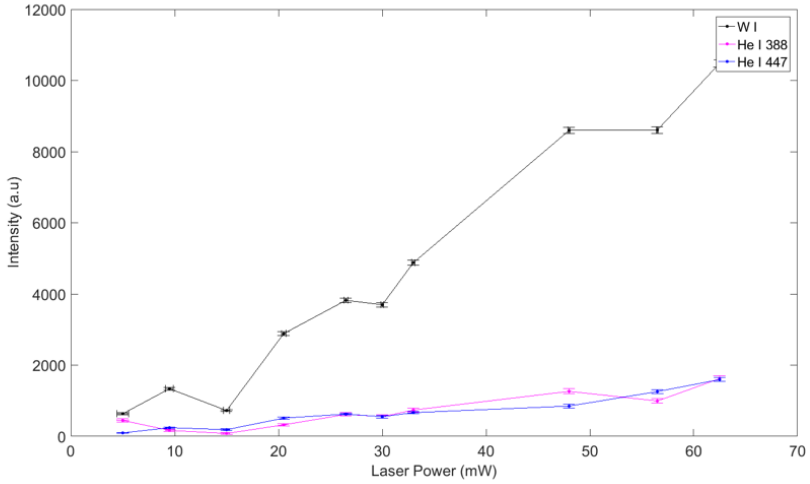

Figure C.2: The variation in W I (Red), He I 388.86 nm (Magenta), and He I (Blue) signal intensity as a function of laser power. Sample 2 was used for this assessment.

11 steps, 0.5 μs for five steps, and 1 μs for the remaining steps, which provides an assessment of the measured signal intensity with variation in gate delay from 0.5 to 11 μs. While there is some scatter, particularly for the shorter time delays, generally the highest intensity of the PC-W and He POIs occurs at 1.0 μs. The relatively quick time delay of both He I signals in comparison to the W I POI indicates other contributing factors. In this LIBS facility, the gate delay could not be lower than 0.5 μs to avoid potential damage to the ICCD (laser light exposure), and thus it was difficult to determine whether an optimal gate delay at shorter times might exist. It is known, however, that the He light intensity decays faster than W, due to differences in the recombination behavior of W compared to He. Jobiliong et al. [37] have previously shown the gate delay evolution of He intensity, in which the He intensity increased and then decreased quickly between 200 ns to 500 ns. It should also be noted that the gate width was not varied. A gate width of 750 μs is considered long and is known to influence line intensity as well as the background. The gate delay was investigated and had found that there needs to be more experiments performed at lower gate delays. He has been shown to decay quick in comparison to W in the laser-induced plasma. In future experiments, a temporal evolution of the He intensity will be investigated. We are currently establishing a new laser station at ORNL, and in the future we will re-evaluate the gate width, as well as smaller gate delays.

Crater Analysis

Depth and width measurements of the laser ablation site were performed on an unexposed,unpolished PC-W control sample (Specimen 1) following multiple laser pulses. Figure C.4 shows a schematic illustrating the total pulse accumulation at each laser ablation site on this sample in which the distance between sites is 0.25 mm both laterally and vertically. A Keyence Digital Confocal Microscope was used to provide a 3-D map of the ablation site from which the depth and width in each location were determined. The first step in this analysis was to accurately focus the camera into the deepest point at the site and capture an image. The focal plane was then moved to the

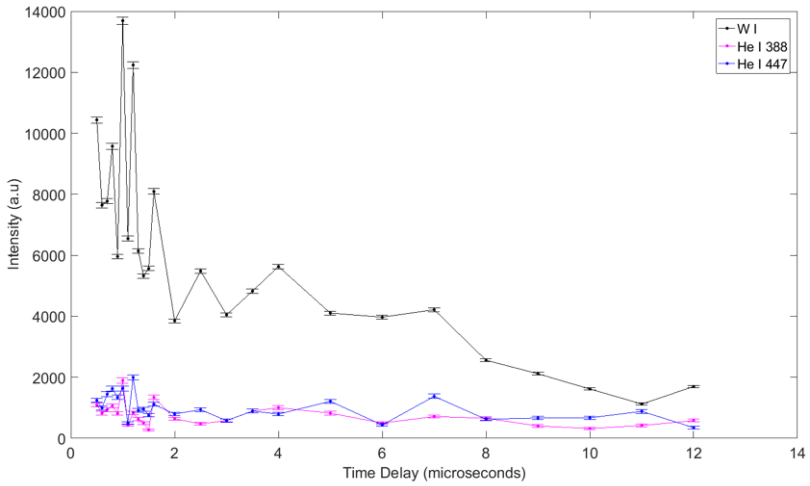

Figure C.3: The change in W I (Red), He I 388.86 nm (Magenta), and He I 447.15 nm (Blue) signal intensity as a function of an increase in gate delay, as measured during laser ablation on W Sample 3.

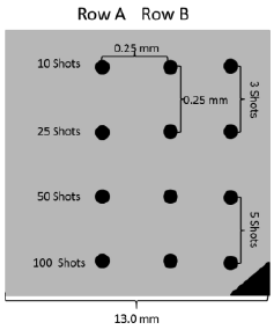

Figure C.4: Schematic illustrating the laser ablation orientation and laser shot accumulation for each ablation depth.

surface surrounding the site, and another image was captured. It is important to note that focusing on the surface was often difficult due to surface roughness following laser exposure, which we attribute to a combination of droplet formation as well as redeposition of ablated material. The Keyence software stitched together a z-stack of images starting from the bottom focal point to the top surface, using the position of the two images, rendering a 3-dimensional (3-D) image as shown in Figure C.5. After rendering the 3-D image, a cross-section line analysis tool was used to determine depth and width of the ablation sites. From this analysis, the depth and width of the location shown in Figure C.5 were determined to be 9.23 μm and 185 μm, respectively, following 100 shots. Table C.2 also provides a summary of the resulting average depth and width per 50 mJ laser ablation pulse, respectively.

Table C.2 presents the average, experimentally measured depth and width per shot, but it is important to point out that the results reported in Table C.2 do not follow a linear trend with the number of laser ablation shots. Figure C.6 plots the experimentally measured accumulated depth and width data presented in Table C.2, along with a comparison to both a linear and

Table C.2: The depth and width measurements performed on cumulative laser ablations for W Sample 1 without He implantation

Specimen 1					
	Row 1		Row 2		Avg. per shot
Ablations	**Depth (μm)**	**Width (μm)**	**Depth (μm)**	**Width (μm)**	**Depth (μm)**
100	8.69	192	9.23	185	0.22±0.13
50	7.97	178	6.22	175	
25	3.07	147	2.88	128	**Width (μm)**
10	2.15	78.9	1.78	98.7	9.01±6.97
5	1.68	64.5	1.62	71.9	
3	1.25	58.2	1.38	62.1	

polynomial fit. The polynomial fit showed a better agreement with the sparse experimental data and provides a continuous function capturing the data trend. The depth and width of a single ablation cannot be experimentally measured using the Keyence Digital Microscope due to focusing limits, so the polynomial fit was used to interpolate the depth and width of a single ablation using information from multiple ablations. The depth and width of a single ablation, from the polynomial interpolation, was 0.18 μm and 5.17 μm, respectively. The estimated depth and width, from the experimentally measured values, for a single ablation using a linear averaging technique, are 0.22 $\pm$ 0.13 μm and 9.01 $\pm$6.97 μm. The polynomial extrapolation compares nicely with the calculated average; however, the polynomial values were used for the remaining experiments. The uncertainty was determined by taking the standard deviation of the measured depths and widths.

LIBS Results of He Depth Profiling

Based on this depth analysis of the laser ablation shots, we have analyzed the depth dependence of the He signal intensity in PC-W specimen 4 following 200 keV He ion implantation to a fluence of about 10^{23} m^{-2}. Figure C.7 shows the measured He I intensity a POI at 447.15 nm s a function of the number of laser ablations for Specimen 4. Figure C.7a shows that the He I intensity initially increases from two to four ablations, and then decreases to a background level by the tenth ablation. Figures C.7b and C.7c plot the He I intensity versus the number of accumulated laser ablations and depth, respectively. Figure C.7d plots the helium implantation profile calculated by SRIM [33] for 200 keV He implantation into W. The calculated depth distribution of the implanted range of 200 keV He on W does not include any assessment of He diffusion during or after the implantation, nor consider any possible channeling or crystallographic effects that could impact the depth profile.

For this 200 keV He ion implantation, SRIM predicts that 0.0124 Atoms/Ions of tungsten are sputtered from the surface, which results in a predicted sputtering of 1.96 monolayers at an implanted helium fluence of 1x10^{23} He m^{-2}. While He is highly mobile as an interstitial atom in W, it is likely that it rapidly becomes trapped as a substitutional atom in one of the vacancies created upon slowing down, which would substantially decrease the helium diffusivity. Figure C.7d shows that SRIM predicts the range for 200 keV He+ ions implanted into PC-W with a peak

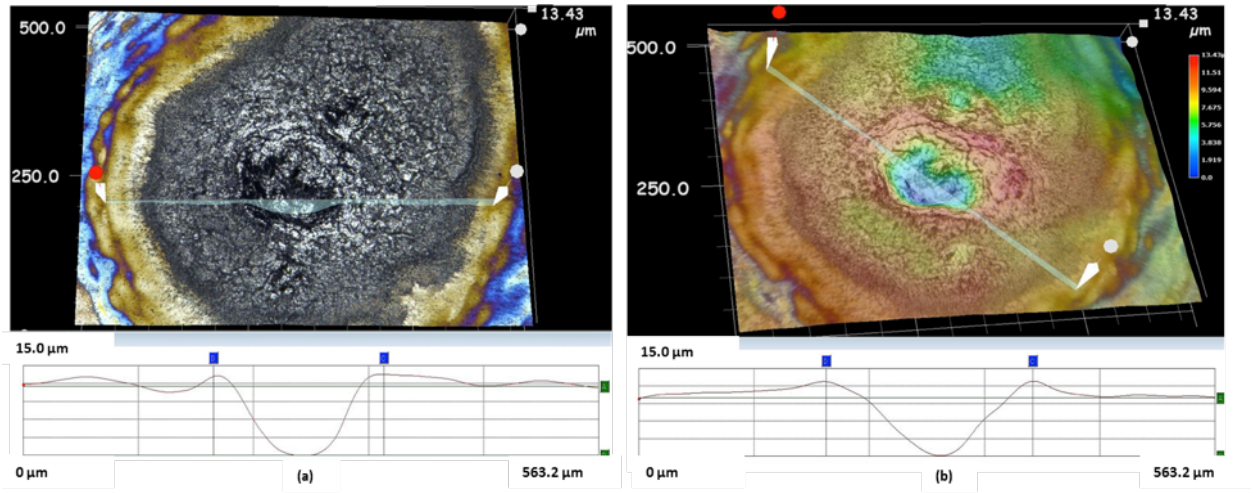

Figure C.5: Digital confocal microscope images of an ablation site on W Sample 1, without He exposure, following 100 accumulated laser shots. (a) side-angled to show the depth of the cumulative laser ablation, (b) top down view of the crater. The color map in (a) shows changes in surface topography (height). (b) shows the natural discoloration and surface damage from the laser impact. The white line on both images show the location of a surface height trace, which is shown below each image.

about 500 nm below the surface and that the range extends to about 750 nm. Figure C.7c shows the corresponding measured He I peak intensity as a function of depth resulting from accumulated laser ablations. The cumulative laser ablations were converted to depth using the results from the observed 3rd order polynomial scaling behavior. This leads to a depth correlation for 2, 4, 6, 8, and 10 ablations of 0.35, 0.67, 1.02, 1.35, 1.67 Îijm depth, respectively, based on the interpolation shown in Figure C.6a. The horizontal error illustrated in Figure C.7c is the mean standard deviation from the experimentally measured ablations in Section 2.4.4. The vertical error is the standard deviations of the entire signal for the He I 447 nm POI.

After a single laser ablation, a crater results, and the corresponding He intensity is measured. However, it is important to note, as indicated in Figure C.6, that the crater expands in both depth and width with each laser shot. The width of the crater increases much more rapidly than that of the depth over multiple laser ablations. For example, the initial laser pulse creates a crater of Z depth and X width. A subsequent laser pulse results in a crater of increased depth, Z+deltaZ and increased width X+deltaX. Hence, the He signal in the subsequent pulse will contain both âĂIJnewâĂİ depth information, as well as a contribution of He from the previous (but now wider) layer of material. Thus, in converting the measured He I signal per laser pulse to a depth dependence, it is imperative to use an iterative approach. Such that the average concentration of He from each previous âĂIJknownâĂİ layer is removed (since the horizontal expansion with subsequent laser pulses has been measured), and the He concentration as a function of depth is corrected for the horizontal spreading inherent in subsequent laser pulses. The widths and depths interpolated by the polynomial function, Figure C.6, for 2, 4, 6, 8, and 10 accumulated ablations where used to calculate the Z+deltaZ and X+deltaX, and for simplification, a cylindrical volume was assumed. To clarify, after the first set of ablations (2 total), a crater is formed with a depth and width of 0.35 μm and 10.28 μm, respectively. Then the second set of ablations takes place creating

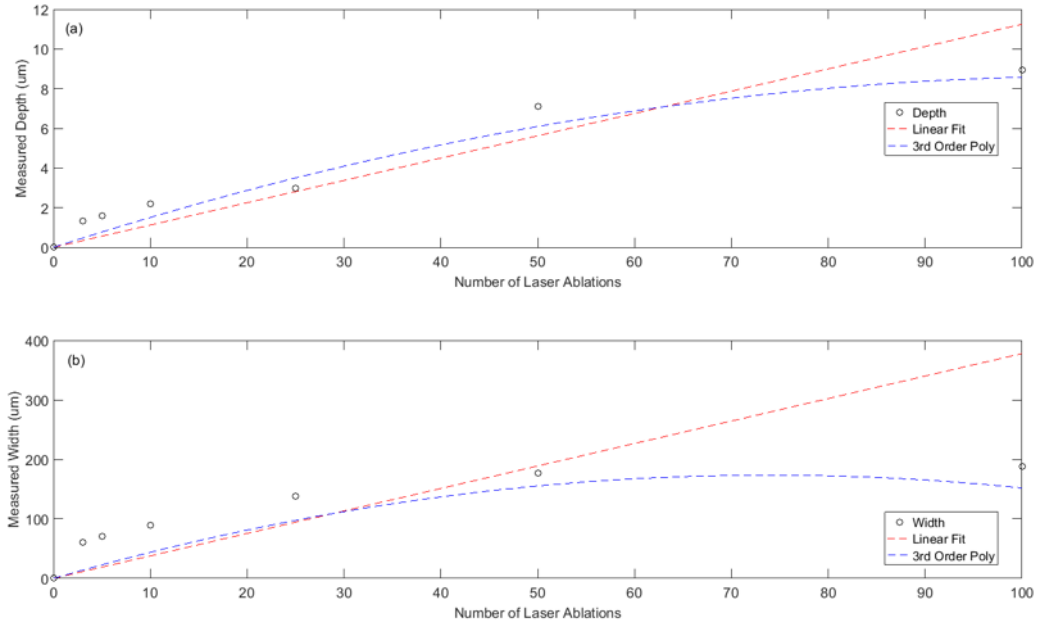

Figure C.6: The measured a) depth and b) width of the laser ablation crater, as a function of the number of cumulative 50 mJ laser ablation exposures. The experimentally measured depth and width values are fit to a linear (red) or 3rd order polynomial (blue) in order to establish the accumulated ablation volume trend.

a larger crater with a depth of 0.69 μm and a width of 20.31 μm. The X+deltaX were determined and was used to correct the He intensity for the horizontal spreading. This calculation was done for all accumulated ablations. Figure C.8 illustrates the expansion of the accumulated crater in depth and width with additional laser pulses. In Figure C.8, the area (blue region) is the volume ablated due to width expansion. The blue region of the fourth laser shot is spread across layers 1-3, which signifies the volume where there is a potential for the release of He across those layers (depths).

Figure C.9 shows the resulting corrected He intensity as a function of depth (black), as compared to the original depth dependence (red). As indicated in the preceding paragraph, the corrected He intensity is increased at shallower depths, due to the broadening of the crater with subsequent laser ablations that releases additional He near the surface. Correspondingly, the corrected intensity decreases at deeper crater depths, such that the correction procedure that has been developed ensures that the total He intensity is conserved. It is important to note that while this initial correction methodology does provide a basis to modify the measured helium depth profile, a large uncertainty exists, which we plan to further evaluate in future research by performing numerical simulations of the helium profile during implantation and laser ablation to provide a better metric for comparison than the SRIM implantation profile. As well, we plan future experiments with a cross-comparison of experimental measurement techniques to further confirm the depth profiling capability of LIBS to detect H below tungsten surfaces.

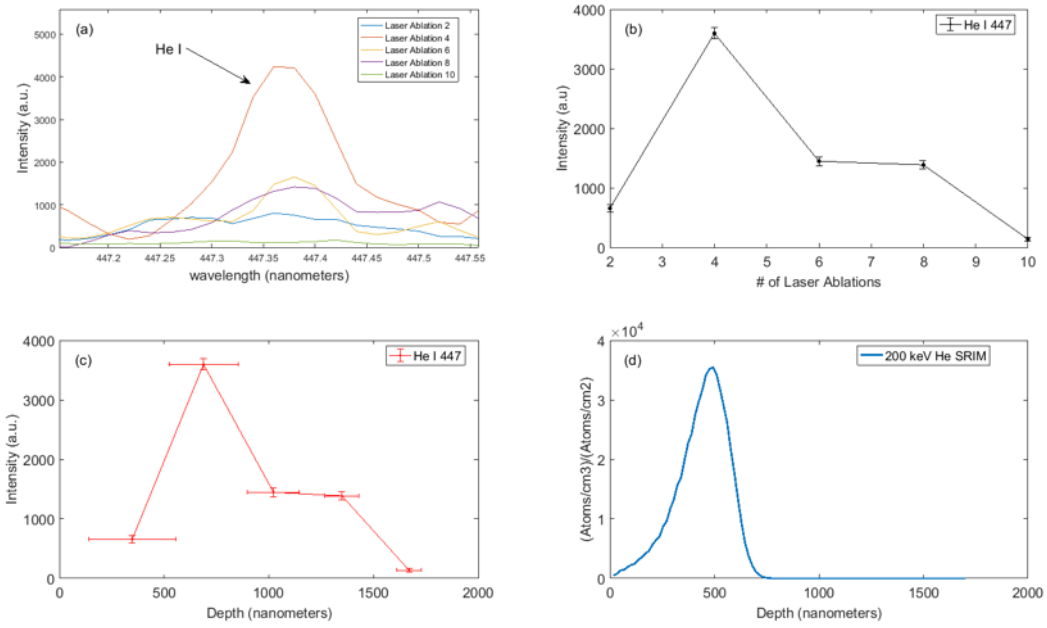

Figure C.7: (a) The raw data of the He I 447.14 nm over 10 total ablations, in which the He I intensity initially increases from shots 2 to 4, and then decreases with increasing number of ablations. (b) The integrated He I 447.14 nm signal intensity measured from sample 4 as a function of the number of laser ablation shots. (c) The He I 447.15 nm signal intensity measured from Sample 4, re-plotted as a function of depth below the surface. (d) The implanted He distribution as calculated by SRIM [33] for 200 keV He ions in W

Conclusion

We have performed a systematic series of LIBS measurements that demonstrate the ability to not only identify He from PC-W samples that were ion irradiated with 200 keV He ions but also to assess the relative He intensity as a function of depth. Measurements include an evaluation of laser operating parameters to determine the impact on the He I signal, as well as an analysis of the depth resolution per laser ablation pulse. These studies indicated that a laser power of 50 mJ and a gate delay of 0.5 μs provided a good signal to noise ratio for the selected W and He I peaks of interest, and provided conclusive measurement of He implanted in W. The gate width was not varied in this experiment, which could influence the overall He intensity. Future experiments, which we plan to perform with laser shots under an ultra-high vacuum environment, will be performed to investigate this influence. The laser ablation crater depth and width was analyzed as a function of the number of laser ablation shots. These results showed that the crater volume grows in a non-linear fashion, in which the average depth of 0.18 Îijm and width of 5.17 μm of a single ablation was determined. A proof-of-principle experiment was performed to determine a relative depth profile for He implanted in W, and did identify a clearly distinguishable peak in the helium intensity at a depth of about 700 nm below the surface. A comparison to SRIM predictions of the depth profile of the implanted He are in reasonably good agreement with our measured He I intensity with depth, providing confidence in the ability to perform future depth-resolved He concentration measurements in W.

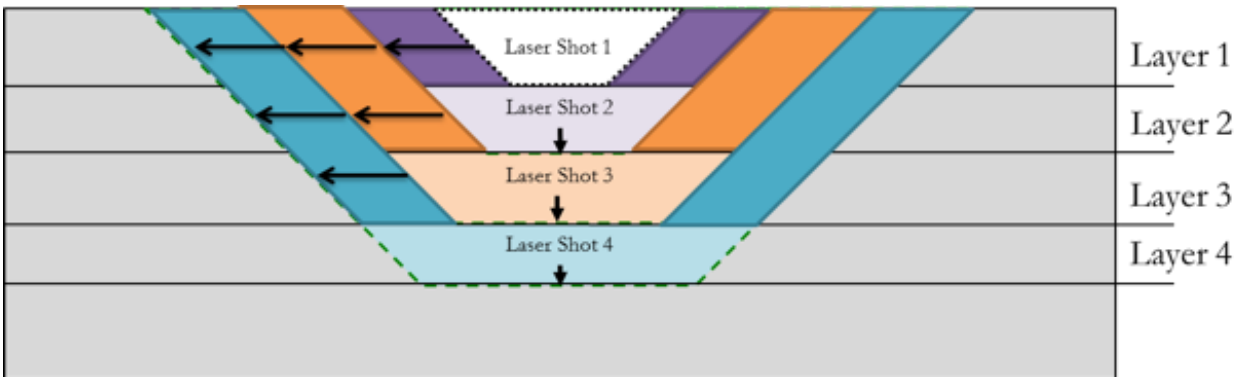

Figure C.8: An illustration of the crater volume with increasing number of ablations that have been used to perform a volume correction analysis. The white region represents the first ablation. The purple region represents the second set of ablations. The dark purple represents the width expansion and the light purple represents the depth expansion. The dark orange and blue represent the width expansion for subsequent laser ablations. These dark regions show that it ablates material from previous layers.

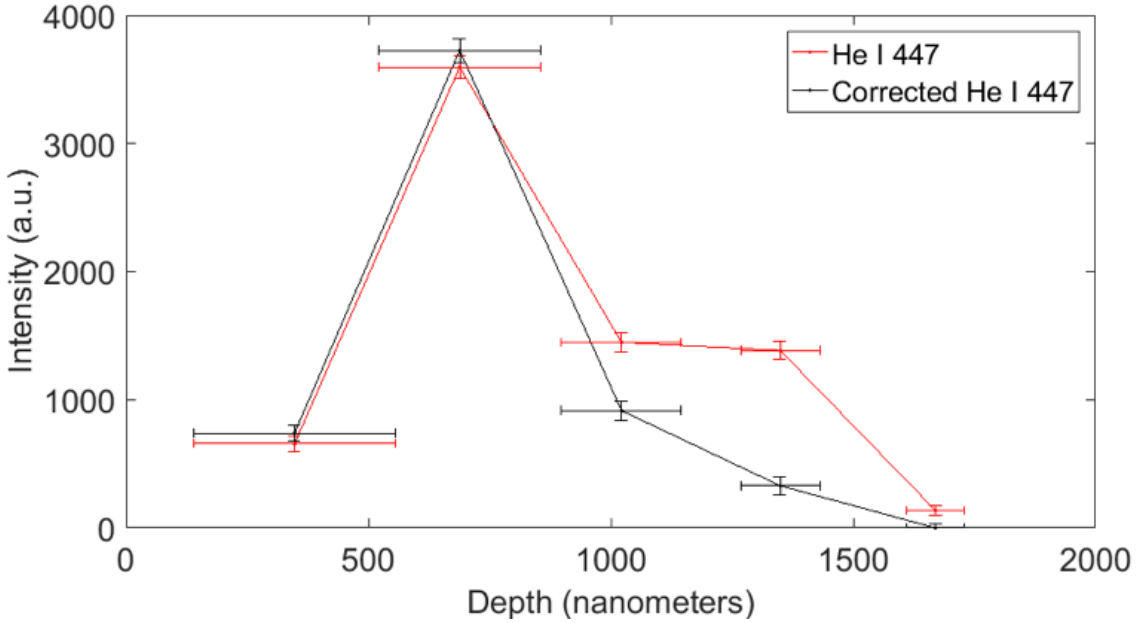

Figure C.9: Signal intensities corrected for crater width expansion are shown in the black symbols/lines, as compared to the measured signal intensity (red points/lines) from Figure C.7b.

Future experiments will be conducted in an ultra high vacuum environments, and compare to other analysis techniques to confirm the self-consistency of the results.

Acknowledgements

The research was sponsored by the US Department of Energy Office of Fusion Energy Science under grant DE-AC05-00OR22725 with UT-Battelle LLC, and grant DOE-DE-SC0006661 with the University of Tennessee, Knoxville. This research was also sponsored by the Laboratory Directed Research and Development Program of Oak Ridge National Laboratory, managed by UT-Battelle, LLC, for the U.S. Department of Energy.

References

C.1 Davis, J., et al., Assessment of tungsten for use in the ITER plasma facing components. Journal of nuclear materials, 1998. 258: p. 308-312.
C.2. Pitts, R., et al., A full tungsten divertor for ITER: physics issues and design status. Journal of Nuclear Materials, 2013. 438: p. S48-S56.
C.3. Wirth, B., et al., Fusion materials modeling: Challenges and opportunities. MRS bulletin, 2011. 36(03): p. 216-222.
C.4. Iwakiri, H., K. Morishita, and N. Yoshida, Effects of helium bombardment on the deuterium behavior in tungsten. Journal of nuclear materials, 2002. 307: p. 135-138.
C.5. Nishijima, D., et al., Suppression of blister formation and deuterium retention on tungsten surface due to mechanical polishing and helium pre-exposure. Nuclear fusion, 2005. 45(7): p. 669.
C.6. Ueda, Y., et al., Simultaneous irradiation effects of hydrogen and helium ions on tungsten. Journal of Nuclear Materials, 2009. 386: p. 725-728.
C.7. Miyamoto, M., et al., Microscopic damage of tungsten exposed to deuteriumâĂŞhelium mixture plasma in PISCES and its impacts on retention property. Journal of Nuclear Materials, 2011. 415(1): p. S657-S660.
C.8. Baldwin, M., et al., The effects of high fluence mixed-species (deuterium, helium, beryllium) plasma interactions with tungsten. Journal of Nuclear Materials, 2009. 390: p. 886-890.
C.9. Ueda, Y., et al., Helium effects on tungsten surface morphology and deuterium retention. Journal of Nuclear Materials, 2013. 442(1âĂŞ3, Supplement 1): p. S267-S272.
C.10. Donovan, D., et al., Characterization of a compact ECR plasma source and its applications to studies of helium ion damage to tungsten. Physica Scripta, 2016. 2016(T167): p. 014040.
C.11. Donovan, D.C., et al., Characterization of helium bubble growth in tungsten exposed to low-flux plasmas. 2014, Sandia National Laboratories (SNL-CA), Livermore, CA (United States).
C.12. Woller, K., et al., Helium concentration in tungsten nano-tendril surface morphology using Elastic Recoil Detection. Journal of Nuclear Materials, 2013. 438: p. S913-S916.
C.13. Alimov, V.K., et al., The effect of displacement damage on deuterium retention in ITER-grade tungsten exposed to low-energy, high-flux pure and helium-seeded deuterium plasmas. Journal of Nuclear Materials, 2012. 420(1): p. 370-373.
C.14. Lanford, W., Analysis for hydrogen by nuclear reaction and energy recoil detection. Nuclear

Instruments and Methods in Physics Research Section B: Beam Interactions with Materials and Atoms, 1992. 66(1-2): p. 65-82.
C.15. Pisonero, J., et al., Quantitative depth profile analysis of boron implanted silicon by pulsed radiofrequency glow discharge time-of-flight mass spectrometry. Solar Energy Materials and Solar Cells, 2010. 94(8): p. 1352-1357.
C.16. Henriksson, K.O., et al., The depths of hydrogen and helium bubbles in tungsten: a comparison. Fusion science and technology, 2006. 50(1): p. 43-57.
C.17. Radziemski, L.J. and D.A. Cremers, Handbook of Laser Induced Breakdown Spectroscopy. 2006, John Wiley & Sons, West Sussex, England.
C.18. Martin, M.Z., et al., Investigation of laser-induced breakdown spectroscopy and multivariate analysis for differentiating inorganic and organic C in a variety of soils. Spectrochimica Acta Part B: Atomic Spectroscopy, 2013. 87: p. 100-107. C.19. Singh, J.P. and S.N. Thakur, Laser-induced breakdown spectroscopy. 2007: Elsevier.
C.20. Noll, R., Laser-induced breakdown spectroscopy, in Laser-Induced Breakdown Spectroscopy. 2012, Springer. p. 7-15. C.21. Nagy, T.O., et al., Atomic emission stratigraphy by laser-induced plasma spectroscopy: Quantitative depth profiling of metal thin film systems. Applied Surface Science, 2014. 302: p. 189-193.
C.22. Li, T., et al., Laser-induced breakdown spectroscopy for on-line control of selective removal of cobalt binder from tungsten carbide hardmetal by pulsed UV laser surface ablation. Applied surface science, 2001. 181(3): p. 225-233.
C.23. Harilal, S.S., et al., Reactivity of lithium exposed graphite surface. Applied Surface Science, 2009. 255(20): p. 8539-8543.
C.24. Aguilera, J., C. Aragon, and F. Penalba, Plasma shielding effect in laser ablation of metallic samples and its influence on LIBS analysis. Applied surface science, 1998. 127: p. 309-314.
C.25. Farid, N., et al., Laser-induced breakdown spectroscopic characterization of tungsten plasma using the first, second, and third harmonics of an Nd: YAG laser. Journal of Nuclear Materials, 2013. 433(1): p. 80-85.
C.26. Piip, K., et al., LIBS analysis of tungsten coatings exposed to Magnum PSI ELM-like plasma. Journal of Nuclear Materials, 2015. 463: p. 919-922.
C.27. Paris, P., et al., Determination of elemental depth profiles by multi-spot averaging technique of LIBS spectra. Fusion engineering and design, 2011. 86(6): p. 1125-1128.
C.28. Mercadier, L., et al., Analysis of deposited layers on plasma facing components by laser-induced breakdown spectroscopy: Towards ITER tritium inventory diagnostics. Journal of Nuclear Materials, 2011. 415(1): p. S1187-S1190.
C.29. Mercadier, L., et al., Plume segregation observed in hydrogen and deuterium containing plasmas produced by laser ablation of carbon fiber tiles from a fusion reactor. Spectrochimica Acta Part B: Atomic Spectroscopy, 2010. 65(8): p. 715-720.
C.30. Parish, C.M., et al., Effect of tungsten crystallographic orientation on He-ion-induced surface morphology changes. Acta Materialia, 2014. 62: p. 173-181.
C.31. Meyer, F., et al., Flux threshold measurements of He-ion beam induced nanofuzz formation on hot tungsten surfaces. Physica Scripta, 2016. 2016(T167): p. 014019.
C.32. Meyer, F.W., et al., Recent activities at the ORNL multicharged ion research facility (MIRF). Proceedings of ECRIS2010, Grenoble, France, http://accelconf. web. cern.
ch/AccelConf/ECRIS2010/papers/mocobk04. pdf, 2010.
C.33. Ziegler, J.F., M.D. Ziegler, and J.P. Biersack, SRIMâĂŞThe stopping and range of ions

in matter (2010). Nuclear Instruments and Methods in Physics Research Section B: Beam Interactions with Materials and Atoms, 2010. 268(11): p. 1818-1823.
C.34. El Haddad, J., L. Canioni, and B. Bousquet, Good practices in LIBS analysis: Review and advices. Spectrochimica Acta Part B: Atomic Spectroscopy, 2014. 101: p. 171-182.
C.35. S. Rock, A.M., C. Sabanayagam, N. Melikechi, Laser-Induced Breakdown Spectroscopy Elemental Spectra Database.
C.36. Eseller, K.E., et al., Helium detection in gas mixtures by laser-induced breakdown spectroscopy. Applied optics, 2012. 51(7): p. B171-B175.
C.37. Jobiliong, E., et al., Spectral and Dynamic Characteristics of Helium Plasma Emission and its Effect on a Laser-Ablated Target Emission in a Double-Pulse Laser-Induced Breakdown Spectroscopy (LIBS) Experiment. Applied spectroscopy, 2015. 69(1): p. 115-123.

Vita

Guinevere Chamberlain Shaw was born in Washington D.C. to the parents of Tammy Lea Chamberlain and Sumner Taylor Shaw. She attended Franklin County High School, where she was a captain of the JROTC Color Guard and during her senior year made varsity swim team. She attended Florida Institute of Technology were she walked onto the woman's varsity rowing team. After the completion of her first year, she was awarded an athletic scholarship for NCAA Woman's D-II Varsity Rowing. In December 2012, she earned a Bachelor of Science degree in Solar, Earth, and Planetary Science. Immediately following graduation, she accepted an internship at Oak Ridge National Laboratory. During her internship, she was accepted into the Bredesen Center for Interdisciplinary Research and Graduate Education PhD program in Energy Science and Engineering. Guinevere will earn her PhD in Energy Science and Engineering on August 2018